



The  
University  
Of  
Sheffield.

# **Two-Colour Temperature Measurement Based on High Speed Imaging**

**Mr. Zhen Ma**

**Combustion and Flow Diagnostics Research Group**

**Department of Mechanical Engineering**

*This thesis is submitted to the University of Sheffield for the degree of Doctor of Philosophy,*

2016

# CONTENTS

<b>LIST OF FIGURES.....</b>	<b>V</b>
<b>LIST OF TABLES.....</b>	<b>XII</b>
<b>NOMENCLATURE .....</b>	<b>XIII</b>
<b>ABSTRACT .....</b>	<b>XVIII</b>
<b>DECLARATION.....</b>	<b>XIX</b>
<b>ACKNOWLEDGEMENT .....</b>	<b>XX</b>
<b>PUBLISHED WORKS.....</b>	<b>XXI</b>
<b>INTRODUCTION .....</b>	<b>1</b>
1.1.    MOTIVATION .....	1
1.2.    OBJECTIVES.....	4
1.3.    OUTLINE OF THESIS .....	6
<b>2.    LITERATURE REVIEW .....</b>	<b>8</b>
2.1.    INTRODUCTION .....	8
2.2.    COMBUSTION AND FLAME .....	8
2.3.    THE CORRELATION AMONG THE TRUE, COLOUR AND BRIGHTNESS TEMPERATURES.....	17
2.4.    SILICON CARBIDE MATERIAL .....	19
2.5.    REVIEW OF TEMPERATURE MEASUREMENT .....	20
<b>3.    BACKGROUND OF TWO-COLOUR METHOD.....</b>	<b>28</b>
3.1.    DIGITAL IMAGE PROCESSING .....	28
3.2.    THEORETICAL BASIS OF TWO-COLOUR MEASUREMENT .....	32
3.3.    CALIBRATION OF TWO-COLOUR SYSTEM .....	35
3.4.    SUMMARY .....	53
<b>4.    OPTICAL STUDY OF SOOT FLAME TEMPERATURE FOR DIESEL-IN-WATER EMULSION DROPLET COMBUSTION .....</b>	<b>55</b>

4.1.	BACKGROUND OF THE DROPLET COMBUSTION .....	55
4.2.	EXPERIMENTAL METHOD.....	58
4.3.	RESULTS AND DISCUSSION.....	61
4.4.	SUMMARY .....	88
<b>5.</b>	<b>NUMERICAL ANALYSIS OF SIC FIBRE THERMAL BEHAV-IOUR NEAR FLAME</b>	
	<b>OUTER BOUNDARY LAYER.....</b>	<b>89</b>
5.1.	INTRODUCTION .....	89
5.2.	COMPARISON BETWEEN EXPERIMENTAL AND NUMERI-CAL METHOD .....	91
5.3.	THE PROCEDURE OF NUMERICAL SIMULATION .....	93
5.4.	RESULTS AND DISCUSSION .....	103
5.5.	SUMMARY .....	120
<b>6.</b>	<b>APPLICATION OF SIC FIBRE FOR FLAME CHARACTERISTIC STUDY USING</b>	
	<b>OPTICAL METHOD.....</b>	<b>121</b>
6.1.	INTRODUCTION .....	121
6.2.	EXPERIMENT SETUP AND INSTRUMENTATION .....	123
6.3.	CASE 1: FLAME TEMPERATURE MEASUREMENT.....	128
6.4.	CASE 2: COMPARISON OF OSCILLATION FREQUENCY BETWEEN THE FLAME AND THE FIBRE	
	EMISSION .....	147
6.5.	SUMMARY .....	150
<b>7.</b>	<b>MEASURING TEMPERATURE OF A FLAME PROPAGATING THROUGH A QUARTZ</b>	
	<b>TUBE.....</b>	<b>152</b>
7.1.	INTRODUCTION AND BACKGROUND.....	152
7.2.	EXPERIMENTAL METHOD.....	155
7.3.	RESULTS AND DISCUSSION .....	158
7.4.	SUMMARY .....	181
<b>8.</b>	<b>CONCLUSION AND RECOMMENDATIONS FOR FUTURE WORK .....</b>	<b>182</b>

8.1.	CONCLUSION .....	182
8.2.	AREAS OF FUTURE WORK .....	187
	<b>REFERENCES .....</b>	<b>190</b>

## LIST OF FIGURES

Figure 2-1 Reaction zones in the candle flame [7] .....	9
Figure 2-2 Concentration profiles through a laminar diffusion flame [8] .....	11
Figure 2-3 Schematic of diffusion flame shape varying with flow velocity, presenting the development from a laminar to a turbulent flame [8].....	12
Figure 2-4 The actual cone shape of the premixed flame with the part of flame front at the burning velocity $S_u$ towards the flow $U$ , $\Theta$ is the angle between the flame surface and the direction of flow $U$ .....	15
Figure 2-5 Limiting conditions for various premixed flames [8] .....	16
Figure 2-6 The profile of the fibre emission [17].....	19
Figure 3-1 Architectures of the CCD and CMOS sensors [28] .....	28
Figure 3-2 Structure of colour-filter-array pixel filter .....	30
Figure 3-3 Structure of imaging setup for calibration .....	36
Figure 3-4 Flowchart of the computing system.....	37
Figure 3-5 Schematic setup of spectral evaluation.....	38
Figure 3-6 R, G and B channel responses of the PHOTRON SA-4 system at different wavelengths in the VIS region .....	39
Figure 3-7 Calibration of the tungsten lamp.....	40
Figure 3-8 True temperature of tungsten filament against the brightness temperature that pre-calibrated at wavelength 660nm.....	43
Figure 3-9 Tungsten lamp brightness temperature calibration curve .....	44

Figure 3-10 Variation of the tungsten emissivity along with wavelengths .....	45
Figure 3-11 Distribution of emissivity ratio between the wavelengths 580nm and 630nm .....	46
Figure 3-12 Grey-level ratio (RG) response of the imaging system along with true temperature	47
Figure 3-13 Instrument factor against grey level ratio between R and G channels.....	48
Figure 3-14 Comparison between the measured and the true temperatures of tungsten .....	49
Figure 3-15 The grey level responses of the camera in the R, G and B channels at different exposure time.....	51
Figure 3-16 Measured temperatures of the tungsten filament .....	52
Figure 3-17 Measured temperatures for different focal lengths .....	53
Figure 4-1 The original bundle of SiC fibre .....	59
Figure 4-2 Diameter of filament was imaged and inspected by a digital microscope.....	59
Figure 4-3 Experiment setup .....	60
Figure 4-4 Sequence of backlit images at 1000 fps for 30% D/W droplet. The last image captured droplet micro-explosion. [Note: 1mm=36 pixels] .....	62
Figure 4-5 Lifetime of the single droplet combustion of diesel and of 10% ,20% and 30% diesel-in-water.....	63
Figure 4-6 D/W emulsion droplet before and after micro-explosion. Images (a-b) at 1000 fps, images (c-h) at 40000 fps. [Note: a-b, 1mm=36 pixels; c-h, 1mm=25 pixels].....	65
Figure 4-7 Time history of soot flame at puffing stage when burning 10% D/W emulsion .....	68
Figure 4-8 Time history of soot flame at puffing stage when burning 20% D/W emulsion .....	69
Figure 4-9 Time history of soot flame at puffing stage when burning 30% D/W emulsion .....	70
Figure 4-10 Grey-level of flame illuminations at 10%, 20% and 30% fuel emulsions .....	72

Figure 4-11 Flame extinction due to the droplet micro-explosion at 30% D/W emulsion.....	74
Figure 4-12 Grey-level of flame illumination at micro-explosion .....	75
Figure 4-13 (a) Sample of a droplet flame at 10% D/W emulsion (b) The reproduced flame profile at threshold=0.15 (c) The reproduced flame profile at threshold=0.1 (d) The reproduced flame profile at threshold=0.05 .....	77
Figure 4-14 Visualization of flame temperature using the colour-map, and histograms of temperature distribution at 10 % D/W fuel emulsion [Note:1mm=10 pixels] .....	79
Figure 4-15 Visualization of flame temperature by the colour-map, and histograms of temperature distribution at 20% D/W fuel emulsion [Note:1mm=10 pixels] .....	81
Figure 4-16 Visualization of flame temperature by the colour-map, and histograms of temperature distribution at 30 % D/W fuel emulsion [Note:1mm=10 pixels] .....	83
Figure 4-17 Time-dependent average flame temperature variation in the droplet lifetime in pure diesel fuel .....	85
Figure 4-18 Time-dependent average flame temperature in the droplet lifetime at 10% D/W fuel emulsion .....	85
Figure 4-19 Time-dependent average flame temperature variation in the droplet lifetime at 20% D/W fuel emulsion .....	86
Figure 4-20 Time-dependent average flame temperature variation in the droplet lifetime at 30% D/W fuel emulsion .....	86
Figure 4-21 Average soot flame temperature at the three heights from SiC fibre.....	87
Figure 5-1 Flame temperature measurement using SiC fibre.....	90
Figure 5-2 Flowchart of implementing control-volume base finite difference method .....	94

Figure 5-3 Heat conduction through the fibre along with heat dissipated by convection and radiation .....	95
Figure 5-4 The main difference between differential equation and algebraic equation [1].....	97
Figure 5-5 The nodes and volume elements for the finite difference method.....	98
Figure 5-6 Transient Temperature distribution a) The fibre diameter is 15 $\mu$ m, b) The fibre diameter is 18 $\mu$ m, c) The fibre diameter is 21 $\mu$ m, d) The fibre diameter is 24 $\mu$ m. ....	105
Figure 5-7 Fourier number at the steady-state.....	106
Figure 5-8 Temperature difference distribution .....	107
Figure 5-9 Transient Temperature distribution a). The fibre ambient temperature at $\theta=0.1875$ , b) The fibre ambient temperature at $\theta=0.3125$ , c) The fibre ambient temperature at $\theta=0.4375$ , d) The fibre ambient temperature at $\theta=0.5625$ .....	109
Figure 5-10 Transient Temperature distribution a). The fibre ambient medium heat transfer coefficient $h =1000\text{W}/\text{m}^2.\text{K}$ , b) The fibre ambient medium heat transfer coefficient $h =2000 \text{W}/\text{m}^2.\text{K}$ , c) The fibre ambient medium heat transfer coefficient $h =3000 \text{W}/\text{m}^2.\text{K}$ , d) The fibre ambient medium heat transfer coefficient $h =4000 \text{W}/\text{m}^2. \text{K}$ . ....	111
Figure 5-11 The reduction of the fibre temperature at time=1.729ms .....	112
Figure 5-12 The fibre temperature variation at different locations, a) The heat source temperature variation at frequency 100Hz. b) The heat source temperature variation at frequency 400Hz. a) The heat source temperature variation at frequency 700Hz. a) The heat source temperature variation at frequency 1000Hz. ....	114
Figure 5-13 The variation of the phase angle.....	115
Figure 5-14 Schematic of the global and local discretization errors of the finite difference at a node point [1] .....	117

Figure 5-15 The number of time steps needed to achieve the steady-state at different mesh sizes .....	118
Figure 5-16 Comparison of the fibre temperature responding to the variation of the number of elements at various positions along the fibre at the steady-state.....	119
Figure 6-1 Schematic layout of the combustion unit.....	124
Figure 6-2 High speed camera PHOTRON SA-4 .....	125
Figure 6-3 The diameter of the burner's nozzle .....	125
Figure 6-4 (a) Pentax stereo adapter, (b) Kenko ND filter .....	126
Figure 6-5 The image of SiC fibres' positions at the flame, captured at 50 fps.....	127
Figure 6-6 The arrangement of SiC fibres placed inside the flame, imaged at 500 fps. ....	127
Figure 6-7 (A) Premixed CH <sub>4</sub> +air flames at equivalence ratio conditions (a) $\Phi=0.90$ , (b) $\Phi=0.95$ , (c) $\Phi=1.00$ , (d) $\Phi=1.05$ , (e) $\Phi=1.10$ ; (B) The fibre emission at the corresponding flame in (A)...	129
Figure 6-8 Measured temperature of the hot gas surrounding the corresponding fibre, and the fuel and air mixture at $\Phi=0.9$ .....	131
Figure 6-9 Measured temperature of the hot gas surrounding the corresponding fibre, and the fuel and air mixture at $\Phi=1.0$ .....	132
Figure 6-10 Measured temperature of the hot gas surrounding the corresponding fibre, and the fuel and air mixture at $\Phi=1.1$ .....	133
Figure 6-11 Measured average flame temperature varying with equivalence ratio at different heights of the flame (a) fibre 6 (b) fibre 5 (c) fibre 4 (d) fibre3 .....	134
Figure 6-12 Variation of corrected flame temperature .....	138

Figure 6-13 Corrected flame temperatures based on the previous research proposed correlations .....	139
Figure 6-14 Images of the glowing fibres with different diameters .....	140
Figure 6-15 Fibre temperature varying with the fibre diameter .....	141
Figure 6-16 Structure of the optical path of IMPAC IS 5 .....	143
Figure 6-17 Points are selected in the temperature comparison experiment .....	144
Figure 6-18 Time-varied fibre temperature variation.....	146
Figure 6-19 Image of the flame and glowing fibres was captured using the high-speed camera with a stereo adaptor. The Left image is used for the detection of flame frequency, the right image is used for the calculation of the emission oscillation frequency of the fibres. ....	148
Figure 6-20 Flame intensity oscillation frequency .....	149
Figure 6-21 Intensity oscillation frequency of the fibre emission.....	150
Figure 7-1 Original experimental rig.....	155
Figure 7-2 Experimental rig with the vacuum pump and pressure transducer .....	156
Figure 7-3 Sketch of the experimental configuration for flame temperature measurement; there are two fibres were placed 5mm apart at each end of the tube and one in the tube middle. ....	158
Figure 7-4 Time history of the glowing fibres when flame flows across the fibres at the left-end of the tube. ....	160
Figure 7-5 Time history of the glowing fibres when flame flows across the fibres at the middle of the tube. ....	162
Figure 7-6 Time history of the glowing fibres when flame flows across the fibres at the right-end of the tube. (Note: further image enhancement applied) .....	163

Figure 7-7 Flame propagation rate inside the tube .....	165
Figure 7-8 Comparison of laminar burning rate of Methane/air mixture with other results [89]	166
Figure 7-9 Transient fibre intensity variation.....	168
Figure 7-10 Time-dependent fibre intensity variation at $\Phi=1.1$ . (a), (b) and (c) Experimental heat-up and cool-down cycle at Left-end, Middle and Right-end of the tube. (d), (e) and (d) present the main frequency of intensity oscillation of corresponding fibres .....	170
Figure 7-11 The pressure readings inside the tube at $\Phi= 1.1$ .....	171
Figure 7-12 Time history images of the glowing fibre placed at the middle of the tube during the flame propagation throughout it, the fuel/air mixture (a) $\Phi=0.9$ (b) $\Phi=1.0$ (c) $\Phi=1.1$ (d) $\Phi=1.2$ . Time interval between the images in each image sequence is 0.01s, the first image in each row counts as time=0.....	173
Figure 7-13 Time-dependent flame temperature distribution, detected on fibre 3 (Tube middle) .....	176
Figure 7-14 Transient average flame temperature at different positions inside the tube; the fuel/air mixture at $\Phi=1.1$ . (a) Tube inlet (b) In the middle of the tube (c) Tube exit .....	178
Figure 7-15 Corrected flame temperature .....	179
Figure 8-1 Schematic of the prototype model for the two-dimensional temperature measurement. ....	188

## **LIST OF TABLES**

Table 3-1 Calibration of the tungsten lamp verified by manufacturer [42].....	41
Table 5-1 SiC fibre thermal properties .....	100
Table 5-2 Variation of the parameter in each case .....	101
Table 5-3 The setting of the finite volume method .....	101
Table 6-1 Correlation of cross flow forced convection over cylinder .....	136
Table 6-2 Variation of the fibre and the corrected gas temperatures .....	142
Table 6-3 Spot size in the corresponding measuring distance [73] .....	144

## NOMENCLATURE

<b>Greek</b>	<b>Definition</b>
$\alpha$	Thermal diffusivity
$\lambda$	Wavelength
$\rho$	density
$\Phi$	Equivalence Ratio
$\varepsilon$	Emissivity
$\tau_s$	Transmission factor
$\theta$	Dimensionless temperature
$\delta$	Phase angle
$\tau$	Fourier number
$f$	Frequency
<b>Symbol</b>	<b>Definition</b>
$\Theta$	Angle of premixed reaction cone
$\mu\text{m}$	Micrometre
$\text{nm}$	Nanometre

ms	Millisecond
$\mu$ s	Microsecond
S	Instrument factor
$S_\lambda$	Spectral sensitivity
$S_u$	Burning velocity
U	Flow velocity
R	Red colour component of RGB
G	Green colour component of RGB
B	Blue colour component of RGB
D	The infra-pyrometer aperture
$Re$	Reynolds number
a	Measuring distance
M	Spot size
$Nu$	Nusselt number
$Pr$	Prandlt number
RGB	Red, Green and Blue
fps	Frame per second

$T$	True temperature
$f$	Lens aperture
$I$	Radiant energy of blackbody
$t$	Time
$A_c$	Cross-sectional area
$A_s$	Surface area
$i$	Node number
$j$	Time step
$C_1$	The First Planck's Constant
$C_2$	The Second Planck's Constant
$r$	Radius of SiC fibre
$L_d$	Diameter of SiC fibre
$R_g$	Ideal gas constant
$R_{rg}$	Grey-level ratio
$C_p$	Specific heat
$T_{surr}$	Surrounding temperature
$T_s$	Heat source temperature

$T_b$	Brightness temperature
$T_a$	Ambient temperature
$T_c$	Colour temperature
$T_f$	Fibre temperature
$T_i$	Node temperature
$m_f$	Mass of fuel
$I_R, I_G, I_B$	Intensity in the channels of R, G and B
$m_o$	Mass of oxidiser
$a_m$	Number of molecules
V	Fluid velocity
X	Dimensionless length
P	Colour image sample

**Abbreviation**

**Definition**

ADC	Analogue-to-Digital Converter
a.u.	Arbitrary Unit
CFA	Colour Filter Array
CCD	Charge Couple Device

CMOS	Complementary Metal Oxide Semiconductor
MATLAB	Matrix Laboratory
FFT	Fast Fourier Transform
ISO	Standard Indication of Camera Sensitivity
SiC	Silicon Carbide
TFP	Thin filament pyrometer
VIS	Visible Radiation
1D	One-Dimension
2D	Two-Dimension
3D	Three-Dimension
<b>Chemical Symbols</b>	
CH <sub>4</sub>	Methane
CO <sub>2</sub>	Carbon Dioxide
H <sub>2</sub>	Hydrogen
H <sub>2</sub> O	Water
N <sub>2</sub>	Nitrogen

## **ABSTRACT**

This thesis reports an optical temperature measurement based on the two-colour method using colour-band filters to examine the application of it in novel ways. This technique uses a high-speed camera to detect the visible radiation from grey bodies. As a result of using the R and G channels, this modified two-colour method was found to be calibrated well with the standard temperature. The uniqueness of this research is the use of SiC fibre as a grey body emitter, allowing the temperature measurement to carry out in the situation of the hot gas and flame with soot deficiency. By conducting the numerical analysis the time taken to achieve the thermal equilibrium between the fibre and its adjacent gas was found to be in a few milliseconds.

Through directly imaging the process of combustion of the diesel-in-water emulsion droplets, the flame temperature fluctuation and the extent of secondary atomization were both found to vary with increase in water-content. Because of secondary atomization a great number of sub-droplets were formed, giving rise to a high degree of premixed combustion. Consequently, the high temperature was found to inevitably surround these sub-droplets.

Other two applications focus on temperature measurement of premixed flames and both involve using SiC fibre. One is to detect the temperature of the premixed CH<sub>4</sub>/air Bunsen flame, revealing how the flame temperature varies from the flame base to the flame tip at various equivalence ratios; the prime finding of another application shows the flame temperature variation when the flame propagates through a quartz tube. In addition, the correlation between the fibre and the flame temperatures has been found, and the measured fibre temperature shows an apparent tendency to decrease when the thickness of the fibre increases.

The work described in this thesis can be regarded as a solid base for the future development of 2D or 3D temperature measurement based on SiC fibre.

## **DECLARATION**

**No portion of the work referred to in the thesis has been submitted in support of an application for another degree or qualification of this or any other university or institute of learning.**

## **ACKNOWLEDGEMENT**

I am greatly obliged to my parents for their encouragement and considerateness during my study, as well as financial support in the past four years. All this has given me the inspiration to overcoming the obstacles I encountered during my research.

My sincere appreciation goes to Prof. Yang Zhang for research supervision. His valuable suggestions were a continuing source of enlightenment when I struggled to pinpoint the right material for experiments, and when I was confused with the orientation of my research.

I would also like to thank all members of the Combustion Research Group in the University of Sheffield. My gratitude goes to Dr. Hua Wei Huang, Dr. Swee B.Chin, Dr. Hussain Saeed, Mr. Paco Carranza Ch for their guidance on my project. Thanks also go to Miss. Yiran Wang, Mr. shuada Ji, Mrs. Lukai Zheng, Mr. Songyang, Mr. Huangxu Zhou and Mr. Houshi Jiang, for their useful comments on my research.

Special thanks are given to: Mr. Stephen Gordon for his contribution to my academic writing; Mr. Mike, as my personal gym trainer smoothing out the working stress by well-planned workouts; Mr. Jiayu Shen, Miss. Shuting Liu and Miss. libaihe Sun, as their friendship and assistance have been a source of encouragement when progress was challenged.

Finally, thanks for EPSRC offering the equipment loan service.

## **PUBLISHED WORKS**

Papers presented and published during the author's PhD project

1. Ma, Zhen and Yang Zhang, High Temperature Measurement Using Very High Shutter Speed to Avoid Image Saturation AIP Conference Proceedings, 1592, 246-253 (2014)
2. Yang, J., Ma, Z., and Zhang, Y. A Novel Flame Chemiluminescence Measurement using a Digital Colour Camera, 25th ICDERS Conference, 2015
3. Ma.Z. · Ebieto C. E. · Zhang Y. and Woolley R. Measuring the Temperature of a Flame Propagating Through a Quartz Tube Using High Speed Colour Imaging and Thin SiC Filament Based Two Colour Method. 12th International Conference on Heat Transfer, Fluid Mechanics and Thermodynamics, At Costa del Sol, Spain
4. Halleh Mortazavi, Yiran Wang, Zhen Ma and Yang Zhang. The Investigation of CO<sub>2</sub> Effect on the Characteristics of Methane Diffusion Flame, 12th International Conference on Heat Transfer, Fluid Mechanics and Thermodynamics, At Costa del Sol, Spain (awarded best paper)

# Chapter 1

## INTRODUCTION

### 1.1. MOTIVATION

For the development of combustion systems such as internal combustion engine and gas turbine there is a continuing demand for optimal diagnostics for monitoring the process of fluid motion, gas composition and temperature during combustion.

Temperature, as one of the most fundamental parameters in combustion research, defines the degree of hotness or coldness of an object. Heat is a form of energy associated with continuous motion of molecules. Temperature is a measure of heat. Hence, temperature is an expression denoting the physical state of a substance [2]. Also, temperature is the most frequently parameter for controlling and measuring the industrial manufacturing process such as in the case of making alloys, heat treatment and in forging.

Flame temperature can affect fuel vaporisation, combustion rate and heat transfer [3]. The measurement of high flame temperature in a confined space is complicated and challenging by the rapid fluctuations of temperature and by a harsh environment. These difficulties have been the cause of extensive research and many temperature diagnostics have been developed over the past decades; these will be discussed in the next section.

### **1.1.1. METHODS OF TEMPERATURE MEASUREMENT TECHNIQUES**

A considerable number of techniques have been developed over time for the measurement of gas temperature, but can be classified into three main categories including: intrusive, semi-intrusive and non-intrusive measurements.

Among typical intrusive measurements, thermocouples are the most frequently used because of low cost, and easy set-up. The use of thermocouple for the measurement of flame temperature is challenged by the great fluctuation of flame temperature both in time and space. The experimental requirements imposed by high temperature and pressure can also reduce the capability of thermocouples in temperature measurement, such as the measurement conducting in a combustion chamber. Another negative aspect is the intrusive nature of the thermocouple which may disturb the natural flow pattern in experiments. One must take care when measuring temperature, that the detected temperature is really of the temperature identical with the actual temperature of the measured object. Under some conditions, a temperature gradient can occur between the measuring instrument and the object. This means that the measured temperature is different from the actual value. In this situation, measured temperature can be affected not only with the actual temperature of the object, but also by heat-transfer properties [2].

Some temperature detection systems allow a temperature sensitive material to be applied to a surface. The variation in heat-induced colouration of the surface coating can be monitored remotely [4]. This sort of technique is called semi-intrusive measurement. However, it only applies when measuring the flow of hot gas adjacent to the coated surface. Measurement of an open flame temperature such as a Bunsen flame does not work with such a technique.

Intrusive instrumentation has to be able to survival at the temperatures encountered. In high temperature environment such as flame, this instrumentation may gradually degrade with time; once directly over material melting point, it will disintegrate thoroughly. Non-intrusive

measurement is not bound by this limitation. Frequently used non-intrusive techniques include infrared pyrometers, laser-based techniques and acoustic methods.

Infrared pyrometers, based on detecting thermal radiation in the infrared spectrum, can measure temperature ranging from 50 to 6000K [4]. Usually, this system requires knowledge of an object's emissivity. The use of infrared spectrum will need to take account of the effect of wall reflection in the case of flame temperature in a confined space, such as a combustion chamber.

Laser-based technique, such as Rayleigh scattering method, needs a knowledge of the pressure and the gas composition in a small control volume where the temperature is being detected. Being restricted to a single-point measurement is another limitation of laser-based techniques. Furthermore, the heavy investment and complicated set-up required both limit the application of this technique mostly in academic research institution.

With reference to acoustic methods, an acoustic pyrometer can be used to measure either fluid or solid surface temperature. As for gases, this system relies on the relationship between the static temperature of a gas and the speed of sound. The highly non-uniform gas properties and temperature distribution in tube flame propagation make this measurement unsuitable in such research.

Two-colour method is a well-established technique that can be applied conveniently to high temperature measurement, and suits well for the measurement of soot flame temperature based on the assumption of soot distributing evenly in the flame. This technique actually detects the temperature of flame soot particles, but their infinitesimal size allows equality of soot temperature with that of the surrounding gas. After combining imaging techniques, the two-colour method has the ability to yield a 2D temperature distribution.

Currently, there are two main types of two-colour method, both based on expansion of Planck's radiation. One is called Ratio temperature [5] which detects true temperature from the ratio of

radiation intensity from an object. Another, 'KL factor' [6] is used to measure soot temperature and can also estimate soot concentration. However, these two methods are both based on blackbody radiation and are only able to detect temperature of soot flame and the surface temperature of grey bodies. As for gas deficient in soot such as premixed flame, a conventional two-colour method may be not applicable and suffers complicated setup and under exposure at low-light condition because of the use of the narrow-band filtering method. This rules out the possibility of many practical applications.

In this research, a new two-colour temperature technique proposed hereby exploits the ratio temperature method based on the use of colour-band filters, which can virtually eliminate the defect of under exposure because these filters allow more visible wavelengths to pass through for temperature measurement. And because of the use of a high-speed imaging system the response time is rather short and can vary with shutter speed. To combine SiC fibre, as a blackbody radiation emitter, with the proposed two-colour system will lead to a solution for the temperature detection of gas with soot deficiency.

## **1.2. OBJECTIVES**

The main objectives of this research are classified into two categories and are listed as follows:

### **The preparation of the two-colour pyrometer**

1. To investigate the spectrum response of the high-speed imaging system, then to confirm the adequate wavelengths for temperature measurement.
2. To establish the relationship between temperature and the corresponding ratio of spectrum response of the high imaging system via calibrating the two-colour system with a standard temperature source (a pre-calibrated tungsten lamp).
3. To investigate the thermal behaviour of SiC fibre through conducting a controlled volume based numerical method

### **Applications of the proposed two-colour method**

- ❖ Diesel-in-water emulsion droplet combustion (without SiC fibre involved)
  1. To observe the secondary atomization phenomenon, with the aid of extend lens tube.
  2. To trace soot flame temperature variation during the lifetime of droplet combustion and to explore impact of different water-content within diesel droplet on combustion instability.
  3. To visualize soot flame temperature distribution during secondary atomization.
- ❖ Temperature measurement of a premixed Bunsen flame (with SiC fibre involved)
  1. To design a frame holding SiC fibres enables flame temperature measurement.
  2. To carry out temperature measurement at different height of the premixed flame.
  3. To determine the temperature difference between the flame and the fibre via previous published methods for the radiation loss correction.
  4. To compare the two-colour method temperature measurement with those of conventional techniques such as the Infra-pyrometry
  5. To assess the impact of fibre thickness on flame temperature measurement.
- ❖ Flame propagation via a quartz tube (with SiC fibre involved)
  1. To install the fibres into the quartz tube for the implementation of flame temperature measurement as the flame propagates through the tube
  2. To quantify the extent of flame oscillation during the propagation via the FFT analysis of the brightness intensity of each fibre
  3. To investigate how flame temperature varies with equivalence ratio.

### 1.3. OUTLINE OF THESIS

This thesis is organised in 8 chapters and describes the application and development of image processing and experimental techniques to the evaluation of flame temperature as follows:

- Chapter 2 is a literature review of the most important topics related to the implementation of the two-colour method.
- Chapter 3 describes the fundamental background of the proposed two-colour method and evaluates the performance of the imaging system used for temperature determination.
- Chapter 4 presents an application of the proposed technique for pure diesel and D/W droplet flame temperature measurement. The disruptive burning induced by secondary atomization has been imaged successfully. The topic related literature is referred in order to explain the necessity of conducting such research.
- Chapter 5 presents and discusses the use of a numerical approach to studying the thermal behaviour of SiC fibre. This gives the fundamental knowledge required in order to use SiC fibre in temperature measurement.
- Chapter 6 presents the first application of SiC fibre, involving a premixed flame temperature measurement in this thesis. The factors associated with the measurement accuracy are assessed.
- Chapter 7 presents experimental research on measuring flame temperature during a flame propagating rapidly through an open-ended quartz tube.

- Chapter 8 lists the main conclusions, and suggestions for future work

## **2. LITERATURE REVIEW**

### **2.1. INTRODUCTION**

This chapter introduces the background of combustion and its associated flame temperature diagnostic method. The chapter consists of three major aspects. The first section contains a general introduction on flame and combustion. This will include basic fundamentals, flame type, and combustion stability. The second section surveys the correlation between the true temperature, the brightness temperature and the colour temperature, and reviews the feasibility of using SiC as a grey-body radiation emitter for temperature measurement, as well as the knowledge of heat transfer mechanisms. The third section reviews a number of the temperature measurements applicable to flame research, covering the measurements from the intrusive to the non-intrusive techniques. The objective of this literature survey is to provide necessary background knowledge for understanding the content of this thesis, and to give some insights into the work that has been carried out in the relevant field of research that presented in the following sections.

### **2.2. COMBUSTION AND FLAME**

Combustion phenomena arise from the interaction of chemical and physical processes. Heat release originates in chemical reactions, but its exploitation through combustion. A combustion reaction can be summed up as a process including rapid oxidation, followed instantly by a release of radiation energy sensed by heat and light. Even in their simplest composition, the chemical reactions often require the involvement of both fuel and oxidant components. In the event of reaction, energy is released in the form of very active intermediates, such as atoms or free radicals. These species/radicals become involved in the complex chain reaction during the combustion process. In ordinary combustion, the rate of formation of the active species is equal to the rate of

their removal as radicals are usually produced from stable molecules during the chain initiation events. Subsequent propagation reactions involve that the molecules reacting with reactants to produce new products and radicals to sustain the reaction. Finally, when all the radicals' resources are exhausted, the reaction is stopped. The visual flame perception is that which arises from the burning hydrocarbon fuel, the emissive characteristic of various product radicals, which lies within the range of human vision. Premixed and diffusion flames are the typical examples of how variance in fuel and oxidiser mixing conditions can affect the physical and chromatic perception from the resultant flame.

### 2.2.1. DIFFUSION FLAMES

A candle flame is one of the most typical examples of diffusion flame as shown in Figure 2-1. The burning rate of this small scale of laminar diffusion flame is subject to the rate of inter-diffusion between fuel and surrounding oxidiser to reach a necessary mixture for combustion to take place along the boundary of this inter-diffusion. However, terms of large scale diffusion flame, turbulence plays an critical role in which the involvement of additional air because of flame movement could further influence on the combustion rate.

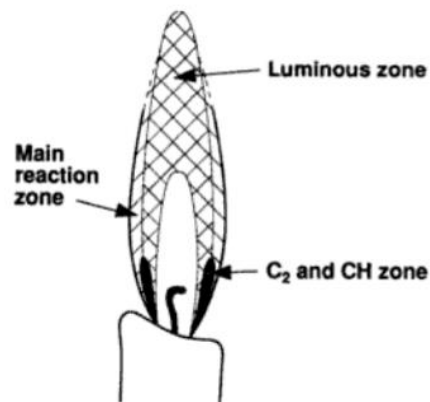


**Figure 2-1** Reaction zones in the candle flame [7]

In diffusion flames the combustion process takes place within a very narrow reaction zone. A considerable amount of reaction occurs on each side of the so-called 'true' flame boundary. A general effect is the pyrolysis of fuel, and for oxidant to form reactive radicals. Whereby these reactants occurring in the 'true' reaction zone does not count for their initial gaseous states and compositions. Because of this, the composition of the gases is non-homogeneous and varies from region to region.

In terms of various products and reactants, their concentrations are different across the flame. As shown in Figure 2-2, the fuel concentration is the highest along the flame axis, and fall away rapidly towards the flame boundary. As an opposing trend, the concentration of combustion products decreases from the flame boundary to the flame axis, and eventually vanishes into the surrounding atmosphere. Accordingly, the oxygen concentration shows a decrease in concentration as it approaches to the flame front and is completely consumed at the front. Therefore, the boundary of diffusion flame stringently outlines the area where complete combustion takes place. In addition, the reaction boundary of diffusion flame is also idealised as the place where the fuel to oxygen ratio can be approximate to stoichiometric ratio. As the flame height increases with exit fuel jet velocity, the fuel concentration will decline accordingly. And the reaction front will contract to the flame axis and converge at the flame tip in which all fuel is consumed. Whereby the appearance of a conical shape flame can be observed.

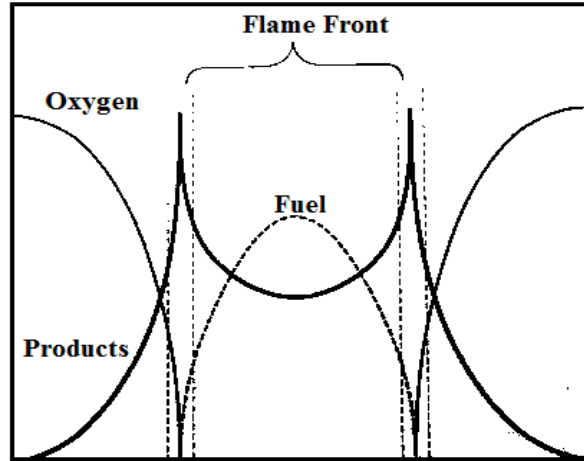


**Figure 2-2** Concentration profiles through a laminar diffusion flame [8]

Figure 2-3 shows changes in the diffusion flame appearance along with the increment of fuel velocity. At velocities below the critical  $Re$ , increase in fuel velocity results in a linear increase of flame height without loss of the original laminar cylindrical flame shape. However, with further increase in fuel velocity, the onset of turbulence takes effect in the shape of diffusion flame shape. It begins with the breakdown of the conical shape at the flame tip with distinct laminar lower, and turbulent upper, flame appearance. The dotted-curve that distinguishes the turbulent portion of the flame from the laminar flame profile is called the break-point. With further development of fuel velocity, it will result in upstream propagation of the turbulent flame feature, accompanied by a reduction of the laminar flame height. Finally, a fully turbulent flame structure is established when the break-point has reached the burner's nozzle exit.

In the period of the combustion process, a considerable amount of heat and light are emitted, and appears to have a discrete reaction zone, where the appearance varies with burning conditions. Because of the high concentration of soot particles in the combustion product, diffusion flames are normally featured by intense luminosity with a perceptible yellow-red colouration.

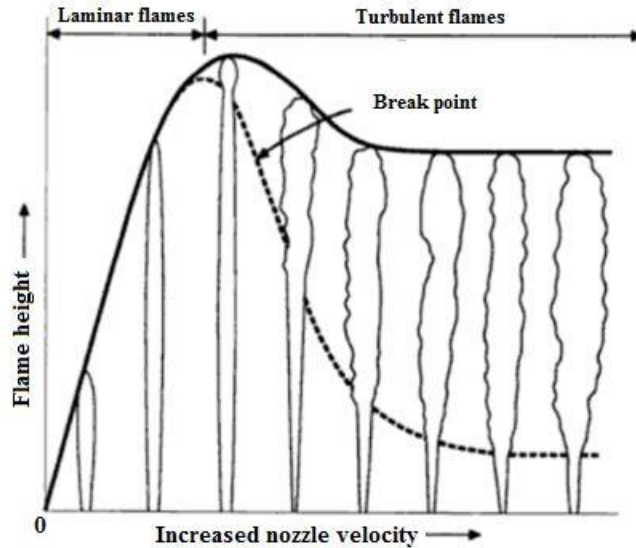


**Figure 2-3** Schematic of diffusion flame shape varying with flow velocity, presenting the development from a laminar to a turbulent flame [8]

### 2.2.2. PREMIXED FLAMES

Premixed flame is produced when the fuel and air are homogeneously mixed prior to the onset of combustion process. The Bunsen burner is a typical example of a device that produces such flames; air flows into the bottom of the burner and is allowed to blend with the fuel along the channel of burner passage towards the burner's exit. This mixture of fuel and oxidant results in more intense combustion to occur.

In terms of its appearance, the colour and shape of premixed flame is in direct contrast to the incandescence of yellow-red emission observed from diffusion flames, and depends on the mixture ratio between fuel and oxidant. For instance, if air (oxidant) were gradually added to initially diffusion  $\text{CH}_4$  flame, the yellowness of soot emission will subside and be replaced by a bluish sheath. Further addition of air will eventually result in the complete disappearance of the luminous soot, accompanied by a reduction of visible flame height. As the combustion reactants become increasingly fuel-lean, an inner cone structure becomes more evident.

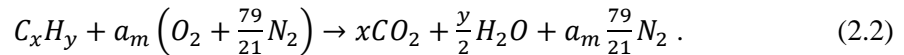
### 2.2.3. EQUIVALENCE RATIO

Equivalence ratio is generally a dimensionless parameter for premixed flame analysis; the reason for this can be associated with the degree of mixing between fuel and oxidant. This ratio states the proportion of the actual fuel-to-oxidiser against the stoichiometric fuel-to-oxidiser ratio. The stoichiometric ratio expresses the required proportion of fuel and oxidant to release the process of complete combustion. The value of equivalence ratio greater than one always indicates a greater amount of fuel in the premixed reactant stream than that required for complete combustion. On the other hand, ratios less than one indicate either the presence of excessive amount of oxidant or a deficiency of fuel in the combustion stream. The obvious advantage of using equivalence ratio is to make the comparison between various fuels possible, irrespective of the different amount of fuel and oxidiser being used. Mathematically,  $\Phi$  is defined as [9]:

$$\Phi = \frac{\text{fuel-to-oxidiser ratio}}{(\text{fuel-to-oxidiser ratio})_{St}} = \frac{\frac{m_f}{m_o}}{\left(\frac{m_f}{m_o}\right)_{St}}. \quad (2.1)$$

Where  $m$  is the molecular mass, and suffix  $S_t$ ,  $m_f$  and  $m_o$  denotes for stoichiometric condition, mass of fuel and of oxygen respectively.

A widely accepted way to determine the stoichiometric ratio for different fuel-to-air combustion is through balancing the chemical Equation to convert combustion reactants to products. For mixtures of hydrocarbon fuel and air constituents, the chemical reaction can be balanced via [10]:



Thus, stoichiometric ratio can be given as:

$$\left(\frac{m_f}{m_o}\right)_{St} = \left(\frac{m_{C_xH_y}}{a_m \times m_o}\right). \quad (2.3)$$

#### 2.2.4. PREMIXED BURNING VELOCITY

In the case of a laminar flow burner,  $U$  is very low close to the wall of the burner, but increases towards the burner centre, resulting in a parabolic velocity profile. As the flow velocity exceeds the burning velocity, the height of the flame tends to increase prior to the equilibrium between the burning velocity and the flow velocity normal to the flame front. This is demonstrated by the occurrence of a conical flame. Measurement of the burning velocity is built on the basis of the gas velocity ( $U$ ) and the cone angle ( $\Theta$ ), as shown in Figure 2-4. The main difficulty in measuring burning velocity measurement is that a stable and distinguishable flame front can only be produced in a certain range of equivalence ratios, also requiring a stable and accurate fuel system. Ideally, a narrow flame front propagates into the flowing gas, the burning velocity of which can be defined as follows:

$$S_u = U \sin(\Theta), \quad (2.4)$$

where  $S_u$  is the burning velocity of the flame,  $\Theta$  is the cone angle between the gas flow and the flame surface. In most cases of the practical premixed flame, the flame front is not fully straight; it involves a curvature and rounding at the flame tip. Despite these, the angle and the consequent  $S_u$  can still be defined qualitatively by taking this theoretical cone flame model.



**Figure 2-4** The actual cone shape of the premixed flame with the part of flame front at the burning velocity  $S_u$  towards the flow  $U$ ,  $\theta$  is the angle between the flame surface and the direction of flow  $U$

### 2.2.5. FLAME STABLITION

For laminar premixed flames, the use of a burner matches the following objectives:

- It is a place for fuel and oxidant to be mixed into a certain degree.
- It allows the establishment of a laminar flame
- It acts as a heat-sink capable of restricting the flame movement

The metallic nozzle causes heat removal from the flame, resulting in a reduction of the burning velocity in its vicinity. The height of the flame front depends on the magnitudes of both the burning velocity and the flow velocity of the supplied gas mixture. When  $S_u$  is larger than  $U$  the flame will propagate upwardly, until the equilibrium is established between these two velocities. On the other hand, once the  $U$  is greater than  $S_u$ , the flame will move downwards until the two velocities are balanced.

The value of the gas velocity at the limits of flammability is subject to the dimensions of the burner and the reactant conditions of the flow. Foat [11] reported that the entrainment of atmospheric air

will result in the reactant mixture becoming leaner above the rim of the burner, and then reaching the stoichiometric state. By increasing the gas velocity, a lifted-flame can be formed some distance above the burner-rim. The lifted flame features with two stability limits:

- When the gas velocity tends to reduce the flame will re-attach itself onto the nozzle exit.
- With a further increase in gas velocity, the flame tends to lift off further, and eventually become extinguished.

Figure 2-5 interprets schematically how the flow velocity and the gas mixture affects the flame stability.

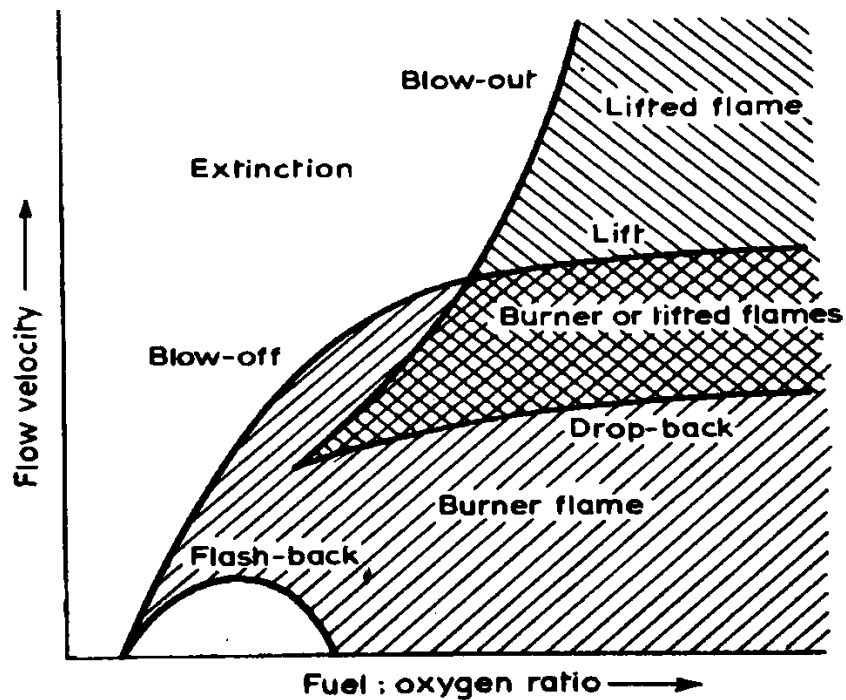


Figure 2-5 Limiting conditions for various premixed flames [8]

### **2.2.6. FLAME SOOT**

The main source of carbonaceous soot found in the flame products is from the incomplete combustion of crudes oil and other organic matters [12]. The solids of ash, coke and soot are formed when combusting organic fuels. These products are different in chemical morphological and are subject to the processes of combustion which leads to their formation. Soot particles are the results of gas phase chemical reaction, and the generation of these particles is regarded as an energy loss pertaining to the incomplete combustion.

As for the flame emission, the presence of soot particles can change the radiation characteristics of a flame and affect the total energetics of a combustion system. When burning different fuels the radiative emission characteristics of flames depend mainly on the soot concentration in flames [12]. For flame temperature, soot particles behave like blackbody, which emit infrared and visible radiations following Planck's law. This characteristic is applicable to the two-colour method for soot temperature measurement by exploiting its radiation. Soot temperature can approximate to flame temperature owing to the fact that the temperature difference between soot and flame is negligible [6].

### **2.3. THE CORRELATION AMONG THE TRUE, COLOUR AND BRIGHTNESS TEMPERATURES**

G.A.W.Rutgers [13] produced an equation for calculating relationship between colour, brightness and true temperature for a tungsten filament. De Vos [14] showed how to measure the measurements of the emissivity of tungsten. In pyrometer, one defines the brightness temperature of the tungsten filament as being subject to the temperature of a blackbody with same radiant energy as the emission from the tungsten filament surface at a fixed wavelength. In colorimetry, the colour temperature governs the properties of light sources. These two temperatures can obtain both from

the true temperature. The following mathematical models describe the relationship between the true temperature and the other two temperatures.

***Brightness temperature.***

The correlation between the brightness temperature  $T_b$  and the true temperature  $T$ , is expressed as

$$I(\lambda, T_b) = \tau_s \varepsilon(\lambda, T) I(\lambda, T), \quad (2.5)$$

where  $I(\lambda, T_b)$  and  $I(\lambda, T)$  denote the radiant energy from a blackbody at temperature  $T_b$  and  $T$  respectively.  $\varepsilon(\lambda, T)$  represents the emissivity of the tungsten ribbon.  $\tau_s$  is the transmission factor of the tungsten window.  $\lambda$  is the radiation at the wavelength of the tungsten filament. Applying Wien's radiation law in Equation 2.5 the relation become as follows:

$$\frac{1}{T_b} - \frac{1}{T} = -\frac{\lambda}{c_2} \ln(\tau_s \varepsilon(\lambda, T)). \quad (2.6)$$

Where  $c_2$  is the second Planck's constant. The difference  $(T-T_b)$  has been calculated by G.A.W.Rutgers [15].

***Colour temperature***

The colour temperature is the temperature of a blackbody with the same colour distribution in the visible spectrum. In other words, the colour temperature of a light source can be considered as the temperature of a blackbody appearing with the identical colouration with the light. The proposed method by G.A.W.Rutgers [13] is based on the determination of the ratio of the radiation intensity emitted to two different wavelengths in the visible region.

The colour temperature can be defined by

$$\frac{I(\lambda_2, T_c)}{I(\lambda_1, T_c)} = \frac{I(\lambda_2, T)}{I(\lambda_1, T)}, \quad (2.7)$$

where  $\lambda_1$  and  $\lambda_2$  are the wavelengths selected in the visible range.  $T$  is the true temperature.  $T_c$  denotes the colour temperature of the radiator.

## 2.4. SILICON CARBIDE MATERIAL

In 1982, silicon carbide fibres were manufactured commercially by Nippon Carbon. The research of this industrial production started in 1970s and was conducted by Professor Yajima in Japan [16]. Currently, there are four main types of SiC, known as 2H-SiC, 4H-SiC, 6H-SiC and  $\beta$ -SiC. Only the latter is used for high temperature measurement because of a high melting point and lower thermal conductivity. The others are more commonly used in the electronics area.

This semiconductor material was first applied to a  $H_2-N_2$  jet diffusion flame for temperature measurement, carried out by V. Vilimpoc [17] where several  $\beta$ -SiC fibres of diameter  $15\mu m$  were inserted into the jet diffusion flame for the fibre temperature measurement. Subsequently, the corrected flame temperature was derived from the fibre temperature via a heat loss correction. In addition to this research, he carried out an experiment on the temporal response of the fibre to a rapid change in temperature. The response was detected experimentally using a laser to heat the fibre for a short period of time. The radiation emitted from the fibre was then measured by an InGaAs detector. As a result, shown in Figure 2-7, the resultant response time is around 1.5 ms, well matching his predications.

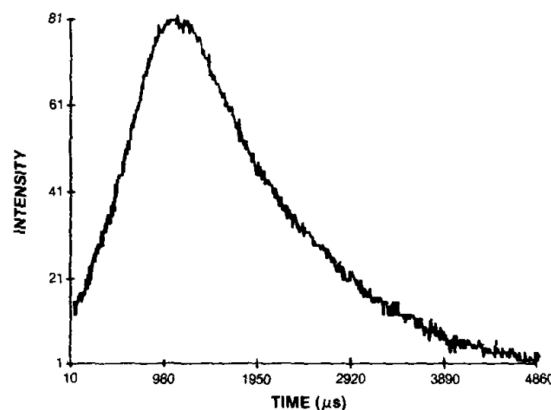


**Figure 2-6** The profile of the fibre emission [17]

Unlike this pioneered research focusing only on the open static flame for temperature measurement. In this thesis, the author has examined the possibility of using the fibre for fast flame propagation research associated with flame temperature.

## **2.5. REVIEW OF TEMPERATURE MEASUREMENT**

The unit of thermodynamic temperature, also referred as absolute temperature, is denoted by kelvin (K) and is defined in terms of range between the absolute zero and the triple point of pure water (273.16 K) [4]. The triple point of a substances is the pressure and temperature where the phases (liquid, gas, and solid) coexist in the thermodynamic equilibrium. In addition to the thermodynamic temperature the scale of Celsius ( $^{\circ}\text{C}$ ) temperature is identical with the thermodynamic temperature reducing 273.15, and the magnitude of  $1^{\circ}\text{C}$  is numerically identical with 1K [4]. The current international temperature scale, ITS-90 (International Temperature Scale of 1990), depicts a scale covers the entire temperature range.

Numerous temperature techniques have been developed for temperature measurement by utilizing diverse phenomena such as thermoelectricity, the resistance of electrical conductors varying with temperature, fluorescence and spectral radiation. For convenience, the various temperature diagnostics based on these phenomena can be summarised into three groups subject to the nature of contact between the object (such as gaseous, solid, liquid medium of interest) and detecting devices. The section reviews the types of temperature measurement including intrusive, semi-intrusive and non-intrusive techniques. Each category lists out several frequently used measuring devices with consideration given to their cost, sensitivity, accuracy, temperature of operation, and dynamic response.

### 2.5.1. INTRUSIVE MEASUREMENT

Intrusive measuring device always involves installing a physical sensor on or within the object, such as an aircraft engine or a medium of interest such as with the exhaust gas. There is a broad selection range of intrusive instrumentation including gas and liquid-in-glass thermometers, resistance temperature devices and thermocouple. However, an inevitable effect of the use of intrusive techniques causes a flow disturbance when measuring the temperature of either gas or liquid. As a result, the determined temperature using intrusive instrumentation may deviate far from its actual temperature. And this measured temperature is based on the equilibrium of the convective heat transfer from either gas or liquid to the detector surface. Conduction occurs in detector itself connections and supports, radiative heat transfer between the sensor and its ambient environment.

#### *A. Temperature measurement utilizing thermal expansion*

The variation of material expansion is subject to temperature. This can be used to measure temperature. Fluid thermometry covers a series of devices from the constant pressure to the constant volume gas thermometers. In addition, the solid expansion is also popular in measuring devices

##### **1. Gas thermometry**

The mechanism of gas thermometry is on the basis of the ideal gas law; the temperature is derived from the variation of either pressure or volume. Through this mechanism the accuracy is much subject to the value of the gas constant [18]. This constant needs to be found experimentally for a given system via calibrating with known temperature value.

Gas thermometers are frequently utilized for measurements that suits the range from a few K to around 1000K. The accuracy of gas thermometry technique is subject to the temperature range. For instance, Pavese and Steur [19] reported an accuracy of 0.5mK for temperature measurement ranging between 0.5K and 30K. This indicates better accuracy may be obtained

when detecting low temperature. This method is frequently used in calibration, and scientific experiment, and doesn't suit the industry application well.

## **2. Solids thermal expansion**

Solids thermal expansion utilize the difference in material thermal expansion usually between different metals.

Ribbons of two dissimilar metals are attracted together to form a bimetallic ribbon. When heating the side having the higher coefficient of thermal expansion will expand further than another side, subsequently causing the assembly to bend [20, 21]. And this bending can be translated a reading of temperature with an accuracy of around  $\pm 1^\circ\text{C}$  [18]. The main advantage of this technique is operating without a power supply.

Most applications of this thermal expansion technique is the production of temperature controllers.

### ***B. Thermoelectric measuring devices***

A thermocouple is a device designed to measure temperature. Its mechanism is based on the contribution of Seebeck [22]. The findings of his work showed that a small electric current will flow in a closed circuit consisted of two dissimilar metallic-conductors when their conjunction remains at different temperature. The production of the electromotive force under this condition is known as the Seebeck effect. To simplify this process, a thermocouple is a device converting thermal power to electric power; the amount of produced electric power can be applied for temperature measurement.

As a type of thermoelectric devices, thermocouples are frequently used by reason of their simplicity, low cost, easy setup and temperature range. Their sensitivity is suitable for a great number of applications as is relative fast dynamic response but thermocouples are relatively not accurate [18]. In general, thermocouples can be classified as non-metal, high temperature

metal, base metal and noble metal. Noble metals, such as platinum oxidized around 600°C, are relatively inert. The use of this metal is commonly in manufacturing the thermocouple stems. Base metals such as iron suit for low and moderate temperature measurement. As for the applications of higher temperature measurement, the high temperature metals such as rhenium and tungsten can be used for temperature measurement. Although tungsten and rhenium have ultra-high melting point, 3140°C and 3280°C [18], they oxides fast and degrades instantly in oxidizing atmospheres at high temperature. Non-metals such as carbon, carbide and boride compounds are fragile with low strength in tension. The thermocouple made of these materials can result in the probe with a large diameter. This is undesirable for the temperature measurement of the flow with a high velocity.

### **2.5.2. SEMI-INTRUSIVE TEMPERATURE MEASUREMENT**

Applying a heat sensitive material to temperature measurement is an available solution. The optical characterises of the surface coating will vary with temperature and can be observed remotely. This method is classified as semi-intrusive, because it involves modification of measuring objects, and thus the disturbance to the measurement at the place of interest is not avoidable. Currently a great deal of heat sensitive material exists, such as thermochroic liquid crystals, heat sensitive paints and thermographic phosphors.

Thermographic phosphors suit to temperature measurement ranging from cryogenic level to 2000°C by exploiting the thermal dependence of phosphor fluorescence. This technique normally involves depositing the material such as yttrium oxide (Y<sub>2</sub>O<sub>3</sub>) on a surface, and its radiation can be observed remotely through an optical detection system such as CCD/COMS cameras. This method can provide sensitivity of 0.05°C, with the reading error of 0.1-5% in the Celsius scale. An application of thermographic phosphors for measuring temperature of rotating turbine blade at up to 10500 rpm has been conducted by Tobin [23].

As for the use of non-reversible heat sensitive paints, it is suitable for the application just requiring an indication of the maximum temperature achieved. These paints have been applied for indicating critical temperature in rocket motor and on turbine blade over the past decades, which are able to operate continuously at low temperature level or intermittently up to 1350°C [4].

### **2.5.3. NON-INTRUSIVE TEMPERATURE MEASUREMENT**

Intrusive and semi-intrusive techniques must be able to operate at temperature measured. In harsh environment application or high temperature such as flames, most intrusive techniques can degrade with time. As temperature of interest passes over material limits, these techniques can disintegrate entirely. However, non-intrusive techniques are not bound by this limitation. Most non-intrusive measurements detect temperature by exploiting the electromagnetic radiation. Infrared pyrometers are sensitive to the long wavelengths(>700nm) in the electromagnetic spectrum. Optical devices such as line reversal, scattering and luminescence operate in the visible region commonly and involves the use of the laser as part of the system. Unlike the optical pyrometer using the radiation for temperature measurement, acoustic temperature measurements rely on the measurement of sound speed instead of detecting the emission of objects.

#### ***A. Infrared technique***

Temperature detection systems built on the basis of thermal radiation in the infrared spectrum are capable of measuring the temperature ranging from 50K-5000K [4]. The infrared part of the electromagnetic spectrum can be classified as three regions: the near-, mid- and far-infrared, which are named according to their relations to the visible wavelengths. The principle of this technique is based on Planck's distribution for the temperature estimation. As for the accuracy of an infrared temperature measurement, it is subject to the radiation attenuation between the object and the infrared pyrometer, background radiation sensed using the pyrometer, errors in estimation of the target's

emissivity, and the errors occurring in the infrared pyrometer. In most situation, it is desirable to use the narrow band filtering method to minimise the influence of the error in emissivity.

### ***B. Spectral line reversal***

This method is frequently used in the measurement of the static temperature of a gas, capable of measuring temperature ranging from 1000 to 2800K with the accuracy of approximately  $\pm 15$  K [4]. Application includes flames, combustion chamber and rocket exhausts. According to Gaydon [24] the method was originally devised by Kurbaum and Fery and comprises of seeding the non-luminous flame with sodium, carbon or other metals particles, and comparing the radiation from the flame with that from a standard light source such as a filament tungsten lamp. The flame should be placed between the photodetector and the light source on the same line of sight. However, this method doesn't suit the soot flame measurement because the radiation from incandescent soot particles masks the signal [25].

### ***C. Acoustic pyrometer***

For gas temperature measurements, this technique is on the basis of the thermodynamic relationship between the velocity of sound and the temperature of a gas [4]. Theoretically, the temperature of a gas can be calculated by measuring the time of a sound signal travelling throughout a known distance between a pair of acoustic sensors.

However, this technique has poor spatial resolution and complicated setup, and the temperature obtained is the average gas temperature between those two sensors. Because of considerations of these limitations acoustic pyrometer is not applicable to the investigation of flame propagation in a tube.

### ***D. Rayleigh scattering method***

As a laser involved measurement system, Rayleigh scattering technique can make velocity, temperature and gas density measurements in harsh environment according to Mielke [26]. Rayleigh scattering is the result of light scattering from gas molecules. The light from a laser beam penetrate through a gas, the resultant scattered light is shifted in frequency because of the motion of the gas molecules; this phenomenon is called the Doppler effect. The frequency spectrum of the scattered light contains information about temperature, the gas density and velocity. Gas temperature is determined using the ideal gas law, and based on the assumption that the gas composition and pressure are either known or constant in a small control volume. In the case of diesel droplet combustion, it is struggling to determine the gas composition and the signal from molecular scattering tends to be overlapped by the light scattering from soot particles [25].

#### ***E. Two-colour method***

As a non-intrusive technique the two-colour method usually combines with image processing techniques [27] for 2D temperature measurement. In principle the two-colour method requires the monochromatic radiation energies of two wavelengths from the same radiation source by using some complex optical systems, thereby a colour-band filtering technique is introduced to the two-colour method for simplicity. This new filtering technique can obtain monochromatic images at different wavelengths via image processing technique. Whereas the radiation energy collected through the filtering technique is not exactly monochromatic and varies with using different image acquisition system. Therefore, the colour-band based two-colour method must be taken with care when doing temperature calibration, to ensure that the difference between the measured and the reference temperatures falls into a reasonable margin.

#### 2.5.4. SUMMARY

Apparently, the use of the intrusive temperature measurement is the easiest way to detect either flame or the hot gas temperature with acceptable accuracy and low cost; however, this technique suffers the laminations of slow thermal response, disintegration in harsh environments, and poor spatial resolution.

Semi-intrusive measurements require the heat sensitive paints coating on the surface of interest. After the paints is heated up by its surrounding hot gas, the resultant colour or radiation of the paints can be used to determine temperature. But both the intrusive and the non-intrusive techniques can result in flow disturbance, this is not desirable for gas temperature determination.

Considerations of these factors divert the choice of the proposed temperature to the non-intrusive technique. Laser based techniques, of course, can give fast response and relatively high accuracy once known the gas composition. But, high cost and complicated setup limit the use of the laser technique in the laboratory. In addition, acoustic pyrometer requires the knowledge of transit time of a sound signal between known distance and of the gas constant, and yields the measured temperature with poor spatial resolution.

As the proposed temperature measurement, the two-colour method features with fast response, easily setup, low cost and without knowing the emissivity of the measured target. The detailed information of this method will be described in chapter 3.

### 3. BACKGROUND OF TWO-COLOUR METHOD

#### 3.1. DIGITAL IMAGE PROCESSING

##### 3.1.1. PRINCIPLE OF DIGITAL IMAGING SYSTEM

In comparison with a traditional film-based imaging system, the greatest innovation in digital imaging lies in the way where light information can be captured and directly be converted into colourful images. The most frequently used sensors for digital image systems are either complementary-metal-oxide-semiconductor (CMOS) or charge-coupled-device (CCD). Both CCD and CMOS use 2D array of tiny solar lighting collecting cells with their sensitive range in the VIS and NIR. The main difference between these two sensors exists in the architecture of their photosite construction, as shown in Figure 3-5.

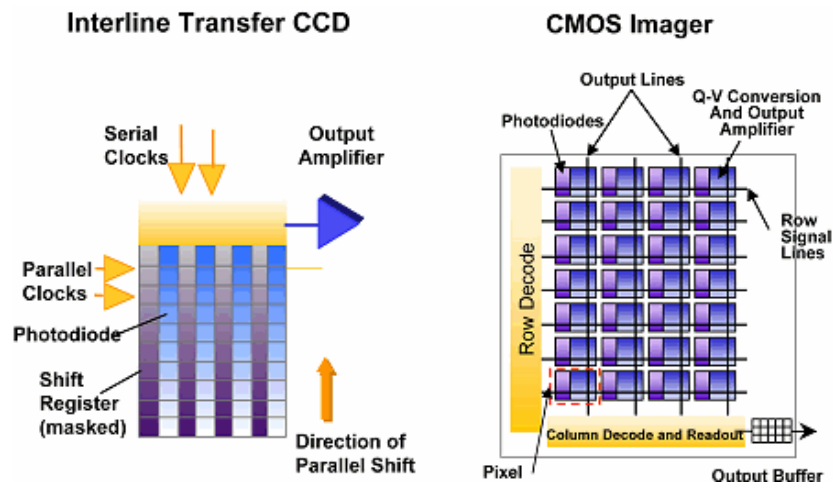


Figure 3-1 Architectures of the CCD and CMOS sensors [28]

With a CCD sensor, only the photon-to-electron conversion is carried out in the CCD itself. All the image processing is performed off the sensor, away from the photo-sensing layer. This architecture design allows maximum space for each pixel to collect the incident photon. After the

conversion of the photon-to-electron, the charge leaves the CCD sensor in an analogue form, then enters an external circuitry. In this circuitry, an analogue-to-digital converter(ADC) collects and translates this charge into digital signal via measuring the accumulated charge at each pixel location. By contrast, both the photon-to-electron and electron-to-voltage processes are conducted within the COMS chip. Each pixel is equipped with an independent ADC converter to amplify and transfer the electric charge. Thus, the signal readout from each pixel is in digital form, without the need of an external circuitry. However, a negative effect of this design is the reduction in space for photo reception per pixel in comparison with a similar dimensioned CCD sensor. Whereas, CMOS allows switch-off fields of unused pixels, thus leading to a power efficient device.

In the early digital-era, the CCD sensor was regarded as a high quality and low-noise imager. By contrast, CMOS sensor suffers from low-grade sensitivity because of the inclusion of each independent transistor. However, as a result of the rapid development in modern fabrication, the performance of current COMS sensors is in line with that of CCD.

### **3.1.2. COLOUR QUANTIFICATION**

Each pixel on a digital image camera sensor contains light sensitive photosites (cells) detecting the brightness of light. These photosites are monochrome device without the ability to discriminate wavelengths of the incident radiation, which can thus only measure the total luminance of light striking on the sensor surface. Because of this, the use of different colour coating across the imaging sensor area is a way of establishing colour information in compliance with the fundamental requirement of RGB colour composition. Bayer [29] proposed a Colour Filter Array(CFA) arrangement which is regarded as such a solution. Figure 3-6 shows the allocation of the primary colour filters arranged in a form of an uneven distribution, in accordance with the CFA scheme. A unit of the RGB sensor usually composed of four pixels; within this region, the proportion of G to

R and B filters is at a ratio of 2:1:1. The reason behind such uneven distribution is to match the biological human vision by collecting G signal at a higher rate than the other colours.

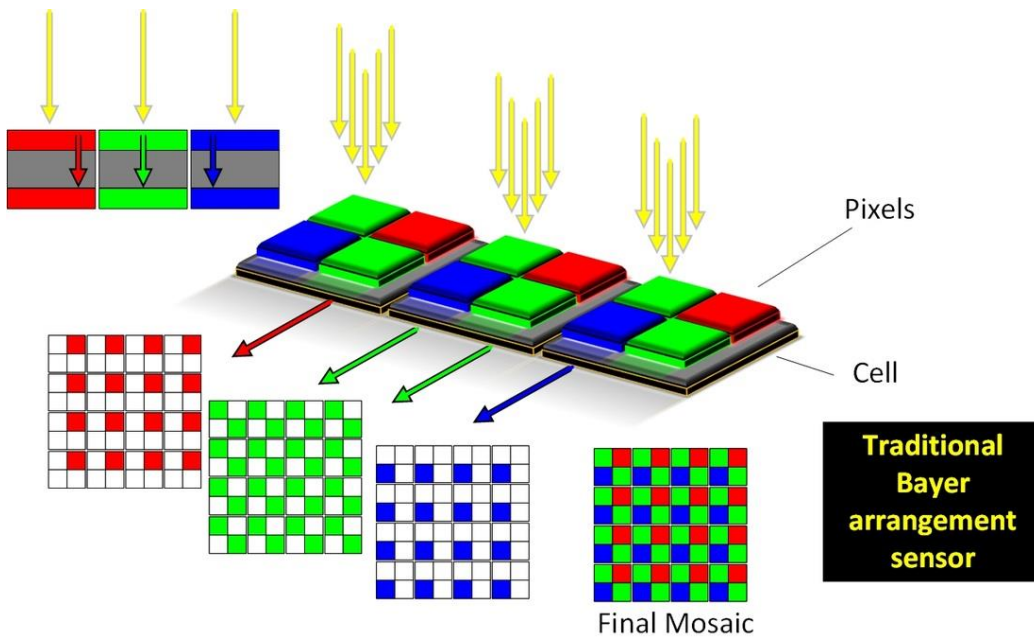


Figure 3-2 Structure of colour-filter-array pixel filter

### 3.1.3. EXPOSURE AND FOCUS

The amount of light capable of reaching the imaging sensor determines the intensity of captured images. Two significant parameters govern this: is the aperture and the shutter speed. The aperture mechanism is analogous to the iris of the human eye. Under intense light, the iris opening is reduced to avoid over-saturation of the observed scene. In digital imaging equipment, this parameter is known as 'f number': the smaller the number, the larger the aperture opening. On the other hand, shutter speed controls the amount of light through the aperture.

### 3.1.4. CAMERA NOISE

The three main noise manifestations in COMS/CCD are photon-noise, dark-noise and read-noise [30].

Photon-noise denotes any noise component reflecting an uncertainty in the measurement of the number of photons collected during a particular exposure interval. Their contribution arises from the effects of inherent statistical variation in the arrival rate of photons striking the image sensor. The resultant electrons produced from the photoelectric effect provides the major constituent of the actual signal. The magnitude of which fluctuates randomly with photon captured at various pixel locations.

Dark-noise results from the variation in electrons, induced by thermal excitation within the structure of the image sensors. This noise occurs usually in the fields where active photon signals are deficient, and the most prominent form of noise contamination is in the perceptually black image background. As described earlier in the section 3.2.1, a pure black perception within the RGB space locates at a 3D coordinate of (0,0,0). Because of the limits of human visual resolution, any minor variation of colour signal would not change resultant colour significantly. Hence, for the most part of this noise in a well-designed camera is visually unnoticeable. To minimise this noise, the cooling mechanism may involve: fan-driven air circulation, thermos-electric condition, and in extreme cases, liquid nitrogen may be used.

Read-noise is actually a combination of the overall system noise related to the conversion of electrons into voltage signal. It also accounts for the noise occurred in the subsequent ADC processing of signals. This form of noise contamination can be extremely severe in systems where a pre-amplifier is installed and utilised, resulting in uniform noise contribution at each pixel location.

### **3.1.5. IMAGE PROCESSING BASED COMBUSTION DIAGNOSTICS**

Currently, researchers have begun to take advantage of the colour filtering architecture to extract hidden potential in a multi-wavelength based application. Of considerable interest in the use of RGB colour information is in the field of multi-wavelength temperature investigation of grey-body emitters. The principle of this temperature measurement derives assumption that the monochromatic greyscale images of R, G and B are proportional to the approximate radiation intensities around their peak wavelengths. Simonini [30] utilised the greyscale images of R, G and B from a CCD camera to calculate the temperature profile of soot flame observed from a spark-ignition engine. Tominaga [31] evaluated the usefulness of the colour component intensities from a COMS sensor camera for two-colour temperature and soot density analysis in a diesel engine. Zhou [32] calculated the temperature distribution in a pulverised-coal-fired boiler furnace. Similar methodology was also employed to investigate the effectiveness of RGB colour output for evaluation of Thin Filament Pyrometer (TFP) temperature [33].

## **3.2. THEORETICAL BASIS OF TWO-COLOUR MEASUREMENT**

### **3.2.1. INTRODUCTION**

In 1932, two-colour method was firstly proposed by Hottel and Broughton [34], applied to detect the temperature of the furnace. Afterwards, the most frequent application of this method has been applied to internal combustion and to soot concentration in the flame. However, over the last decade, this approach has been expanded to infer the temperature of open flames and the surface temperature of grey-body. This chapter aims to clarify the principle of two-colour measurement and temperature calibration procedure. In addition, the effect of factors on the accuracy of the measurement will be discussed.

### 3.2.2. MEASUREMENT PRINCIPLE

Hot objects emit visible light above a temperature of 723K, but the greater part of radiation is emitted in the infra-red region. Even at ambient temperature, the emission of infrared radiation still can be used for accurate measurement by radiation techniques; it means that the detectable range of temperature is much wider than using the emission of visible radiation.

Two-colour measurement is a type of radiation thermometry, which depends on measuring radiated energy of objects to determine the temperature from the governing radiation law.

Planck's law describes the energy distribution from a perfect radiator of maximum and unity emissivity according to the Equation 3.1

$$E(\lambda, T) = \frac{C_1}{\lambda^5} (e^{\frac{C_2}{\lambda T}} - 1)^{-1}, \quad (3.1)$$

where  $\lambda$  is the wavelength of radiation, T is the true temperature (K),  $E(\lambda, T)$  represents the radiation intensity emitted at the wavelength  $\lambda$  per unit area of the object and  $C_1$  and  $C_2$  are the first and second Planck's radiation constant.

However, no actual objects can emit maximum radiation and are called grey bodies whose emissivity coefficient  $\epsilon < 1$ . A black body is a non-attainable in practice.

Thus, grey body radiance is multiplying the Equation 3.1, and given by

$$E(\lambda, T) = \epsilon_\lambda \frac{C_1}{\lambda^5} (e^{\frac{C_2}{\lambda T}} - 1)^{-1}, \quad (3.2)$$

where  $\epsilon_\lambda$  is the emissivity of a grey-body at wavelength  $\lambda$ . Due to  $\frac{C_2}{T\lambda} \gg 1$  within this region, the radiance of a grey body is described by Wien's radiation:

$$E(\lambda, T) = \epsilon_\lambda \frac{C_1}{\lambda^5} e^{-\frac{C_2}{\lambda T}}, \quad (3.3)$$

By referring to Y.Huang's [35] work the grey-level  $G(\lambda, T)$  output of the imaging system was found to be proportional to the radiance of the measured object and dependent on the spectral sensitivity  $S_\lambda$  of the imaging system; the equation of grey level output is given by

$$G(\lambda, T) = RS_\lambda \varepsilon_\lambda \frac{C_1}{\lambda^5} e^{-\frac{C_2}{\lambda T}}, \quad (3.4)$$

where R is instrument constant which incorporates various factors including radiation attenuation caused by lens properties, ambient environment, imaging system and optical path distance.

The two-colour method based on the ratio of between the two grey levels at selected wavelengths  $\lambda_1$  and  $\lambda_2$ , which is given by

$$\frac{G(\lambda_1, T)}{G(\lambda_2, T)} = \frac{S_{\lambda_1} \varepsilon_{\lambda_1}}{S_{\lambda_2} \varepsilon_{\lambda_2}} \left(\frac{\lambda_2}{\lambda_1}\right)^5 \exp \left[ \frac{C_2}{T} \left( \frac{1}{\lambda_2} - \frac{1}{\lambda_1} \right) \right]. \quad (3.5)$$

By rearranging Equation 3.5

$$T = \frac{C_2 * \left( \frac{1}{\lambda_2} - \frac{1}{\lambda_1} \right)}{\ln \frac{G(\lambda_1, T)}{G(\lambda_2, T)} + \ln \frac{S_{\lambda_2}}{S_{\lambda_1}} + \ln \left( \frac{\lambda_1}{\lambda_2} \right)^5 + \ln \frac{\varepsilon_{\lambda_2}}{\varepsilon_{\lambda_1}}}, \quad (3.6)$$

$T$  is the true temperature of the object. Spectral sensitivities  $\frac{S_{\lambda_2}}{S_{\lambda_1}}$  is named instrument factor and can be attained via calibration using the pre-calibrated tungsten lamp as reference temperature. As for the ratio between the two-spectral emissivity  $\varepsilon_{\lambda_1}$  and  $\varepsilon_{\lambda_2}$  grey-body behaviour is assumed as  $\frac{\varepsilon_{\lambda_1}}{\varepsilon_{\lambda_2}} = 1$  by reasons of selected wavelengths being closed to each other. The term of  $\ln \frac{\varepsilon_{\lambda_2}}{\varepsilon_{\lambda_1}}$  can thus

be cancelled out [36]. Equation 3.6 can be simplified as follows:

$$T = \frac{C_2 * \left( \frac{1}{\lambda_2} - \frac{1}{\lambda_1} \right)}{\ln \frac{G(\lambda_1, T)}{G(\lambda_2, T)} + \ln \frac{S_{\lambda_2}}{S_{\lambda_1}} + \ln \left( \frac{\lambda_1}{\lambda_2} \right)^5}. \quad (3.7)$$

### **3.3. CALIBRATION OF TWO-COLOUR SYSTEM**

#### **3.3.1. INTRODUCTION**

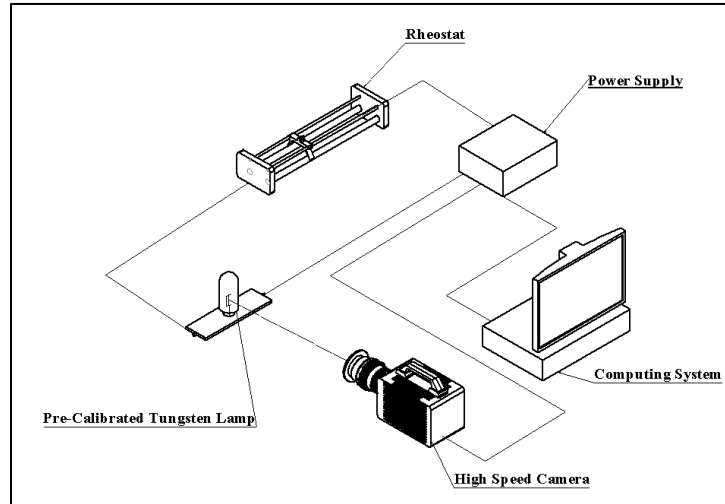
For optical pyrometers, the accuracy of temperature measurements is significantly based on how well the system is calibrated with known temperature source. The process of calibration is to establish the correlation between unknown temperature and acquired signal; for example, thermocouple technique is based on the relationship between temperature and voltage, optical pyrometers rely on the linkage between the irradiance of object and digital signal.

This section aims to present the calibration procedure and analyse errors arising from calibration source, the apparatus and the measurement algorithm used in temperature measurement.

#### **3.3.2. IMAGING SYSTEM SETUP**

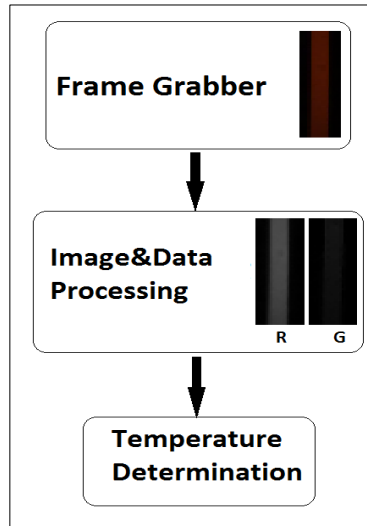
In this study, the imaging system has been facilitated to avoid using the complex system configuration of previous two-colour techniques using the narrow-bandpass and beam splitting filtering method; that could result in time-consuming setup, system importability, signal attenuation and high cost. Instead, the measurement system used here calculates the temperature of objects from the relationship between the main colours of images captured by the high-speed camera with built-in the colour-banded filter. The colour-banded filter, also called RGB filter, can separate the colour image into three channels corresponding to the red(R), green(G) and blue(B) sub-images[37]. By taking advantage of any combination of two-channels temperature can thus be determined . The two-colour measurement system established here is based on the R and G channels.

Figure 3-7 describes the structure of a measurement system, including a rheostat, a power supply system, a pre-calibrated tungsten, and a Photon SA-4 high speed camera. The power supply is a 38Ah car battery, fully charged, it can continuously power the tungsten lamp up to 20 minutes with a relatively stable current output. The rheostat can adjust current by changing its resistance in the circuit. The irradiance of the tungsten ribbon can thus vary with current.



**Figure 3-3** Structure of imaging setup for calibration

Figure 3-8 shows the processing procedure of the computing system. The high-speed camera (frame grabber) captures the image of the tungsten lamp, and converts COMS's analogue signal into a two-dimensional RGB digital image with 8-bit digitization, saved in a built-in SSD memory of Frame Grabber, then transferred to the computer for imaging processing. This is done within a specially written algorithm in MATLAB. The image captured by the frame grabber was then separated into the R and the B channels; the ratio between the two channels were calculated pixel by pixel to form a two-dimensional RG ratio distribution. And, according to that RG ratio distribution, the object is true temperature which can be inferred by Equation 3.7.



**Figure 3-4** Flowchart of the computing system

### 3.3.3. SPECTRUM RESPONSE OF THE IMAGING SENSOR

The function of camera sensor is to convert photons of different spectral radiation that strike onto its surface into corresponding RGB channels aided by built-in colour-banded filters. However, for the sake of competition in the market, spectral information on the proportion of R, G and B signals across its operating spectral region is hard to obtain from the manufacturer. Knowing the peak spectral response of R and G channels is important for the two-colour measurement. Based on these factors, an investigation was conducted to infer the spectral response of the SA-4 PHOTRON camera used in the temperature. This study is similar to the previous works which were carried out by Tankeuchi [38] and Simonini [39]. As for the schematic setup shown in Figure 3-9, a manually tuneable monochromator was used to produce monotonic spectral variations for the high-speed camera to capture. The built-in light splitting system was composed of a fixed entrance and an exit slit, a group of focusing mirrors and a rotatable diffraction grating. Upon entry, the incident flux of the tungsten lamp, considered as a nearly black-body radiator, is dispersed into its spectrum. The monochromator can be adjusted to the specific wavelengths manually. As diffraction grating

rotated, the radiation, peaked at the requested wavelength, is isolated and pointed onto the exit slit. Then, the corresponding spectral colour is recorded by capturing the radiation emitted from the exit slit. Following this method, the camera spectral responses were tested from 400nm to 680nm with 10nm interval using the tungsten brightness temperature of 2473K.

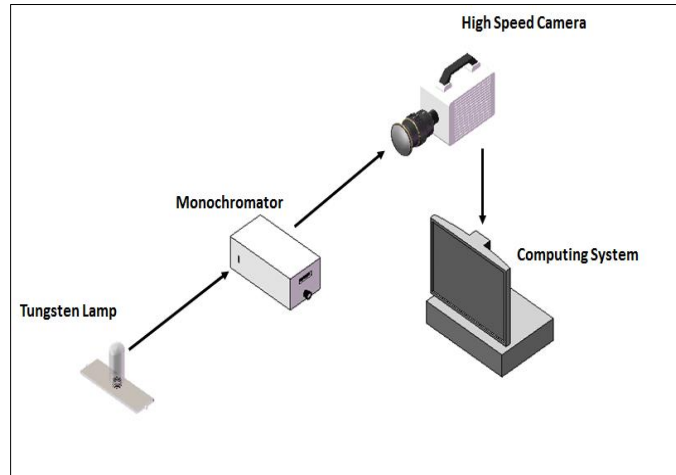


**Figure 3-5** Schematic setup of spectral evaluation

Figure 3-10 presents the intensity variations of R, G and B channels of the PHOTRON SA-4 camera within the VIS range. Colours at shorter wavelengths are mainly determined by the B signal with limited or no contribution from the other signals. At 480 nm, the G signal starts to appear, and its distribution rises along with wavelength. The surge of the G signal is synchronised with the B channel approaching the peak. From 450nm onwards, the B signal follows a limited decline by 470nm, then rises to its maximum intensity. After 500nm, the B signal begins to experience a reduction, eventually hitting the bottom at around 560nm. At 520nm, the R channel begins to respond and increase as the imaged wavelengths increase. The peak of R channel is at 630nm, followed by a levelling off. After 660nm, the R signal begins to fall down until its intensity disappears at around 680nm. The G signal fluctuates between 540nm and 580 nm, peaking at 580nm, finally zeroing at around 640nm.

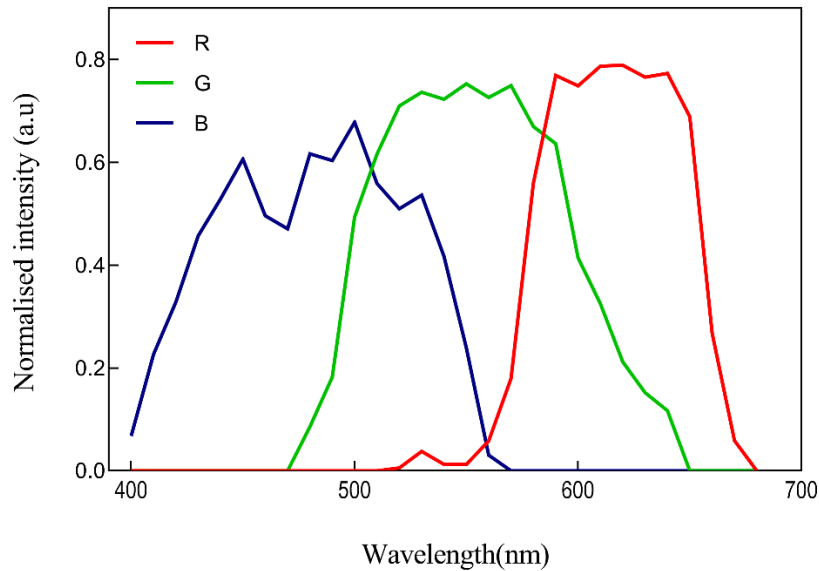


**Figure 3-6** R, G and B channel responses of the PHOTRON SA-4 system at different wavelengths in the VIS region

### 3.3.4. TEMPERATURE CALIBRATION SOURCE

The instrument factor  $\frac{S_{\lambda_1}}{S_{\lambda_2}}$  is the ratio between the spectral sensitivities of the camera sensor at the selected wavelengths, and has to be known for determination of the temperature. This can be determined through the calibration procedure using a standard temperature source. The tungsten lamp was utilised in the calibration for this purpose. Previous studies have proven that using a tungsten lamp as a standard light source is possible [6, 40].

The tungsten lamp used here was pre-calibrated and manufactured by Land as a known temperature source for calibration purpose. Matsui [40, 41] carried out a calibration source comparison between a tungsten lamp and blackbody, and found that temperatures obtained by the blackbody and the tungsten lamp calibrations showed good agreement, with only a small difference (10K) in the vicinity of 2000K.

The specification of the calibrated tungsten lamp can be found in the calibration certificate [42], and its brightness temperature measured at wavelength of 660nm, which is presented against the current input to the tungsten lamp. This group of data is reproduced in Table (3-1) and plotted in pre-calibrated region of Figure 3-11. In order to expand the range of measured temperature for the two-colour method, the brightness temperature of the tungsten lamp was interpolated down to 1173K for temperature calibration purpose, which is presented as an estimated region of Figure 3-11. Once the temperature is lower than 1173K, the radiance of the tungsten became very weak and is not suitable for the temperature calibration. To ensure the accuracy of the estimated temperature region, pre-calibrated temperatures were compared with the corresponding temperatures calculated by using curve-fitting. They were both in good agreement, with maximum error of as little as 6.77K at 2473K.

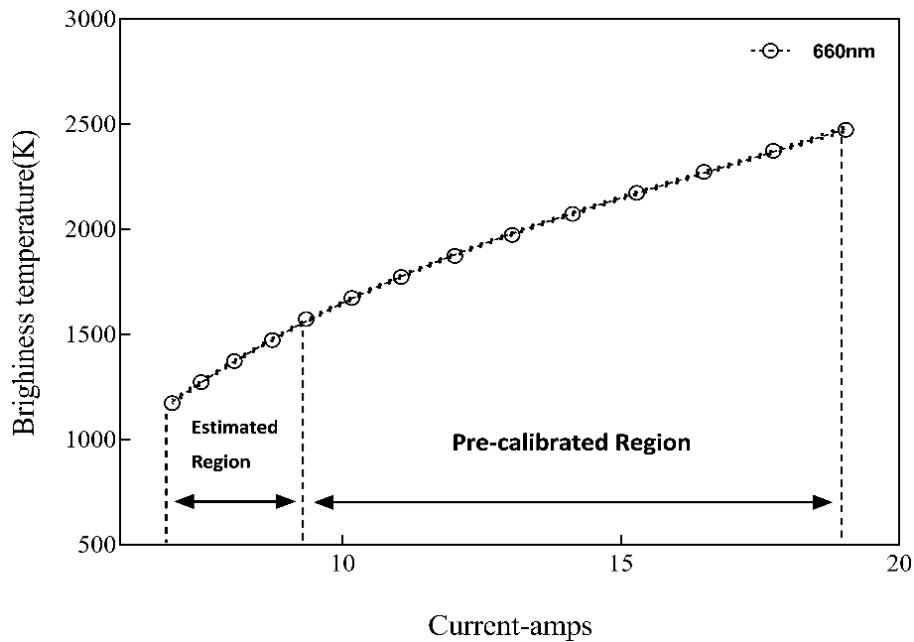


Figure 3-7 Calibration of the tungsten lamp

Dynamic range is a term of describing the sensor's maximum number of signal electrons compared with its total dark temporal noise level [28], which means that the range of light intensities that can be recorded by cameras, and cameras vary in their ability to handle dynamic range. The wider the

dynamic range of the camera, the more information the camera can capture. The employed high-speed imaging system can deliver high dynamic range; this allows the camera to cover a wider temperature range without changing either shutter speed or aperture.

**Table 3-1** Calibration of the tungsten lamp verified by manufacturer [42]

Brightness Temperature(K)	Current(Amperes)	Uncertainty +/- K
1573	9.345	7
1673	10.165	7
1773	11.055	8
1873	12.015	8
1973	13.045	9
2073	14.135	9
2173	15.285	10
2273	16.490	10
2373	17.740	11
2473	19.040	11

The correlation between the true and the brightness temperature can be considered as a function of tungsten emissivity. It can be expressed as

$$\frac{1}{T} = \frac{1}{T_b} + \frac{\lambda}{c_2} \ln(\varepsilon_\lambda), \quad (3.8)$$

where the tungsten emissivity  $\varepsilon_\lambda$  is in turn a function of the temperature and of the wavelength, the Equation is proposed by Larrabee [43] and written as

$$\varepsilon_\lambda(\lambda, T) = 0.4655 + 0.01558\lambda + 0.2675 \times 10^{-4}T - 0.7305 \times 10^{-4}\lambda T, \quad (3.9)$$

where  $T$  and  $T_b$  are the true temperature and brightness temperature respectively, both in K.

$\lambda$  is the wavelength in  $\mu\text{m}$ . To obtain the true temperature of the tungsten used in calibration, the iterative method has to be applied, and executed by MATLAB

Rearranging the Equation 3.8

$$T_b = \frac{TC_2}{C_2 - (\lambda \times T \times \ln(\epsilon_\lambda))}. \quad (3.10)$$

The iterative steps were processed as follows:

- (1) Substitute Equation 3.9 into Equation 3.10, and input the brightness temperature at  $0.66\mu\text{m}$ .
- (2) Set True Temperature  $T$  range from 1000K to 3000 K, with an interval 0.001
- (3) Balance the two sides of Equation 3.10 by using iterative MATLAB codes with the  $T$  range in step 2
- (4) The programme will abort the execution and give the true temperature, once the difference matches the criteria (below 0.01)

By using this method, the true temperature of tungsten ribbon can be inferred. Once known, the true temperature which can be used to determine the brightness temperature and the emissivity of any wavelength in the visible band. Figure 3-12 shows comparison between the true and brightness

temperature. It appeared that the true temperatures are higher than the brightness temperatures at 660nm with a linear relationship between them. The decrease of tungsten emissivity in Figure 3-14 leads to true temperature increasing faster, and being higher than the brightness temperature at 660nm. This finding was also found and interpreted by G.A.W.rutgers [15].

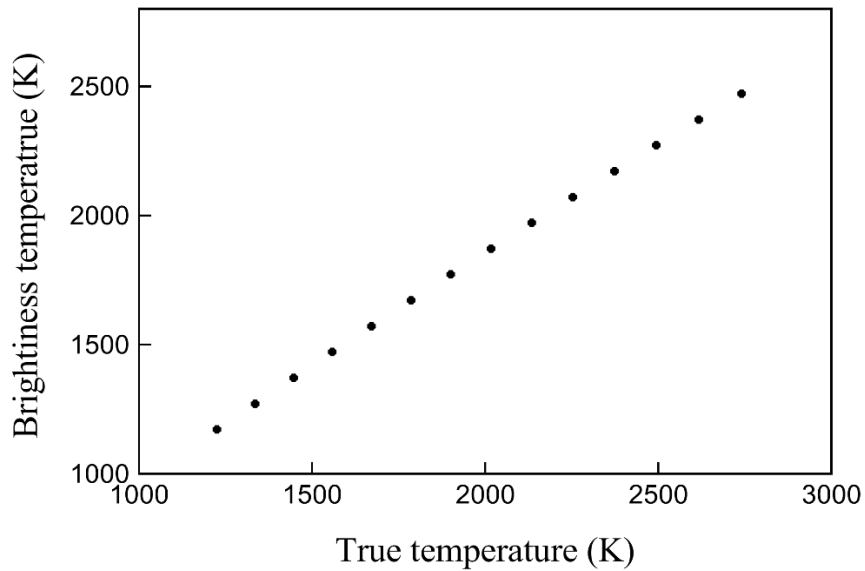


**Figure 3-8** True temperature of tungsten filament against the brightness temperature that pre-calibrated at wavelength 660nm

The brightness temperature of wavelengths used in measurement at 580nm and 630nm can be obtained once true temperature is known. Comparison of brightness temperature between these wavelengths is shown in Figure 3-13. The higher brightness temperature is found at 580nm, and increases slightly faster than the temperatures at 630nm.

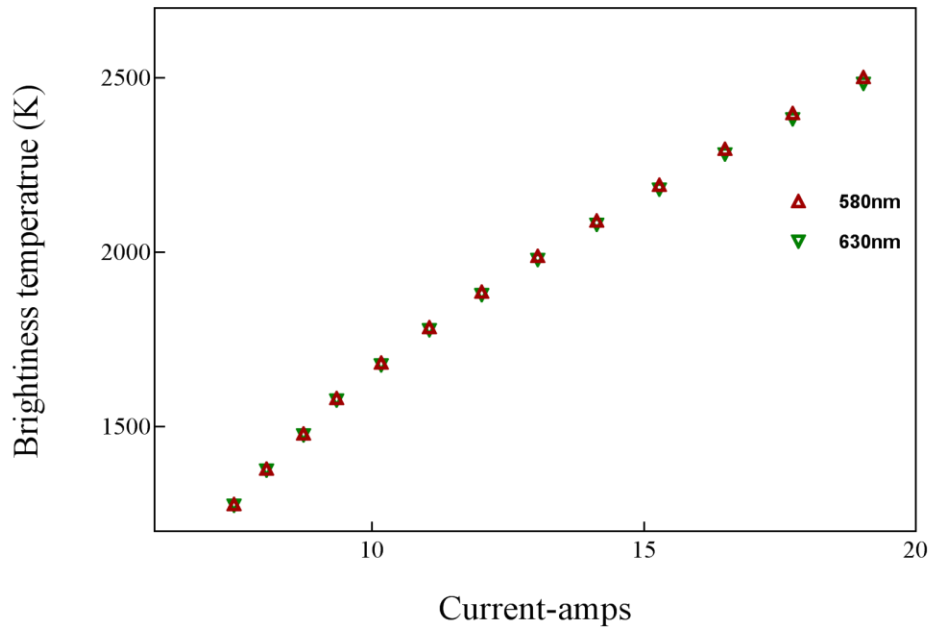


**Figure 3-9** Tungsten lamp brightness temperature calibration curve

In Figure 3-14 the emissivities of the tungsten peak at short wavelengths, and tail off as the wavelength increases. Emissivity can also be affected by the temperature, especially, at longer wavelengths; the temperature determines the variation of emissivity. Bear in mind that the two-colour measurement assumes the ratio between the emissivities at selected wavelengths is 1; thus the wavelengths used should be close to each other. Here, the wavelengths selected are 580nm and 630nm, respectively. Figure 3-5 shows a consistency of emissivity ratio crossing the pre-calibrated temperature range of the tungsten, which follows the assumption well.

BACKGROUND OF TWO-COLOUR METHOD

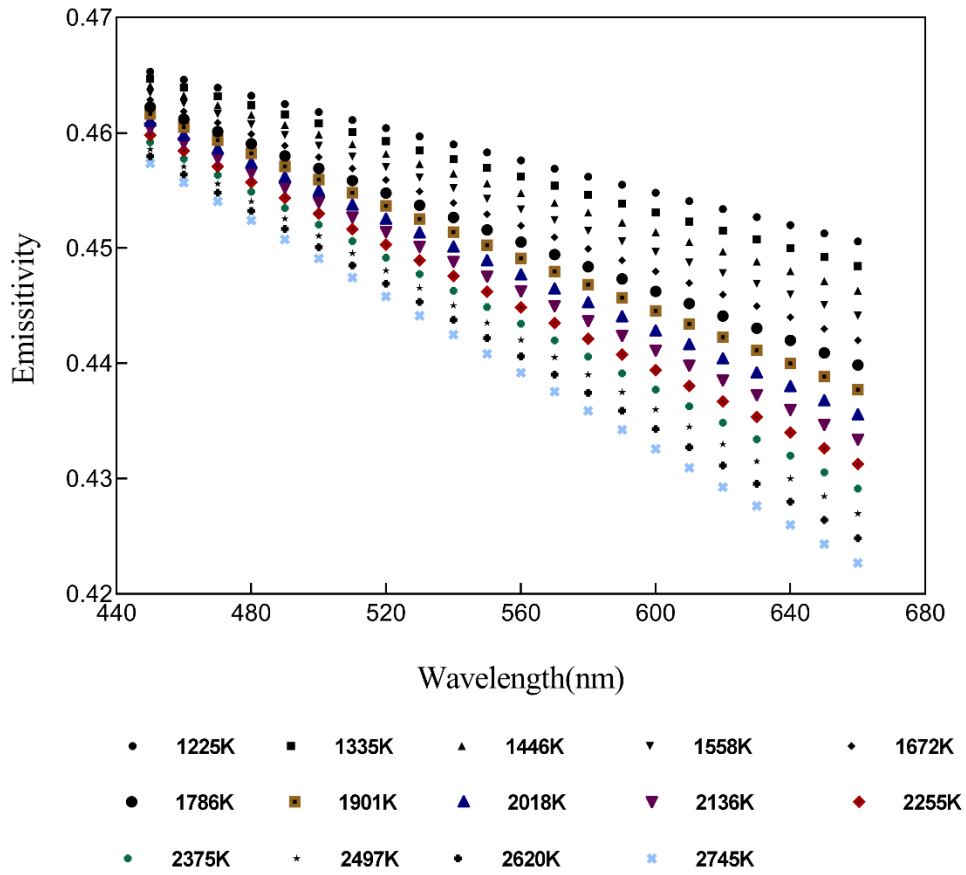
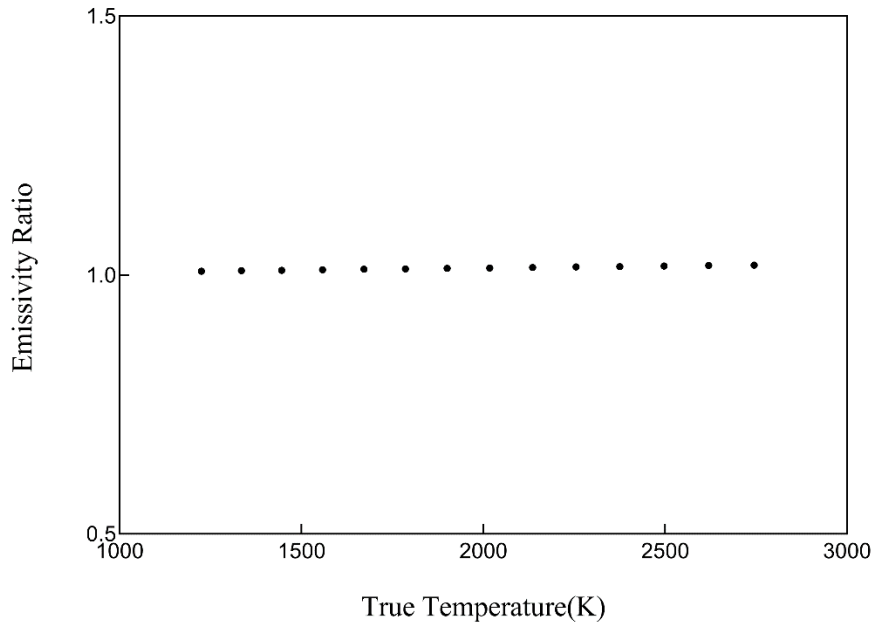


Figure 3-10 Variation of the tungsten emissivity along with wavelengths



**Figure 3-11** Distribution of emissivity ratio between the wavelengths 580nm and 630nm

### 3.3.5. CALIBRATION OF THE INSTRUMENT FACTOR

RG ratios were obtained through measuring radiance of the tungsten filament from the true temperature 1225.75K to 2497 K, with the use of the colour band filtering method. These ratios can be applied to determine the instrument factor  $S = \frac{S_{\lambda_R}}{S_{\lambda_G}}$  by rearranging the Equation 3.6

$$S = \frac{e^{c_2 \left( \frac{1}{\lambda_G} - \frac{1}{\lambda_R} \right) / T}}{\frac{G(\lambda_R, T) \cdot \epsilon_{\lambda_G} \left( \frac{\lambda_R}{\lambda_G} \right)^5}{G(\lambda_G, T) \cdot \epsilon_{\lambda_R}}}, \quad (3.11)$$

where the  $\lambda_R$  (630nm) and  $\lambda_G$  (580nm) are the peak wavelengths in the red and the green channels shown in Figure 3-4. These two peak wavelengths are analogous to the wavelengths used in the narrow-band filtering method.

In the calibration process, the images of the tungsten filament were captured, and then the grey levels of the pixels over the tungsten filament were averaged to obtain the RG ratios against the true temperatures of the tungsten lamp. As shown in Figure 3-16, there is a decrease in the RG ratio as the true temperature decreases. This process was repeated 4 times, and they all showed good consistency in trend. Extra care is needed with regard to the camera setting, such as shutter speed and aperture in order to avoid image saturation.

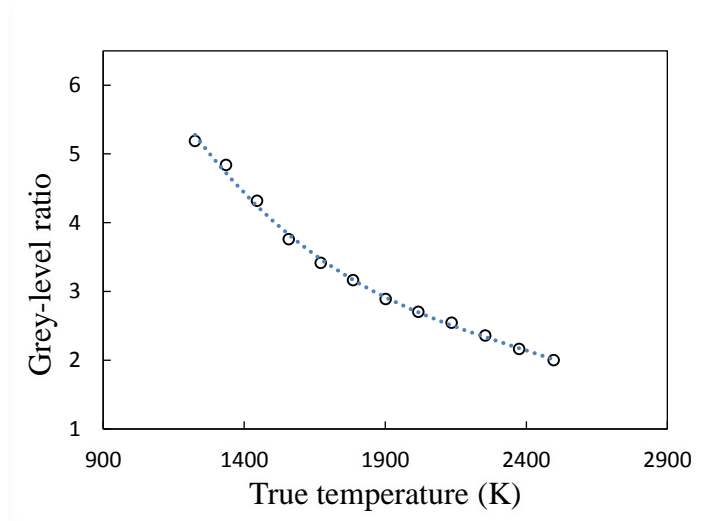


**Figure 3-12** Grey-level ratio (RG) response of the imaging system along with true temperature

Based on the above RG ratio curve, the instrument factor can be calculated by Equation 3.11. The correlation between instrument factor and the grey-level ratio was tabulated in Figure 3-17, where the points marked with solid colour yield the linear relationship indicated by the blue dotted line.

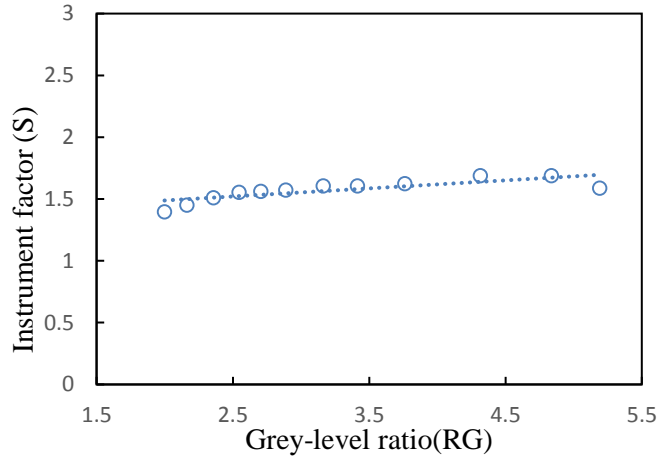


**Figure 3-13** Instrument factor against grey level ratio between R and G channels

$$S = 0.0861R_{rg} + 1.2745 \quad (3.12)$$

The accuracy of the two-colour measurement was validated by applying the technique when measuring the true temperature of the tungsten, and also compared to Infra-pyrometer which will be described in a later chapter.

This validation test of measuring the temperature of the tungsten has been repeated three times using the same camera setting in all tests. Figure 3-18 shows the results of these three tests compared with the reference temperatures marked by the dotted line. Each data point averages ten samples in each test. The maximum error of 73 K occurred at the true temperature of 1900K, corresponding to a relative error of 6%. The average errors of test 1, 2, and 3 are 27K, 34K and 35K, which are equivalent to 3.4%, 2.4% and 3.1% of the system measurable range respectively.

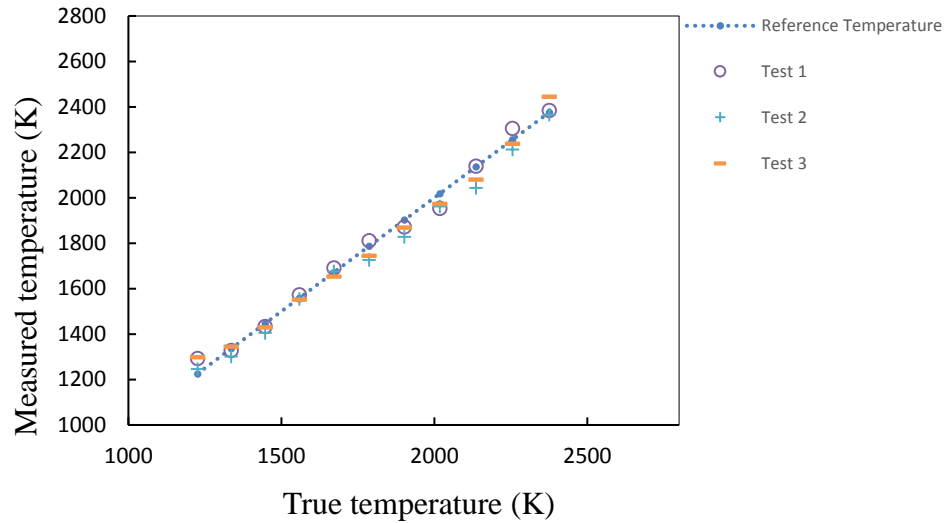


**Figure 3-14** Comparison between the measured and the true temperatures of tungsten

### 3.3.6. EVALUATION OF THE IMAGING SYSTEM

Two-colour temperature measurement is a type of optical pyrometer, which correlates the radiation of the grey body with the response of the RG ratio of the digital camera; this correlation was obtained by calibrating the RG ratio with the irradiance from the tungsten lamp at the corresponding temperature. Although based on the correlation, the system can perform accurately on measuring the temperature of the tungsten filament at the camera settings used in the calibration procedure. It is still worth assessing the characteristic of the measurement system by using different camera settings. Similar studies have been conducted on using different exposure time, aperture and viewing distance by Duo Sun [37], apart from that, the effect of camera focal length will be also evaluated in this section.

The evaluation of system linearity was conducted by using different exposure settings of the camera to image the filament of the tungsten lamp set at a constant brightness temperature. The captured images were separated into the R, G and B channels, and the grey level of each one was averaged as the intensity response at the corresponding channel; the captured images were saved as 16-bit

TIFF format, it indicates that the maximum intensity can be up to 65536. Figure 3-19 shows the correlation between the intensity of each channel and different exposure time when the tungsten lamp was set at the brightness temperature of 1573K.

The exposure time was normalized to the longest exposure time where the images were close to saturation. In Figure 3-19 the imaging system performs excellent linearity in the R, G and B channels. It can thus be speculated that the effect of exposure time on the accuracy of temperature measurement is infinitesimal. This finding is apparently important because the irradiance of different objects is not identical even at the same temperature, so the camera exposure time has to be changed to avoid images saturation. Again in Figure 3-19, the intensity of the R channel shows a faster rate of increase with respect to the other two channel. This could easily lead captured images to be over-exposed in the R channel and under-exposure in the G and B channels, without an appropriate exposure time.

Even though there are many methods, such as either using narrow-banded filters or changing Gama factor of the camera, can adjust the response of the R channel to a relative low level, the original colour profile of the glowing object is therefore changed, and also if the system calibration is based on such conditions, this can result in a complicated system configuration, and inconvenient in practical applications.

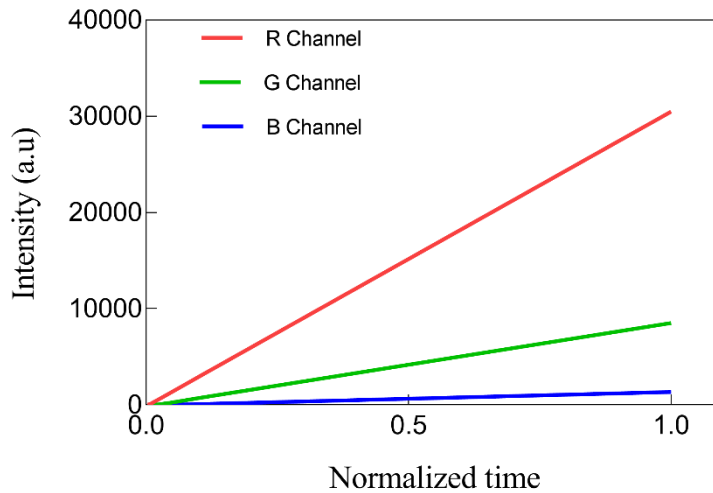


**Figure 3-15** The grey level responses of the camera in the R, G and B channels at different exposure time.

As for viewing distance between the imaging system and the measured object, it is a frequently changed parameter in temperature measurement because in practical applications the viewing distance is very unlikely to be identical with the distance used in the lab. It is thus worth knowing the effect of the viewing distance on accuracy and sensitivity of the two-colour pyrometer. This evaluation test was conducted on imaging the tungsten filament at the different viewing distances varying from 40 to 80cm with an interval of 20cm. The temperature of tungsten was set at 1673K over the all cases to give a stable irradiance. Each measured temperature shown in Figure 3-20 was inferred from an average of the RG ratios of 10 instantaneous images. Variations of temperature was also found when measured at different viewing distances, showing a good consistency, with as little as 9.6K in mean temperature difference.

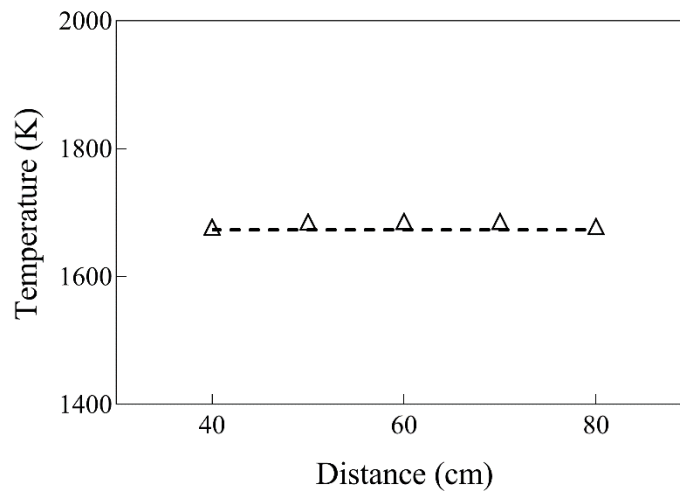


**Figure 3-16** Measured temperatures of the tungsten filament

The effect of the image being out of focus may affect the measurement accuracy. In advance of measuring the temperature of an object, the imaging system needs to focus on the target by changing the focal length to avoid blurring viewing which could lead to inaccuracy of temperature measurement. Focal length, habitually denoted in millimetres, is a basic description of lens, which indicates that an optical distance from the point where light rays converge to form a sharp image of the object to the sensor of the imaging system. Some images were captured slightly out of focus since the judgement of the image as being either in or out focus can vary from one observer to another's. In the experiment the focal length was set from 50.4 to 53mm, while using still to use the tungsten lamp as a stable emitter. Figure 3-21 shows measured temperature variation, along with the focal length, from the image being in focus at 50.44mm gradually towards slight out of focus. It was found that the average temperature difference was less than 7K and the maximum temperature difference was 19K. It means that the slight local of focus on the object will not significantly affect the accuracy of temperature measurement.

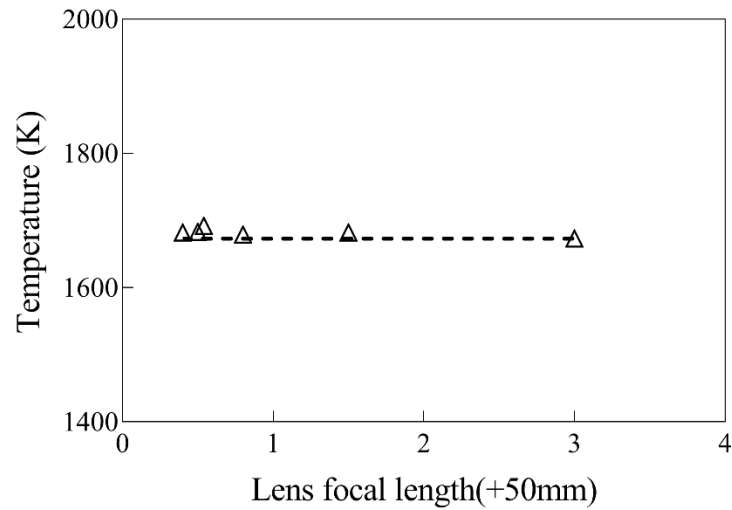


**Figure 3-17** Measured temperatures for different focal lengths

### 3.4. SUMMARY

This main work in this chapter is concluded as follows:

- ❖ The principle of the proposed two-colour method has described in detail. The reason for using the colour-banded method instead of the narrow-band filter has explained. Along with the temperature increasing the RG ratio obtained from the imaging system experienced a monotonic decrease.
- ❖ The pre-calibration of the tungsten lamp was based on the brightness temperature. The process of the transformation from the brightness temperature to the true temperature clarified. It was found that the true temperature of the tungsten lamp is higher than the brightness temperature. The emissivity of the tungsten lamp was found to decrease as wavelength increased.
- ❖ Through the test of the camera spectrum response the peak wavelengths, at the G and R channels, was found to be at 580nm and 630nm respectively. Based on the selection of these two wavelengths the proposed two colour measurement was found to calibrate

with the standard temperature source well. The other combinations of two wavelengths yield the measured temperature deviating far from the reference temperature. Moreover, the emissivities at the two selected wavelengths are nearly identical, and remain constant along with the temperature variation.

- ❖ In temperature validation, the calibrated two-colour system was applied to measure the tungsten ribbon temperature. As a result, the maximum error of 73K occurred at the true temperature of 1900K, and the average error of three tests was 2.9%.
- ❖ The characteristic of the proposed measurement system was assessed by changing the camera factors includes: the exposure setting; the focal length, and viewing distance. It was found that these factors would not significantly affect the accuracy of the two-colour system.

## **4. OPTICAL STUDY OF SOOT FLAME TEMPERATURE FOR DIESEL-IN-WATER EMULSION DROPLET COMBUSTION**

### **4.1. BACKGROUND OF THE DROPLET COMBUSTION**

At present the world's primary energy consumption mainly depends on liquid fuel owing to its high-energy density and ease of storage. However, owing to the fact that the prices crude oil prices have increased in the last decade and that more stringent emission regulations have been implemented, the exploration of alternative liquid fuels is becoming an urgent task.

One of the likeliest alternative is emulsified fuel; it has been received much attention in the combustion industry for many years. This fuel does not exist naturally in the world; it is artificially manufactured by blending two or more miscible liquids with adding an emulsifier (or surfactant agent) [44]. This process is called emulsification.

Diesel oil is a common liquid fuel, usually used in heavy-duty vehicles to achieve a better fuel consumption. Compared with gasoline engines, diesel engines will produce more pollutants such as soot and NO<sub>x</sub> formation, which are toxic particles. The emergence of fuel emulsion offers a simple way to enhance the combustion efficiency of liquid fuels, as well as reducing pollutants from the exhaust of internal combustion engines.

Armas [45] has studied the effect of oil-in-water emulsified fuel on the pollutant emission and the performance of diesel engine. One of the most attractive effect that was found by burning this type of fuel emulsion is associated with an interesting phenomenon named secondary atomization [46]. During the combustion of emulsified fuel droplets, the water, inside the droplet, can achieve a superheated temperature. A liquid at this temperature could lead to bubble nucleation [47]. This

rapidly expanding vapour bubble can either completely or partially break up a droplet of emulsified fuel. This physical phenomenon is categorized into two types: micro-explosion and puffing. A droplet suddenly transforming into small fine droplets is named micro-explosion. The expulsion of water vapour from the droplet surface in the form of small droplets is named puffing.

Secondary atomization is broadly agreed as an effective way to reduce pollutant emissions from most spray combustion systems [46]. M.Abu-Zaid [48] and Armas [45] have both carried out the combustion of emulsified fuel in diesel engines. The former demonstrated the reduction of exhaust gas temperature without losing thermal efficiency, the latter showed the reduction of pollutant emission.

In addition, most research focuses on the study of a single droplet of emulsified fuel in order to have a better observation of the secondary atomization. H.Watanabe [49] used mono-colour high speed imaging to capture the phenomena of puffing and micro-explosion and found that 50-70% water-content by volume of fuel emulsion can transfer the emulsified fuel into water vapour instantly at the occurrence of micro-explosion. Yoshiyuki [46] found that increasing the dispersed water droplet diameter in the emulsified fuel droplets can easily trigger micro-explosion, and revealed the average temperature needed to initiate the puffing of droplets. Fu [50] explained the micro-explosion of droplets emulsified fuel in detail, and also assessed the effect of various parameters on the occurrence of micro-explosion.

In terms of droplet temperature measurement, most previous research aimed to detect the inner droplet temperature [49] and the gas temperature field surrounding the burning suspended droplets [51] both by thermocouples. The linkage between the droplet temperature variations and the droplet secondary atomization can thus be revealed.

Not much attention has been paid to the flame temperature during the combustion of emulsified fuel droplets. W.L.Saw [52] detected the surface temperature of the flame produced by burning pure black liquor droplets; flame temperature was inferred using two-colour optical pyrometer

based on the two narrow-banded wavelengths in visible spectrum. The results show the maximum flame surface temperature surrounding the outermost layer of flame and the flame surface temperature variation ranging from 1213-1473K. But the noise ratio equivalent flame temperature was not eliminated from the final visualized two-dimensional flame temperature distribution. As a result, the profile of flame boundary is difficult to identify in the images

For these reasons, it is worth investigating temperature in the flaming region of emulsified fuel droplets. Two-colour method is a desirable diagnostic technique for soot flame temperature measurement, allowing non-intrusive measurement and fast response time; in particular, this technique is capable of providing two-dimensional temperature measurement which is an obvious advance on thermocouple technique.

During the combustion of diesel-in-water fuel emulsion, the combustion products of soot particles and gaseous combustion are present. The intense radiation of soot particles dominates the luminosity of diesel combustion. Because the two-colour technique can use blackbody radiation from soot particles, it can directly detect the particles temperature. The temperature of combustion gases is not directly measured. In addition, H.Zhao [6] reported that the temperature difference between the soot particles and the combustion gases can be ignored (less than 1K) as the soot particles and its adjacent hot gases have reached thermal equilibrium, which can be achieved in  $10^{-5}$ - $10^{-6}$  s within a cylinder such as an internal combustion chamber. As a result, the temperature of soot particles can simultaneously vary with the temperature variation of its surrounding gases. The flame temperature can thus approximately refer to the soot particle temperature.

This chapter aims to detect soot flame temperature during emulsified fuel droplet combustion. The temperature measurements have been carried out on pure diesel, and 10%, 20% and 30% water-content by volume of diesel-in-water emulsions. Time-varied average flame temperatures of emulsified fuels have been calculated throughout droplet lifetime. Also, during the secondary

atomization occurring in the fuel emulsion cases, soot flame temperature distribution has been visualized using the colour map.

The following sections give the experiment method, the results and discussion; the experiment setup with relevant material preparation and the obtained flame temperature results have been described and presented respectively. The chapter ends with an overall conclusion.

## **4.2. EXPERIMENTAL METHOD**

### **4.2.1. EMULSION PREPARATION**

Diesel-in-water (D/W) emulsions were prepared in advance according to the method followed and described by [53, 54] Where an emulsifier (Polysorbate 80: HLB=15) was added and stirred with the exact amount of diesel to be emulsified, then the required water quantity was added gradually to the mixture. A 20000 rpm electric blender was used for mixing the liquids for more than five minutes until a homogeneous milky white liquid is produced. 10%, 20%, and 30% water content by volume of D/W emulsions have been prepared and tested throughout this work in addition to the base diesel fuel. The D/W emulsions were stored in containers during the tests; no visible changes were observed throughout the testing period.

### **4.2.2. SiC FIBRE PREPARATION**

The greatest difficulty is to prepare SiC fibre which is manufactured by COI ceramics, and was ordered from the UK distributor Goodfellow. Figure 4-1 shows a 5 m long SiC bundle that contains 500 ultra-thin filaments; the diameter of each filament should be around 15 $\mu$ m. The greatest challenge is to manually separate each filament out from the bundle because each filament is brittle. In order to confirm that the separated filaments are all the required diameter (15 $\mu$ m); these filaments were sent to the chemical department for diameter inspection. As shown in Figure 4-2, the filament of measured diameter was imaged by an inverted fluorescence microscope.

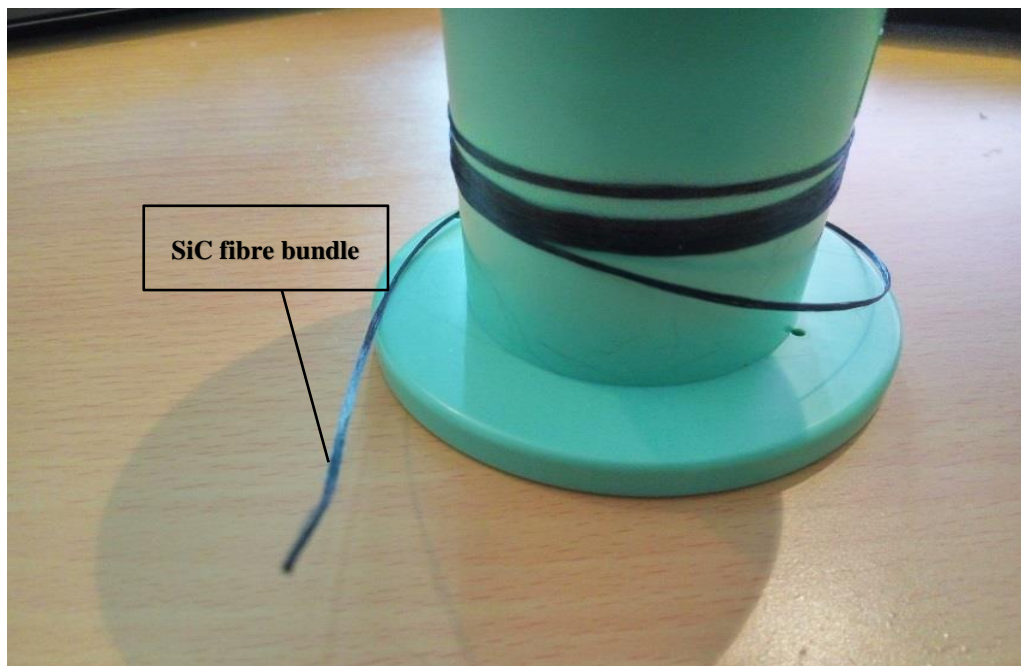


**Figure 4-1** The original bundle of SiC fibre



**Figure 4-2** Diameter of filament was imaged and inspected by a digital microscope

### 4.2.3. EXPERIMENTAL SETUP

The schematic drawing of the experimental setup is shown in Figure 4-3. A micro-fine syringe with hypodermic (0.33\*12.7mm) needle has been used to generate and suspend the fuel droplet on a 75  $\mu\text{m}$  cross-shaped silicon carbide (SiC) fibre mesh under room conditions. Optical setup consisted of a PHOTRON -SA4 high speed colour camera with Nikon AF Micro NIKKOR 60mm f/2.8 lens attached to a 55mm macro extension tube set (for backlit droplet imaging), and Sigma zoom 24-70mm f/2.8 EX DG macro lens (for self-illuminated flame colour imaging). For backlit imaging, two 6-volt LED lights with white light diffuser have been used behind the droplet opposite to the camera lens. The droplet is ignited by a pilot butane flame produced by a micro lighter, and the images are recorded for the period of time between droplet ignition and flame extinction. It was found that the sideways heating of the SiC fibre produces the most reliable and repeatable ignitions. At the same time, the impact of the pilot flame has also been kept to the minimum. The tests have been carried out on pure diesel, 10%, 20%, and 30% D/W emulsions using both backlighting and self-illumination imaging techniques. Each test has been repeated three times, with the droplet initial diameter being fixed at  $2 \pm 0.2$  mm. The acquired images were stored in (TIFF) format and processed by specifically written algorithms using MATLAB.

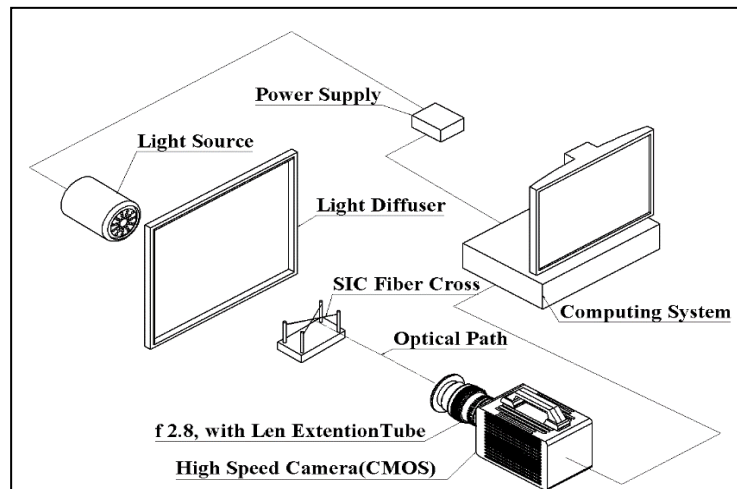


Figure 4-3 Experiment setup

### 4.3. RESULTS AND DISCUSSION

#### 4.3.1. DROPLET COMBUSTION ANALYSIS

Backlit imaging has been applied to capture the droplet dynamics at 1000 and 40000 fps. The latter fps is chosen to resolve the details of droplet micro-explosion. Figure 4-4 shows a sequence of images of 30% D/W emulsion droplet combustion at 1000 fps. While this is good enough to observe the change of the droplet profile, only the last image captures the micro-explosion.

Three major characteristics have been observed for the combustion of D/W emulsion droplets compared with that of diesel droplet. Firstly, very small fluctuations are seen on the surface of the D/W emulsion droplet, which then increase in intensity when droplet swelling takes place. In comparison, a diesel droplet burns smoothly without any disturbance. The instability inside the droplet resulting from nucleation and bubble formation leads to droplet puffing and micro-explosion. Secondly, both homogeneous nucleation and heterogeneous nucleation have been noticed in the combustion of D/W droplets, as shown in Figure 4-4, for time intervals 783, 805, and 920 ms respectively. Homogeneous nucleation takes place due to the temperature gradient inside the droplet between its core and surface; therefore, it happens within this area [55, 56]. Whilst, heterogeneous nucleation takes place in the interface between the liquid and the surrounding surfaces [56, 57] hence, it has been shown to occur nearby the SiC fibre. Thirdly, in the last third of their lifetimes, the D/W droplets experience remarkable periodic shape irregularities prior to micro-explosion. As a result, the droplet semi-circular configuration is not observed anymore. Because of reducing exposure time figure 4-6 reveals the progress of the droplet burning in advance of micro-explosion more than that shown in figure 4-5.

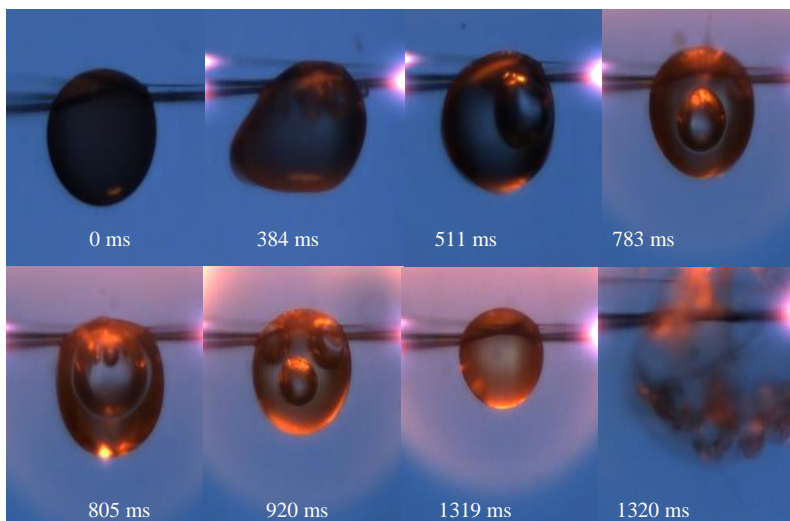


**Figure 4-4** Sequence of backlit images at 1000 fps for 30% D/W droplet. The last image captured droplet micro-explosion.  
[Note: 1mm=36 pixels]

Figure 4-5 shows the lifetime of single droplet combustion of the diesel and the D/W emulsions. The complete droplet combustion process from the appearance of soot flame to the flame extinction was recorded using the high-speed camera at 1000 fps and 1/39000s shutter speed in order to avoid image saturation. As expected, the period of time between the droplet ignition stage and the flame extinction decreased when more water was added into diesel fuel. As can be seen in Figure 4-5, the curve is in line with the predication. 0% represents the droplet of pure diesel fuel; 10%, 20% and 30% represent the amount of water by volume added into diesel fuel. The initial droplet diameter is fixed at  $2 \pm 0.2$  mm, the variance in the droplet size can lead to either slight increase or decrease the duration of single droplet combustion. The top of error bars indicates the longest burning time found in each case, on the other hand, the bottom of the bars points out the shortest durations of the droplet burning. Each point averaged four samples of the droplet combustion duration. The results show that the longest duration is the diesel droplet and the shortest one is 30% D/W emulsion droplet.

Additionally, it can be seen that droplet lifetime of the 30% emulsion is about one-third of the diesel droplet lifetime, in contrast to the diesel droplet which continues to burn until reaching complete consumption.

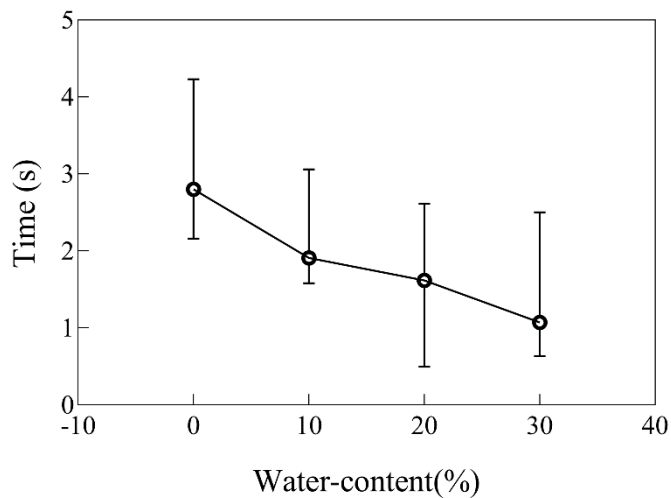


**Figure 4-5** Lifetime of the single droplet combustion of diesel and of 10% ,20% and 30% diesel-in-water Emulsions

### 4.3.2. MICRO-EXPLOSION OF FUEL EMULSION

The occurrence of micro-explosion during the combustion of diesel-in-water emulsions has been investigated in the present work. Backlit imaging has been used at 1000 and 40000 fps. As mentioned in the introduction, a frame rate larger than 5000 fps is required for tracking the full event [58]. However, the tests demonstrate that the camera was unable to track the micro-explosion process until a frame rate of 40000 fps was applied. It is observed that the droplet –and sometime the flame- simply disappear, as shown in Figure 4-6(a-b). Figure 4-6(c-h) is a sequence of droplet imaging at 40000 fps leading to micro-explosion. The explosive mist is first observed at image e and close to full mist at image h. The process is observed to take less than 100  $\mu$ s. In some extreme cases, sudden flame extinction was observed immediately after droplet micro-explosion. This kind of extinction has been observed many times, especially at 30% D/W emulsion, so it is not an uncommon or unrepeatable phenomenon.

Additionally, it has been noticed that the micro-explosion phenomenon is accompanied by a distinctive popping sound whose intensity increased with an increase in the amount of water in the emulsion; and no audible sound could be heard for pure diesel droplet combustion. The water-in-diesel droplet micro-explosion may have generated a shock wave that is sometimes powerful enough to extinguish the flame. This again needs further investigation.

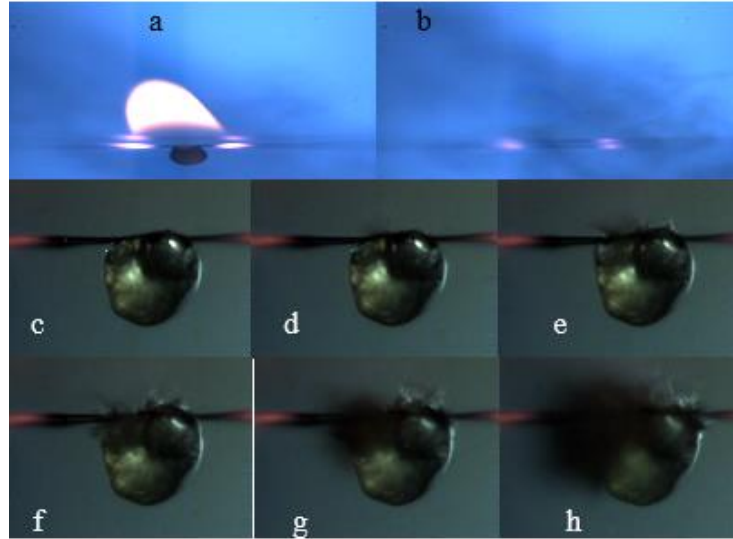


**Figure 4-6** D/W emulsion droplet before and after micro-explosion. Images (a-b) at 1000 fps, images (c-h) at 40000 fps. [Note: a-b,1mm=36 pixels; c-h,1mm=25 pixels]

### 4.3.3. DROPLET FLAME ANALYSIS

This sub-section aims to study the flame variation in terms of illumination and temperature when the secondary atomization (puffing and micro-explosion) occurs during the combustion of the fuel emulsions. Imaging processing technique is used to analyse the flame illumination, quantified by image greyscale. Flame temperature is measured using the two-colour system described in Chapter 3.

#### 4.3.3.1. Observation of the Flame illumination at Puffing State

In addition to the observation of the bubble nucleation inside the droplet and the evaluation of the droplet combustion duration, the soot flame variations induced by droplet puffing are also worthy of investigation, giving an insight into the effect of water-content involved combustion.

Figure 4-7, Figure 4-8 and Figure 4-9 show how droplet flame reacts to the droplet puffing at 10%, 20% and 30% D/W emulsions respectively. Puffing is the process of sub-droplets being emitted from the surface of the droplet due to bubble nucleation

An obvious indication of puffing is the fast-moving red-hot spot whose brightness is much stronger than that of its surrounding flame. Figure 4-7 shows one complete cycle of puffing at 10% D/W emulsion. The red-hot spot occurred initially at 1.747s with stronger illumination than that of its adjacent flame. Subsequent images illustrate more sub-droplets emitted from the droplet, and then travelling quickly throughout the flame, leading to the overall flame brightness intensity increasing dramatically. These changes are easily perceived with naked eye.

Figure 4-7 and Figure 4-8 illustrate the variation of flame shape and illumination at 20% and 30% fuel emulsions respectively; the camera settings used are identical with the one used at 10% fuel emulsion to make the combustion of each fuel-water mixture comparable. At 30% fuel emulsion the strongest puffing was found, which initiated at 2.196s and terminated at 2.235s to form a complete cycle of droplet puffing.

Partial image saturation was found in the combustion of fuel emulsions even with such a high shutter speed(1/39000s), signalling a higher gas temperature in the area of saturated pixels; this is predominantly caused by disruptive burning that occurred only in the case of D/W droplets, breaking them up into micro-droplets that burn either individually in their own flames, or in groups or clusters of more than one micro-droplet. The extent of the disruptive burning mainly depends on the evaporation rate of the water in droplet emulsions. Rapid water evaporation can further intensify the mixture of fuel and oxidizer, leading to a higher degree of premixed combustion [59]. As evidence of this, from 2.204 to 2.21s, the strongest emission from soot was observed, accompanied by along with the rapid expansion in the flame area. After this period, soot emission gradually reduced, evident from the bright yellow flame turning to a dark red one.

With reference to 20% D/W emulsion, Figure 4-8 displays droplet puffing in a complete cycle. It was found that the droplet puffing induced disruptive burning was weaker than that found at 30% D/W emulsion but stronger than the disruptive burning occurring in 10% D/W emulsion. The second row of images shows that a number of sub-droplets occurred during this period, leading to a stronger disruptive burning. As a result, the flame illumination becomes much stronger than that shown in the first row; meanwhile the flame area expands dramatically due to this stronger disruptive burning as well. The flame shape is affected strongly by the droplet puffing, meaning that the conical flame no longer exists.

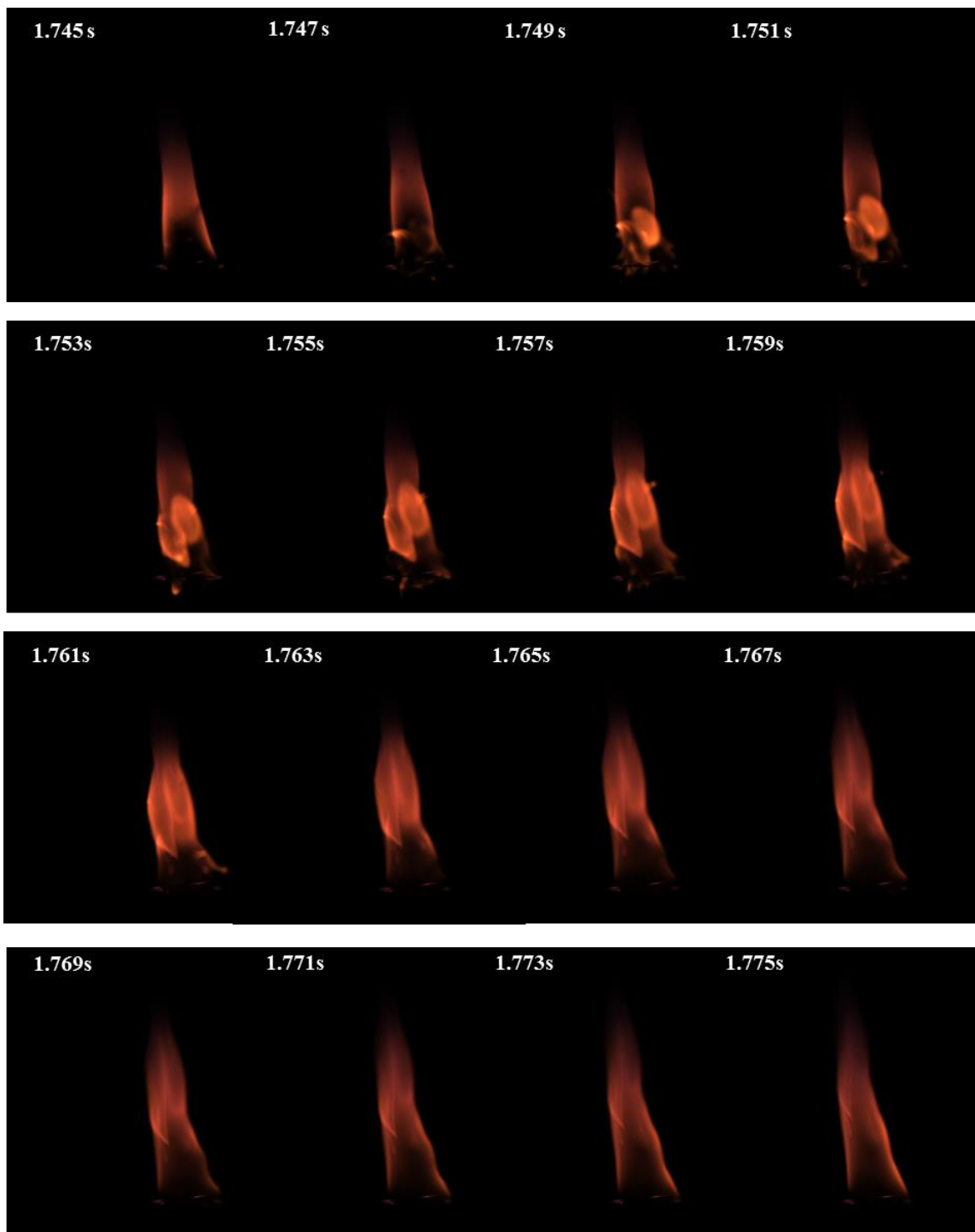


**Figure 4-7** Time history of soot flame at puffing stage when burning 10% D/W emulsion

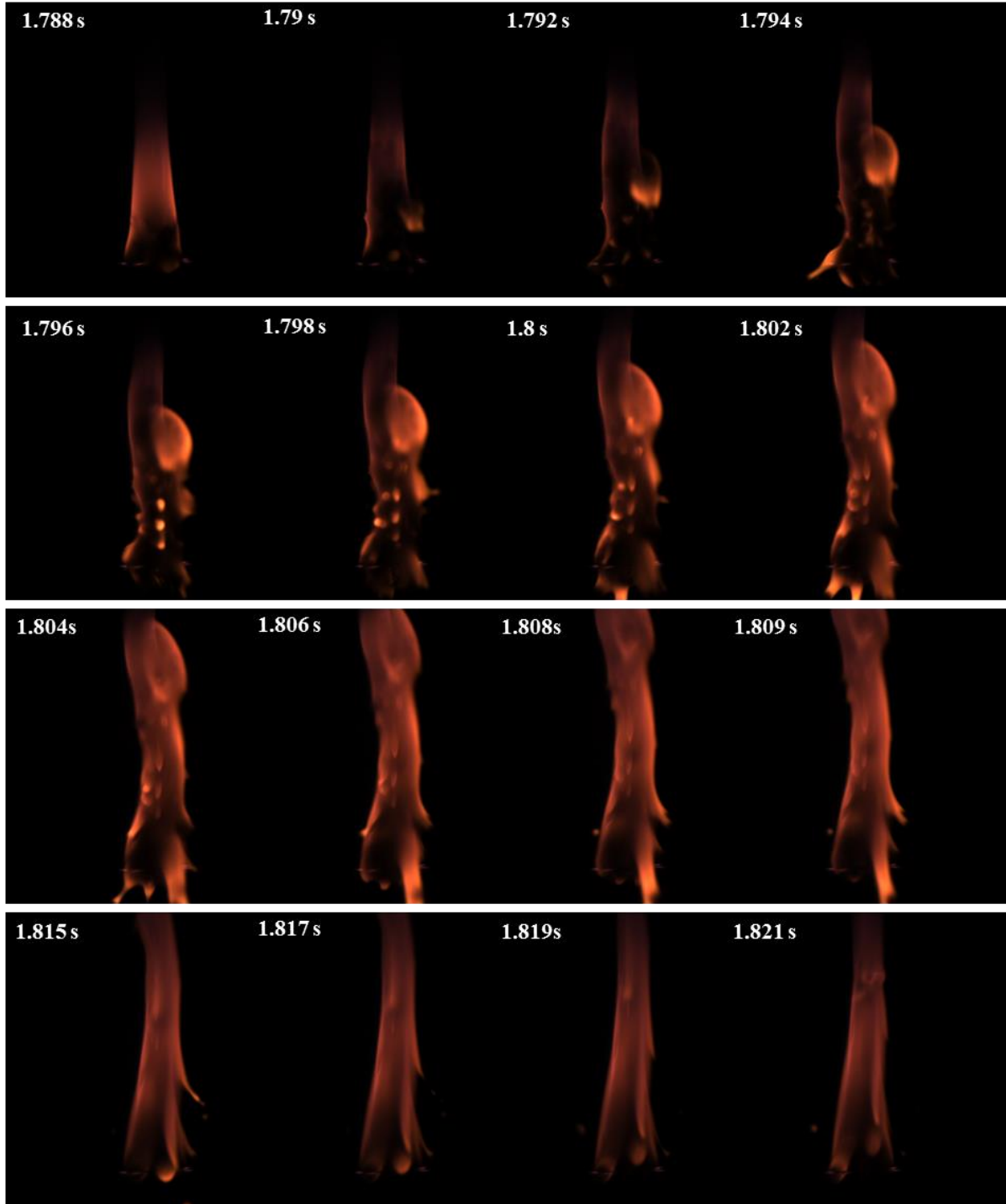


**Figure 4-8** Time history of soot flame at puffing stage when burning 20% D/W emulsion

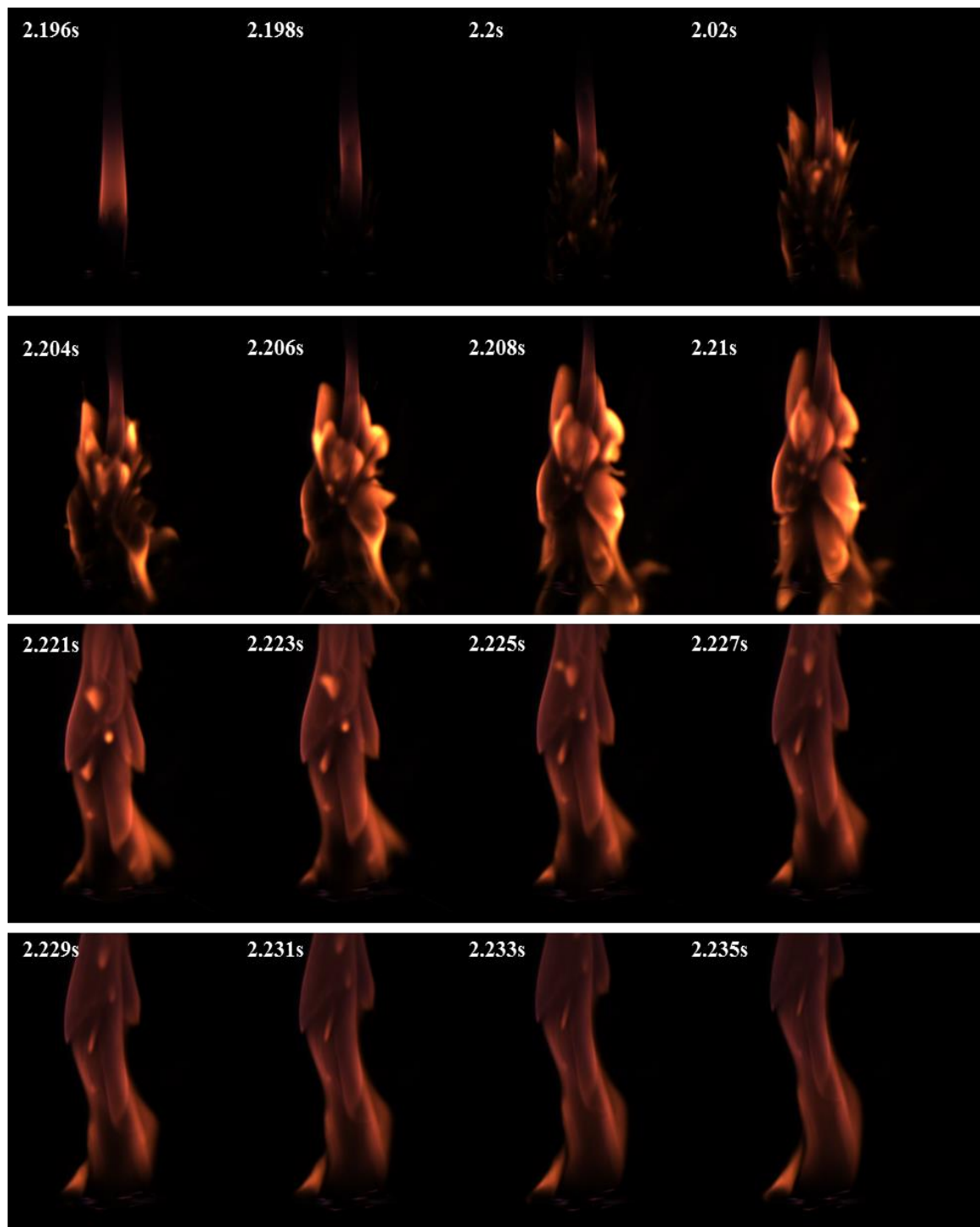


**Figure 4-9** Time history of soot flame at puffing stage when burning 30% D/W emulsion

The grey-level of image can be correlated to the irradiance of grey-body, which can be used to track the radiation variation from any grey-body. A flame soot particle can be considered as a grey-body, and its emissivity is very close to blackbody ( $\varepsilon=1$ ). Although this method may not detect exactly the amount of radiation emitting from grey-body exactly, it can reflect the trend of radiation variation in term of grey-level. In order to analyse the irradiance of flame soot at puffing state quantitatively, three groups of soot flame images presented previously were processed using a built-in function of MATLAB, which can be expressed as

$$I = \text{rgb2gray}(P), \quad (4.1)$$

where  $I$  is grey-level output of the imaging system ranging from 0(black) to 255 [60] for an 8-bit-deep image.  $P$  is an input colour image including three channels corresponding to R, G and B channel. The function of `rgb2gray` converts a colour image to a greyscale image. The high-speed camera uses a 12-bit COMS sensor; the soot flame captured by the camera can be either saved as 8-bit or 16-bit images. Although a 16-bit image gives a smoother gradient from 0(black) to 65535 [60], it doesn't help to reduce the current noise of camera dark and to avoid image saturation. On the contrary, saving as a 16-bit image could even magnify this dark noise. And imaging system will spend more time and occupy more memory space to save 16-bit images.

Figure 4-10, a, b and c) present the total flame illumination intensity (or grey-level) variation at puffing state. In each image total flame intensity is obtained by converting the colour images to greyscale ones. Only the grey-level intensity of pixels within the flame counts for the calculation of a total brightness intensity. Each point represents a total flame brightness intensity that is calculated from the corresponding image.

The Figures (a), (b) and (c) indicate that droplet puffing tends to increase flame illumination instantly. Increasing the water-content in diesel causes the puffing to become more violent. Figure 4-10 (d) presents the peak grey-level found at 10%, 20% and 30% D/W emulsions, exhibiting a near linear relationship between flame intensity and the amount of water content in diesel.

Additionally, in Figures (a), (b) and (c) it is interesting to note that each minimum reading of grey-level occurred before a sudden increase in flame intensity; the reason for this is still unknown to the author, a further investigation is necessary.

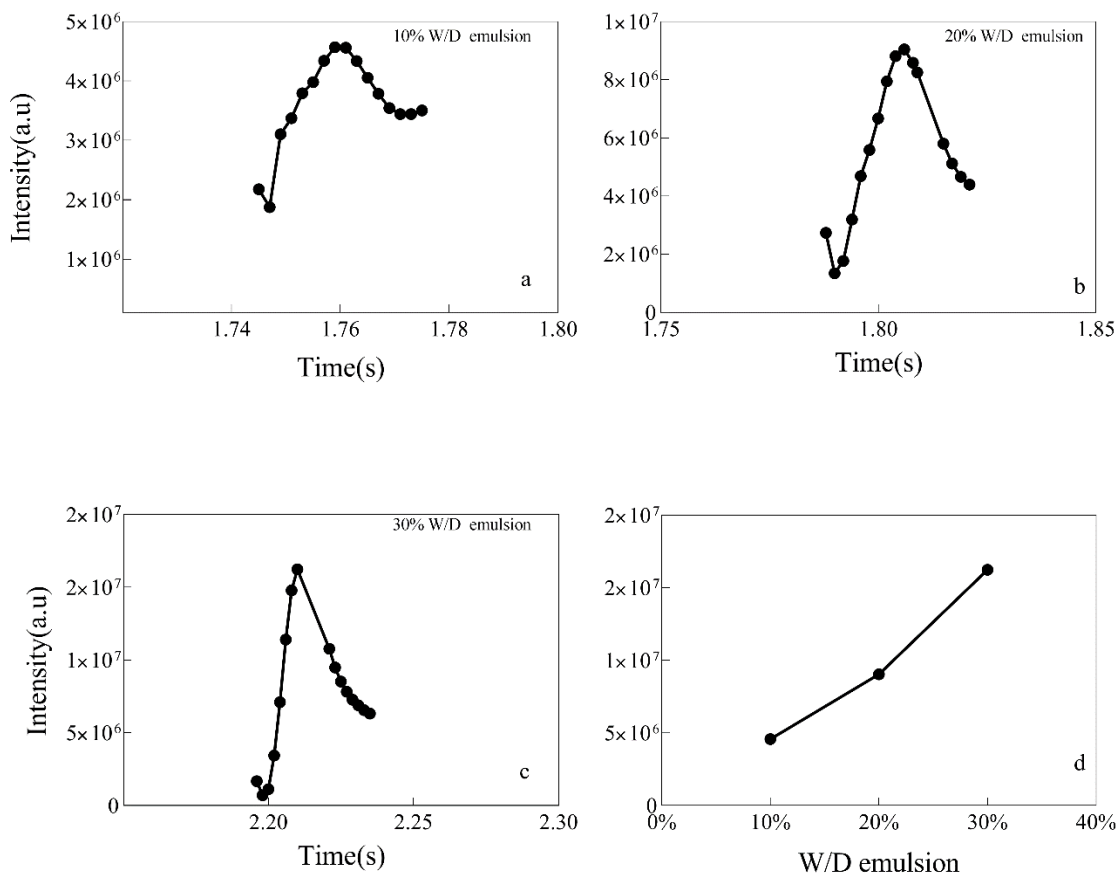


**Figure 4-10** Grey-level of flame illuminations at 10%, 20% and 30% fuel emulsions

#### 4.3.3.2. Observation of Flame illumination at Micro-Explosion State

Micro-explosion is part of the secondary atomization characteristic of the fuel emulsion combustion. This physical phenomenon was observed frequently when burning 30% D/W fuel emulsion in the

experiment; it normally occurs in the final stage of the droplet combustion, accompanied by flame extinction because of the shock wave generated thereby.

The process of forming a cloud of sub-droplets due to micro-explosion is shown in Figure 4-6 (f), (g) and (h). These images were captured at 40000 fps with the backlit imaging technique which uses a 2000w LED lamp as light source to make droplets visible to the imaging system. However, this configuration is not suitable for imaging the soot flame that is above the droplet because image saturation occurred in the flame field and the image dimension is only 320×240 pixels using that ultra-fast fps, which is thus only able to capture the droplet area. Consequently, simultaneously imaging the droplet and its flame is not possible with this configuration.

The captured time-series flame images shown in Figure 4-11 use the imaging system setting at 1000 fps and 1/39000s shutter-speed without the backlit technique. With this configuration the soot flame variation due to the micro-explosion can be recorded entirely. As shown at 2.181s in Figure 4-11, a cone-shape flame is present without disturbance by secondary atomization. Other images indicate the change in the flame shape and illumination prior to flame extinction, which is caused by the micro-explosion that can completely break up the droplet into a great number of sub-droplets. Although these sub-droplets could burn either individually in their own flame or in groups, the observed shock wave was able to either partially or completely extinguish them.

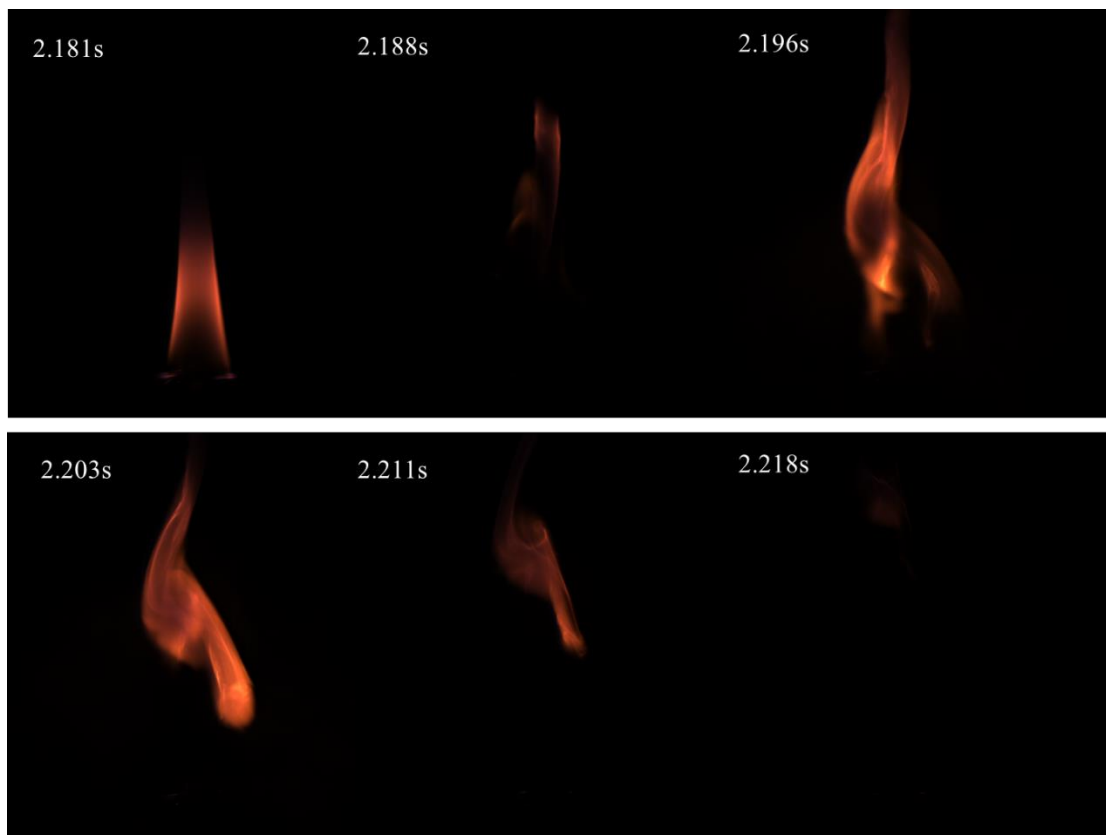


**Figure 4-11** Flame extinction due to the droplet micro-explosion at 30% D/W emulsion

Figure 4-12 gives the grey-level variation of the flame shown in Figure 4-11. The technique used to calculate the total flame illumination intensity is identical with the method applied in section 4.3.3.1. As shown in Figure 4-12, the flame intensity was  $2 \times 10^6$  at 2.18s without the secondary atomization disturbance; the fuel emulsion droplet can thus burn steadily as same as the combustion of diesel fuel. Subsequently, the flame intensity experiences a reduction before the intensity increases, and finally the intensity approaches 0. This trend was also found in puffing-induced the flame intensity variation, shown in Figure 4-10.

The sudden flame intensity increase is shown in Figure 4-12 in the period of time from 2.188s to 2.203s, which is mainly attributable to micro-explosion. This leads to that the droplet, suspended

on SiC fibres, disintegrating into fine sub-droplets; these sub-droplets can burn more efficiently because of their increased surface area [61].

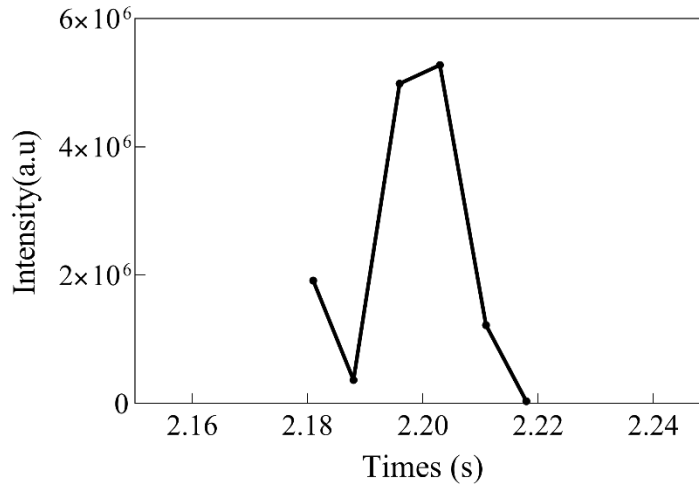


**Figure 4-12** Grey-level of flame illumination at micro-explosion

### 4.3.3.3. Flame Temperature Measurement Using Two-Colour Method

#### 4.3.3.3.1. Visualization of Flame Temperature during the Secondary Atomization

From Figure 4-7 to Figure 4-9, these three groups of images show the droplet flame when secondary atomization occurs during the combustion of fuel emulsions; in each group four images are selected at 4 image intervals, used for flame temperature determination. The whole process is performed using MATLAB with the special-written codes.

Firstly, prior to the calculation of soot flame temperature the saturated pixels in selected images need to be identified and subtracted. This can be achieved by checking the R, G and B channels of every pixel in each image. Once any of these channels reaches the maximum greyscale (255), this pixel will be subtracted without proceeding temperature calculation. And it is worth noting that few pixels found in the images only contain R signal without G signal, these cannot be used for temperature determination either.

Secondly, the flame boundary profile of flames that shown in the selected images has to be identified using a built-in function in MATLAB as follows

$$BW=im2bw (P, threshold), \quad (4.2)$$

this function converts the grayscale image  $M$  into a binary image. The output image  $BW$  replaces all pixels in the image  $P$  with illumination intensity greater than threshold, with 1 [60] and replaces all other pixels with 0 (black). The threshold ranging from 0 to 1 is set to 0.05 in this case. Figure 4-13 (a) shows a sample of droplet flame, which was processed using this function with different thresholds. Figure (d) shows that the flame area [60] is nearly identical with the sample flame. However, the flames shown in Figure (b) and (c) do not reproduce the sample flame profile completely; the details of the flame tip and four hot spots at base of the flame are all omitted in comparison with the sample flame. With reference to soot flame temperature calculation, the pixels only within the reproduced flame profile are used for temperature determination.

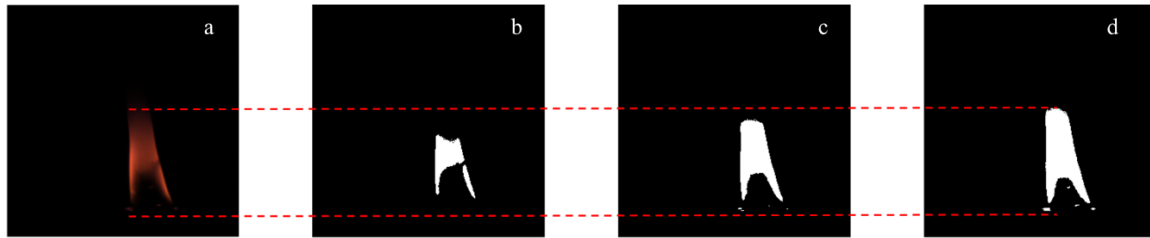
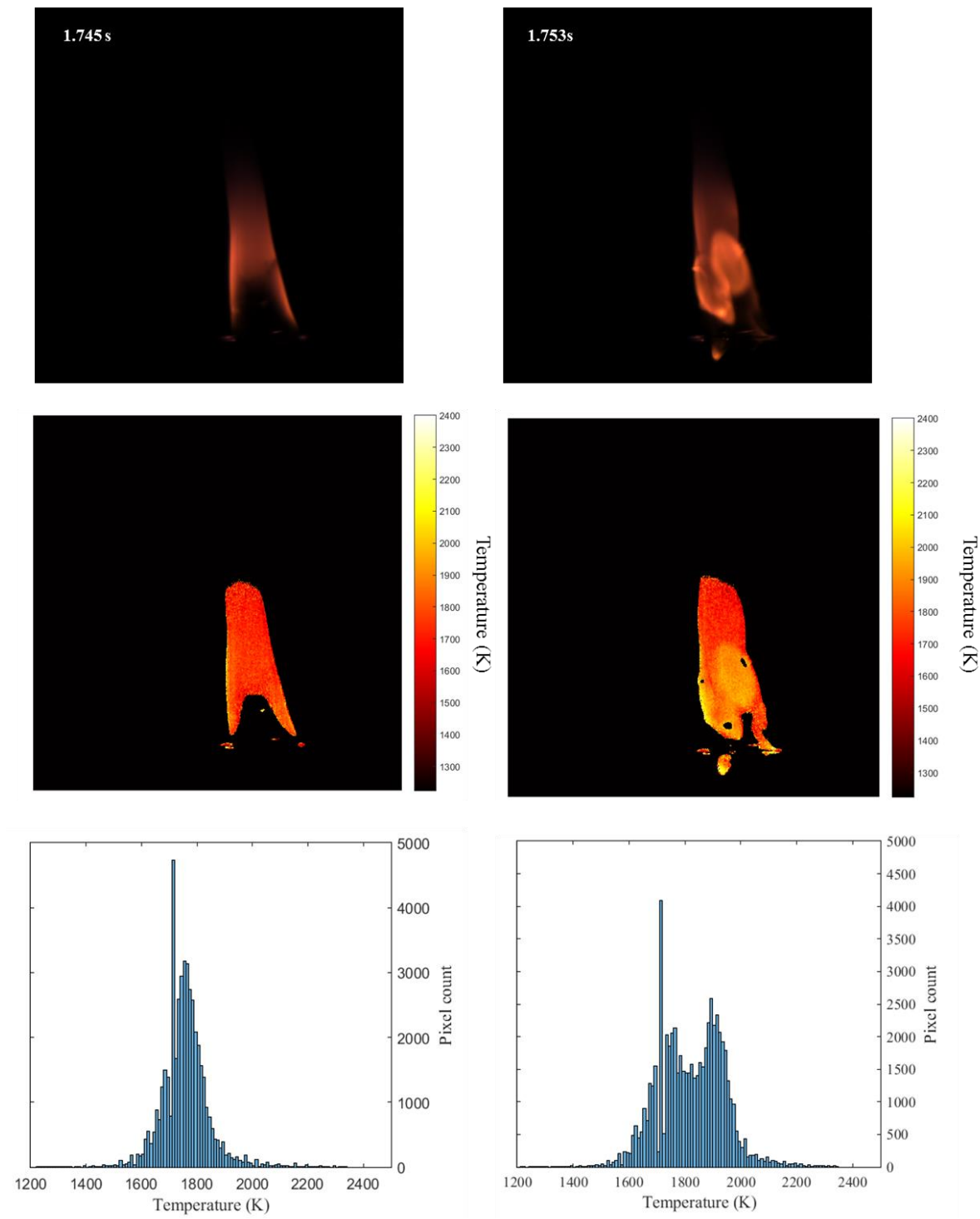


**Figure 4-13** (a) Sample of a droplet flame at 10% D/W emulsion (b) The reproduced flame profile at threshold=0.15 (c) The reproduced flame profile at threshold=0.1 (d) The reproduced flame profile at threshold=0.05

Finally, after the subtraction of the saturated pixels and the pixels outside the profile in each selected images, the remaining pixels are used to determine the droplet flame temperature by two-colour method.

The results of measured flame temperatures are presented in Figure 4-14, Figure 4-15 and Figure 4-16. The first row in these Figures give the original flame images selected from the aforementioned three groups. The images in the second row are the visualisation of the flame temperature using the colour-map, and the last row gives histograms of the flame temperature distribution.

The data presented in Figure 4-14 is the measured flame temperature when combusting a 10% D/W droplet. By observing the temperature colour-map the highest temperature is found to be situated mainly along the flame outer edge. When sub-droplets occurred due to the puffing, higher soot flame temperature was found in the region of the hot spots; this was also found at 20% and 30% emulsions. The overall flame temperature thus exhibits an increasing trend during droplet puffing. Some small black holes found in the colour-map indicate saturated pixels in these areas, meaning to that the temperature measurement cannot be perform using these pixels. Stronger puffing exacerbated the problem of the image saturation at 20 % and 30% D/W emulsions; the number of black holes thus increased.



The figure will continue on next page

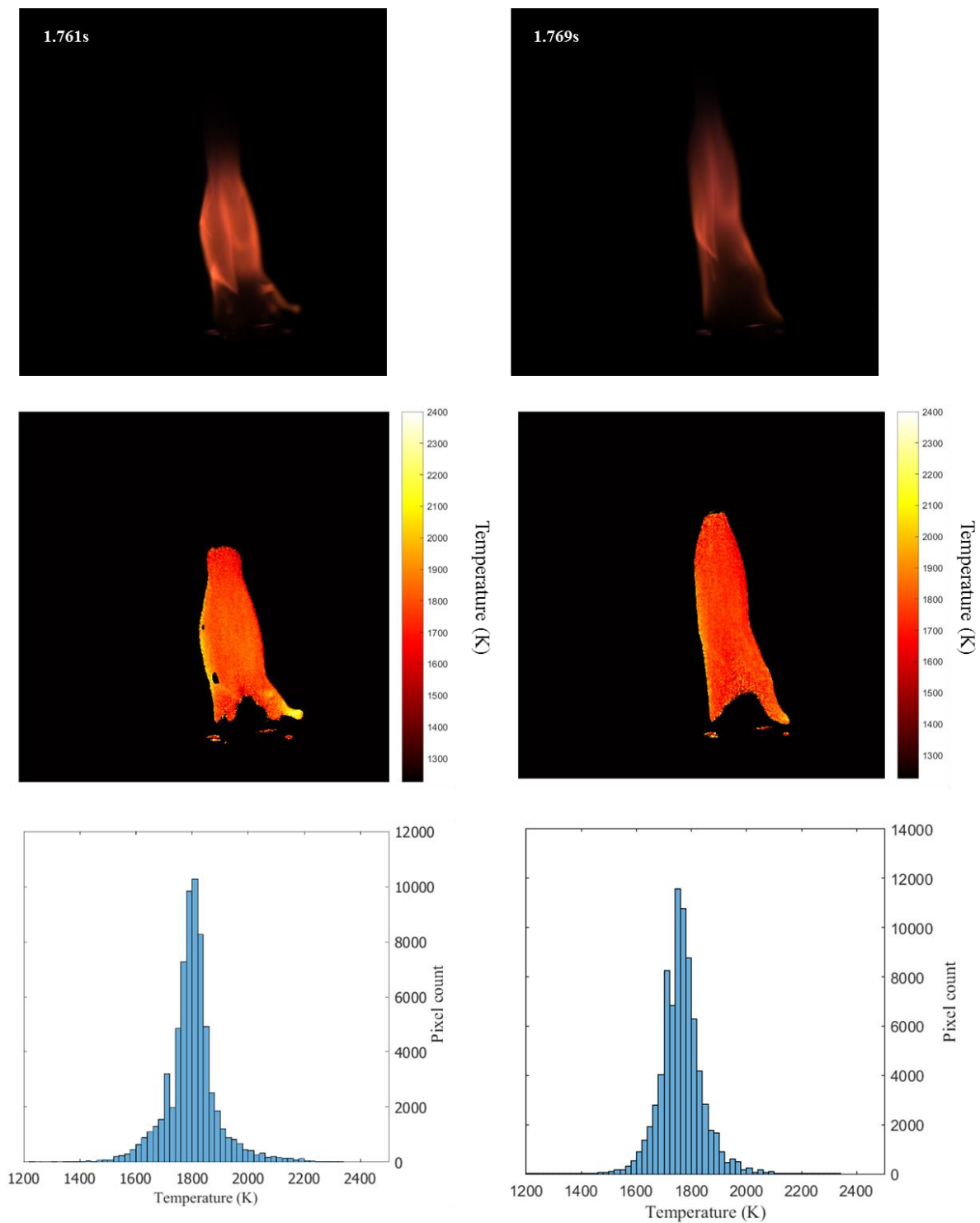
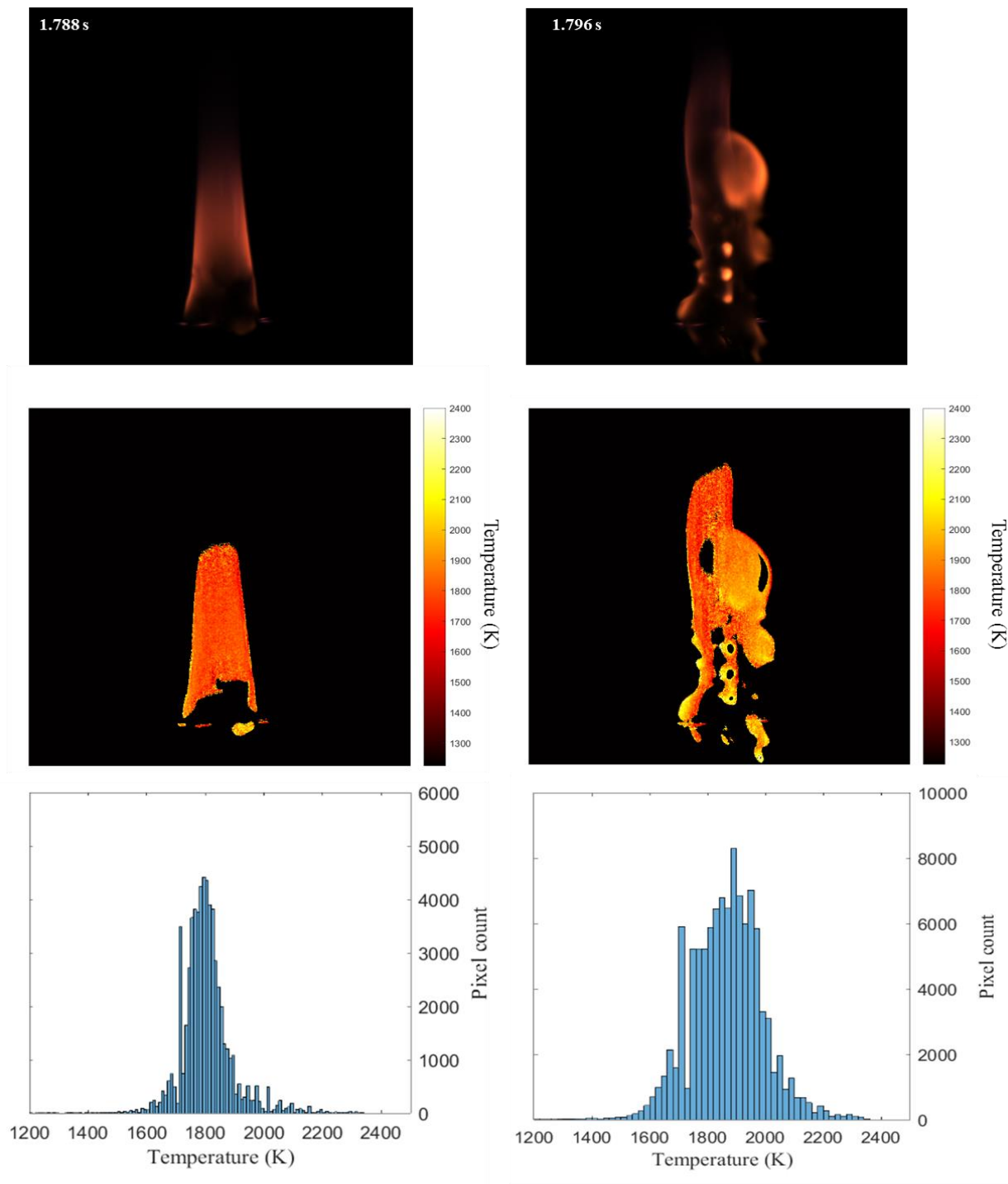


**Figure 4-14** Visualization of flame temperature using the colour-map, and histograms of temperature distribution at 10 % D/W fuel emulsion [Note:1mm=10 pixels]



The figure will continue on next page

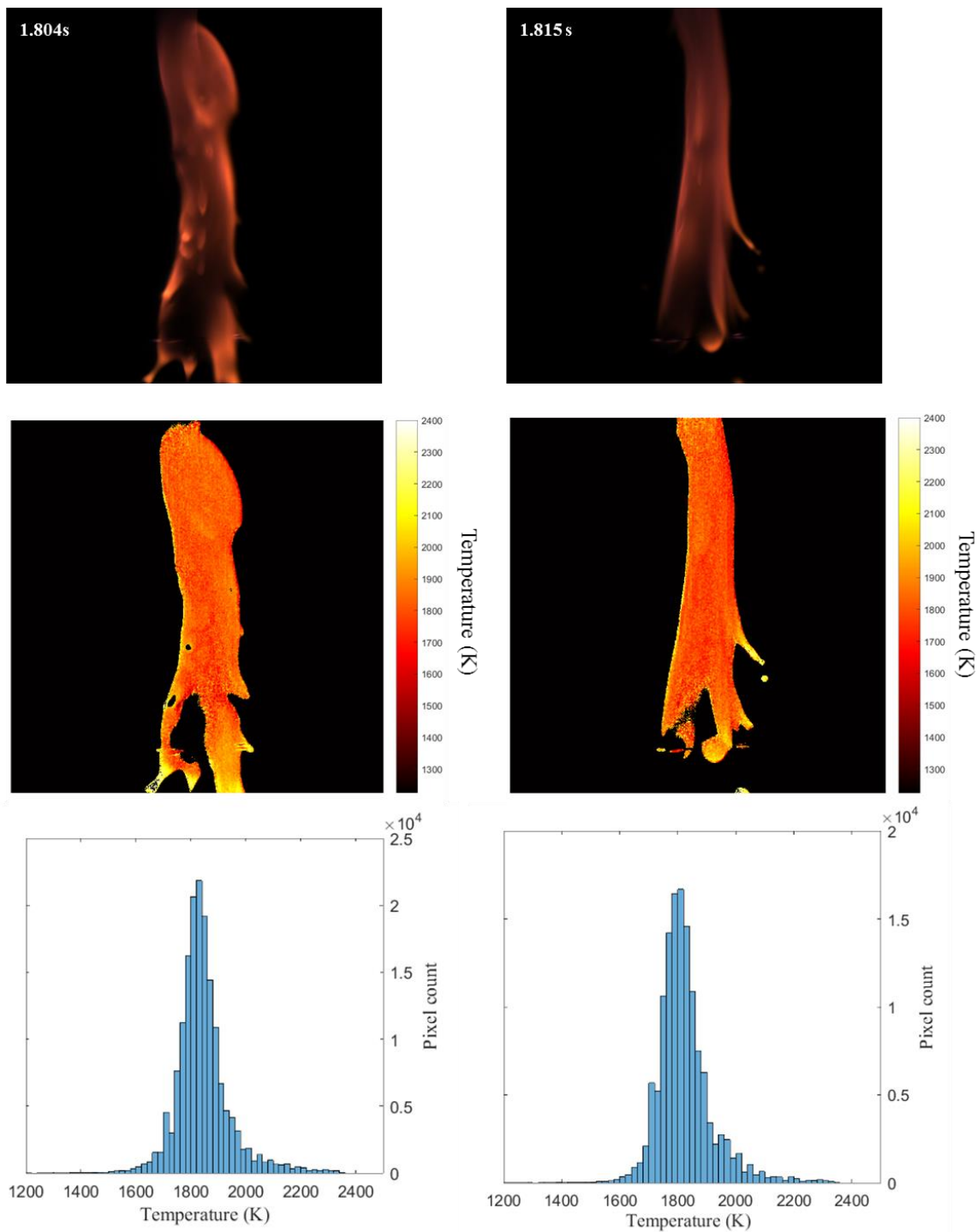
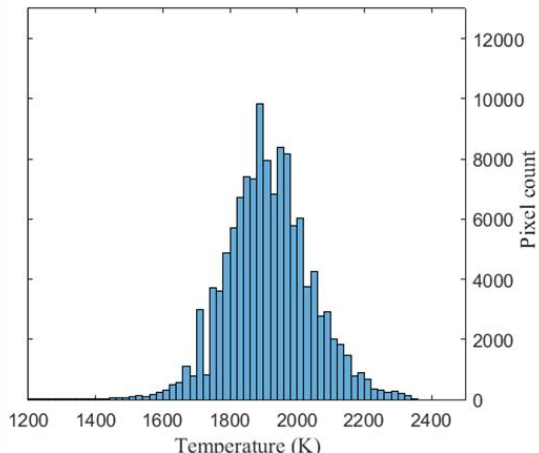
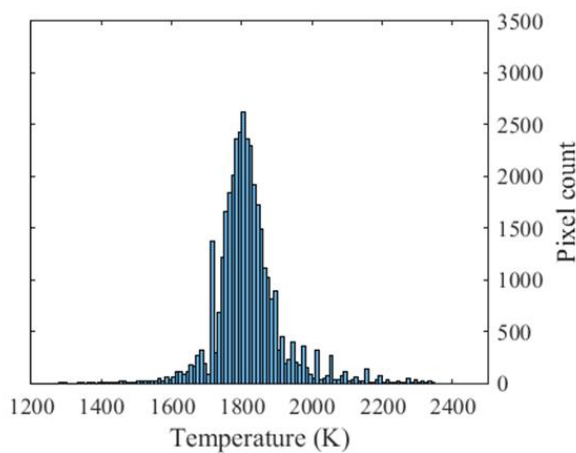
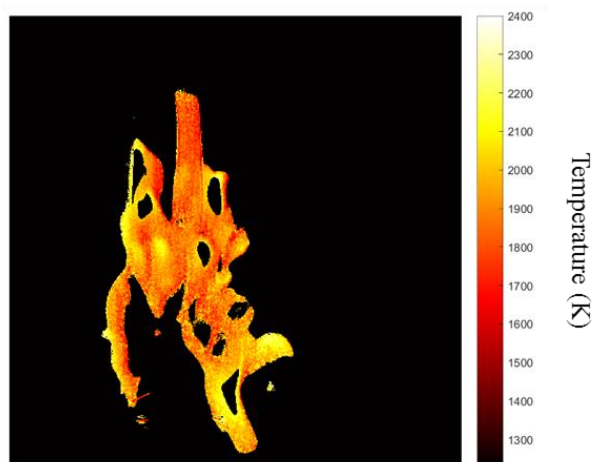
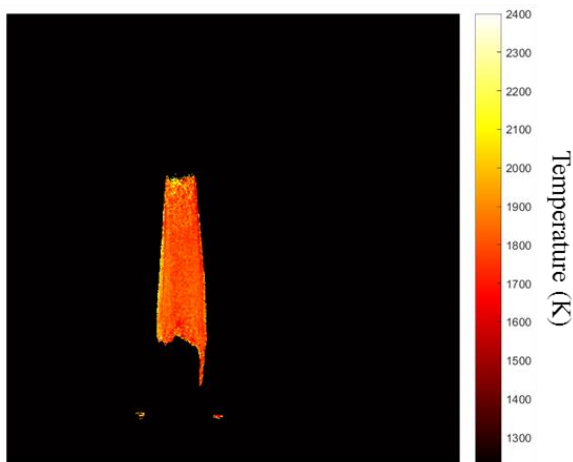
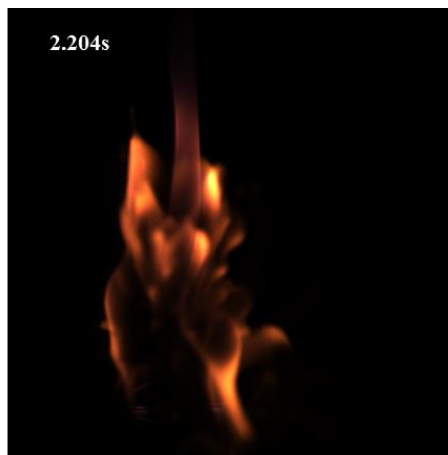
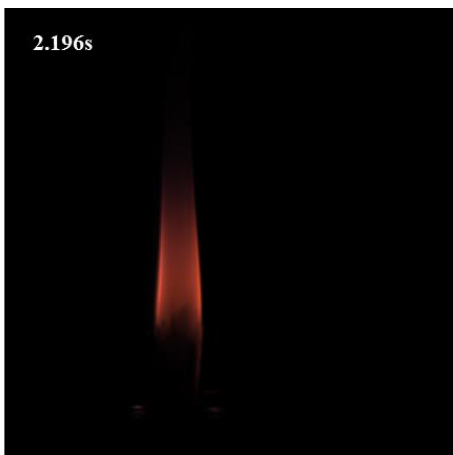


**Figure 4-15** Visualization of flame temperature by the colour-map, and histograms of temperature distribution at 20% D/W fuel emulsion [Note: 1mm=10 pixels]



The figure will continue on next page

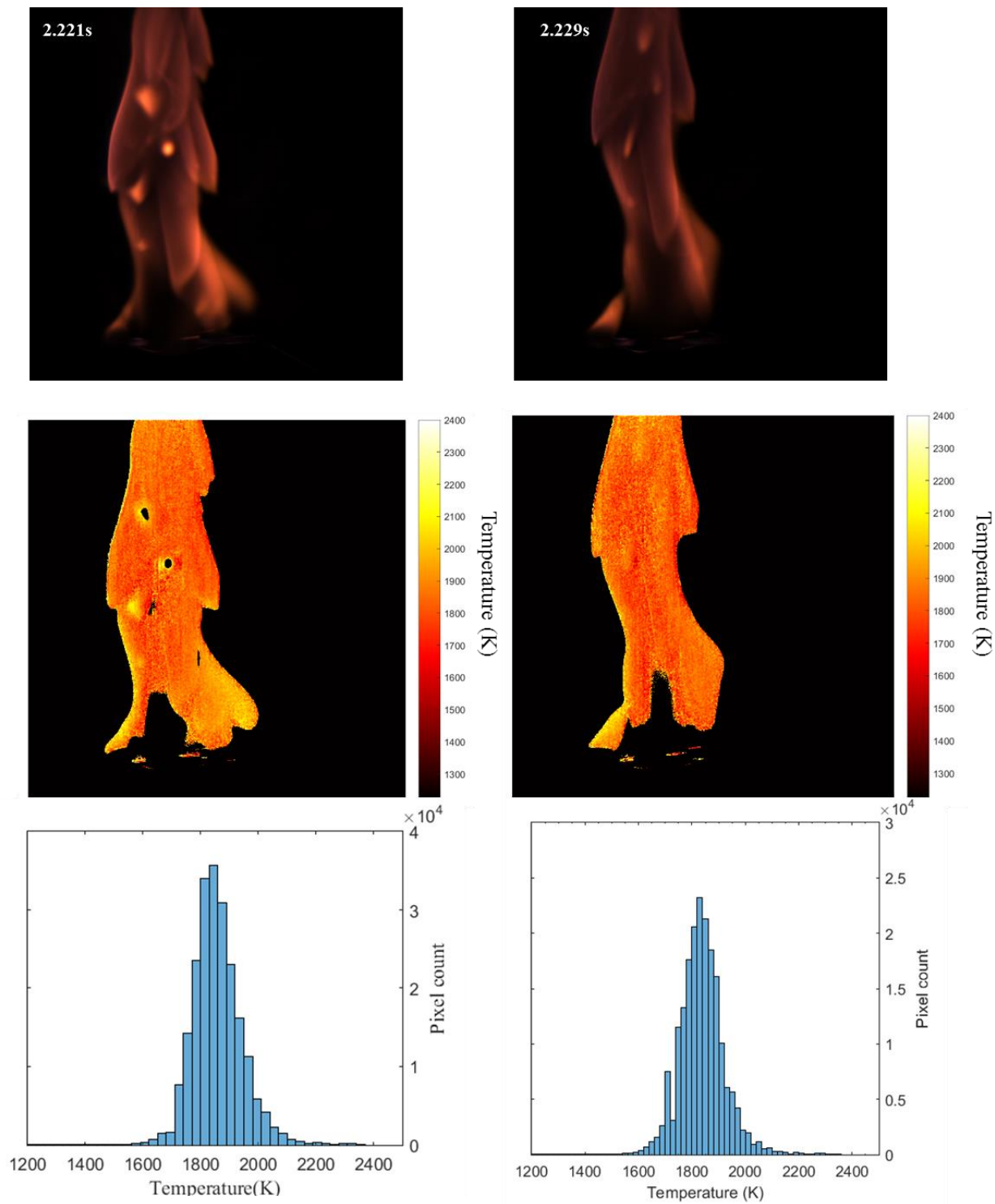


**Figure 4-16** Visualization of flame temperature by the colour-map, and histograms of temperature distribution at 30 % D/W fuel emulsion [Note:1mm=10 pixels]

#### 4.3.3.3.2. Time-Varied Average Flame Temperature Variation

With reference to the impact of the water content in the droplet combustion, the average soot flame temperature variation in the droplet lifetime has been calculated using the two-colour method. Each type of fuel emulsions has been tested three times to show a consistency. The data presented in from Figure 4-17 to Figure 4-20 show the time history plots of the flame temperature variations at pure diesel, 10%, 20% and 30% fuel emulsion respectively.

Figure 4-17 gives a complete profile of soot flame temperature variation in diesel fuel. At the early stage of droplet combustion, it was found that flame temperature fluctuated strongly between the peak temperature (around 2300K) and the lowest one (around 1700K). This flame temperature instability initiated at the flame ignition event ( $t/t_{\text{total}}=0$ ) and terminated at  $t/t_{\text{total}}=0.1$ ; this period corresponds to one-tenth of the droplet lifetime and is much shorter than that found in fuel emulsions. Moreover, the period of this instability shows a strong correlation to the amount of water added into diesel. As a result, at 30% fuel emulsion the duration of flame instability extended to the half of the droplet lifetime, shown in Figure 4-20.

Subsequently the observed soot flame temperature oscillation decreases sharply, and then tend to a relatively stable state. As shown in Figure 4-17, the flame temperature fluctuates weakly around 1800K. As more water is added into diesel, the flame temperature decreases gradually in the steady state; it can be seen in Figures 4-18 and 4-19 that the temperatures were brought down to around 1600K and 1700K respectively. However, at 30% fuel emulsion the flame temperature at the steady stage was almost identical to the soot flame temperature in pure diesel.

Additionally, apart from the case of 30% fuel emulsion, other types of emulsion, and pure diesel, show that soot flame temperatures all increased gradually, and then experienced a drop in the final stage of droplets combustion. This difference between 30% emulsion and other fuels is caused by micro-explosion because it is powerful enough to extinguish the flame rapidly.

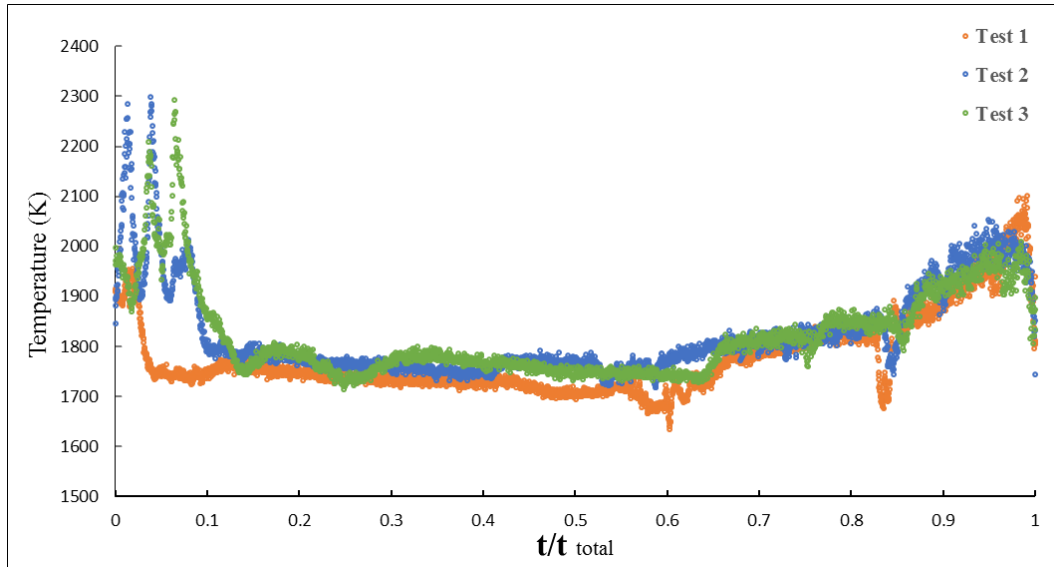


**Figure 4-17** Time-dependent average flame temperature variation in the droplet lifetime in pure diesel fuel

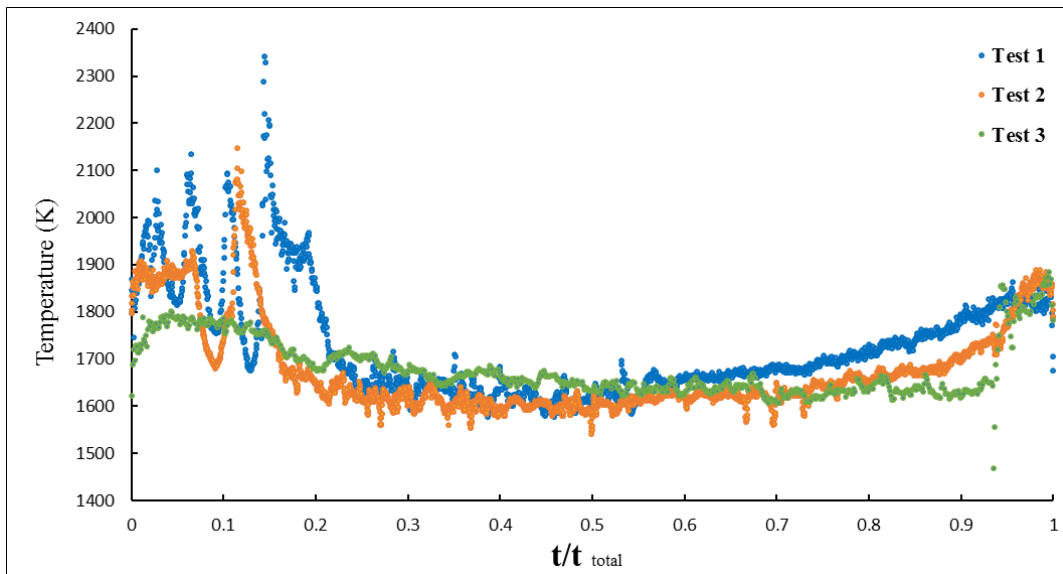


**Figure 4-18** Time-dependent average flame temperature in the droplet lifetime at 10% D/W fuel emulsion

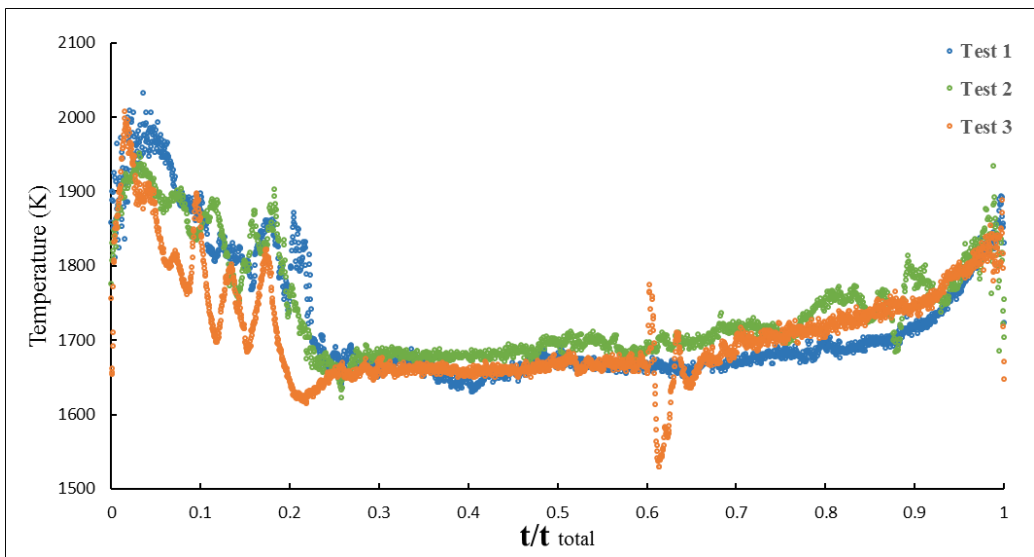


**Figure 4-19** Time-dependent average flame temperature variation in the droplet lifetime at 20% D/W fuel emulsion

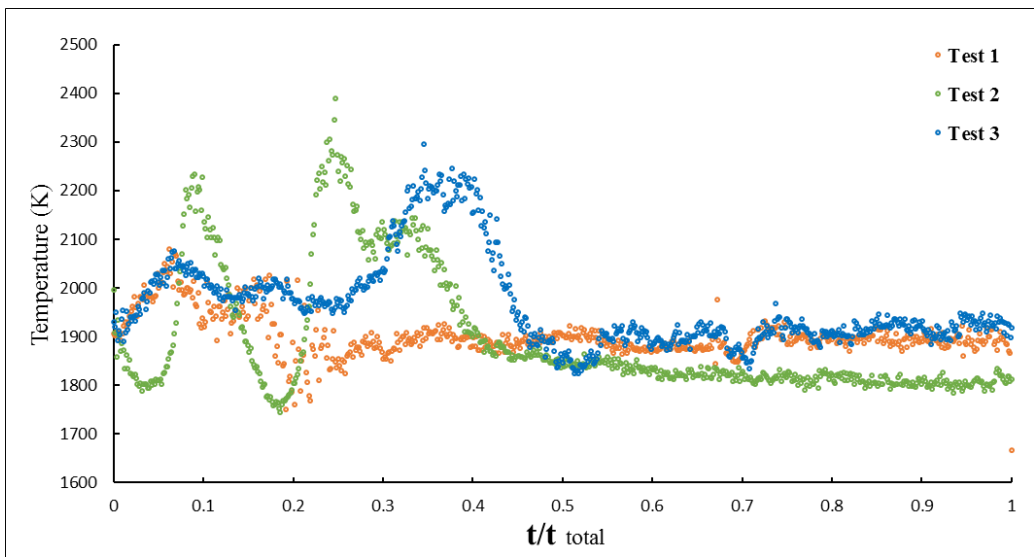


**Figure 4-20** Time-dependent average flame temperature variation in the droplet lifetime at 30% D/W fuel emulsion

#### 4.3.3.3.3. Tracking Local Flame Temperature Variation

Figure 4-21 shows the average estimated soot flame temperature at 0.5, 1, and 1.5 mm above the centre of SiC fibre cross with respect to water-content in the droplet. The fibre has been selected as a reference because it can be traced easily by its light emission, contrary to the droplet whose position is barely observable in a self-illumination image. And an area of 4×4 pixels was cropped at the corresponding position for local flame temperature tracking using the two-colour method. Temperature estimation at 0.5 mm for the 30% D/W droplet combustion was difficult because there is no soot at this position. Figure 4-21 shows that the average soot flame temperature is decreased by increasing water content. Moreover, it can be seen that the greatest difference in soot flame temperature between diesel droplet combustion and its corresponding D/W droplet combustion occurs at 0.5 mm. This can be attributable to increasing the evaporation zone with increasing water content; therefore, the 0.5 mm point lies near –and sometimes within- this zone, resulting in the average temperature at this point being lower than that of the others. Moving further away from the fibre – points 1 and 1.5 mm - show a lower effect of water content on the average temperature, particularly at 1.5 mm, where the temperature is almost the same for the four fuels.

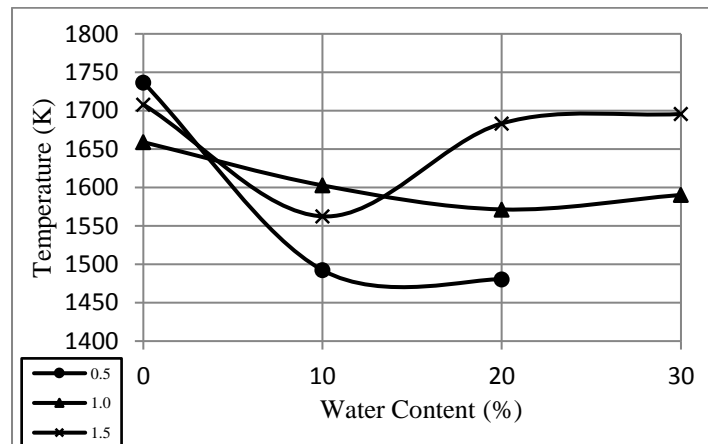


**Figure 4-21** Average soot flame temperature at the three heights from SiC fibre

#### 4.4. SUMMARY

This chapter in terms of the view of soot flame temperature evaluates the effect of water-content in diesel. The characteristics of the fuel emulsion combustion, the secondary atomization, has been successfully observed using the high-speed imaging system.

At droplet puffing state it was found that fine sub-droplets would be continually expelled from the droplet, resulting in soot flame temperature increasing dramatically; with the increase of water-content in diesel fuel, the puffing becomes more violent and leads to the formation of a greater number of sub-droplets. In addition, by using ultra-high fps the process of droplet micro-explosion was imaged; this shows that the droplet disintegrated into a cloud of fine sub-droplets instantly, along with a distinctive popping sound. Meanwhile the droplet flame extinction was also observed. Additionally, it is also noticed that increasing the water-content in diesel fuel could cause the instability of combustion, which reflects on a longer period of flame temperature fluctuation.

Finally, owing to limited research funding, the measured flame temperature using the two-colour technique cannot be validated by other optical pyrometers in this study. However Taifan Fu [62] reported that a maximum temperature around 2300K in pure diesel fuel combustion using multicolour pyrometer. Raul [59] found an average flame temperature of 2200K in spray combustion of water-containing fuel but the amount of water-content is not mentioned by the author. Compared to these findings, the measured flame temperature of the droplet combustion here falls in a reasonable range.

## 5. NUMERICAL ANALYSIS OF SiC FIBRE THERMAL BEHAVIOUR NEAR FLAME OUTER BOUNDARY LAYER

### 5.1. INTRODUCTION

Applying two-colour method to measure the temperature of a soot flame is not a difficult task; the determination of flame temperature can be inferred using the radiation from soot particles which assumed to be a stable emitter and homogeneously distributed along the flame. The temperature difference between the soot particles and the flame is negligible owing to the infinitesimal size of a soot particle.

However, in terms of premixed flame temperature measurement, it becomes a challenge for the application of two-colour technique due to relatively low soot concentration resulting in insufficient soot emission for the calculation of the flame local temperature and to characterize the global temperature distribution of premixed flames.

In order to overcome that difficulty, SiC fibre is introduced to aid the measurement of the premixed flame temperature; the fibre plays the role of a radiation emitter, similar to the function of soot particles. This material has good strength at flame temperature with a high melting temperature enabling the fibre to survive in most flame, and good resistance to catalytic effect and oxidation. Also, since the diameter of the fibre is as small as  $15\mu\text{m}$ ,  $Re$  number of the flow crossing over the fibre is very small; thus it is unlikely disturb the flow of its surrounding hot gas and the chemical reactions of unburned fuel. These properties of the fibre show the potential to be applied in premixed flame temperature. Care has to be taken with the temperature difference between the fibre

and its surrounding gas; this difference is not negligible and is obtained by radiation correction after the fibre temperature gas has been inferred by the two-colour method, unlike soot particle temperature which can approximate to flame temperature without any correction.

The uncertainty remains in using the fibre to detect the flame temperature near the flame outer boundary layer (flame front), the region in which hot flame gas and ambient cold air can meet, and exchange the heat from the hot gas to the cold air. This forms a large temperature gradient in that region, indicated by a black circle in Figure 5-1. This large temperature gradient can enlarge the temperature difference between the flame and the fibre beyond that inside the flame, and as a result, measured flame temperatures near the boundary layer may be far away from their true values.

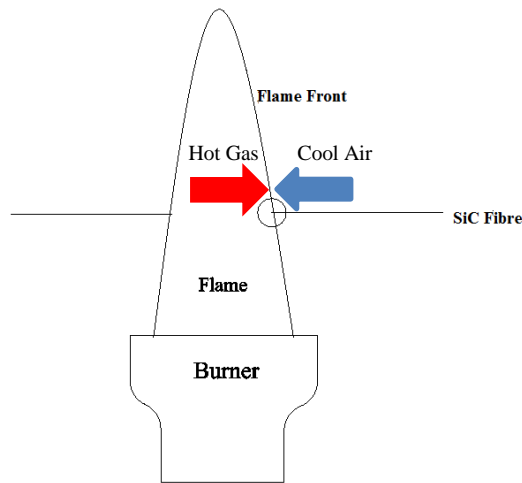


**Figure 5-1** Flame temperature measurement using SiC fibre

Previous work has focused only on the estimation of the time taken for fibre to achieving heat balance inside the flame where the temperature gradient is relatively small, and most research [63] [33, 64, 65] aims to demonstrate that the fibre temperature can rapidly respond to the variation of its surrounding gas temperature. With reference to the thermal behaviour of SiC fibre near the outer boundary layer of the flame, it seems not to have received much attention. How the fibre thermal response performs and how to treat the temperature difference are still unanswered.

Hence, the study here aims to evaluate the fibre temperature distribution varying with its surrounding temperature. This investigation is based on computer simulation; a one-dimensional heat transfer model has been established to govern the real heat transfer process of the fibre in the field of interest shown in Figure 5-1 and marked by a solid circle. In the simulation the flame outer boundary layer is assumed to be a constant heat source denoted by  $T_s$ , and the heat energy stored in the fibre is dissipated by convection and radiation from the fibre. This model can be used to simulate the fibre temperature varying with the change in the variables associated with fibre dimension, ambient heat transfer coefficient, and ambient temperature; with that it could give insight into the fibre thermal behaviour.

This chapter begins with the introduction to the uncertainty realized during flame temperature measurement, followed by the reasons for using the numerical method to solve the proposed study. Subsequently the detailed methodology is described. Then the results are discussed and extrapolated to address the effect of the variables on the flame temperature measurement, finally, an overall conclusion is presented

## **5.2. COMPARISON BETWEEN EXPERIMENTAL AND NUMERICAL METHOD**

Prediction of the fibre heat transfer at the interface between the hot flame gas and its nearby relatively cold air can be obtained by two methods: experimental investigation or numerical method. The investigation of a physical process using experimental method is based on actual measurement; it involves performing experiments either on full- or small- scale models. Full-scale tests are not feasible to conduct in university labs because of budget, limited space, and health and safety reasons. An alternative way is to conduct tests on small-scale models, with the results obtained from these models extrapolated to full scale ones. In this, there are no general rules to follow, and sometimes

the approach is not appropriate. Finally, one must bear in mind that some difficulties of measurement may not be eliminated during experiments, and the measuring equipment may not be free from errors [66].

Turning to numerical methods, they are a theoretical prediction based on processing a mathematical model rather than carrying out measurement on an actual physical model. For the prediction of a physical process such as heat transfer, fluid mechanics or static-force analysis, the mathematical model normally is based on a number of differential equations and its corresponding boundary conditions; these Equations contribute to form the mathematical system that describes physical phenomena of practical interest. In the past, engineers used analytical skills to solve important engineering problems; this meant undergoing a rigorous training in mathematics [1], leading to a lower possibility of predicting complicated physical problems.

Fortunately, the ready availability now of high-speed-computers and the development of the numerical method have had a positive impact on the solution of engineering problems and the mechanical designs in the automotive industry. For example, the JAGUAR Motor company has devised a digital full-size vehicle model using numerical method; in this way it is possible to evaluate the performance and the reliability of each component used in vehicles.

The advantages of numerical methods can be categorized into four aspects: low cost, speed, complete information and the ability to simulate either realistic or ideal conditions.

Low cost is the most significant advantage of numerical methods. Especially when applying numerical methods in solving a more complicated physical process, its cost will be much lower than the cost of using the experimental method.

In addition, a computational investigation can be performed with remarkable speed; a researcher can thus study the implications of numbers of different configurations in a half day, and then find the best design, an obvious advance on experimental approaches. Moreover, the numerical method

is able to give a detailed and complete solution of a physical problem; this solution includes the values of all the relevant variables, such as temperature, velocity, pressure and force, throughout the domain of interest. Unlike the situation in an experimental study which is not able to predict the distributions of all variables over the entire domain, there are few inaccessible locations in the numerical solution. Because of this, it is worth obtaining to obtain a numerical solution to supplement the experimental study, even when an experiment is performed.

Finally, realistic and ideal conditions can easily be simulated using numerical methods; whatever the difficulty, such as in treating very low or very high temperature, having very large or very small dimensions, in following a very fast or very slow processes, or in focusing attention on a single parameter of basic physical phenomenon study at the condition of all irrelevant variables eliminated.

According to these reasons mentioned above, a numerical method is used to the study of SiC fibre thermal behaviour. The principle of the numerical method used here is briefly clarified in the following.

There are several methods to form the numerical equations for the heat transfer analysis, such as the finite volume, the finite difference and the finite element method. The main principle of their is based on replacing differential equations by a set of algebraic equations for acquired variables such as the variation and the distribution of fibre temperatures; there are of interest at a number of pre-set nodal points in the medium; the simultaneous solution of these equations gives the values of acquired variables at those discrete nodes [1]. This process is called discretization; it avoids having to solve the complicated governing differential equations together with corresponding boundary conditions as with using analytical methods.

### **5.3. THE PROCEDURE OF NUMERICAL SIMULATION**

In previous sections, the advantages and the basic principle of numerical methods have been described and interpreted. This section introduces the methodology used in the study of SiC

thermal behaviour, and the sequence of explaining this methodology follows the procedure presented in Figure 5-2.

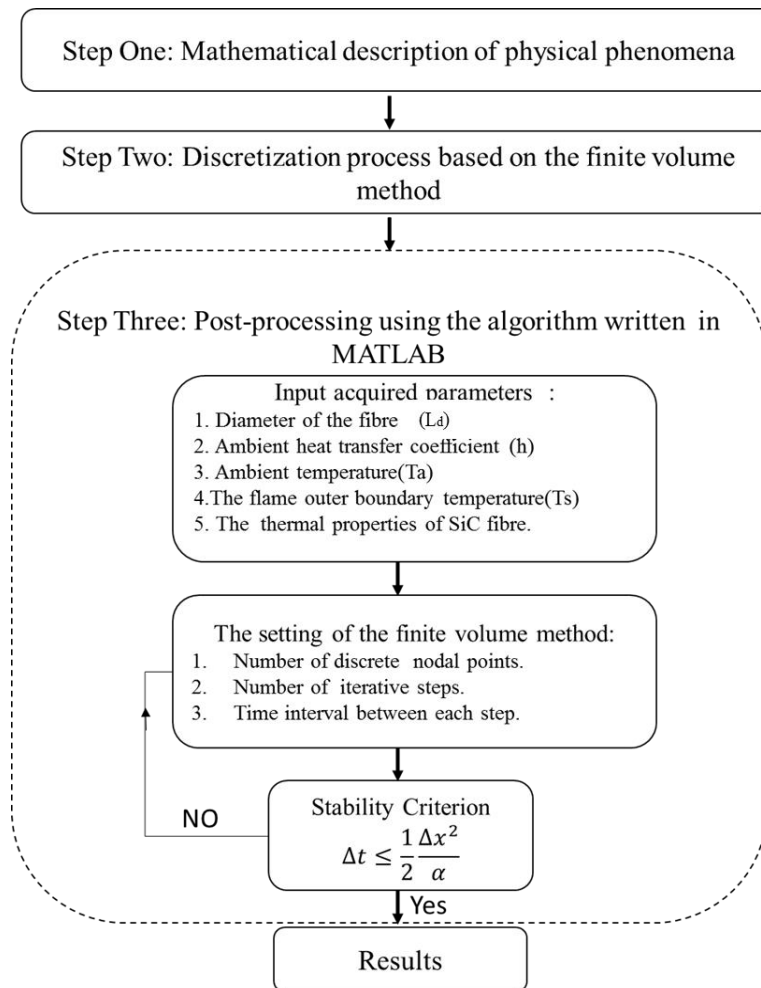


**Figure 5-2** Flowchart of implementing control-volume base finite difference method

➤ **Step One: Governing equations of the heat transfer process in the region**

A transient heat transfer problem can be described by mathematical terms, using the conservation equations such as heat, mass, momentum, and energy balance. In addition, assumptions were made to simplify the mathematical equations and to define appropriate boundary conditions to the conservation equations. As can be seen in Figure 5-3, the model was heated at the left end, the heat was spread from left to right by conduction and dissipated from the fibre surface by radiation and convection.

It is desired to obtain the temperature profile of SiC fibre. Intuitively, the fibre temperature should decrease at a distance away from the heat source. The effect of physical properties of SiC fibre and the variation of the fibre ambient gas conditions are also of interest in this study.

The acquired heat transfer model is a one-dimensional mathematical model because the ratio of the fibre circumference to cross-sectional surface area is large; it results in Biot number much smaller than 0.1, it meant that temperature distribution inside the fibre can be ignored. A thermal energy balance on a segment  $\Delta X$  shown in Figure 5-3 is expressed as

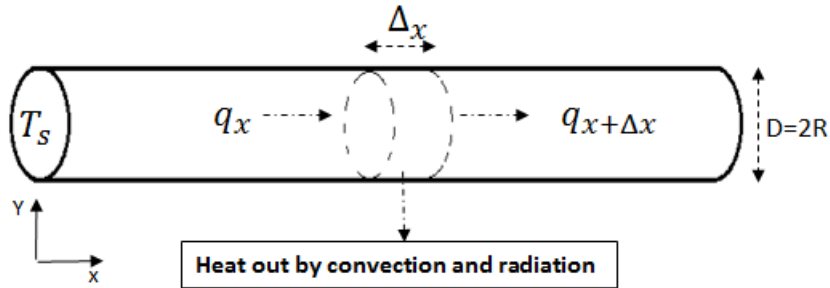


**Figure 5-3** Heat conduction through the fibre along with heat dissipated by convection and radiation

$$\rho * C_p * A_c * \frac{\partial T_f}{\partial t} * dx = k * A_c * \frac{\partial^2 T_f}{\partial x^2} * dx - h * dA_s * (T_f - T_a) - \epsilon * \sigma * (T_f^4 - T_{surr}^4) * dA_s , \quad (5.1)$$

where at the left side equation is the internal energy change. At the right side, the first item presents heat flow into the fibre by conduction, the others are heat loss by convection and radiation,

respectively.  $A_c = \pi r^2$  is the cross-sectional area of the fibre and  $dA_s = 2\pi r dx$  is the surface area of the segment indicated in Figure 5-3. The  $h$  and  $C_p$  are heat transfer coefficient and specific heat of the fibre respectively.  $T_a$  and  $T_f$  are the ambient and the fibre temperatures.  $T_{surr}$  is the surrounding surface temperature. The fibre emissivity and Stefan-Boltzmann constant are denoted by  $\varepsilon$  and  $\sigma$  respectively.

The initial and boundary conditions applied in the established heat transfer model are expressed as follows

**Initial Conditions:**

$$t=0; T_f = 300K,$$

where initial conditions assume the fibre temperature equals room temperature at  $t=0$ .

**Boundary Conditions**

$$T_f = T_s \text{ at } x=0; dT/dx=0 \text{ at } x=3\text{mm},$$

the end of the fibre surrounded by the flame was set as the prescribed temperature  $T_s$  around 1600K which is equivalent to the flame temperature at the region concerned; since the fibre has low thermal conductivity and small size in diameter(15 $\mu$ m), another end of the fibre was assumed to be insulated for simplifying the process of the built heat transfer model; the amount of heat loss from this end was negligible. The length of the fibre was set to 3mm.

➤ **Step Two: Convert the governing equation into algebraic equations**

The step converts the governing differential equation 5.1 to algebraic equations; these algebraic equations can be solved using control volume based explicit finite difference method. Compared with differential equations, algebraic equations are only valid at discrete points rather than differential Equation can be valid at every point of a medium; it is graphically depicted in Figure 5-4. By contrast, the advantage of using differential equation is able to have an exact solution of acquired variables. However, this method results in a complicated mathematical calculation.

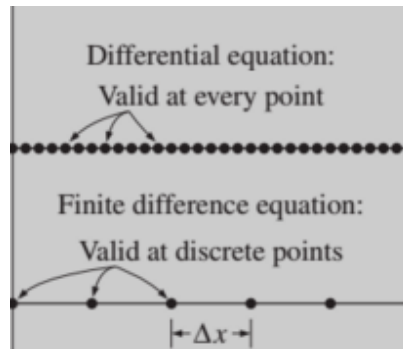


**Figure 5-4** The main difference between differential equation and algebraic equation [1]

As can be seen in Figure 5-4, the control volume-based finite difference method used here involves the work of sub-dividing the entire domain of the heat transfer model into a sufficient number of volume elements and then applying the energy balance at generated elements. This process is done by firstly discretizing the one-dimensional model into  $i$  nodal points at which temperature is to be determined. Then the formation of the control volumes over the nodes can be done by sketching the dotted lines through the midpoints between the nodes. The average properties, such as temperature, of the control volumes are represented by the node in each control volume.

Again unlike Equation 5.1 which governs the heat transfer process through the entire domain of the heat transfer model, the algebraic equations only govern the heat transfer process at the

corresponding discrete points shown in Figure 5-4. The heat transfers energy balance which occurs on discrete nodes shown in Figure 5-5 has to be treated separately.

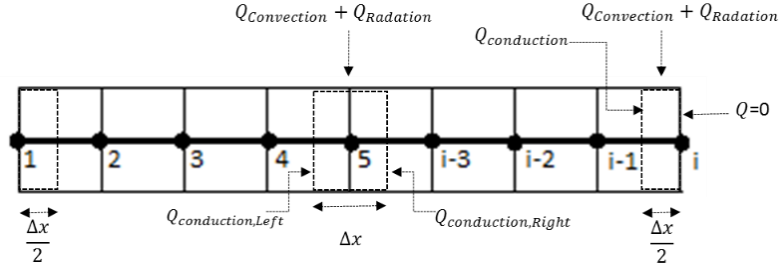


**Figure 5-5** The nodes and volume elements for the finite difference method

For node 1,

$$T_1 = T_s;$$

Where  $T_1$  represents the temperature at the point where the heat comes from the flame at outer boundary layer.

For node 2 to  $i-1$ ,

$$k\pi R^2 \frac{T_{i-1} - T_i}{\Delta x} + k\pi r^2 \frac{T_{i+1} - T_i}{\Delta x} + 2h\pi r \Delta x (T_a - T_i) + 2\varepsilon\sigma\pi R \Delta x (T_{sur}^4 - T_i^4) = \rho\pi r^2 \Delta x \frac{T_i^{j+1} - T_i^j}{\Delta t} \quad (5.2)$$

Where  $k$  and  $r$  are the thermal conductivity and the radius of SiC fibre.  $\Delta x$  is the length of each element. Node number and time step are denoted by  $i$  and  $j$ , respectively.  $\sigma$  is Stefan-Boltzmann constant, and  $\varepsilon$  is the emissivity of the fibre.  $T_{sur}$  is the temperature of surrounding surface.

By arranging the Equation 5.2, a more manageable form can be obtained as

$$T_i^{j+1} = (1 - 2\tau - \tau A)T_i^j + \tau T_{i-1}^j - B\tau(T_i^j)^4 + \tau T_{i+1}^j + \tau C. \quad (5.3)$$

Where A B C and  $\tau$  represent the constant coefficient in the equation above, and they are given as

$$A = \frac{2h\Delta x^2}{kr} \quad B = \frac{2\varepsilon\sigma\Delta x^2}{kr} \quad C = AT_a + BT_{sur}^4 \quad \text{and} \quad \tau = \frac{\alpha\Delta t}{\Delta x^2},$$

Where  $\alpha$  represents the thermal diffusivity of the fibre.  $\Delta t$  is the time interval between each step.

For node i,

$$k\pi R^2 \frac{T_{i-1} - T_i}{\Delta x} + 2h\pi R\Delta x(T_a - T_i) + 2\varepsilon\sigma\pi R\Delta x(T_{sur}^4 - T_i^4) = \rho\pi R^2 \Delta x \frac{T_i^{j+1} - T_i^j}{\Delta t}. \quad (5.4)$$

This equation also can be simplified as follows

$$T_i^{j+1} = (1 - 2\tau - \tau A)T_i^j + 2\tau T_{i-1}^j - B\tau(T_i^j)^4 + \tau C. \quad (5.5)$$

Finally, the combination of the difference Equations 5.3 and 5.4, with the boundary condition of node 1, can govern the heat transfer process which occurs on all the nodes shown in Figure 5-5.

➤ **Step Three: Post-processing with the stability check**

The algorithm for processing the established heat transfer model is based on the algebraic equations presented in the step two. Prior to initializing the heat analysis of the fibre using the algorithm executed in MATLAB, the acquired parameters have to be given as follows.

The manufacturer-declared material properties of SiC fibre can be found in Table 5-1. These parameters are assumed to be constant and do not vary with temperature.

**Table 5-1** SiC fibre thermal properties

Material	Nicalon SiC CF tow
Density	2550 kg/m <sup>3</sup>
Thermal Conductivity	12 Wm <sup>-1</sup> K <sup>-1</sup>
Specific Heat	1120 JK <sup>-1</sup> kg <sup>-1</sup>
Emissivity	0.88

Furthermore, the study here focuses on the estimation of the possible effect of the following variables: fibre diameter( $L_d$ ), fibre ambient temperature( $T_a$ ), heat transfer coefficient(h) of fibre ambient medium, and time-varied temperature variation at the heat source( $T_s$ ). In order to evaluate impacts of these, four case studies have been carried out. The variable parameter in each case is provided in Table 5-2;

**Table 5-2** Variation of the parameter in each case

Case 1	Case 2	Case 3	Case 4
Fibre diameter ( $L_d$ ), $\mu\text{m}$	Ambient temperature( $T_a$ ), K	Heat transfer coefficient(h), $\text{W/m}^2\cdot\text{K}$	Heat source ( $T_s$ ), Hz
15	300	1000	100
18	500	2000	400
21	700	3000	700
24	900	4000	1000

The parameters associated with the setting of the finite volume method include: a number of discrete nodal points, a number of iterative steps and the time interval between each step. This information is provided in the following table.

**Table 5-3** The setting of the finite volume method

Discrete nodes	Iterative steps	Time interval
501	1000-2000	4.3 $\mu\text{s}$

Total time spent in numerical simulation is subject to the pre-set number of iterative steps. To obtain a fully converged solution requires a specific number of steps. If less than this number, the obtained solutions will not reach a steady-state or not be fully converged. However, more than this number wastes the computing power and time.

Care has to be taken with those parameters used in the finite volume method; the setting of these parameters has to remain constant in each case.

The difference equations derived here were based on the explicit finite difference method, which is easy to use but it suffers from an undesirable feature that severely restricts the applicability of

the explicit method. In this method, the largest bearable value of the time step is limited by the stability criterion. If the time step  $\Delta t$  is insufficiently small, the solutions given by the explicit method may oscillate strongly and deviated from the actual solution. In order to avoid the divergent stability criterion. Furthermore, different algebraic equations for different nodal points may cause different limits on the size of time step  $\Delta t$ , and the stability criterion that is most restrictive has to be used in the numerical analysis. A general rule is to select the equation having the smallest primary coefficient because this is the most restrictive, and to decide the largest value of  $\Delta t$  set as the stability criterion to that equation only as shown in equation 5.6. A time step given in this way will match the stability criterion for all the equations in the system.

$$\begin{aligned} T_0^{i+1} &= a_0 T_0^i + \dots \\ &\vdots \\ T_1^{i+1} &= a_1 T_1^i + \dots \\ &\vdots \\ T_m^{i+1} &= a_m T_m^i + \dots \\ &\vdots \\ T_M^{i+1} &= a_M T_M^i + \dots \end{aligned}$$

Stability criterion:

$$a_m \geq 0, m=0,1,2,\dots,m,\dots,M \tag{5.6}$$

The smallest primary coefficients in the difference Equations 5.3 and 5.5 are both  $1 - 2\tau - \tau A$ , and their values both equal zero, based on the time step  $\Delta t$  that is determined by the following equation

$$\Delta t \leq \frac{1}{2} \frac{\Delta x^2}{\alpha} \tag{5.7}$$

## 5.4. RESULTS AND DISCUSSION

The formulation of the heat-transfer problems for the determination of one-dimensional transient temperature distribution along SiC fibre results in complicated partial differential equations, which can be solved by the finite difference method. The numerical solution normally contains the number of parameters such as  $x$ ,  $L$ ,  $t$ ,  $T_f$ ,  $\alpha$ ,  $h$  and  $T_s$ , which are not suitable for making any graphical presentation of the results. In order to decrease the number of that, the numerical results are presented graphically using the following dimensionless quantities.

*Dimensionless temperature:*

$$\theta = \frac{T_f}{T_s}$$

*Dimensionless distance fromt the heat source:*

$$X = \frac{x}{L}$$

*Dimenionsless time:*

$$\tau = \frac{\alpha t}{L^2} \text{ (Fourier number)}$$

Where dimensionless temperature is obtained by the fibre temperature ( $T_f$ ) normalized to the heat source temperature( $T_s$ ), and  $X$  is the dimensionless distance,  $L$  is the total length of the fibre and  $x$  is a coordinate in the length of direction. This nondimensionalization allows us to present the temperature distribution in terms of three parameters:  $\theta$ ,  $X$ , and  $\tau$ . The solution can thus easily be presented in graphical form.

### *Case1*

Case1 is to simulate the variation of the fibre diameter ranging from 15 to 24 $\mu$ m, and to estimate the effect of different fibre in thickness on the thermal responding-time in the region near the flame outer boundary layer.

The effect of the diameter of SiC fibre on time taken to reach the steady-state has been estimated by the finite difference method. As shown in Figure 5-6, the numerical results all show a similar time taken to achieve the balance between the fibre and its surrounding temperatures. In Figure 5-6 a), the fibre diameter was set to 15  $\mu\text{m}$  which corresponds to the size applied in the flame temperature measurement, and transient temperature distributions were assessed at the time from 1.729ms to 4.322ms to find a converged temperature distribution of the fibre, and by looking at the time=3.488ms the fibre temperature profile was virtually converged and would not vary with time afterwards. The Figures b, c and d present the different fibre diameters that caused the variations in temperature distributions. The resulting temperature distributions were similar to the temperature profile found in Figure 5-6 a). As a result, the size of SiC fibre was unlikely to cause longer time to be taken to reach the steady-state and to significantly change the temperature distributions

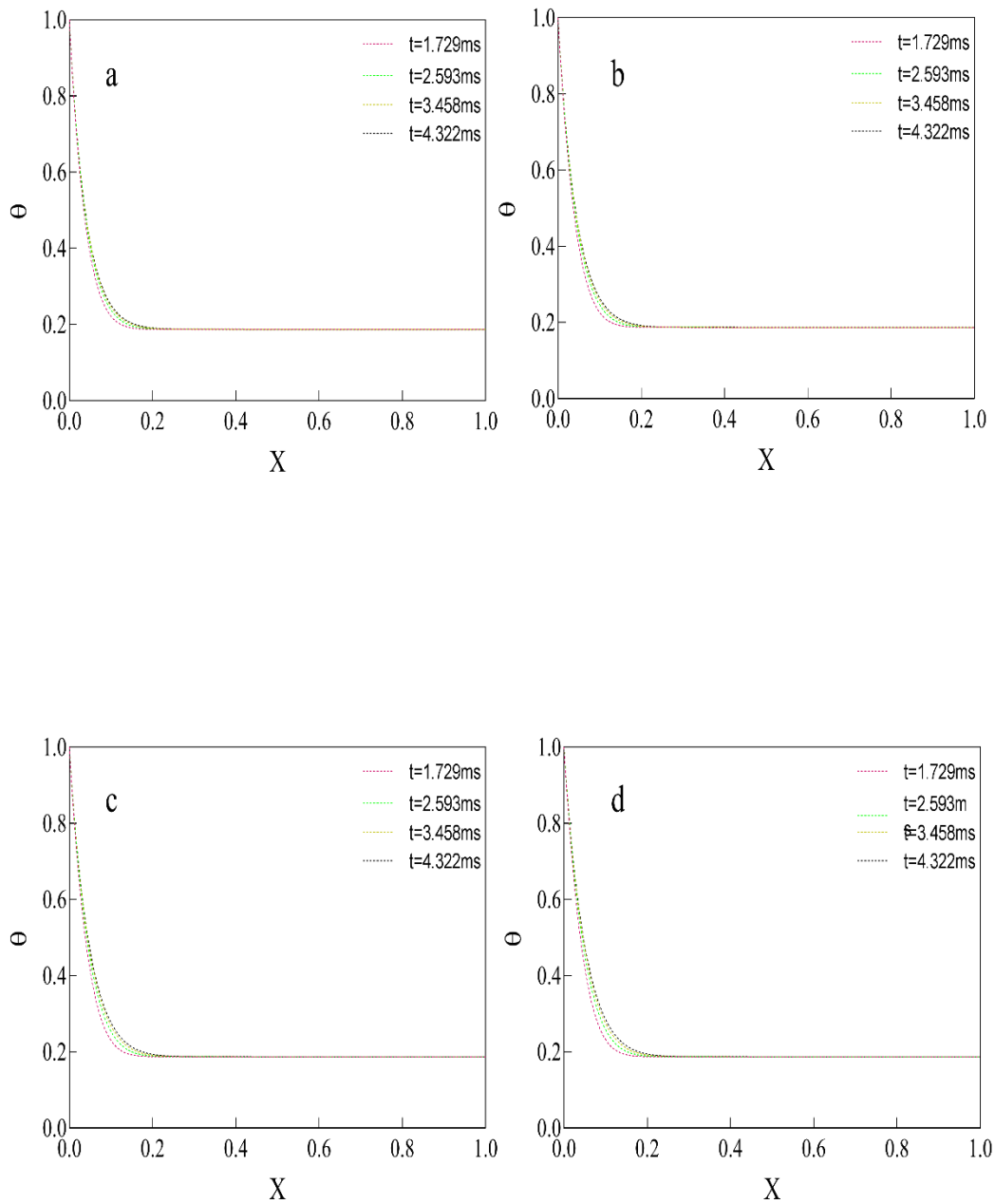


**Figure 5-6** Transient Temperature distribution a) The fibre diameter is 15 $\mu\text{m}$ , b) The fibre diameter is 18 $\mu\text{m}$ , c) The fibre diameter is 21  $\mu\text{m}$ , d) The fibre diameter is 24  $\mu\text{m}$ .

Fourier number is defined as a measure of heat conducted through a body relative to heat stored. A large value of the Fourier number indicates faster propagation of heat through a body, which can lead to a reduction in the time taken to reach a thermal steady-state. Figure 5-8 illustrates the plot of the Fourier number varying with the size of the fibre diameters ranging from 15 to 24  $\mu\text{m}$  with an interval 3  $\mu\text{m}$ ; it shows that the Fourier number was inversely proportional to the fibre diameter. The largest Fourier number 1024 occurred at the fibre diameter 15  $\mu\text{m}$ , which implies that this diameter gives the best performance in heat propagation from the heat source through the fibre. This results in the acceleration of fibre temperature to achieve a steady-state. Moreover, the smallest Fourier number 400 appeared at the diameter at 24  $\mu\text{m}$ ; This could cause a longer time be taken to make the heat transfer between the fibre and its ambient medium balanced, which is attributed to the unit length of the larger diameter fibre having a higher heat capacity.

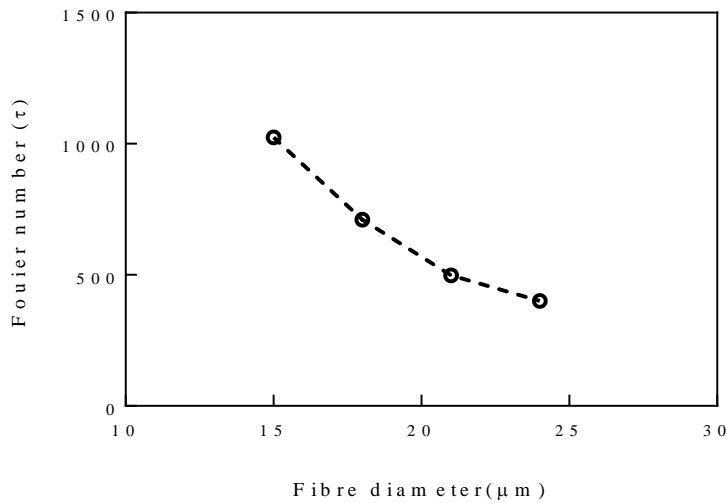


**Figure 5-7** Fourier number at the steady-state

The temperature profiles of the fibres with large diameter have been compared to that of the fibre with original diameter(15 $\mu$ m) at the steady-state. As can be seen in Figure 5-8, the overall trend shows the temperature difference profile increasing with fibre diameter. The peak points of the curves gradually move away from the origin point 0, meaning heat can be transferred further away from the heat source along a larger diameter fibre.

The maximum point of each curve is 0.0236, 0.0424 and 0.0569, which corresponds to 37.76K, 67.84K and 91.04K in temperature difference at the fibre diameters of 18, 21 and 24 $\mu$ m respectively. According to these, the rate of heat dissipation along the fibre can be reduced using a thinner fibre. This may help to maintain the temperature difference between the fibre and the heat source when measuring flame temperature at the flame outer boundary layer. However, a thicker fibre may either prevent flame chemical reactions or disturb the flow of the hot gas surrounding the fibre.

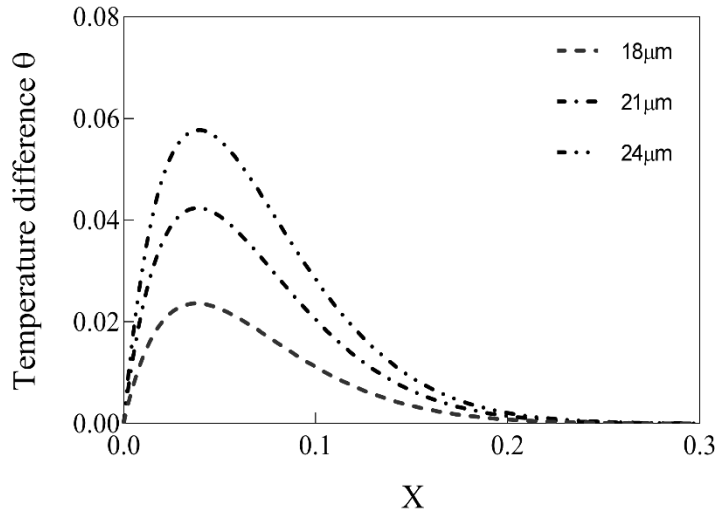


**Figure 5-8** Temperature difference distribution

## *Case 2*

Case 2 focuses on the variation of the fibre temperature distribution, caused only by the change of the fibre ambient temperature ranging from 300 to 900 K with an interval of 200K, which is equivalent to the dimensionless temperature 0.1875, 0.3125, 0.4735 and 0.5625.

In this case the fibre diameter is a constant parameter that equals 15 $\mu\text{m}$ ; other constant parameters include the heat source and the fibre initial temperature, which are identical with the values used in case 1. Thus, only the variable of the ambient temperature influences on the fibre temperature profile.

Figure 5-9 illustrates how the fibre temperature distributions varied with the ambient temperatures. It was found that the time steps needed to reach the steady-state depended on the ambient temperature, and the higher the ambient temperature was, the more time steps were needed.

However, treating the fibre temperature profile into two regions: the first region is the distance from 0 to 0.1 along the x-axis; another is the part after the position 0.1. In the first region the temperature distributions shown in Figure 5-9 can all reach the converged state at 1.729ms; the effect of ambient temperature variations could thus be ignored in this part. In second region, the ambient temperature can seriously influence the fibre temperature. Increasing the ambient temperature significantly increased the time steps required to reach the steady-state.

Moreover, the use of two-colour pyrometer developed here enables detection of the lowest temperature around 1225K corresponding to the dimensionless temperature 0.76. This temperature is falling into the region one mentioned previously, which suggests that the fibre temperature measurement using the two-colour pyrometer could be well implemented without the consideration of the influence of the ambient temperature variation.

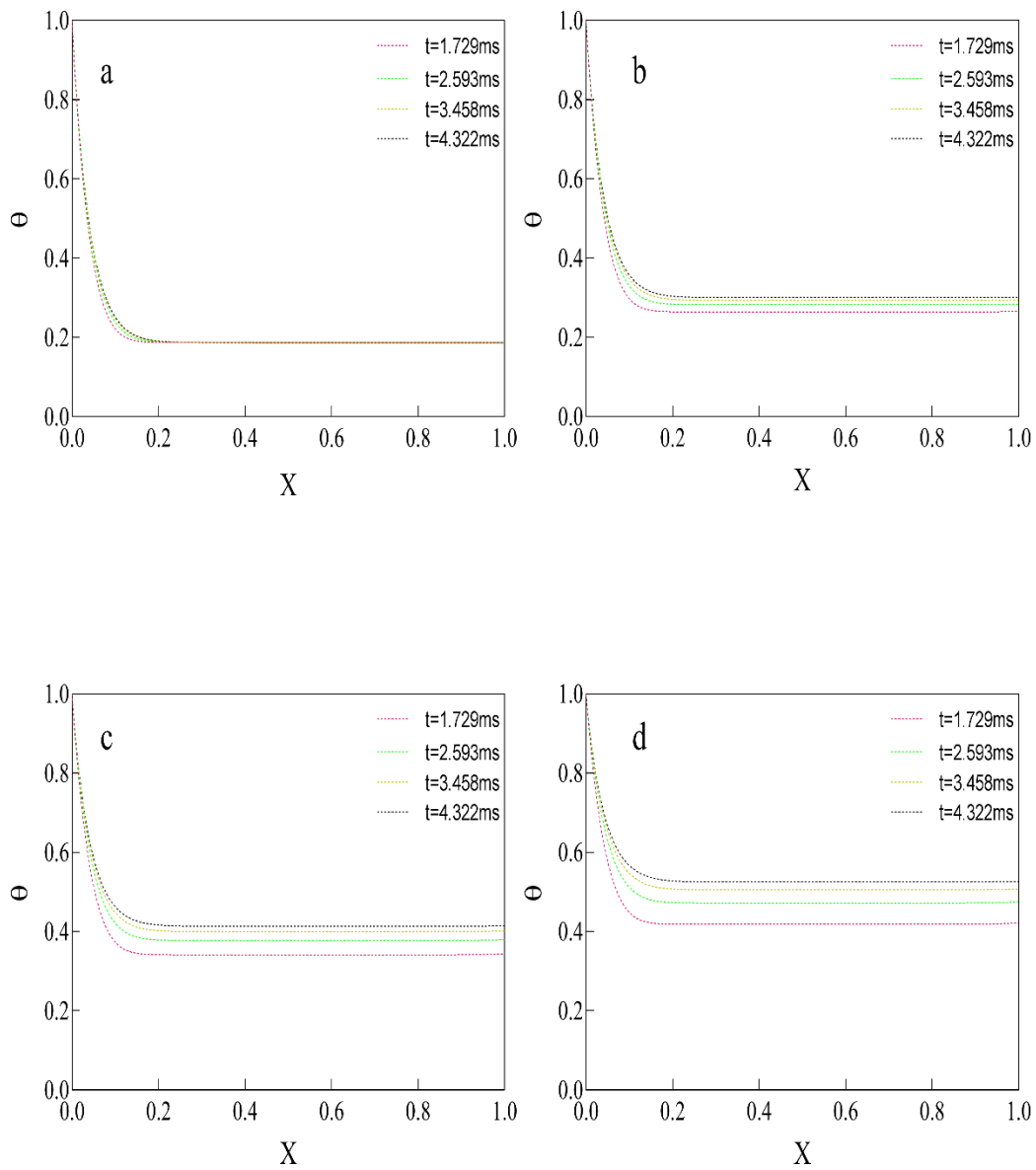


**Figure 5-9** Transient Temperature distribution a) The fibre ambient temperature at  $\theta=0.1875$ , b) The fibre ambient temperature at  $\theta=0.3125$ , c) The fibre ambient temperature at  $\theta=0.4375$ , d) The fibre ambient temperature at  $\theta=0.5625$

### Case 3

Case 3 is to assess the effect of heat convection in terms of heat transfer coefficient. As is well known, convection is one of the heat transfer mechanisms that describes the energy transfer between the surface of a solid and gas or liquid in motion next to it. And this mechanism involves the combined effects of fluid motion and conduction that is another type heat transfer mechanism.

A faster fluid motion can result in a greater convection heat transfer. Given the lack of any bulk fluid motion, heat transfer between the surface of a solid and its ambient fluid is purely governed by conduction. However, an open flame always involves relatively strong fluid motion, the extent of which is mainly attributed to the volume rate set in fuel supply systems. Although the presence of the amount of the fluid motion can accelerate the heat transfer between the surface and the adjacent fluid, it also complicates the calculation of the rates of heat transfer. Because of temperature measurement based on the determination of heat transfer rates is always a challenge.

The convection heat transfer coefficient does not belong to the fluid property. This parameter is determined experimentally and its value mainly depends on the variables affecting convection such as fluid velocity, surface geometry and the nature of fluid motion.

The correlation for average heat transfer coefficients in cross flow over a circular cylinder is determined by the  $Re$  number based empirical Equation. The average heat transfer coefficient in hot gas over SiC fibre could be over  $1000 \text{ W/m}^2\cdot\text{K}$  by this equation. By referring to this estimated coefficient Case 3 sets different heat transfer coefficients from  $1000$  to  $4000 \text{ W/m}^2\cdot\text{K}$  with an interval  $1000 \text{ W/m}^2\cdot\text{K}$ . The fibre diameter and initial temperature, temperature at the heat source and the ambient temperature remain constant through all the simulation tests in Case 3.

Figure 5-10 shows the fibre temperature distribution at different heat transfer coefficients ranging from  $1000$  to  $4000 \text{ W/m}^2\cdot\text{K}$ . The time taken to reach the steady-state reduces as the coefficient increases, from  $3.458 \text{ ms}$  to around  $1.729 \text{ ms}$ .

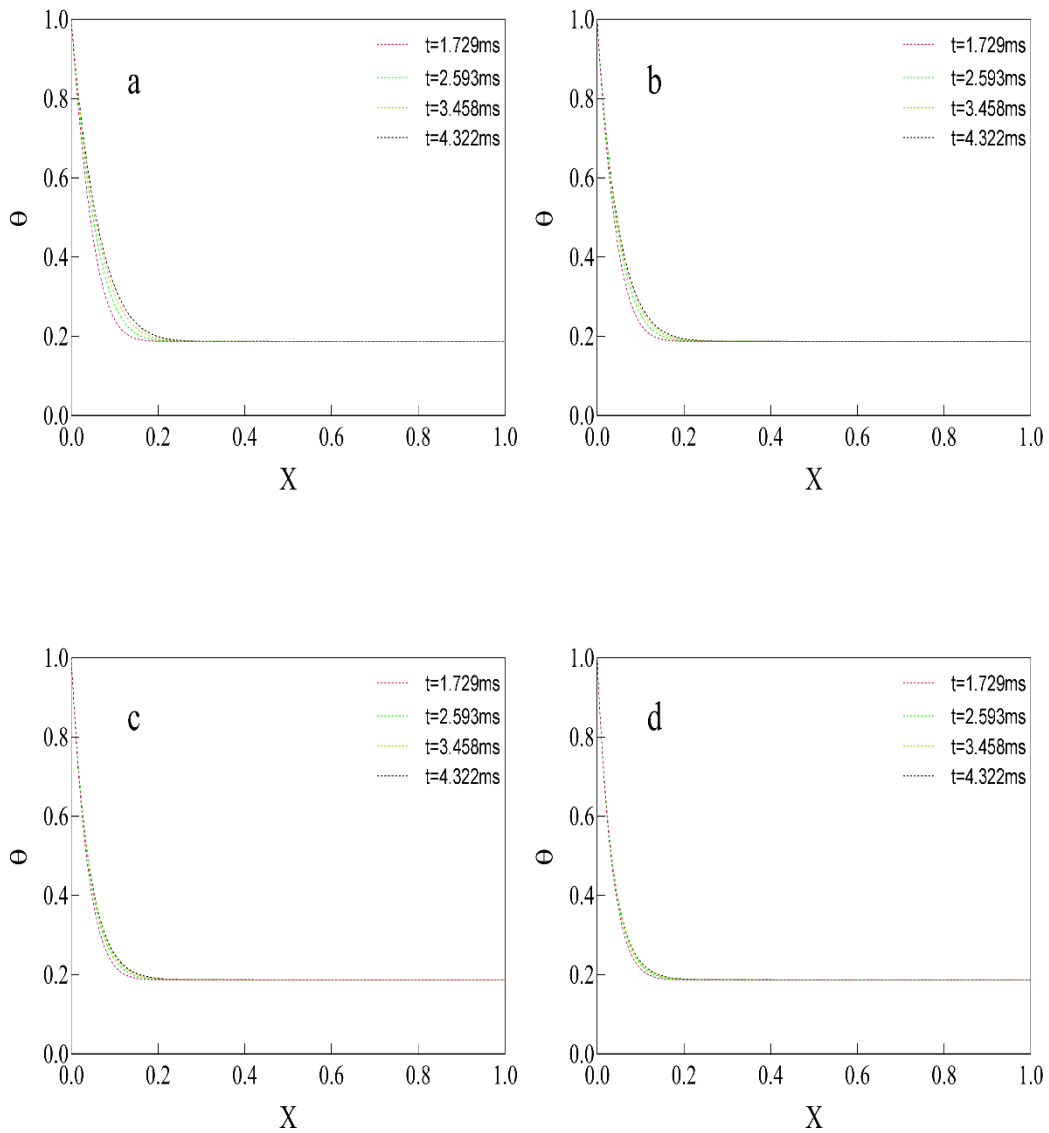


**Figure 5-10** Transient Temperature distribution a). The fibre ambient medium heat transfer coefficient  $h = 1000 \text{ W/m}^2\cdot\text{K}$ , b) The fibre ambient medium heat transfer coefficient  $h = 2000 \text{ W/m}^2\cdot\text{K}$ , c) The fibre ambient medium heat transfer coefficient  $h = 3000 \text{ W/m}^2\cdot\text{K}$ , d) The fibre ambient medium heat transfer coefficient  $h = 4000 \text{ W/m}^2\cdot\text{K}$ .

It is useful to note the reduction in the fibre temperature due to the rise in heat transfer coefficient. Compared with the temperature profile at  $1000 \text{ W/m}^2\text{K}$ , it was found that the maximum temperature reduction was around 0.11 which is equivalent to 176K, occurred at the highest heat transfer coefficient  $4000 \text{ W/m}^2\text{K}$ . 64K and 120K occurred at heat transfer coefficients  $2000 \text{ W/m}^2\text{K}$  and  $3000 \text{ W/m}^2\text{K}$  respectively, shown in Figure 5-11.

In flame temperature measurement, an important step is to determine the temperature difference between the fibre and its surrounding hot gas flame; this difference mainly depends on the diameter of the fibre and the thermal conditions of the ambient environment. Although a high heat transfer coefficient is helpful for the system to reach the steady-state, it increases the heat dissipation rate along the fibre. A fast heat dissipation could further enlarge that temperature difference, with the result that the calculated flame temperature is far away its actual value. In particular, the temperature difference could be larger than that inside the flame when measuring flame temperature at the flame outer boundary layer. This is owing to extreme heat exchange occurring near the outer boundary layer.

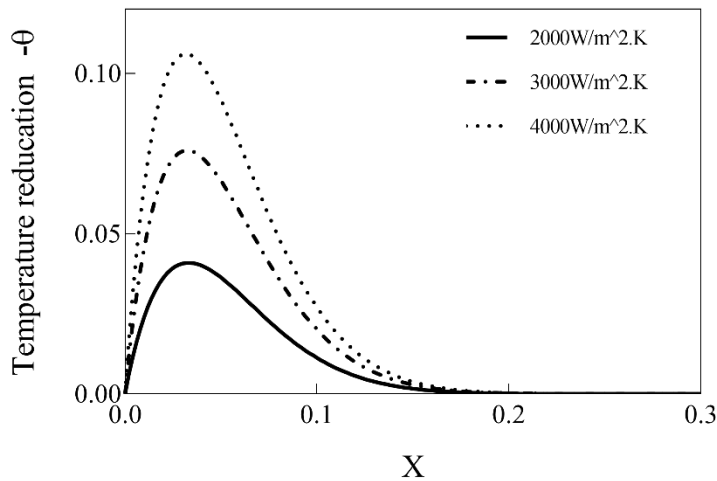


Figure 5-11 The reduction of the fibre temperature at time=1.729ms

#### *Case 4*

The stratified layer between the cold quiescent air and the hot gases of combustion initiates a flame flickering phenomenon, which leads to Kelvin-Helmholtz instability. That will cause instability in the flame temperature in that layer. when conducting flame temperature measurement in that layer using the SiC fibre based technique, the fibre temperature variation should be able to rapidly reflect this flame temperature fluctuation.

In order to confirm this, in Case 4 the heat source was set to a sinusoidal variable instead of constant temperature in the previous cases. This heat source temperature can vary from 300K to 1600K, and the frequency of this temperature oscillation was set from 100 to 1000 Hz with an 300Hz interval to simulate the flame instability induced flame temperature oscillation.

Figure 5-12 indicates the temperature variation at different locations of the fibre. The frequencies of the heat source temperature oscillation were set to 100, 400, 700 and 1000 Hz, shown in Figure 5-12 a), b), c), and d) respectively. The pattern of temperature variation at the four positions reflects rapid the temperature changes at the heat source. And the reduction of amplitude at those locations is proportional to the distance away from the heat source.

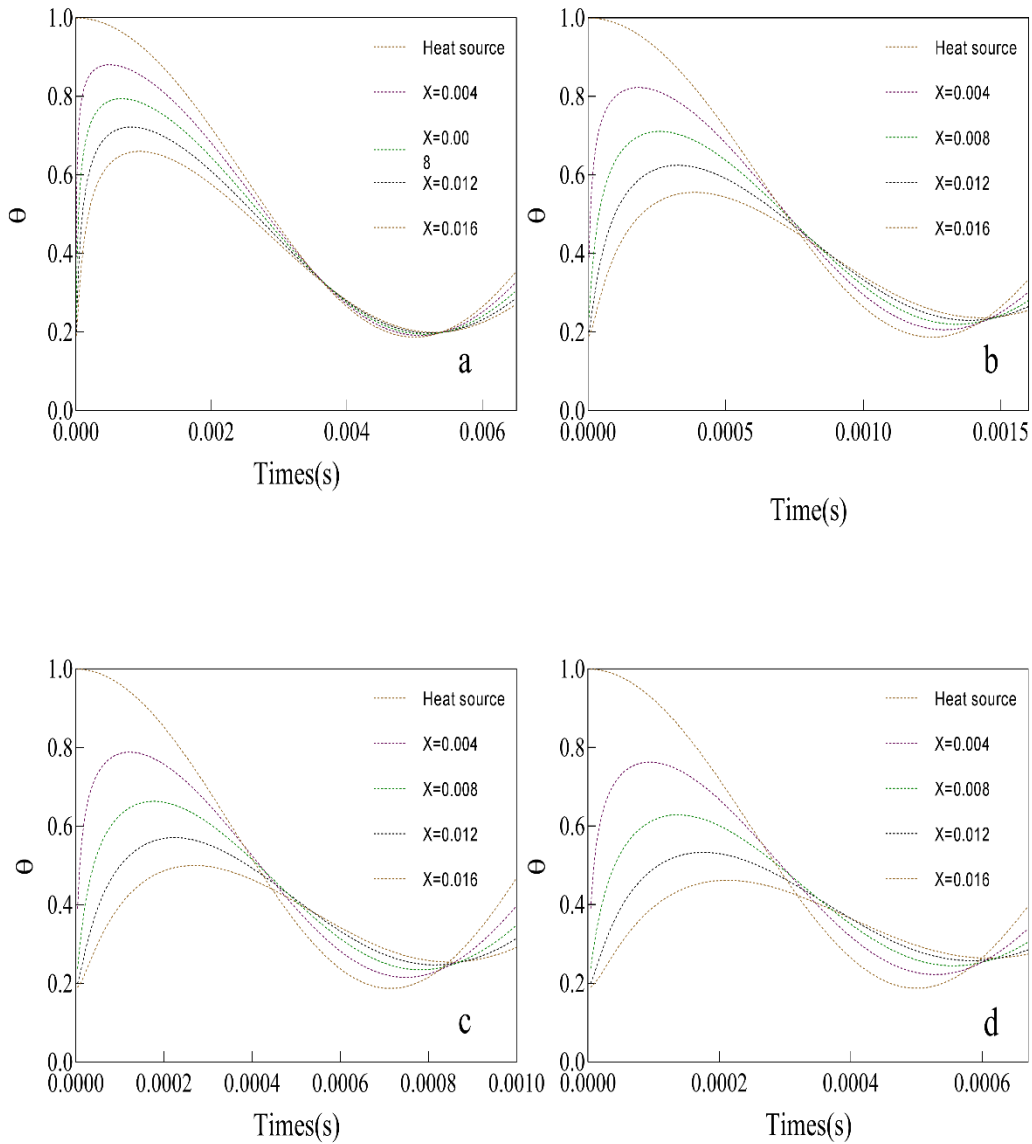


**Figure 5-12** The fibre temperature variation at different locations, a) The heat source temperature variation at frequency 100Hz. b) The heat source temperature variation at frequency 400Hz. a) The heat source temperature variation at frequency 700Hz. a) The heat source temperature variation at frequency 1000Hz.

The time lag between the heat source temperature and the fibre temperature variation was quantified by the phase angle which is determined by the equation as follows:

$$\phi = 360^{\circ} \times f \times \Delta t \tag{5.8}$$

Where  $\phi$  phase angle defines the degree of angle of the fibre temperature profile shifting away from the temperature profile produced at the heat source.  $f$  denotes the frequency of the temperature oscillation.  $\Delta t$  is the time interval between one of peak points of the source temperature profile and an adjacent peak point of the fibre temperature profile.

A small phase angle indicates that the fibre needs less time to respond to the temperature oscillation occurring at the heat source. Increasing frequency of the oscillation at the heat source showed that the fibre temperature profile varied accordingly. Figure 5-13 shows a general increasing trend in phase angle as rising the frequency. The amount of time taken to react to this temperature oscillation shows a linear relationship with the distance away from the location of the heat source applied.

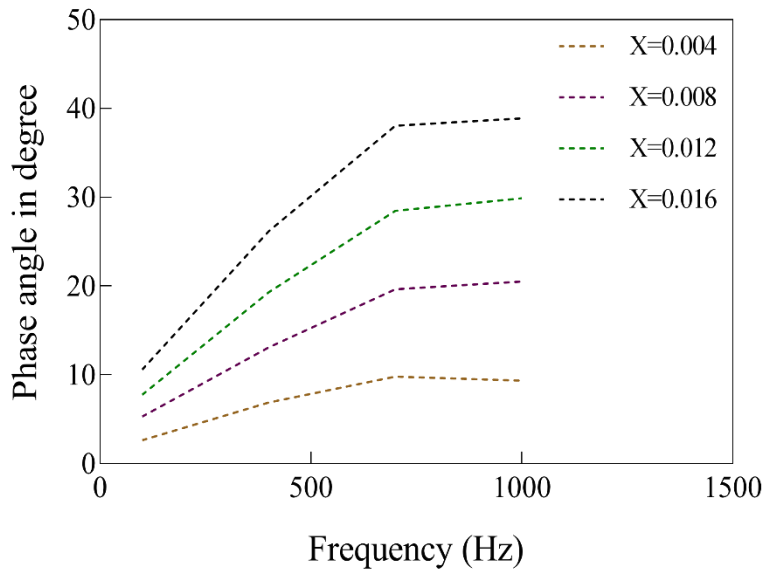
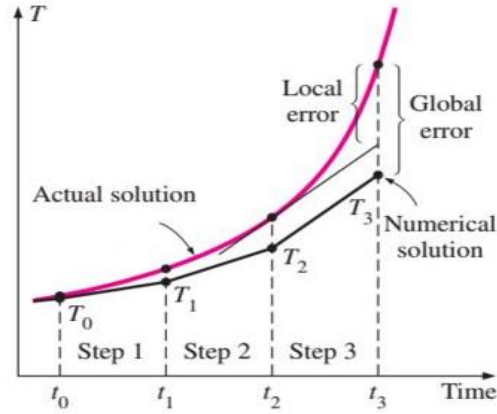


Figure 5-13 The variation of the phase angle

*Uncertainties in the numerical solution*

The results of fibre temperature variations based on the numerical method. The solution values obtained using this method are approximate; they may or may not be close the exact solution determined by solving partial differential equations. The difference between a numerical solution and the exact solution is the error existing in the numerical solution. Reasons for the error depend on many factors but can be classified into two sources: discretization error and round-off error.

Discretization error results from the approximations used in the formulations of the numerical methods; it is caused by replacing partial differential equations by difference equations in each step. In order to clarify the reason, the error occurs, the graph with regard to the difference between the two solutions is shown in Figure 5-14. The red curve and the black solid line are assumed to be the exact and the numerical solutions of a transient heat transfer problem with time at a node. At the beginning, both the solutions would be identical at the first time step. However, as the time increases, the numerical solution deviates from the exact solution. This is due to the approximation at the first time step, and the difference between the two solutions is referred to as the local discretization error, and it will further increase with each step because the second step is based the erroneous result of the first step, as shown in Figure 5-14. This local discretization error continually accumulates as the time step increases. The total discretization error at any step is called the global discretization error. And the discretization error can be reduced by either decreasing the mesh size or the size of the time step. However, this may cause the extra accumulation of round-off error.



**Figure 5-14** Schematic of the global and local discretization errors of the finite difference at a node point [1]

The round-off error results from the computer program that uses a limited number of significant digits, continuously chopping off the digits it cannot retain. However, as long as the computer can retain an infinite number of digits for all numbers, the difference between the numerical and the exact solution would be entirely subject to discretization error. But every computer represents numbers by a finite number of significant digits. For many computers the default value of significant digits is 7, named as single precision; for example, in this mode the computer will register the number 55555.777777 as 55555.78 or 55555.77, which is subject to the rounding method the computer uses. While, in most engineering calculations, they use 15 significant digits for the numbers, named as double precision, applied here to the study here of transient fibre temperature variation. Although performing this study in double precision will require more computing power and computer memory, and a longer execution time, the numerical solution can achieve a higher accuracy than that using single precision.

In addition, the round-off error also depends on the number of iterative steps in the simulation. In finite difference method, the number of calculations increases as the time step or mesh size decreases. This results in the further round-off errors accumulating in the final solution.

Therefore, the most effective way to minimise the round-off error is to reduce the number of time steps (or the number of calculations). Figure 5-15 gives the number of time steps needed to reach a steady-state at different mesh sizes in the numerical study of the fibre thermal behaviour; it indicates that the number of time steps strongly depends on the number of elements.

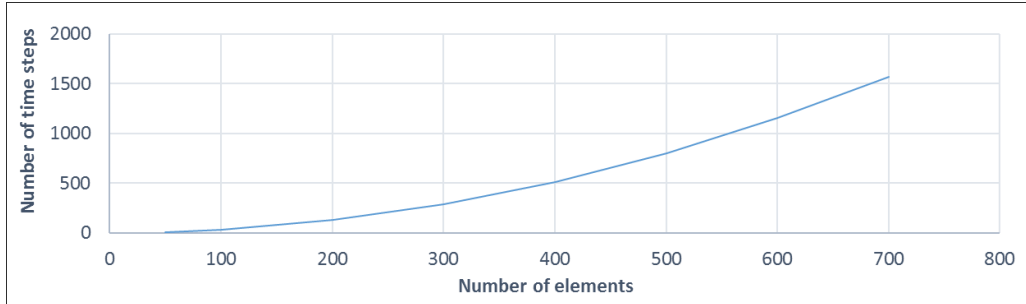


**Figure 5-15** The number of time steps needed to achieve the steady-state at different mesh sizes

However, a small number of elements could increase the discretization error, which is the predominant error in numerical methods. Figure 5-16 illustrates that the fibre temperature variation along the fibre at three different positions when changing the number of elements; they all experience reduction in temperature as the number of elements increases up to 500, then the fibre temperatures remain nearly constant even with more elements added. The number of elements used over 500 is not necessary in the simulation because not only will the discretization error not decrease, but also the extra rounding-off error will accumulate.

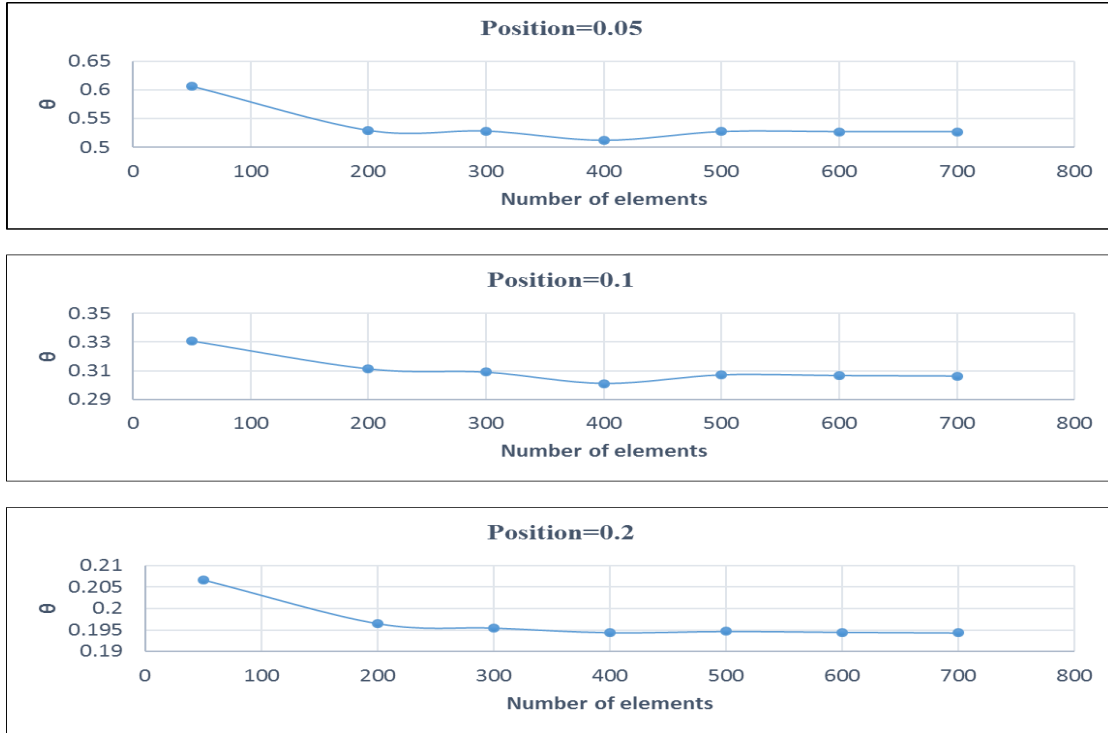


**Figure 5-16** Comparison of the fibre temperature responding to the variation of the number of elements at various positions along the fibre at the steady-state

In addition to the rounding-off errors and the discretization errors in the numerical solutions, some uncertainties abide in the parameters used in the simulations. As well known, the thermal properties of SiC fibre such as thermal conductivity and specific heat are a function of temperature, however they were set to be constant values in the study for simplification purposes; this may mean that obtained results deviate further from the exact results.

To completely and exactly simulate a region involved strong heat exchange is a difficult task, which requires considerable knowledge in computational fluid dynamics and heat transfer, and to predict this region induced the fibre temperature variation further complicates this simulation. Although the numerical solution may not exactly reflect the fibre temperature, the found tendencies of the fibre temperature variations will be useful for a better understanding the underlying defects of SiC-based two-colour pyrometer.

## 5.5. SUMMARY

In the section the explicit based finite difference method has been carried out to simulate the fibre temperature variations, caused by the factors associated with the size of the fibre diameter, the fibre ambient temperature and the heat transfer coefficient variations, and the flame instability caused temperature oscillation. The reasons for using the numerical method have been clarified and the complete process of transferring the partial differential equation to the difference equations has been presented.

The obtained numerical solution indicates that increasing the diameter of SiC fibre can prevent occurrence of fast heat dissipation, but meanwhile, the induced side effects such as the disturbances of the flame chemical reactions and the flow of the hot gas are not avoidable. The ambient temperature variation can significantly influence the fibre converging time. A higher heat transfer coefficient can cause fast heat dissipation that is instrumental in reducing the time taken to reach the steady-state in the stratified region, however it has the potential to reduce the fibre temperature at the flame outer boundary layer, however the temperature difference between the fibre and the flame can be further enlarged. In addition, the fibre shows good ability to rapidly reflect the flame instability induced flame temperature oscillation. As a result, the two-colour method can thus detect this oscillation by monitoring the fibre temperature variation. finally, the inherent errors of the numerical method and the choice of mesh size have been discussed in detail.

## 6. APPLICATION OF SiC FIBRE FOR FLAME CHARACTERISTIC STUDY USING OPTICAL METHOD

### 6.1. INTRODUCTION

Temperature is among the most frequently measured properties in combustion research. Given features including having less-intrusive, short-responding time, and being easily set-up, is pursued of temperature diagnostics make up a key area in combustion research.

The most frequently used techniques for open flame temperature detection are either intrusive (thermocouple) or non-intrusive (laser induced fluorescence). Most intrusive techniques are widely used for turbulent flame temperature measurements [60, 67, 68], suffering very large response times varying with the local temperature and flow velocity. On the other hand, non-intrusive techniques are mostly based on the laser techniques which require considerable amount of investment in material and research, and a complicated setup prior to temperature measurement; these factors result in that the practical application of the laser based measurements is challengeable.

The technique used here is an improvement of  $\beta$  SiC-based two-colour pyrometer, named Thin-Filament Pyrometer(TFP) which is the combination of a high-speed imaging system and ultra-thin SiC fibre(15 $\mu$ m). The radiant energy emitted from SiC fibre stretched across the flame is measured in the visible wavelength band.

TFP can exhibit fast temporal response and high spatial resolution. The advantage of this technique is the low cost and simplicity, with minimum obstruction of flow. An obvious advance on the use of thermocouple is the ability to provide one-dimensional temperature distribution instead of a single-point measurement. These acquired properties match well with the expected features aforementioned.

In 1988 Vilimpoc [17] pioneered the demonstration of the potential of measuring temperature based on SiC fibre and estimated that the time of its temporal response to the surrounding hot gas was around 1.5ms. Bedat [63] applied TFP measurement in a weakly turbulent flame and extended the limit of temperature down to 550 K. Pitts [69] performed TFP in flickering laminar diffusion flame. Struk [65] compared the temperature measured by thermocouple with the temperature measured by TFP and found a 3.5% difference for temperatures above 1200 K. Maun [64] applied a digital colour imaging based TFP measurement with an estimated uncertainty of  $\pm 60\text{K}$  in the range of 1400-2000K. Kuhn [70] compared the thin-filament-derived gas temperature with the computational result, showing strong similarity. Bin [33] compared a laser-based technique and thermocouple with TFP measurement, showing good agreement in measured temperatures. This previous research has demonstrated the great potential of SiC fibre in flame temperature measurement and the worthiness of further development in TFP.

The investigation here aims to measure the premixed methane/air flame temperature at equivalence ratio from 0.9 to 1.1 with a 0.05 interval. Two configurations of fibre mesh were built here: one is for the flame temperature measurement; another is for the comparison between the flame and the fibre intensity-based oscillation frequencies. One-dimensional flame temperature along the length of the fibre has been obtained at  $\Phi=0.9, 1.0$  and  $1.1$ ; at each equivalence ratio ten flame temperature profiles have been calculated during 0.036 sec, corresponding to a responding time of 0.004 sec. Moreover, in order to avoid the misalignment between two grey level images, two-colour pyrometer used hereby replaces the beam splitting and narrow bandpass filtering approach with the camera built-in colour-banded filter method, aiming to avoid complicated configuration and high cost, and the ratio RG from the RGB primary channels is used for the calculation of the temperature. The accuracy of TFP measurement was verified by a commercial Infra-pyrometer. The structure of this chapter is divided into two cases: Case one places emphasis on the flame temperature measurement; Case two focus on the flame and the fibre emission intensity-based oscillation

frequency. Prior to these two cases, experimental method and equipment will be discussed. In the conclusion the findings from this investigation and the measurement uncertainties will be summarized.

## **6.2. EXPERIMENT SETUP AND INSTRUMENTATION**

### **6.2.1. COMBUSTION SETUP**

The schematic layout of the combustion rig and its associated flow system and the flow control system are shown in Figure 6-1. As it can be seen, the combustion facility is configured to produce a premixed flame with acquired equivalence ratio. Fuel and air for the premixed flame are independently supplied and controlled to fulfil safety requirement; Also along the pipelines, flashback arrestors are placed between the fuel cylinder and the pipeline to prevent any undesired effect.

In order to obtain trustworthy results, research grade N4.5 methane combining with the oxidizer (air) was used to produce the required premixed  $\text{CH}_4$ + air flame. All the flows pass through their individual rotameters(flowmeters) and pipelines prior to entering the mixing chamber. Before feeding to the pipeline both the compressed fuel and air pass individually through their own regulator which maintain a constant pressure to the rotameters. Figure 6-2 shows the model of rotameter utilised for controlling the supply of fuel and air. The volume flow capability of the air rotameter ranges from 0.1 to 1.1 L/Min, with 0.3 to 3.4 L/Min for the methane rotameter; these rotameters are pre-calibrated to atmospheric pressure. Prior to entering the burner, both fuel and air pipelines are routed to a mixing chamber placed between the burner and the flowmeters, giving the space for mixing the fuel with the oxidizer.

Taking advantage of soot radiation for temperature detection is not valid in this case because of low soot concentration in the premixed flame. SiC fibres are thus introduced to compensate for the lack of soot; there are placed above the burner nozzle. In this research two different SiC fibre

configurations are built here; one is for temperature measurement, another is used for detecting the oscillation frequency of the fibre emission.

The optical setup includes a PHOTRON SA4 high speed colour camera shown in Figure 6-4, with a Sigma zoom 24-70mm  $f/2.8$  EX lens. This optical configuration is only designed for flame temperature measurement. With regard to flame oscillation frequency, this optical configuration has to be slightly modified by fitting a stereo adapter onto the Sigma Lens, shown in Figure 6-4(a). This modification enables the camera to produce two identical images instantly when capturing an object. In addition, a KENKO ND (neutral density) filter with 50% transmittance is attached onto one entrance of the adapter; the reason for this is to reduce the fibre strong emission from the fibre to prevent image saturation. Another entrance of the adaptor without any filter attached is responsible for capturing of flame intensity. As a result, the comparison between the flame and the fibre emission can be achieved. The combustor is a Bunsen burner with the diameter of the nozzle around 6.8mm, which is designed to give a stable premixed flame, shown in Figure 6-4.

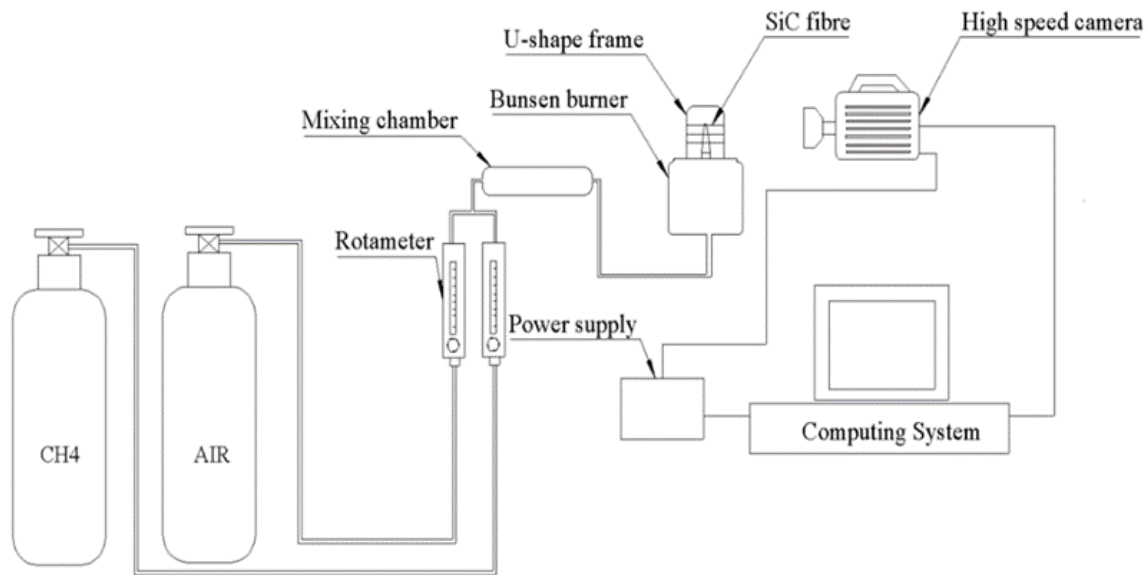


**Figure 6-1** Schematic layout of the combustion unit

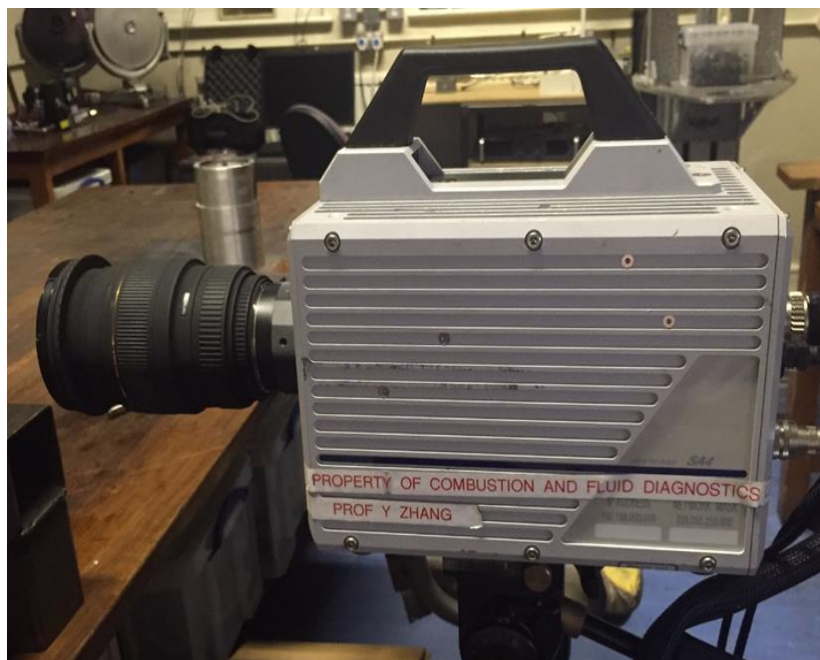


**Figure 6-2** High speed camera PHOTRON SA-4



**Figure 6-3** The diameter of the burner's nozzle



**Figure 6-4** (a) Pentax stereo adapter, (b) Kenko ND filter

## 6.2.2. SiC FIBRE CONFIGURATION

This sub-section gives SiC configurations for the flame temperature measurement and the flame intensity detection. A U-shaped copper frame was used to hold SiC fibres tautly in both configurations. The detail of SiC fibre preparation refers to section 4.2.2.

### ➤ The configuration for temperature measurement

Blackbody radiation is desirable for the optical temperature diagnostic technique. Two-colour pyrometer established here depends solely on this radiation. As usual in the diffusion flame, the flame temperature can directly refer to the soot temperatures; unfortunately, in the case of methane/air premixed flame soot radiation is not sufficient for temperature calculation. An alternative way is to use SiC fibre playing the same role as soot to emit the required radiation. Figure 6-5 shows the fibre configuration in the premixed flame. In all there are six fibres which are placed into the flame at different heights. Five of them were placed above the burner exit with a 1.5cm interval, distributed in the same vertical plane; the other fibre was placed at height around 3.5 cm from the nozzle.

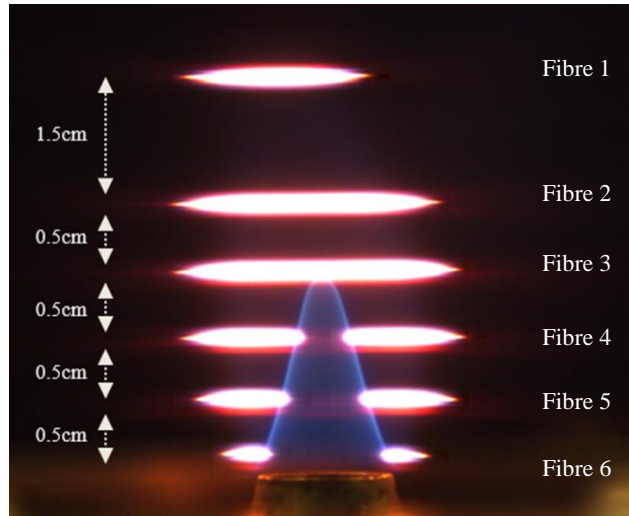


**Figure 6-5** The image of SiC fibres' positions at the flame, captured at 50 fps

➤ **The configuration for flame intensity detection**

In the case of flame frequency detection, the mesh of SiC fibres has been reduced in comparison with the fibre mesh shown in Figure 6-5. Figure 6-6 shows that three fibres are distributed equally from the top to the base inside the flame at the fuel rich condition.

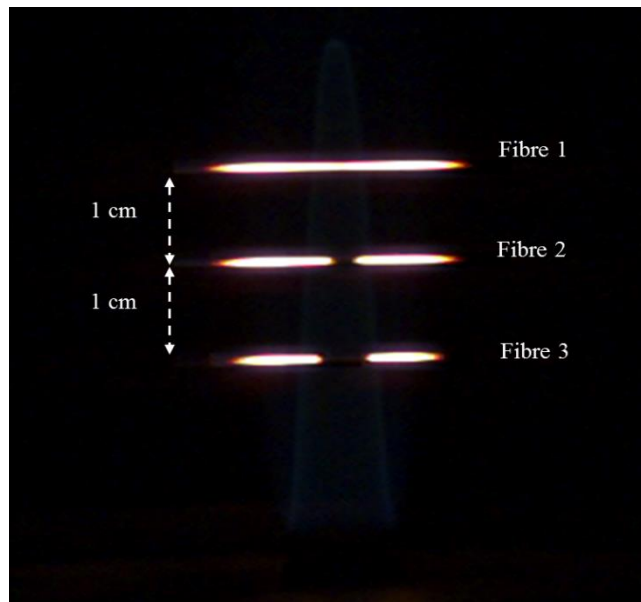


**Figure 6-6** The arrangement of SiC fibres placed inside the flame, imaged at 500 fps.

### 6.3. CASE 1: FLAME TEMPERATURE MEASUREMENT

#### 6.3.1. INTRODUCTION TO THE FLAME AND THE FIBRE EMISSION

In this case the flame temperature measurement was carried out by measuring premixed CH<sub>4</sub>+ air flame temperature at different equivalence ratios; the images of the flame at the corresponding fuel/air mixtures are shown in Figure 6-7(A). The combustion setup and the fibre configuration are referred to Figure 6-1 and Figure 6-5, respectively. The flame images captured use the shutter speed 1/250 sec, and 1/104000 sec for imaging fibre emission; both groups of images use the same fps 1/250 sec.

The colouration of the premixed flame shown in Figure (A) exhibits a trend that is from the dark to bright bluish flame, along with the increase in equivalence ratio. The flame height remains nearly constant before at  $\Phi=1.05$ , subsequently the height increases slightly at  $\Phi=1.1$ .

Figure (B) shows how the fibre emission responds to the change of equivalence ratio from 0.9 to 1.1 with an 0.05 interval. In theory SiC fibre is a type of grey-body, its emission intensity directly depends on the fibre temperature. The higher the fibre temperature is, the stronger the emission. By observing the weak fibre emission inside the white rectangle in the Figure (B), the weakest fibre emission occurred at  $\Phi=0.9$ , which is hard to see with the naked eye; as  $\Phi$  increased the fibre emission become visible gradually, particular at  $\Phi=1.0$  and 1.05 where the emissions are relatively stronger than those found at other equivalence ratios.

This finding is in line with the theory that the fibre temperature should be lowest at  $\Phi=0.9$  and increase continuously until reaching the stoichiometric ratio, after which the fibre temperature will tend to decrease. This inferred fibre temperature tendency will be validated in the next sub-section.

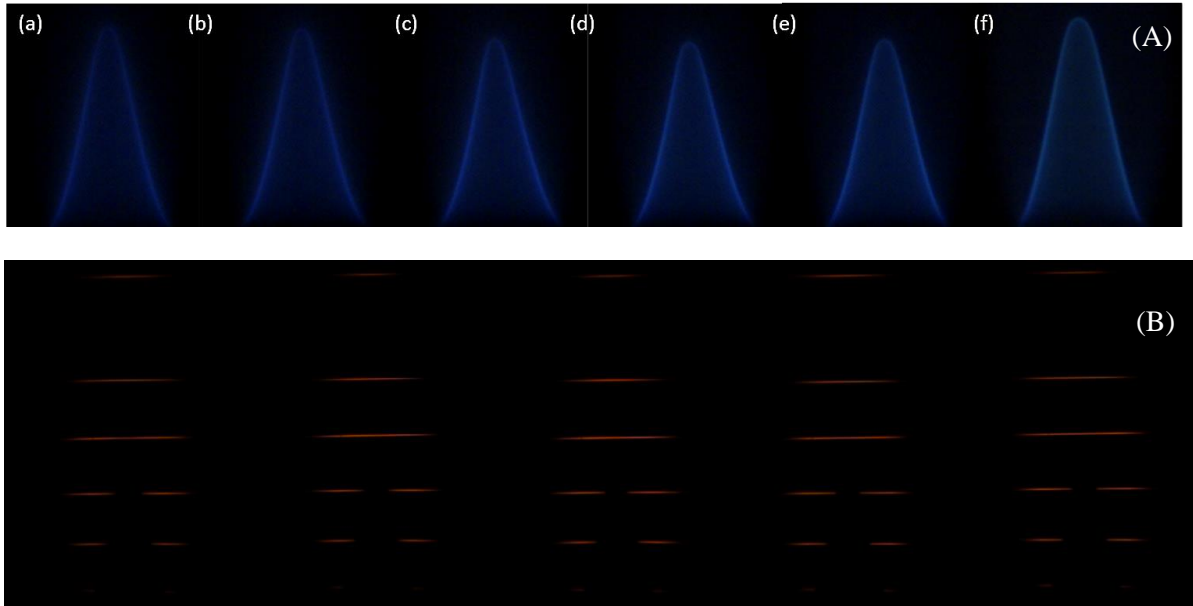


**Figure 6-7** (A) Premixed  $\text{CH}_4$ +air flames at equivalence ratio conditions (a)  $\Phi=0.90$ , (b)  $\Phi=0.95$ , (c)  $\Phi=1.00$ , (d)  $\Phi=1.05$ , (e)  $\Phi=1.10$ ; (B) The fibre emission at the corresponding flame in (A).

### 6.3.2. FLAME TEMPERATURE

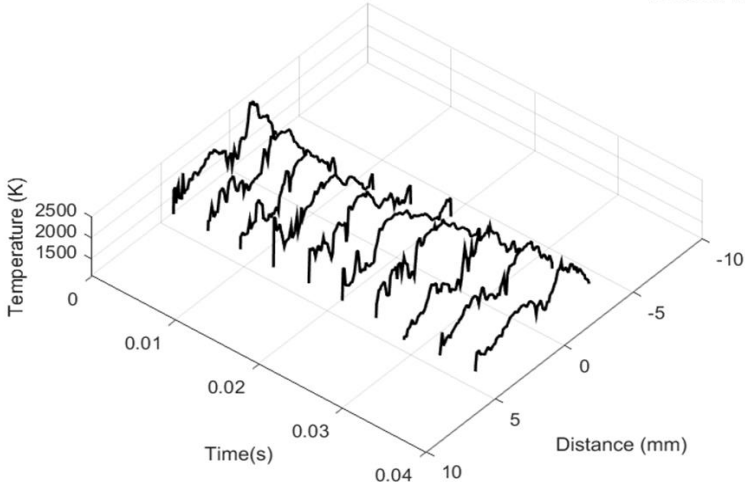
Flame temperature determination is based on the two-colour system established in this project; this system enables measurement of the grey-body surface temperature by using its radiation. However, due to the lack of sufficient radiation from soot particles it is not possible to detect flame temperature by directly applying the two-colour system. The fibre used here replaces the function of flame soot, and its temperature is detected by the two-colour method. Having obtained the fibre temperature, the next step is to estimate the temperature variance between the fibre and its surrounding hot gas, the procedure of which is described in section 6.3.3.

Figure 6-10 gives the measured flame temperature distributions along the length of fibres 1, 3, and 5, respectively. These three fibres are placed at different locations of the flame. Fibre 1 is placed a few millimetres away from the flame tip, fibre 3 is located next to the tip and fibre 5 is close to the exit nozzle; the complete configuration of the fibre setting is shown in Figure 6-5.

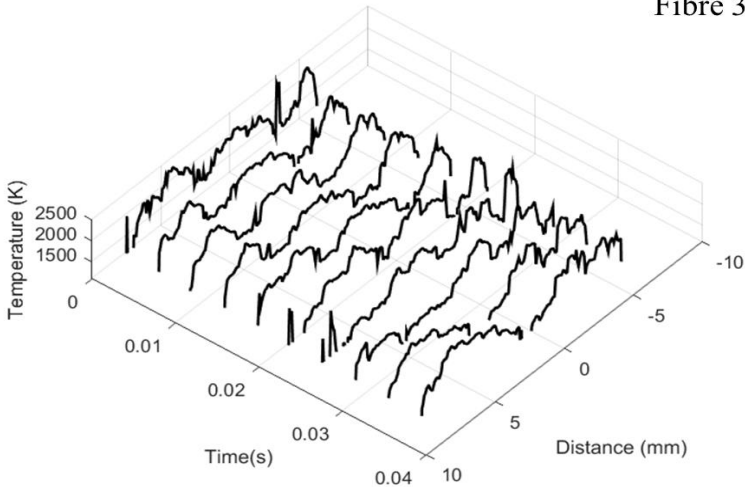
Each fibre gives a group of flame temperature profile variations during 0.036 sec at intervals of 0.004s. Flame temperature profile detected by fibre 1 shows that the flame temperature peaked at around -3mm offset from the centreline of the nozzle; the location of the peak temperature varied slightly with time, and the flame temperature decreased with increasing the distance away from the nozzle, accompanied by a strong fluctuation of the flame temperature. In both fibre 3 and fibre 1 the flame temperature profiles appeared to be a sinusoidal curve because of the strong temperature fluctuation; and it can be noted that a multi-temperature-peak occurs along the fibre, similar to the findings shown in Figure 6-8 and 6-9. This because the position of fibre 2 is near the flame front where the flame temperature is relatively low, and the flame temperature will experience an increase and then decrease towards the ambient environment temperature. By contrast, the flame temperature profile at fibre 5 shows a bell-shaped curve with a weaker temperature fluctuation in comparison to that found in fibre 1 and fibre 3; even with equivalence ratio increases from 1 to 1.1 the flame temperature profile still remains relatively constant, which can be seen in Figures 6-9 and 6-10.

This flame temperature instability can be mainly correlated with the buoyancy-driven oscillation that is associated with the Kelvin-Helmholtz instability and the considerable number of vortices appearing due to the buoyant interaction between the cold ambient air and the hot burnt gases. Shepherd [71] used a joint experimental and numerical approach to demonstrate the formation of the vortices near the flame tip, and to explain how flame flicker results from heat release at the flame front, which compels the burnt gas flow in a radial direction opposed to the rotating vortex motion induced in the pressure field. Hence, reference to Shepherd's research explains convincingly why the temperature instability tends to increase from the flame base to the tip.

Fibre 1



Fibre 3



Fibre 5

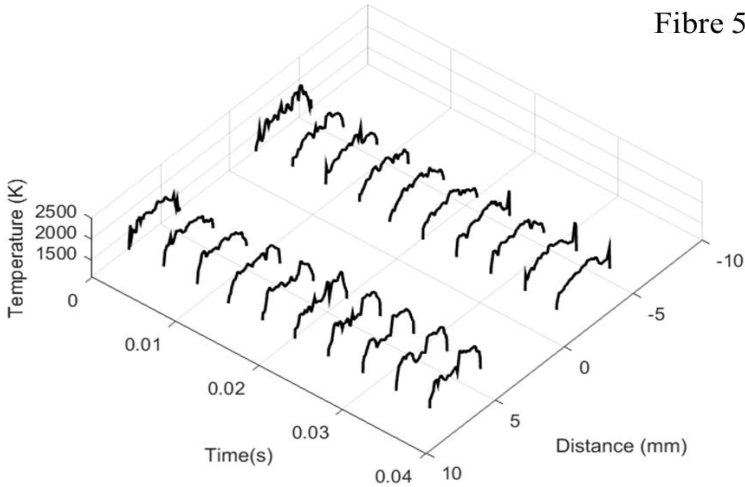
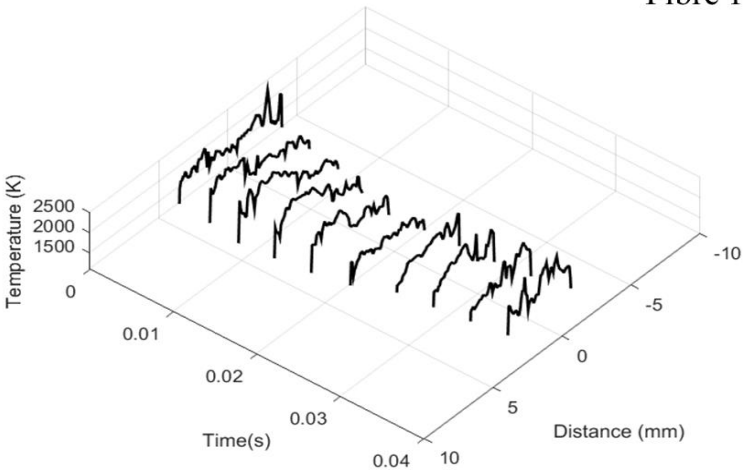
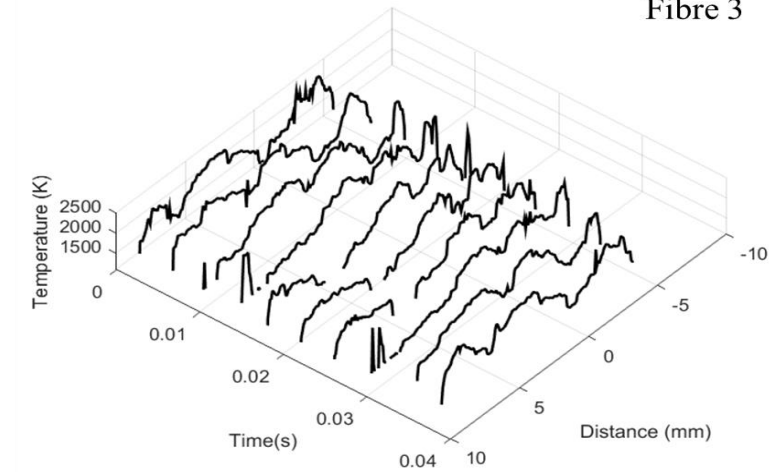


Figure 6-8 Measured temperature of the hot gas surrounding the corresponding fibre, and the fuel and air mixture at  $\Phi=0.9$

Fibre 1



Fibre 3



Fibre 5

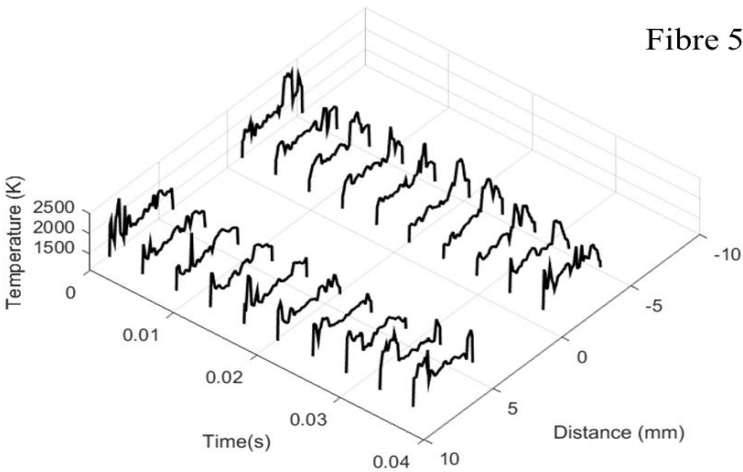
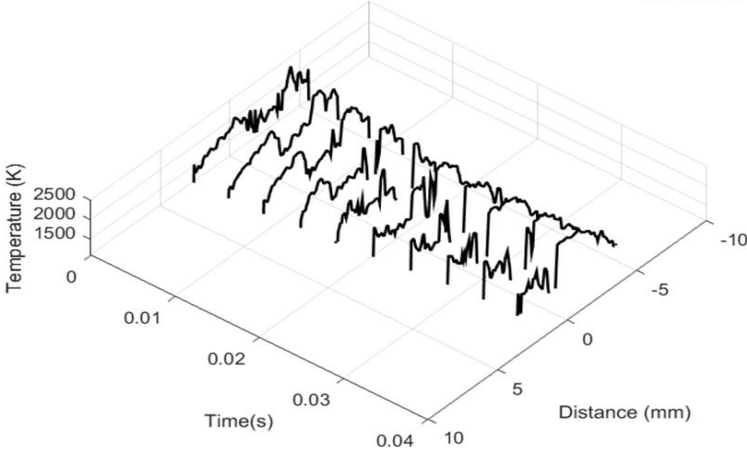
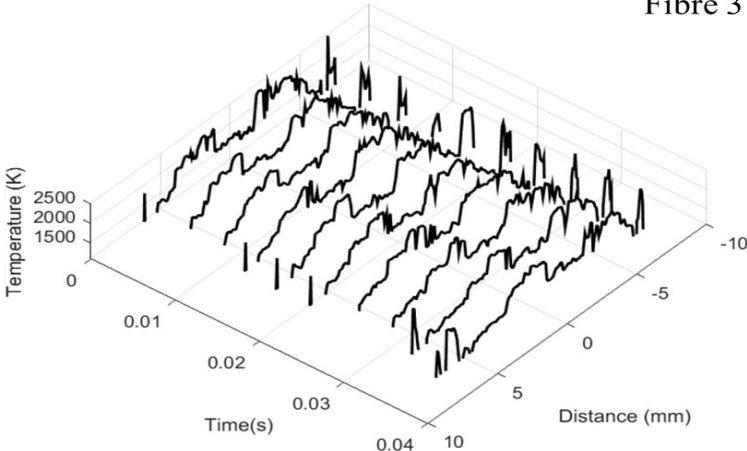


Figure 6-9 Measured temperature of the hot gas surrounding the corresponding fibre, and the fuel and air mixture at  $\Phi=1.0$

Fibre 1



Fibre 3



Fibre 5

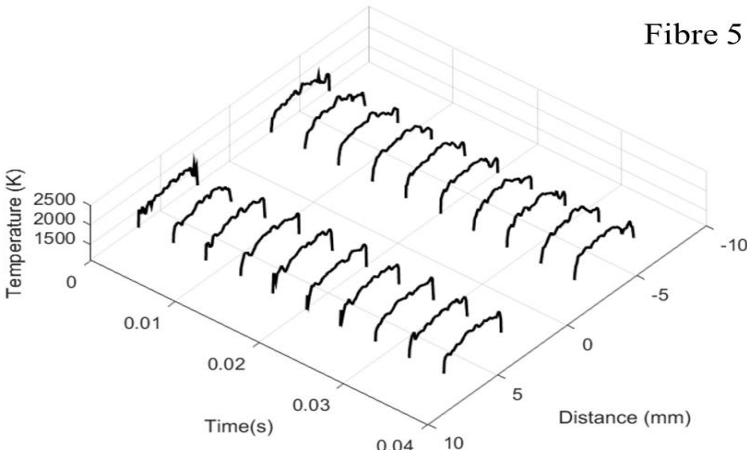
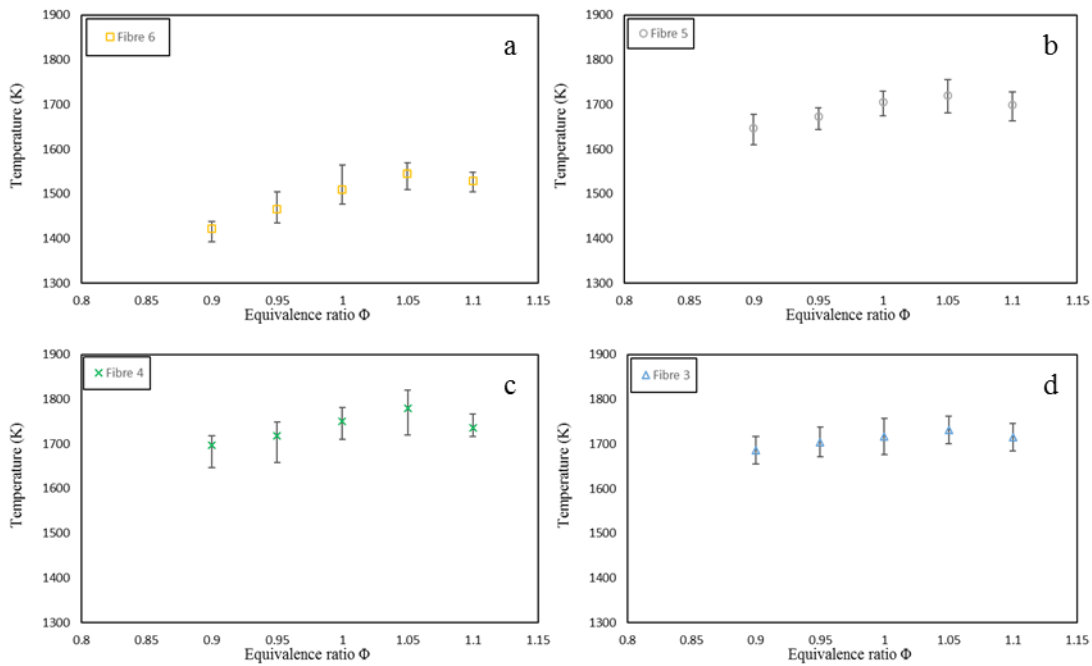


Figure 6-10 Measured temperature of the hot gas surrounding the corresponding fibre, and the fuel and air mixture at  $\Phi=1.1$

Figure 6-11 is the average flame temperature at equivalence ratio from 0.9 to 1.1. The fibre number indicates the detected average temperature at different heights of the flame. The temperature measurement uses the pixels within the glowing fibre to determine the average flame, using the camera setting mentioned in section 6.3.1. Each point represents an averaged value of 100 samples captured in 0.4 sec. At each height of the flame the flame temperature increases from fuel lean 0.9 to fuel rich 1.05, and then begins to decrease by 1.1. As increasing fibre position from the flame base towards the tip, the average flame temperature experienced an increase until the height approaches to fibre 4, subsequently a reduced temperature was found at fibre 3. In addition, the average flame temperatures were also calculated in fibre1 and fibre2, similar to the temperature range measured in fibre 3, but the variation of the average temperature was not governed by equivalence ratio. The reason for this is highly related to the vortex ‘pumping’ phenomenon.



**Figure 6-11** Measured average flame temperature varying with equivalence ratio at different heights of the flame (a) fibre 6 (b) fibre 5 (c) fibre 4 (d) fibre3

### 6.3.3. THERMAL BEHAVIOUR OF SIC FIBRE

#### 6.3.3.1. Radiation Loss Correction

The following describes the interoperation of the heat transfer mechanisms between the fibre and the gas surrounding it, and the procedure for estimating the heat transfer coefficient, based on the Nusselt number derived from a convective heat transfer correlation.

According to the literature survey [17, 65, 70] and the observation of the experiment, this is a classic heat transfer problem as the fibre is heated by its surrounding hot gas and cooled by radiation loss. As for the heat transfer mechanism along the fibre, the conduction loss or gain in the axial direction is negligible because the ratio of the circumferential to cross-sectional area is large; thus, the heat transfer rate by radiation and convection is much higher than the axial conduction heat transfer.

The gas temperature calculation can be obtained by

$$T_g = \frac{\varepsilon\sigma(T_f^4 - T_a^4)}{h} + T_f \quad (6.1)$$

Where  $T_g$ ,  $T_f$ , and  $T_a$  are the gas temperature, fibre temperature and ambient environment temperature respectively.  $\sigma$  is the Stefan-Boltzmann constant and  $\varepsilon$  is the fibre emissivity. The first term on the right-hand side represents the difference between the gas and the fibre temperature. In order to determine the temperature difference, the heat transfer coefficient  $h$  must be determined in advance by the equation given below

$$h = \frac{Nu * k_{gas}}{L_d} \quad (6.2)$$

Where  $k_{gas}$  is the gas thermal conductivity, and  $L_d$  is the fibre diameter. Nu denotes the Nusselt number. Review of previous research suggests multiple empirical Nusselt correlations that have been applied to similar experiments [17, 33, 65]; these empirical correlations are presented in Table 6-1.

**Table 6-1** Correlation of cross flow forced convection over cylinder

Authors	Empirical correlations	
Peter Struck[65]	$Nu = (0.42 \times Pr^{0.2}) + (0.57 \times Re^{0.5} \times Pr^{0.33})$	$Pr = 0.71, 0.01 \leq Re \leq 10,000$
Knudsen[72]	$Nu = C + Re^n Pr^{\frac{1}{3}}$	$C = 0.989, n = 0.330,$ $0.4 \leq Re \leq 4$
V.Vilimpoc[17]	$Nu = CRe^n$	$C = 0.800, n = 0.280$
Bin Ma[33]	$Nu = C \times Re^m \times Pr^{0.37}$	$C = 0.908, m = 0.280,$ $0.09 < Re < 1.$ $C = 0.902, m = 0.384,$ $1 < Re < 35.$

In the table  $Re$  and  $Pr$  are the Reynolds number and the Prandtl number respectively, which are defined by

$$Re = \frac{\rho V L_d}{\mu} \quad \text{and} \quad Pr = \frac{c_p \mu}{k} \quad (6.3)$$

Where  $\mu$  and  $c_p$  are the dynamic viscosity and the specific heat of the fluid.  $L_d$  is the fibre diameter, and  $V$  is the velocity of the fluid at the burner's nozzle, which is easy to obtain through the input volume rate of the fuel mixture.  $\rho$  is the density of the fluid. The determination of these fluid properties must be at the film temperature (average of the filament and gas temperature). Since the gas temperature is unknown, an iterative method has to be applied to the temperature correction.

The algorithm utilised to estimate the heat loss is reviewed below. The fibre temperature determined by the two-colour pyrometer is assumed to be the gas temperature. The mole fraction of major species concentration in the premixed flame is calculated via an adiabatic equilibrium chemical reaction at corresponding equivalence ratio in each case. Then the mole fraction based transport properties can be found and be used to calculate the  $Re$  number, and then determine the Nusselt number by the correlations listed in Table 6-1. Since the quantity required is the average heat transfer coefficient, in principle the average flame velocity passing through the fibre should be used to calculate the  $Re$  number; however, this velocity is hard to obtain owing to the fact that the extreme hot gas can easily melt the velocimetry used in the laboratory. Thus this flame velocity approximates to the average fluid velocity exiting the nozzle. This approximation may cause errors in the temperature correction. The betterment of flame velocity detection needs further investigation. Finally, once the  $Re$  Number is found, the average heat transfer rate can be computed and used to calculate the corrected  $T_g$  in Equation 6.1. The entire process is repeated twice to obtain a more accurate corrected temperature.

Figure 6-12 demonstrates that two iterative steps are effective in obtaining a converged flame temperature using the iteration method. Step 3 gives the corrected flame temperature at 1524.K, which is only 0.037K higher than the temperature obtained at the step 2. This difference is small enough to be discounted.

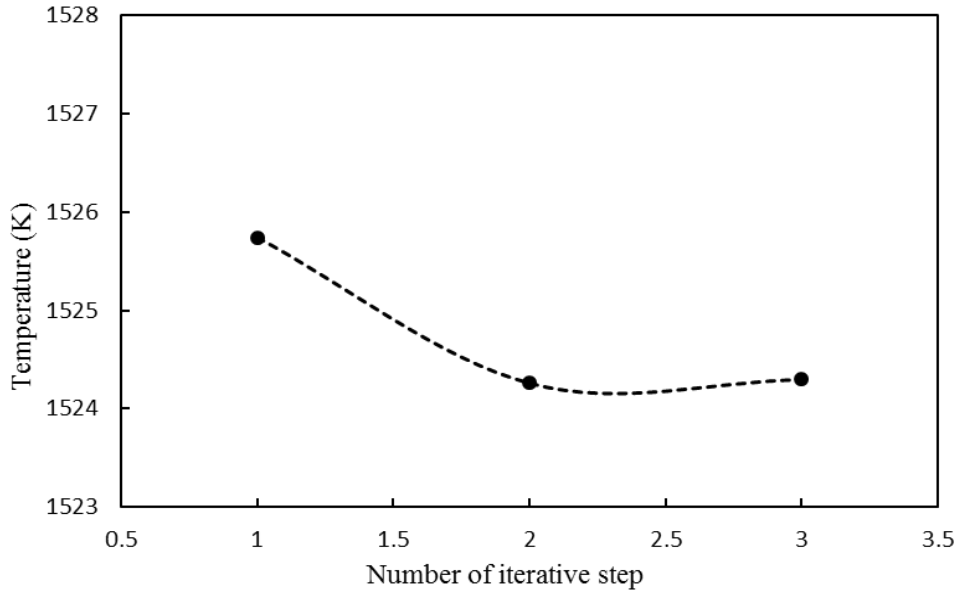


**Figure 6-12** Variation of corrected flame temperature

The aforementioned correlations in Table 6-1 have been implemented to estimate the flame temperature difference between the fibre and the flame temperature surrounding it in previous research. Thus it is important to know the variance in the corrected flame temperatures inferred using those empirical correlations. As shown in Figure 6-13, the correlation, used by V.Vilimpoc, giving the corrected flame temperature, is higher than the estimates by other correlations; in particular when the temperature is beyond 2000K, the temperature variance in comparison to other temperature profiles becomes obvious. The lowest flame temperature was found when using Knudsen proposed correlation. Two other corrected flame temperature profiles, using the correlations utilised by Peter Struck and Bin Ma, mostly coincide with each other. In addition, all corrected temperature profiles fall in the similar range when the temperature is below 1500K, meaning that the four correlations can give similar results at low temperature estimation.

In this study Struck's correlation is preferred in the estimation of the temperature difference because this correlation has a wider range of Reynold number, it can therefore well suit more various flow conditions.

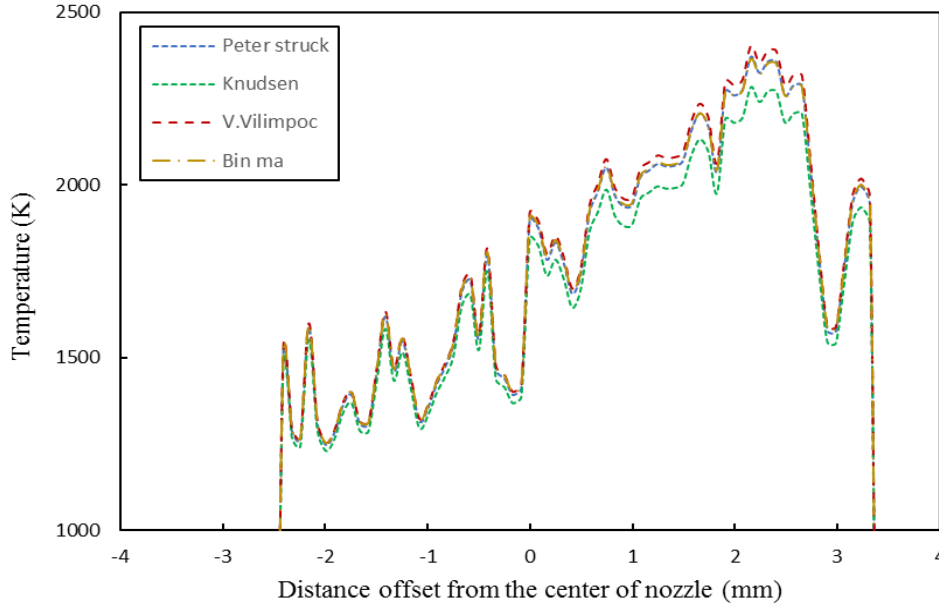


**Figure 6-13** Corrected flame temperatures based on the previous research proposed correlations

### 6.3.3.2. Variation of fibre temperature due to the change in fibre's diameter

Since the diameter of SiC fibre can be manufactured to a micrometre level without losing much strength in tension, it is desirable for Thin-Filament-Pyrometer use in order to detect hot gas temperature, and without seriously obstructing the flow of hot gas. Unlike the nanometre level of a single soot particle whose temperature can be approximated as the surrounding gas temperature, the temperature difference between the fibre and the hot gas is considerable; it is thus not negligible. Intuitively the temperature difference will increase along with increase in the diameter of the fibre; the corrected gas temperature, based on the temperature of the fibre with a larger diameter, could be lower than that based on a smaller diameter of the fibre, which means that the corrected gas temperature could be far away from the actual gas temperature when using a fibre with a relatively large diameter for hot gas temperature determination.

In order to understand the uncertainty arising from the variation of fibre diameter, four fibres different in diameter were prepared for temperature measurement. Then by comparing with each

fibre temperature, the trend of the fibre temperature variation can be revealed. Using the premixed  $\text{CH}_4$  +air flames at  $\Phi=1$  heats up the fibre, and in each test the fibre is placed at the same height in the flame. The experiment starts with the thinnest fibre ( $15\mu\text{m}$ ), and the fibre temperature is determined by the two-colour pyrometer. As shown in Figure 6-14, the intensity of illumination from the glowing fibre gradually subsides as the thickness of the fibre increases, which implies that the temperature of the fibre is also falling, because an increase in temperature of any grey-body is always accompanied by a stronger radiation which is easy to perceive by the naked eye.

In terms of temperature measurement, the pixels within the area of the glowing fibre are used for the determination of fibre temperature; the average fibre temperature is calculated using the average value of these pixels.



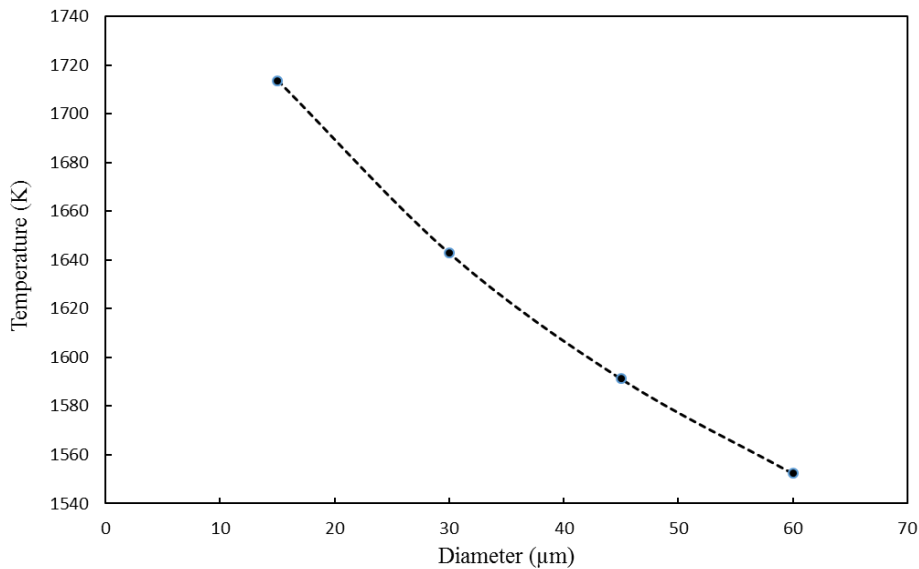
**Figure 6-14** Images of the glowing fibres with different diameters

Figure 6-15 gives the results of the average fibre temperature variation. The measured fibre temperature exhibits a decrease as fibre diameter increases from 15 to  $60\mu\text{m}$  with at intervals of  $15\mu\text{m}$ . This trend is identical with the observation of the change in fibre's illumination shown in Figure 6-14. Each point is an averaged value of 10 instantaneous samples which were captured

using fps 1/250s and shutter speed 1/104000s, with aperture number f /2.8; this camera setting allows elimination of the image saturation problem.

Table 6-2 shows the maximum fibre temperature difference hits 9.5% between the thinnest and the thickest fibres; the corrected gas temperature based on the thickest fibre shows the temperature difference of 4.1% compared to the corrected gas temperature based on the thinnest fibre. This means less impact on the determination of the gas temperature when changing the diameter of the fibre.

The manufacturer claims that the diameter of SiC fibre is 15 $\mu$ m with  $\pm 15\%$  tolerance. This diameter variance would not thus seriously affect the results of gas temperature measurement according to the experimental results shown in table 6-2.



**Figure 6-15** Fibre temperature varying with the fibre diameter

**Table 6-2** Variation of the fibre and the corrected gas temperatures

Fibre diameter( $\mu\text{m}$ )	Fibre Temperature(K)	Difference in Percentage	Gas Temperature(K)	Difference in Percentage
15	1718.0	0.0%	1793.9	0.0%
30	1650.0	4.0%	1766.9	1.5%
45	1590.0	7.5%	1732.6	3.4%
60	1555.0	9.5%	1719.7	4.1%

### 6.3.4. COMPARISON OF FIBRE TEMPERATURE MEASURED BY THE TWO-COLOUR METHOD AND THE INFRA-PYROMETER

#### 6.3.4.1. Introduction

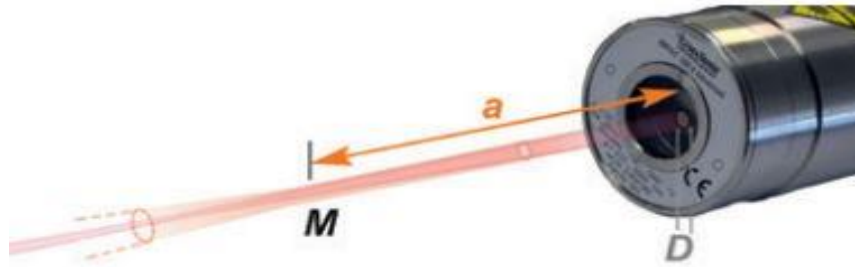
The previous section has quantitatively analysed the effect of the fibre thickness on the determination of the fibre temperature, and estimated the temperature variance between the fibre and its surrounding gas temperature. Prior to the determination of this variance, it is crucial to obtain the fibre temperature; the accuracy of the measured fibre temperature could directly affect the corrected gas temperature. For this reason, a temperature validation test was carried out to compare the fibre temperatures measured by an Infra-pyrometer IS5(MB25) and the two-colour pyrometer.

#### 6.3.4.2. Experimental Method

This comparison experiment used a stable Methane/Air premixed flame performed in a Bunsen burner as shown in Figure 6-3. Fibres were placed in the flame at different heights and hung tautly on a U-shaped frame. An IMPAC Infra-pyrometer was applied here to compare with the two-colour method. The Infra-pyrometer used is manufactured by LUMASENSE TECHNOLOGIES. This pyrometer can measure the temperature span from 800 to 2500°C, within 1% of measurement

reading uncertainty, its response time is less than 2ms and adjustable to an acquired time step. The material suitable for using this pyrometer includes metal, ceramics, graphite, and alloys [73].

Figure 6-16 is the sketch of the optical path of the Infra-pyrometer.  $D$  stands for the pyrometer aperture, and  $a$  represents the measuring distance between the object and the aperture.  $M$  denotes the spot size governing the area size of the object for temperature measurement, and it varies with change in measuring distance.

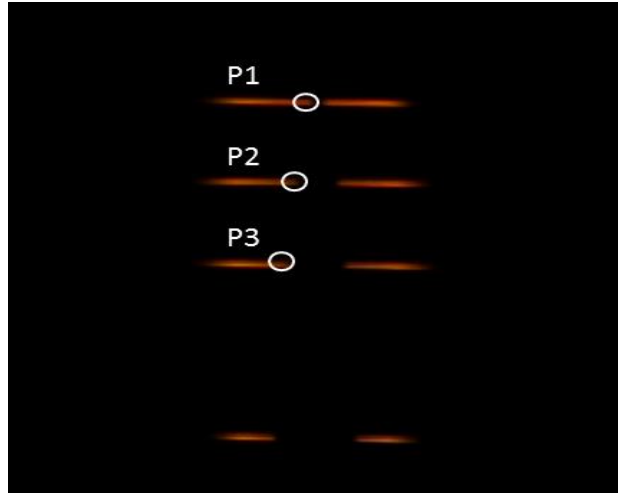


**Figure 6-16** Structure of the optical path of IMPAC IS 5

Table 6-3 reproduces the specification of the spot size against the measuring distance, quoted from the manual booklet. The spot size tends to increase with an increase of measuring distance. The measuring distance is around 500mm, corresponding to 2.4mm in spot size, and each millimetre corresponds to 8 pixels; Figure 6-17 indicates the selected places for the fibre temperature measurement, marked by white circles. These places near the flame front make an obvious point of comparison between the ways; the two kinds of pyrometer measure temperature at the same location.

**Table 6-3** Spot size in the corresponding measuring distance [73]

Measuring distance, a	Spot size M
220	1
300	1.4
500	2.4
800	4

**Figure 6-17** Points are selected in the temperature comparison experiment

### 6.3.4.3. Results and discussion

Figure 6-18 gives the results of measured fibre temperature, detected by the two-colour method and the Infra-pyrometer. These methods are both non-intrusive techniques and use the radiative emission of different wavelengths for temperature measurement. Unlike the Infra-pyrometer requiring the knowledge of emissivity of the target, the two-colour can measure temperature without knowing the emissivity and give 2D temperature measurement. The Figures (a), (b) and

(c) present the fibre temperature variation during 0.1s with an 0.015 secs interval at P1, P2 and P3 respectively. The overview of the results indicates that two temperature measurements both give a similar trend in the time-dependent temperature variation; but the fibre temperatures measured by two-colour method are all slightly higher than that detected by the Infra-system at those selected locations.

Regarding temperature variance between the two-colour and the Infra systems it was found that the maximum temperature difference of 6% occurred at location P1 which is close to the flame tip; in this area the frequent flame movement could easily lead to the partial misalignment of the measured spot area. At P2 and P3 the temperature variances decreased obviously, and were situated at 2.7% and 4.7% respectively, because at these locations flame movement is relatively steady in comparison with the movement at flame tip. In addition, the emissivity of the fibre is also a factor associated with the measurement uncertainty because the manufacturer does not claim that the emissivity can remain at 0.88 in wavelengths of the Infra-pyrometer operating spectral ranging from 800 to 1100nm.

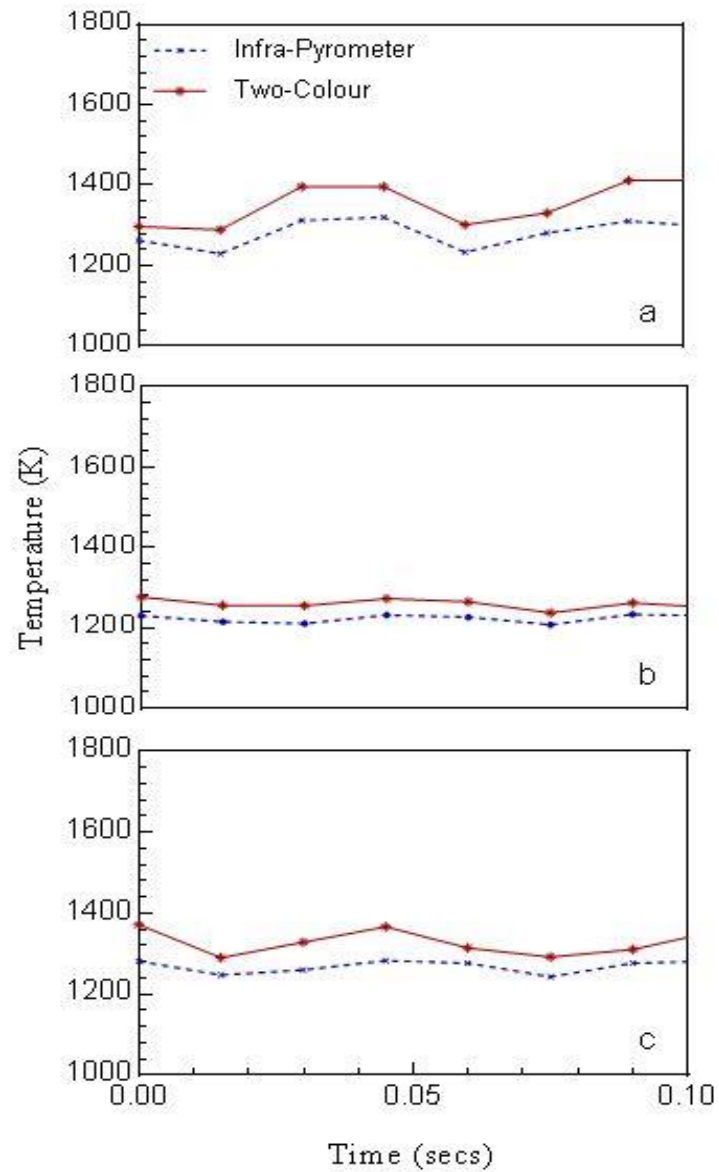


Figure 6-18 Time-varied fibre temperature variation

## **6.4. CASE 2: COMPARISON OF OSCILLATION FREQUENCY BETWEEN THE FLAME AND THE FIBRE EMISSION**

### **6.4.1. INTRODUCTION**

Flame oscillation frequency is one of the important and fundamental parameters in flame characteristics research; it is subject to the combustion of the fuel/air mixture ratio, as well as the configuration of combustion facilities.

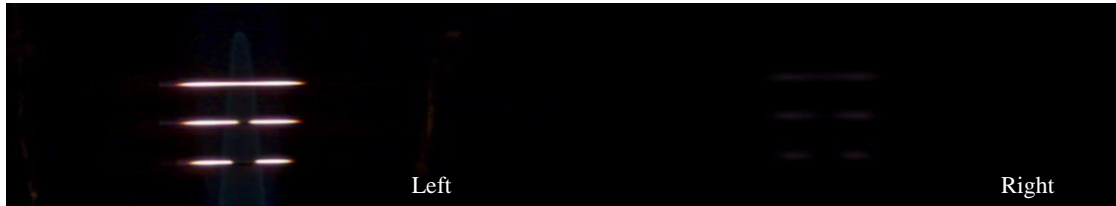
Thanks to the rapid development of high speed imaging system in recent decades, detection of flame frequency has become an easy task, irrespective of considering the limit of the performance of imaging systems. Having combined Fast Fourier Transform (FFT) method with a time series intensity fluctuation obtained from flame images, the flame frequency can be referred to the frequency of the intensity oscillation.

The objective of this section is to investigate the emission variation from the glowing fibre. Using FFT detects the frequency of this variation. Then this frequency will be compared to the frequency of the flame used to heat up the fibre. Prior to combustion, the fuel is mixed with air, at  $\Phi=1$  using a Bunsen burner; the complete configuration of the combustion system is shown in Figure 6-1, with SiC fibre mesh shown in Figure 6-6. The factors that could cause the change of the flame frequency are not considered in this study but will be left for the study in future.

### **6.4.2. RESULTS AND DISCUSSION**

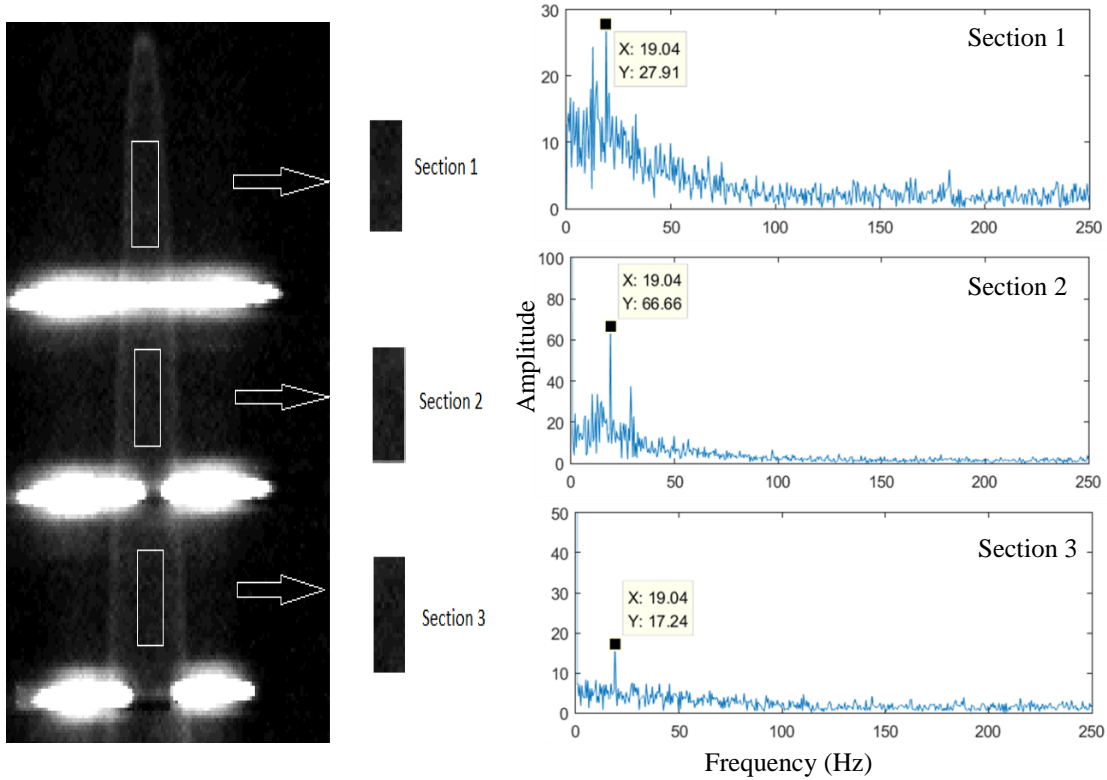
Figure 6-19 gives the flame image on the left side, and the fibre image on the right side filtered by a ND filter shown in Figure 6-4 (b). Both images are captured simultaneously, aided by a Stereo adapter shown in Figure 6-4 (a), and using fps 1/250s to avoid drop-off in flame signal. Despite a slight imaging angle difference between the two images, frequency calculations of the flame and fibre emission will not be influenced significantly. The left part of the image is for flame frequency

detection, without the ND filter; image saturation occurs within the area of the glowing fibre when using that fps. Thus it is not possible to obtain the fibre emission frequency from these saturated pixels. For this reason, the ND filter is fixed to one of the two entries of the adaptor to prevent pixel saturation. As evident in Figure 6-19 right part, the colouration of the fibres' illumination appears to be dark pink instead of bright white.



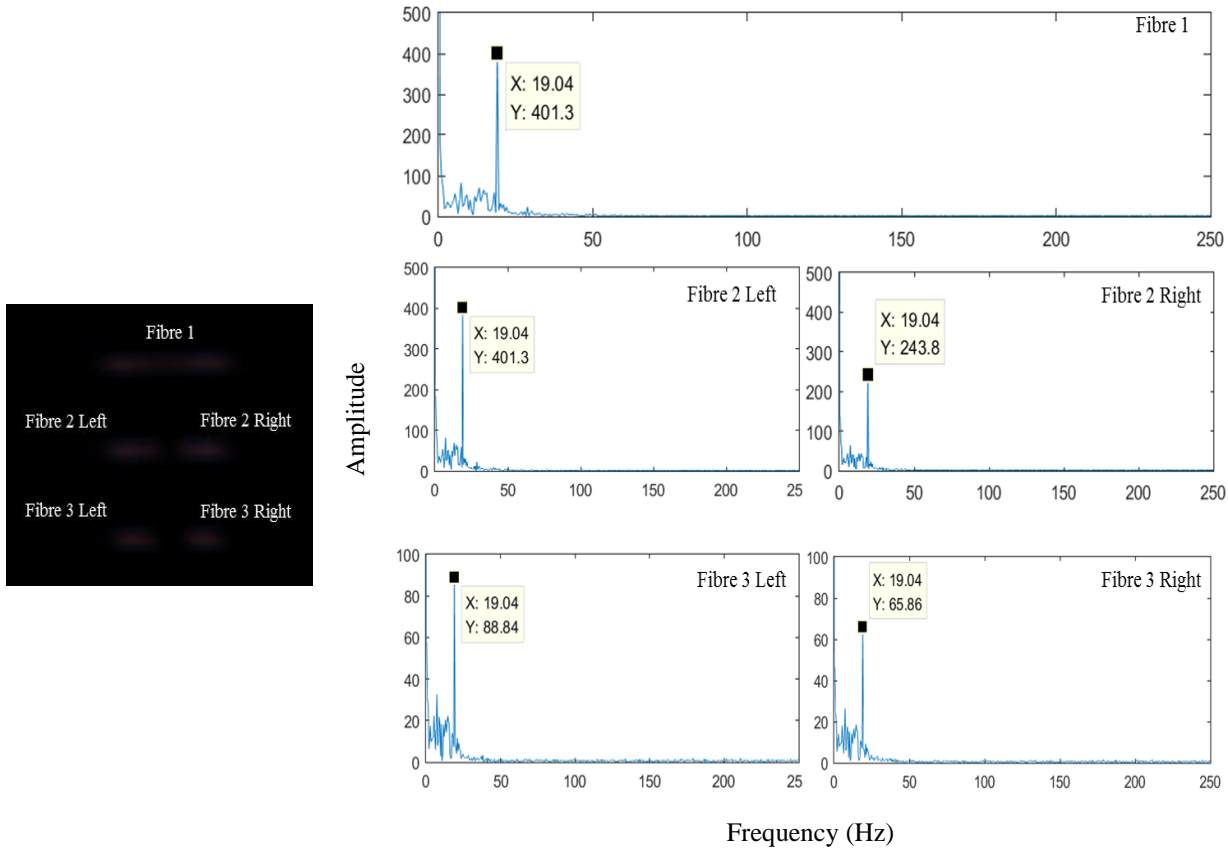
**Figure 6-19** Image of the flame and glowing fibres was captured using the high-speed camera with a stereo adaptor. The Left image is used for the detection of flame frequency, the right image is used for the calculation of the emission oscillation frequency of the fibres.

Figure 6-20 presents the result of the flame frequency at the corresponding section. Instead of detecting the global flame frequency, local flame frequency detection was carried out at the top, middle and near-base of the flame; at each position the detected section corresponds to  $10 \times 30$  pixels. Prior to the analysis of flame frequency, the captured colour images have to be converted into grey-level images to gain the flame intensity variation: a sample of which is shown in Figure 6-20 left side. The results of flame frequency detected from those sections are identical with each other, falling at 19.04Hz but with different amplitudes. The strongest intensity oscillation occurred in the middle section of the flame; its amplitude is nearly three times larger than that found both at the top section and the bottom section of the flame.



**Figure 6-20** Flame intensity oscillation frequency

Figure 6-21 shows the results of fibre emission oscillation frequency. Three fibres were placed in the flame at different heights. The observed emission from the fibres appears to be in five sections shown in Figure 6-21 left part. The frequencies obtained from these sections are shown on the right side. It can be noted that the fibre emission frequency matches the flame frequency exactly, situated at 19.04 Hz. This means that the variation of the fibre emission can vary instantly with the flame intensity at this frequency; this also implies that the fibre emission suits the use of the optical measurement to detect the flame temperature, because the change in the thermal condition instantly reflects on the fibre emission.



**Figure 6-21** Intensity oscillation frequency of the fibre emission

## 6.5. SUMMARY

$\beta$ -SiC fibre to the premixed flame temperature detection is an effective way to compensate the flame soot radiation and, combined with two-colour method leads to successful the premixed flame temperature measurement at the corresponding equivalence ratio. The main achievements and uncertainties in this investigation are concluded as follows:

- ❖ The mean temperature of the premixed  $\text{CH}_4$ +air flame has been determined at different equivalence ratio; the variation of this mean temperature, along with the equivalence ratio, mostly follows the theoretical trend in a bell-shaped curve.

- ❖ At  $\Phi=0.9, 1.0$  and  $1.1$ , flame temperature has been measured successfully in the form of one-dimensional distribution. The fast thermal response of SiC fibre allows the monitoring of any sudden change in flame temperature.
- ❖ The procedure of radiation loss correction has been discussed in detail. Fibre thickness induced temperature variation has been analysed quantitatively; the fibre manufacturer claimed the tolerance in diameter was negligible effect on the flame temperature measurement.
- ❖ In temperature validation test, the fibre temperature was measured both by a commercial Infra-pyrometer, and the two-colour pyrometer; both groups of measured temperature show good similarity. The cause of the difference between the groups is mainly correlated to two aspects: one is the misalignment induced temperature variance; another is the reliability of the manufacturer's claim of a fibre emissivity of  $0.88$  can remain constant in the operating wavelength of the Infra-pyrometer.
- ❖ Based on intensity fluctuation, the frequency of fibre emission matches the flame frequency exactly.

## **7. MEASURING TEMPERATURE OF A FLAME PROPAGATING THROUGH A QUARTZ TUBE**

### **7.1. INTRODUCTION AND BACKGROUND**

When a combustible gas is confined in a channel (tube), the flow caused by the thermal expansion of the gas in a combustion wave is constrained by the channel wall [74]. As a result, the flow is accelerated to much higher velocity than under circumstances of unrestricted expansion in an open flame such as Bunsen flame. The resulting flow acceleration of combustion products can generate pressure pulses induced by unsteady heat release; these pulses may coalesce into shock waves and give rise to detonation when travelling through unburned gas.

Deflagration is the subsonic mode of combustion, occurring at nearly constant pressure during chemical reactions. Contrary to deflagration, the mode of detonative combustion is characterized by supersonic propagation velocities [75]. Hence, the initial deflagration has to accelerate sufficiently to result in the formation of a detonation wave. Because of the complex interaction mechanisms the transition involved, from an ignition to detonation remains a challenging problem in combustion research [76]. A considerable number of different mechanisms have been proposed that may account for this transition: obstacles generating turbulent flames, cellular flames resulting from laminar instabilities, the interactions of shock wave, and acoustic flame instabilities [75]. The last of these mechanisms, acoustic flame instabilities, has been observed in tubes and are considered to be of significance in the spaces within being free of obstruction.

Investigating the research of flame propagations of flames in tubes can date back the onset of combustion research. In 1883 Mallard [77] firstly observed the flame propagation in tubes; experiments on flame in tubes continued in the following century. After nearly 50 years, Richard

Vernon Wheeler [78] utilised high speed imaging systems to capture the flame movement; the aim of his work was for its relevance to mine gas explosions in measurements of the laminar burning velocity. Guénoche [79] carried out further experimental studies within tubes to assess a series of phenomena to understand in-depth the process of non-steady flame propagation. Gaathaug [80] studied deflagration-to-detonation-transition in a tube; by placing one obstacle inside the tube this transition can thus be triggered. The resulting the onset of detonation always occurred at the walls in all experiments. Shen [81] used the premixed hydrogen- and propane-air flames in a tube to give a deep insight into the tulip distortion phenomenon; the results demonstrated that the pressure wave effect is an enhancement rather than a core factor, inciting the flame deformation, acceleration, and deceleration.

With the rapid development of computing power and imaging system in recent decades, numerical approaches become available for research into combustion mechanisms. Gonzalez [82] simulated the propagation of a premixed flame travelling through in a closed tube; a cellular structure of the flame front was observed in the final stage of the propagation, which is mainly correlated to the acoustic waves. Bychkov [83] validated the premixed flame acceleration mechanisms, proposed earlier by Clanet and Searby, using direct numerical simulations; both the theory and the simulation results are in good agreement. Yang [76] applied a DFCD ( Digital Flame Colour Discrimination) combustion quantification scheme, created by Huang [84], to a premixed propane-air flame for the detection of a two-dimensional equivalence ratio distribution along the flame surface area.

Even though extensive research has been on flame propagation carried out, flame temperature during the propagation in a confined space is still paid less attention. As well known, temperature is among the most frequently measured properties in combustion research, and it is a factor that correlates to the mean kinetic energy of the molecule of a substance. When heat is added to the substance, an increase occurs in the average kinetic energy; this energy increment will reflect on temperature by a corresponding increase. Flame propagation always involves the formation of

vortices or flow oscillation because of acoustic waves induced by unsteady pressure. The occurrence of unsteady pressure results from unsteady heat released from combustion; and unsteady heat can cause that flame temperature to vary accordingly. Hence, the flame oscillation induced by acoustic instabilities can be correlated to flame temperature variation.

Unlike previous research on open flame temperature detection, this chapter here extends the application of SiC fibre to flame propagation in tubes for flame temperature measurement. This is a new attempt using the optical method (SiC fibre based thin filament pyrometer) to detect the temperature of fast moving hot gas; similar investigations are scarce in the literature associated with flame propagation in a confined space.

The uniqueness of TFP used hereby is in having less-intrusive, fast-responding time, and in being easily set-up; and this technique has already been proved to be a useful approach to measuring open flame temperature in chapter 6. It provides a one-dimensional profile of temperature measurement along the length of the filament. Typically, TFP uses a  $\beta$ -SiC fibre of 15 $\mu\text{m}$  in diameter. It has good strength, relatively consistent emissivity in the visible wavelength band, resistance to oxidation with no catalytic effect, and it has a high melting point (3325K) claimed by manufacturer (COI, Ceramics).

During the tests SiC fibre is placed into a thermal environment heating up SiC fibre. Subsequently the fibre glows and emits nearly black body radiation, which is detected by an imaging system, and the determination of the fibre temperature is based on the two-colour method. Finally, this temperature is correlated to the local gas temperature through an energy balance correction.

This energy balance is an important step to determine the surrounding gas temperature. The difference between surrounding gas temperature and TFP determined temperature mainly depends on the accuracy of energy balance procedure. SiC fibre is typically considered as a stable emitter and fibre temperature is determined from the incandescence of the glowing fibre by using two-colour method. This technique needs pre-calibration on a known temperature source, typically a

tungsten lamp. Once this is done, it is free of further temperature calibration. In this chapter, TFP is applied to measure propagating flame temperature in an open-ended quartz tube. The variations of temperature and the hot gas velocity through the tube are both calculated. The main originality here is to explore the possibility of measuring fast developing hot gas by taking advantage of the good thermal properties of thin SiC fibre.

## 7.2. EXPERIMENTAL METHOD

### 7.2.1. EXPERIMENTAL INSTRUMENTS

The experimental apparatus used was originally designed and assembled by Cook [85] in 2008, shown in Figure 7-1. Subsequently, the improvement of this experimental rig, carried out by Mossa [86], includes a pressure indicator for the measurement of the vacuum pressure in the rig and a vacuum pump which is responsible for removing combustion product from the pipe after every test, shown in Figure 7-2.

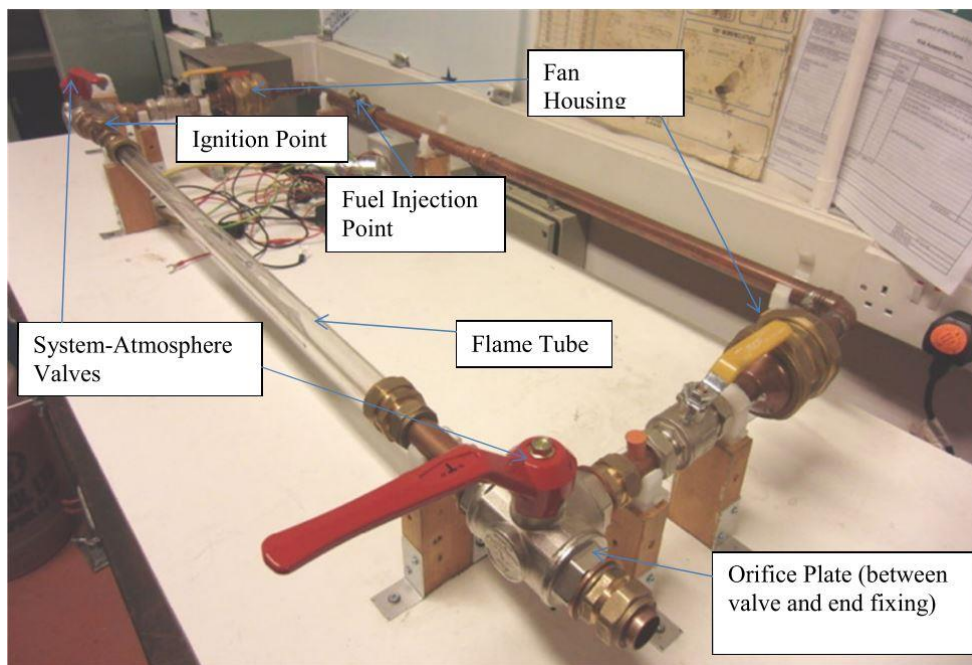


**Figure 7-1** Original experimental rig



**Figure 7-2** Experimental rig with the vacuum pump and pressure transducer

### 7.2.2. EXPERIMENTAL SETUP

As shown in Figure 7-3, the experimental rig consists of a tube of inner diameter of 20 mm and length 1200 mm; the central 700mm length of the tube is quartz providing optical access, opened at both ends (Figure 7-3). SiC fibres were placed at the mid-section and near both ends of the tube, the experiment was conducted at different equivalence ratios of 0.9, 1.0, 1.1 and 1.2. The required volume of methane at each equivalence ratio was measured and injected into the rig using a syringe. Two, standard 12V, 50mm computer cooling fans are in charge of combining the fuel/air mixture to create a homogeneous mixture. The pressure indicator installed on the rig is a Druck Digital pressure indicator type PDCR 810, with a pressure range of 1 bar, which is sufficient for monitoring air evacuation process from the rig, and can also provide the pressure reading inside the quartz tube during the flame propagation. Two three-way valves are fitted to both ends of the quartz tube, and are mainly used for evacuating air and also giving different tube configurations (both ends open

and closed). The study here adopts the tube configuration of both ends open, focusing on flame temperature variation during the transition from an ignition to deflagration.

The flame propagation was recorded using a variety of high speed imaging systems: a multi-colour PHOTRON SA-4 camera equipped with a Sigma EX DG 24-70 mm, f-2.8 zoom lens, framing rate 2000 fps and 1/300000 sec; and a mono-colour Phantom V210 framing at 2000 fps. The former has been used in previous the temperature calibration, and is dedicated here to tracking the glowing filaments during the propagation, for flame temperature calculation. The latter camera is only in charge of tracking the flame shape and its movement when travelling through the tube.

To prevent losing spatial resolution of the glowing fibre, neither imaging systems images all the fibres inside the tube in any single test; the cameras captured the glowing fibre and the flame propagation in sequence from the left-end to middle tube, and finally on the right. At each location, the colour imaging system was placed so as to provide a normal optical path for capturing the glowing fibre; an ultra-fast shutter speed of 1/300000s minimise the pixel saturation occurring within the glowing fibre. The mono-colour system was positioned next to the colour system with a tilted viewing angle to track flame shape during propagation, and was also used to determine the flame velocity. Combustion inside the tube was conducted at  $\Phi$  of 0.9, 1.0, 1.1 and 1.2; each test was carried out three time to ensure consistency.

Ignition was performed using a pilot flame, achieved by opening a port at the left end of the tube and directing the pilot flame into the tube to initiate the flame propagation. Ignition source has been found to considerably influence flame propagation in the tube; spark ignition intensifies the onset of flame oscillation [76]and so was not used here.

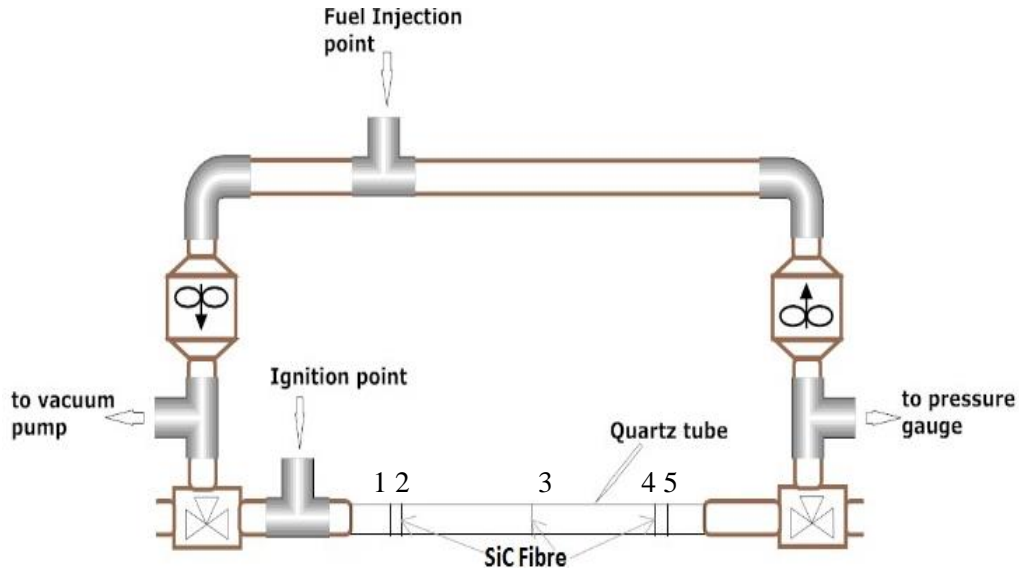


**Figure 7-3** Sketch of the experimental configuration for flame temperature measurement; there are two fibres were placed 5mm apart at each end of the tube and one in the tube middle.

## 7.3. RESULTS AND DISCUSSION

### 7.3.1. FLAME PROPAGATION ANALYSIS

#### 7.3.1.1. Flame Propagation

For  $\Phi=0.9, 1.0, 1.1$  and  $1.2$ , the flame shape variations at the three different locations of the tube has been traced successfully by the mono-colour imaging system, which are presented in Figures 7-4, 7-5, and 7-6.

Figure 7-4 presents the flame propagation through the left-end tube at different equivalence ratios during 0.09s. The ignition was conducted out-of-sight of the cameras with a gas lighter and its occurrence was not monitored, meaning that it was not straightforward to define a consistent time zero and the times used in the Figures relate to when the flame just appeared in the sight of the cameras rather than any specific event. The images of the flame propagation are all enhanced to

have a better visualization of the flame movement, achieved by the Phantom built-in software, and modulating its associated parameters including: Gamma, Brightness and Gain.

By observing the enhanced images illustrated in Figure 7-4, it was found that the flame travelled steadily through the distance in the sight of the camera without being affected by  $\Phi$  variation, and the flame front remained nearly constant when travelling across the fibres. This meant that the ultra-thin fibre would not cause any strong flow perturbation perceivable by human vision. On the other hand, no horizontal fluctuation of the fibre was observed, which remained almost still during the propagation.

Two glowing virtual fibres were occurred mainly due to reflection from the quartz tube. The mono-channel camera was placed next to the multi-colour imaging system that has priority so as to occupy the best position for a normal optical path between the fibre and the camera. At test  $\Phi=1.2$  shown in Figure 7-4 the fourth column from left-side, this tube reflection phenomenon was only occurred next to the first fibre, which the flame firstly passed through, as a result of having modulated the viewing angle of the lens and moving the camera closer to the subject.

The extent of the fibre glowing directly correlates with the amount of heat release from the combustion inside the tube. This emission gets intensified when the combustion becomes violent, implying more heat released in a unit time. The process of the glowing initiated at its middle position, and then intensified and expanded towards its both ends when flame travelled across it. This meant the temperature inside the flame was greater than that at the flame front, and decreased from the centre of flame towards the wall of the tube.

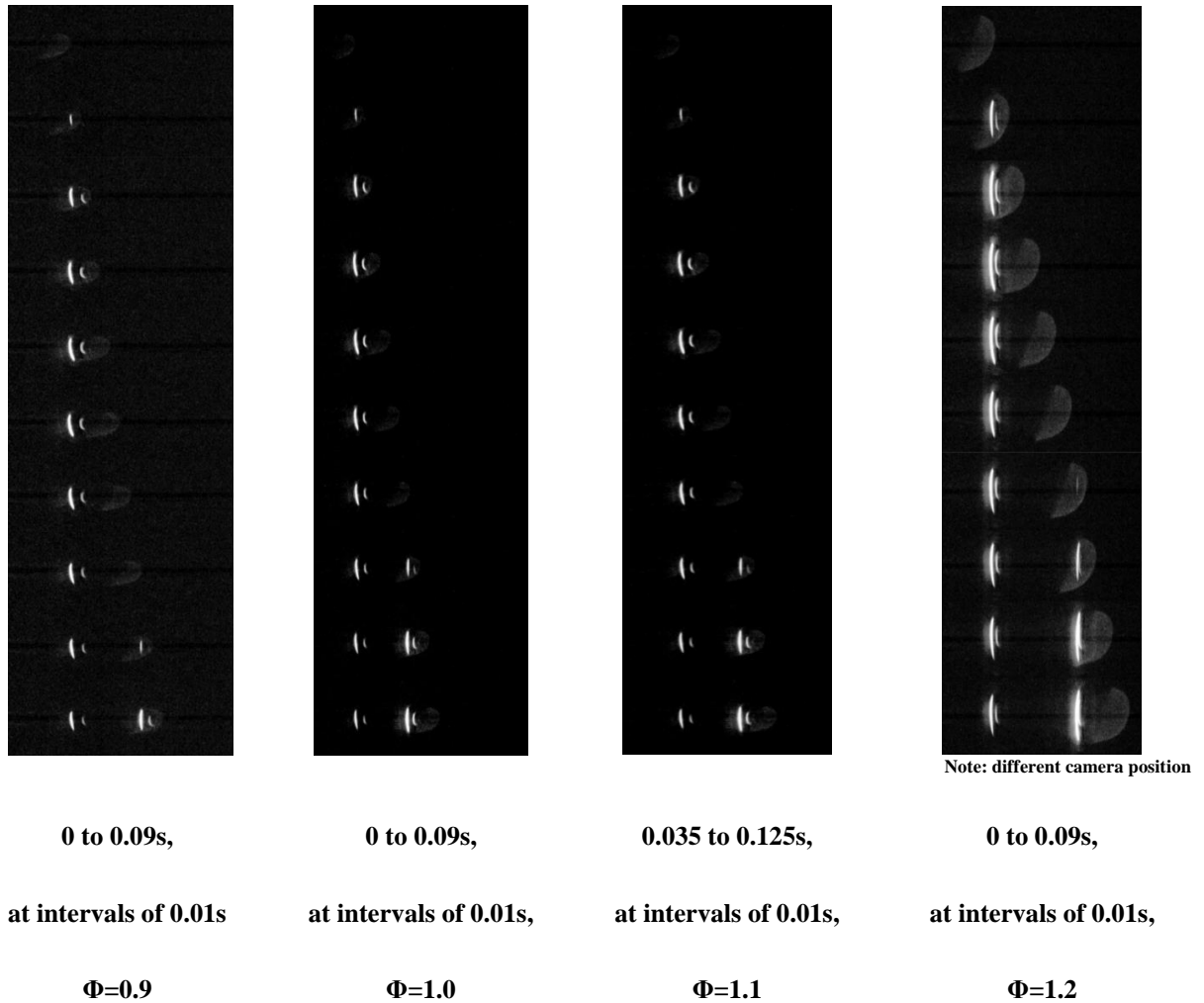


**Figure 7-4** Time history of the glowing fibres when flame flows across the fibres at the left-end of the tube.

Figure 7-5 illustrates four image columns of flame travelling through the tube middle section at  $\Phi$  of 0.9, 1.0, 1.1, and 1.2, respectively. At richest, leanest and stoichiometric conditions, the flame front all appeared to be a semi-spherical shape when travelling through the middle section.

From 0.1025s onwards at  $\Phi=1.1$ , the convex front of the flame in the centre part of the tube diameter tends to approximately planar at 0.1075s. Subsequently, at 0.1125s the area and the shape of the flame expanded and restored to a convex shape, respectively. In the latter part of the image sequence, both the flame shape and area were changing constantly during the flame moving forward; finally, at 0.1375s the flame front regained stability throughout the propagation. In the third frame

of the image sequence, two separated glowing fragments marked by white rectangle were occurred, indicating a sudden temperature drop between these two fragments. By carefully observing the second frame a tiny cusp was noted in the centre of the flame front and its tip towards the burned gas. This suggests the occurrence of hydrodynamic instabilities caused by a pressure gradient moving from unburned gas to burned gas [76]. On the other hand, it well demonstrates that SiC fibre has the ability to instantly respond to temperature change in its surrounding gas.

Bear in mind that this flame oscillation initiated prior to the flame approaching the fibre. This meant that the fibre was not the cause triggering the flow perturbation. On the contrary, the fibre remained still when flame moved throughout it. Interaction between the flow and the fibre is thus negligible.

At the final stage of the flame propagation shown in Figure 7-6, The presented image sequences were enhanced by a further amplification of the intensity of the flame illumination in comparison to the enhancement applied in the other two cases. It was found that a curved shape flame was maintained until the end of the propagation without any effect induced by changing equivalence ratio. Although the flame shape was still barely perceivable even after the special enhancement, the flame propagation was regarded as being steady state, because discontinuity of fibre illumination did not occur.

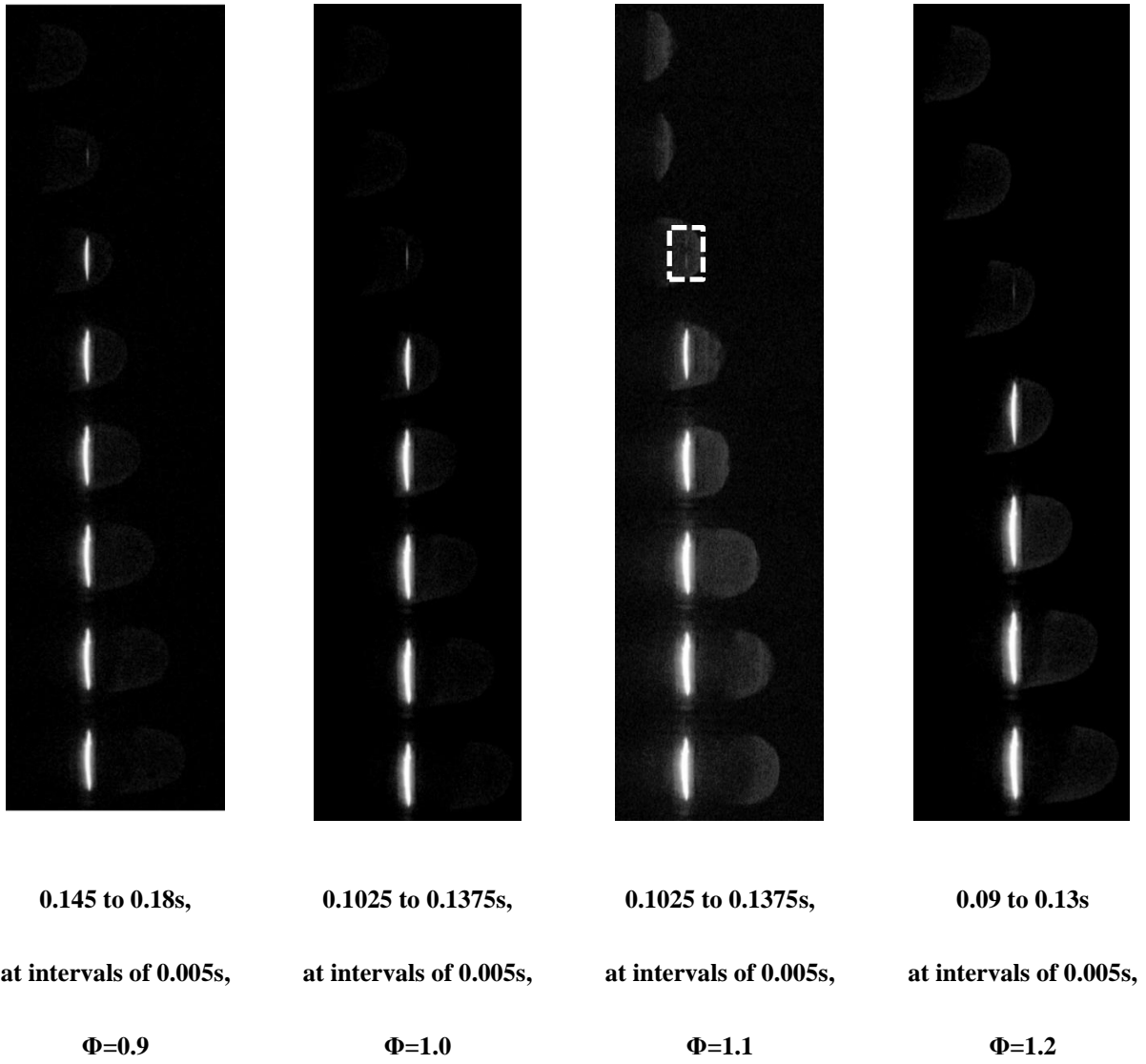


**Figure 7-5** Time history of the glowing fibres when flame flows across the fibres at the middle of the tube.

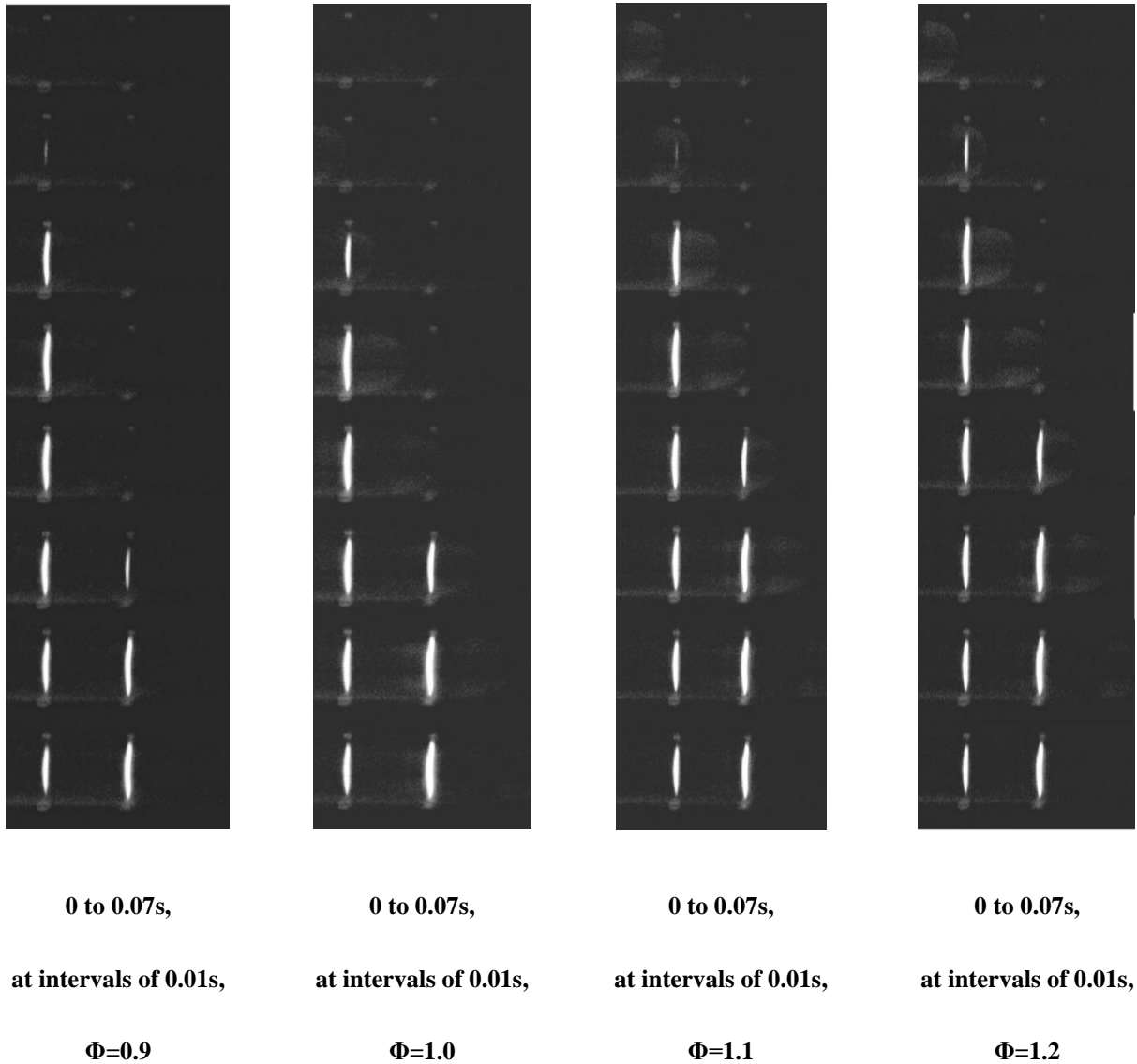


**Figure 7-6** Time history of the glowing fibres when flame flows across the fibres at the right-end of the tube. (Note: further image enhancement applied)

### 7.3.1.2. Flame Velocity

Flame travelling velocity is an important parameter for radiation loss correction. Reynold number is partially subjected to the flame velocity. Unlike the previous charter where flame velocity can could easily defined by the velocity of the flow leaving the nozzle exit, and assumed to be constantly travelling across pre-set fibres in section 6, here the determination of flame velocity is

based on imaging technique. At each end of the tube two fibres was installed. Along with the use of flame temperature calculation, the fibres were used to calculate the flame velocity. Knowing the time taken to both fibres be lit, and the distance between the two fibres the average flame velocity crossing these fibres can thus be estimated. As for the calculation of the velocity at the tube middle section, PCC software provided by the manufacturer of the PhantomV210 was used to trace the leading point of the flame front moving along this section; as a result, distance as a function of time was rendered by the software, and the slope of this function was accounted as the mean flame velocity. This velocity was applied in the heat loss correction.

The travelling velocity subjected to variation was found to highly correlate closely to equivalence ratio, which can be found in Figure 7-7. Equivalence ratio initiated at a fuel-lean condition ( $\Phi=0.9$ ), increasing to a fuel rich state ( $\Phi=1.2$ ) at intervals of 0.1. Each point was the average velocity of three samples. At  $\Phi=0.9$  the lowest flame velocity was occurred. Subsequently, the flame velocity increased with increasing equivalence ratio, peaked at  $\Phi=1.1$ ; then the flame velocity began to experience a reduction by  $\Phi=1.2$ . At each  $\Phi$ , flame travelling velocity always tends to accelerate from the left-end (next to ignition point) towards the right-end (close to the tube exit).

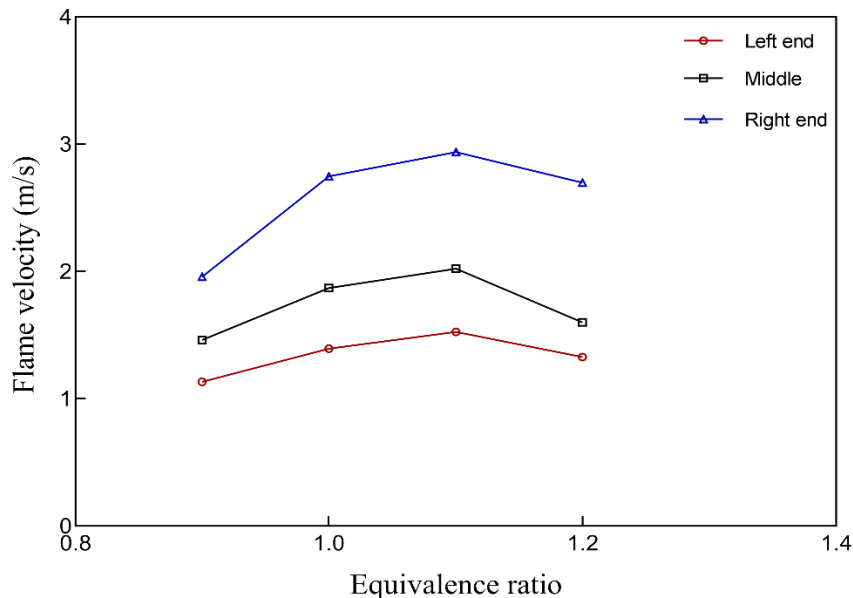


Figure 7-7 Flame propagation rate inside the tube

**7.3.1.3. Burning Rate of Methane/Air Mixture**

Too rich or lean mixture results in a reduction in the burning rate. A fast burning rate indicates that more amount of heat will be released from the exothermic reaction of mixtures in unit time. Leaner mixtures lead to less thermal energy being released, resulting in reduction of flame temperature. On the other hand, richer mixtures lead to incomplete combustion, also resulting in less thermal energy being released [87, 88].

Figure 7-8 shows burning rate of methane/air mixture. The results with respect to ‘present study’ were determined by Celestine [89]; his experiment of burning rate measurement was carried out using a flame tube rig with both ends open, identical to the rig used here. In this Figure his work is compared with the other results of burning rate obtained from literature. The burning rate of his study shows the same trend as the literature results, as well as maximum burning rates occurring all at 1.1 equivalence ratio. This may correlate with the occurrence of the highest flame temperature.

High temperature can further accelerate the gas expansion inside the tube, evident from the finding of peak flame traveling velocity at  $\Phi=1.1$ , shown in Figure 7-7.

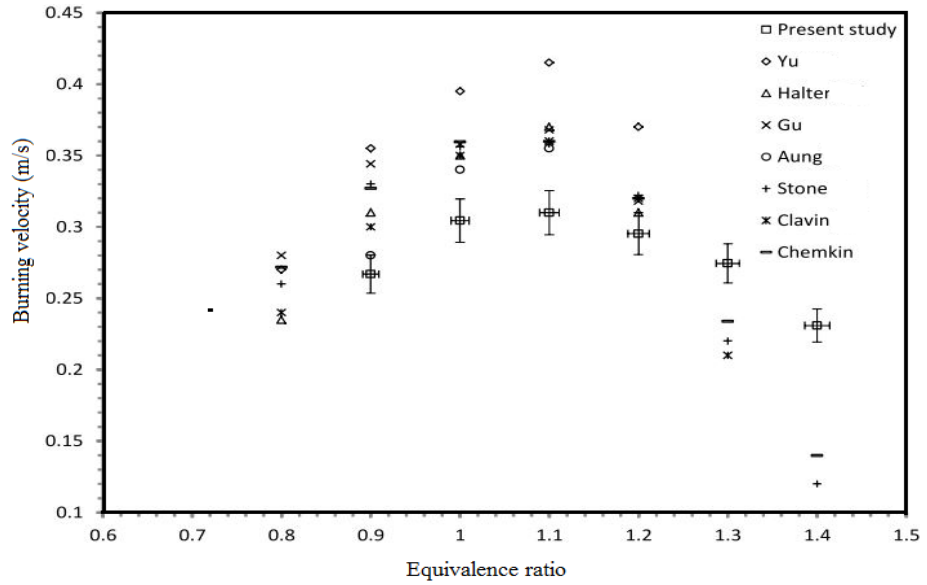


**Figure 7-8** Comparison of laminar burning rate of Methane/air mixture with other results [89]

#### 7.3.1.4. Fibre Intensity Analysis

The brightness of SiC fibre can correlate with the temperature of the hot gas surrounding the fibre; the time taken to reach the equilibrium thermal state between the fibre and its surrounding hot gas was found to be a few milliseconds by reference to the literature and the simulation made in the previous chapter. These properties give the potential to track flame oscillation induced by acoustic instability, by measuring the change in fibre illumination.

SiC fibre will begin to glow when the flame is moving over it, and then dim gradually after the flame leaves the fibre, which is a cycle of heat-up and cool-down. Figure 7-9 shows that the fibre intensity varying with the flame propagation during this cycle at different locations in the tube. This is achieved by summing up the grey-level of each pixel within the area of the glowing fibre as a total intensity; prior to the calculation of this total intensity the colour images of the glowing fibre will have been converted into grey images.

In each fibre that cycle lasted around 0.1s, and the peak total intensity found in each cycle occurred at  $\Phi=1.1$ , indicated by red circles. As shown by fibres 1, 2 and 3, the black triangles give the profile of the intensity variation at  $\Phi=1.2$ , and the peak intensity was less than that found at  $\Phi=1.1$ , indicating that less thermal energy was released as the mixture became richer; on the other hand, when the mixture became fuel-lean (from  $\Phi=1.0$  to 0.9) the total intensity also started to experience a reduction. However, near the tube outlet port, both fibres 4 and 5 yielded a similar trend; and in each of these, both intensity profiles at  $\Phi=1.0$  and 1.2 mostly coincided with each other.

At the tube middle section, it can be noted that the trend of the intensity profile ( $\Phi = 1.1$ ) tended to be jagged during the progress in cool-down stage. However, the other subplots experienced a relatively smooth transition from their peak intensity towards the level undetectable by the colour camera. This apparent intensity fluctuation signalled the existence of a stronger heat exchange between the burned and the unburned gases surrounding fibre 3.

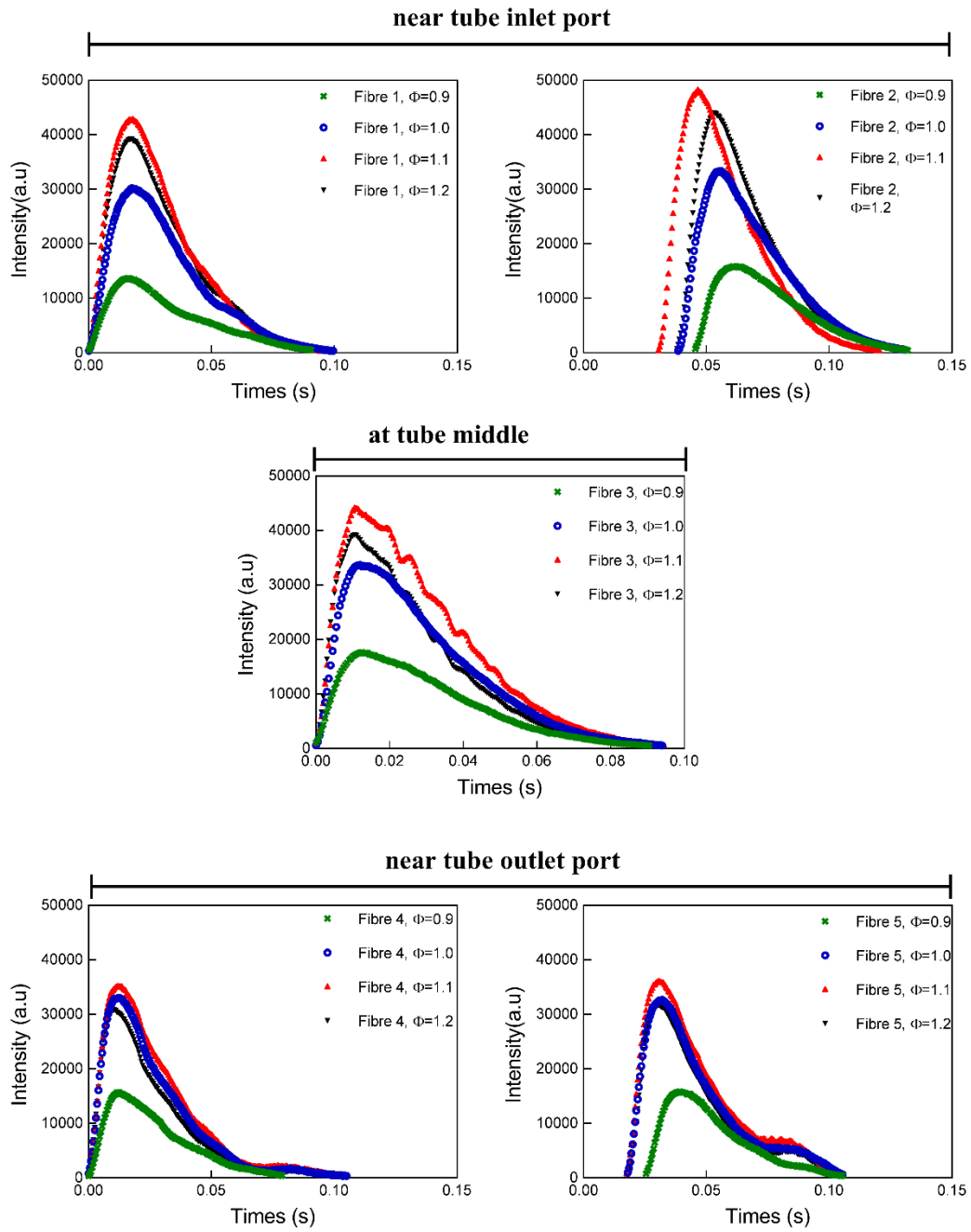
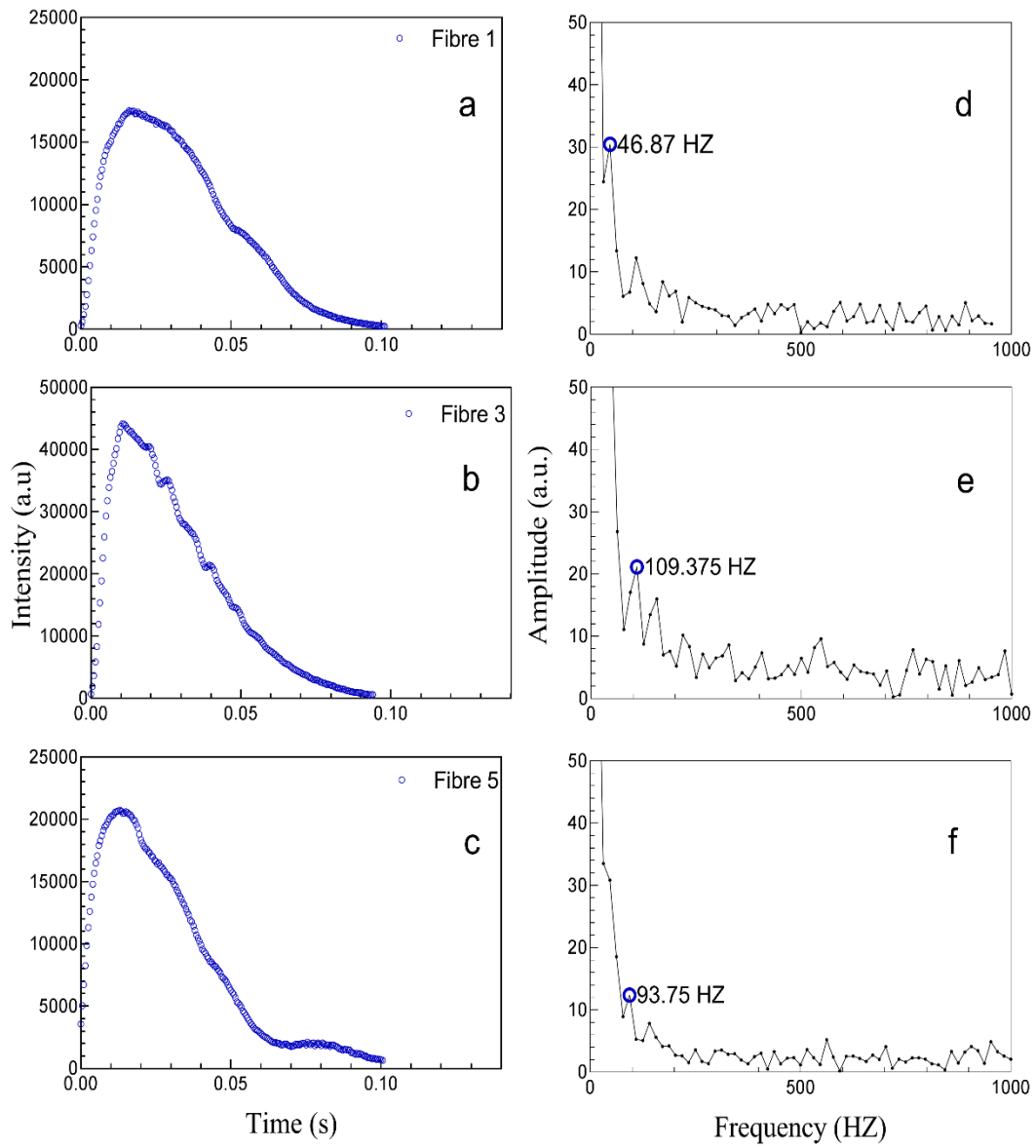


Figure 7-9 Transient fibre intensity variation

To determine the frequency of the intensity oscillation in the case of  $\Phi=1.1$  where the unstable flame movement was perceivable, FFT algorithm was applied to the data giving (a), (b) and (c) in left column of Figure 7-10. The results shown in the right column are the frequency of the intensity oscillation. With fibre 1 the frequency of the intensity oscillation was found to peak at 46.87 Hz shown in Figure 7-10 (d); The flame propagation was found to travel steadily throughout fibre 1, shown in the third image sequences of Figure 7-4. As the flame moved along the middle section and throughout fibre 3, the peak frequency was found to be 109.375 Hz, which is more than twice as high as the frequency shown in Figure 7-10 (d); meanwhile the movement of the flame exhibited a stronger oscillatory behaviour presented in Figure 7-5 in the case of  $\Phi=1.1$ . Finally, the frequency was reduced to 93.75 Hz when the flame approaches to the end of the propagation.

A time series plot of the pressure readings presented in Figure 7-11 describes how the pressure, within the tube, varied with the flame propagation throughout the complete tube. It shows that the maximum amplitude occurred around 0.2s. That was equivalent to the time took on the flame travelling from the tube inlet towards the middle section in the case of  $\Phi=1.1$ . This may explain why the perceivable flame oscillation occurred in the tube mid-section.



**Figure 7-10** Time-dependent fibre intensity variation at  $\Phi=1.1$ . (a), (b) and (c) Experimental heat-up and cool-down cycle at Left-end, Middle and Right-end of the tube. (d), (e) and (d) present the main frequency of intensity oscillation of corresponding fibres

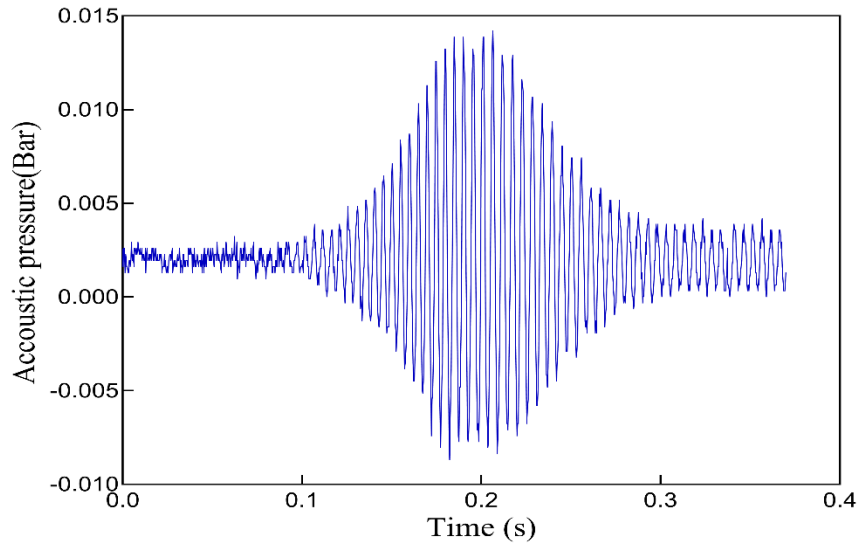


**Figure 7-11** The pressure readings inside the tube at  $\Phi= 1.1$

To summarize: SiC fibre is a material that can be used to quantify the flame characteristics associated with the oscillation induced by acoustic instabilities. The radiation emitted from this material was used to monitor the flame oscillation by tracking the resultant intensity variation of the glowing fibre. FFT algorithm was applied to the imaging data, giving the highest frequency of intensity oscillation as occurring in tube middle. Meanwhile at this location an obvious flow perturbation was also recorded by the mono-camera. The pressure gauge also detected an increased pressure amplitude when this flow perturbation was occurred.

### 7.3.2. FLAME TEMPERATURE

In order to determine the flame temperature in the form of one-dimensional distribution, the glow process of the fibre from the beginning to the end was imaged by the colour camera with 2000 fps and 1/300000s shutter speed. For  $\Phi$  of 0.9, 1.0, 1.1 and 1.2 the progression in fibre glowing in the tube middle section (the position of fibre 3) can be found in Figure 7-12.

The colouration of the fibre was observed to vary with the flame propagation. The first Figure in each image sequence shows a barely visible faint pink colour when the flame tip was just touching the corresponding fibre. This interaction is shown in monochrome in Figure 7-5. Subsequently, a wider glowing area occurred with a brighter yellowish colouration when the residual part of the flame front moved over this fibre. After the flame-front completely left the fibre, the burned gas entered a cool-down stage. As a result, the glowing area started to contract inwardly, and disappeared above the tube centre-axis (the white dot lines) of the tube. This meant a relatively high temperature concentrated in the field close to the top wall of the tube.

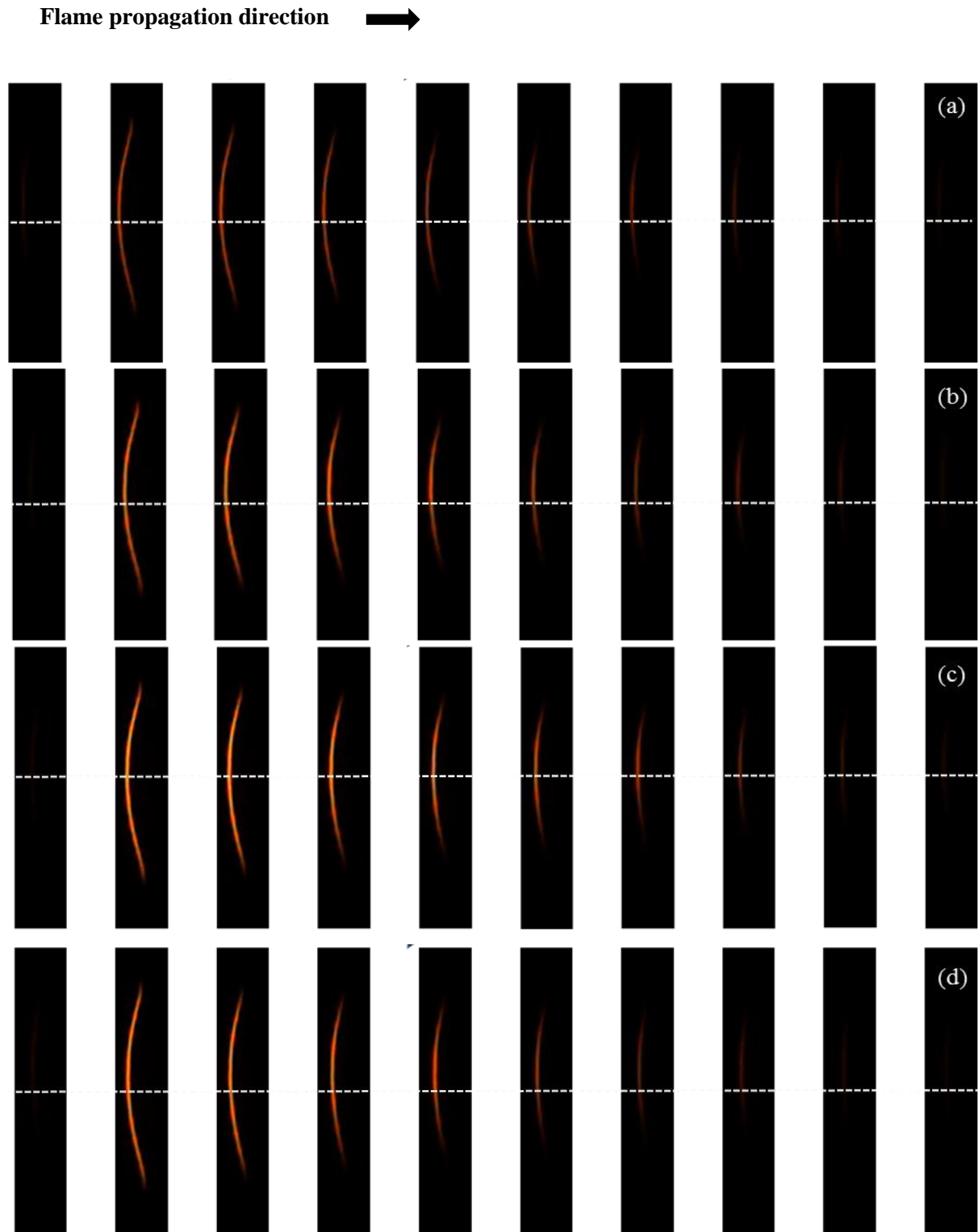


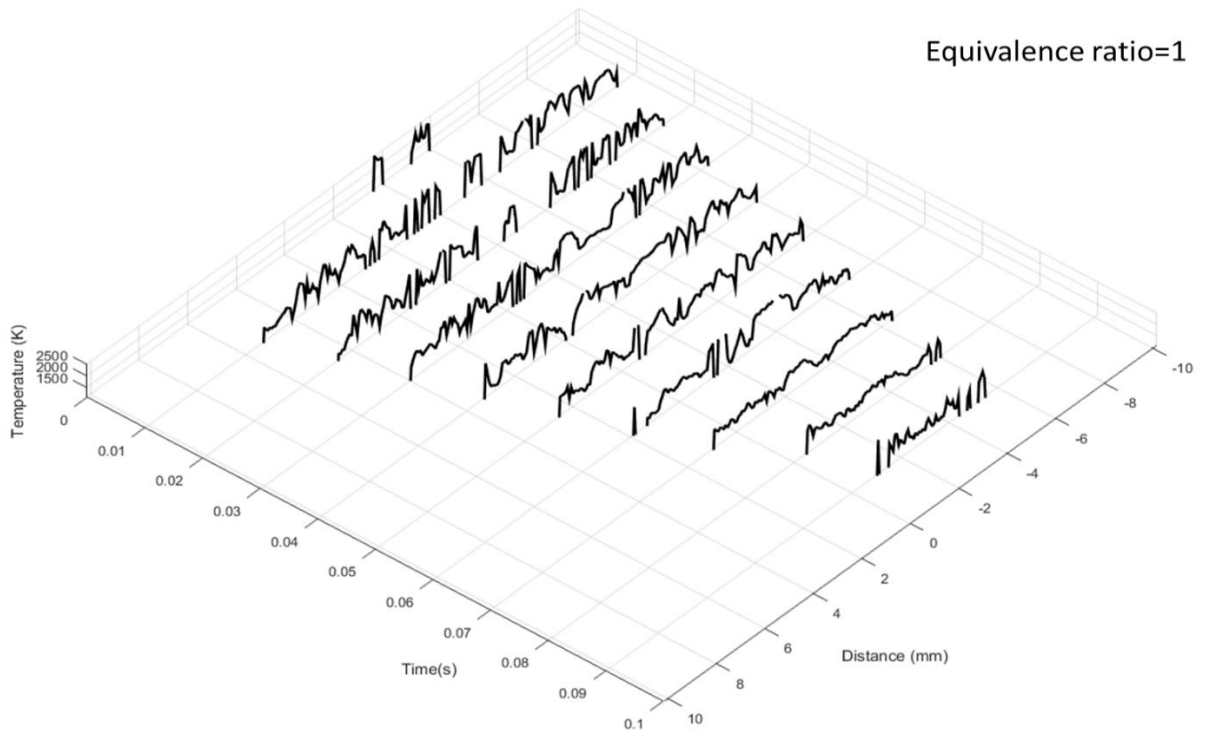
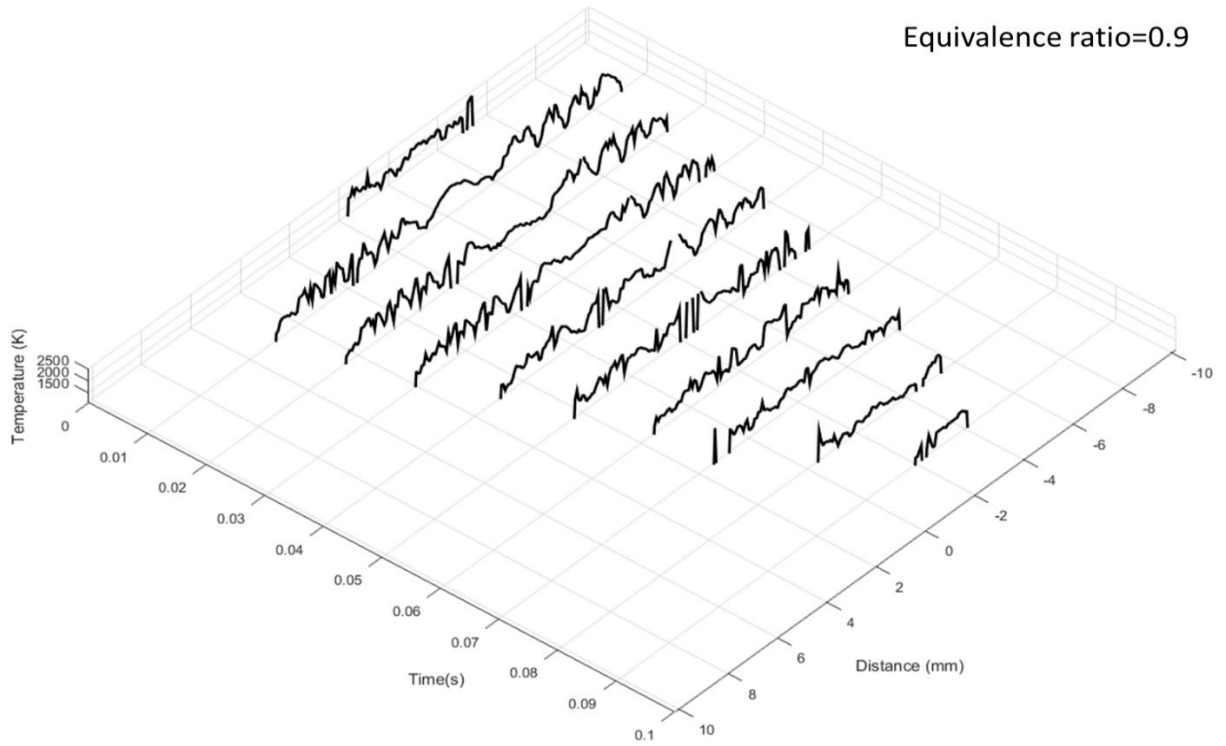
**Figure 7-12** Time history images of the glowing fibre placed at the middle of the tube during the flame propagation throughout it, the fuel/air mixture (a)  $\Phi=0.9$  (b)  $\Phi=1.0$  (c)  $\Phi=1.1$  (d)  $\Phi=1.2$ . Time interval between the images in each image sequence is 0.01s, the first image in each row counts as time=0.

The two-colour method was applied to these image sequences for visualization of the fibre temperature, executed using MATLAB with a self-written code. Once given fibre temperature, a heat loss correction was made to define flame temperature. This correction is an important step to make a bridge between the fibre and its surrounding gas temperature: the process of which involves solving the energy conservation equations on a fragment of the fibre. The detail of this correction has been fully provided in section 6.3.3.1.

The data presented in Figure 7-13 showed the results of time-varied corrected flame temperature distribution derived from the images of Figure 7-12. For  $\Phi=0.9$  in the period of the time from 0.01 to 0.03, the trend of each distribution tended to be more jagged at both ends than that in the middle. This meant a moderate temperature gradient in the centre of the flame and a considerable amount of heat exchanged with unburned gas at interface between the burned and the unburned gas. At the end of the cool-down stage (from 0.07 to 0.09s) the temperature oscillation tended to decrease.

Along with increasing equivalence ratio the flame velocity and heat release rate both tend to increase; the change in these factors could further enhance flame instabilities. Something which was found to be reflected in the flame temperature. For  $\Phi$  of 1.0, 1.1, and 1.2, at the early stage of the measurement, the discontinuity occurred in the temperature distribution, caused by the following factors: high temperature inciting an intensified emission from the fibre resulting in pixel saturation; acoustic wave inducing flow perturbation resulting in a sudden temperature drop by the unburned gas entering into the burned product. Again, at the end of the cool-down stage, all flame temperature fluctuations were reduced.

MEASURING TEMPERATURE OF A FLAME PROPAGATING THROUGH A QUARTZ TUBE



The figure will continue on next page

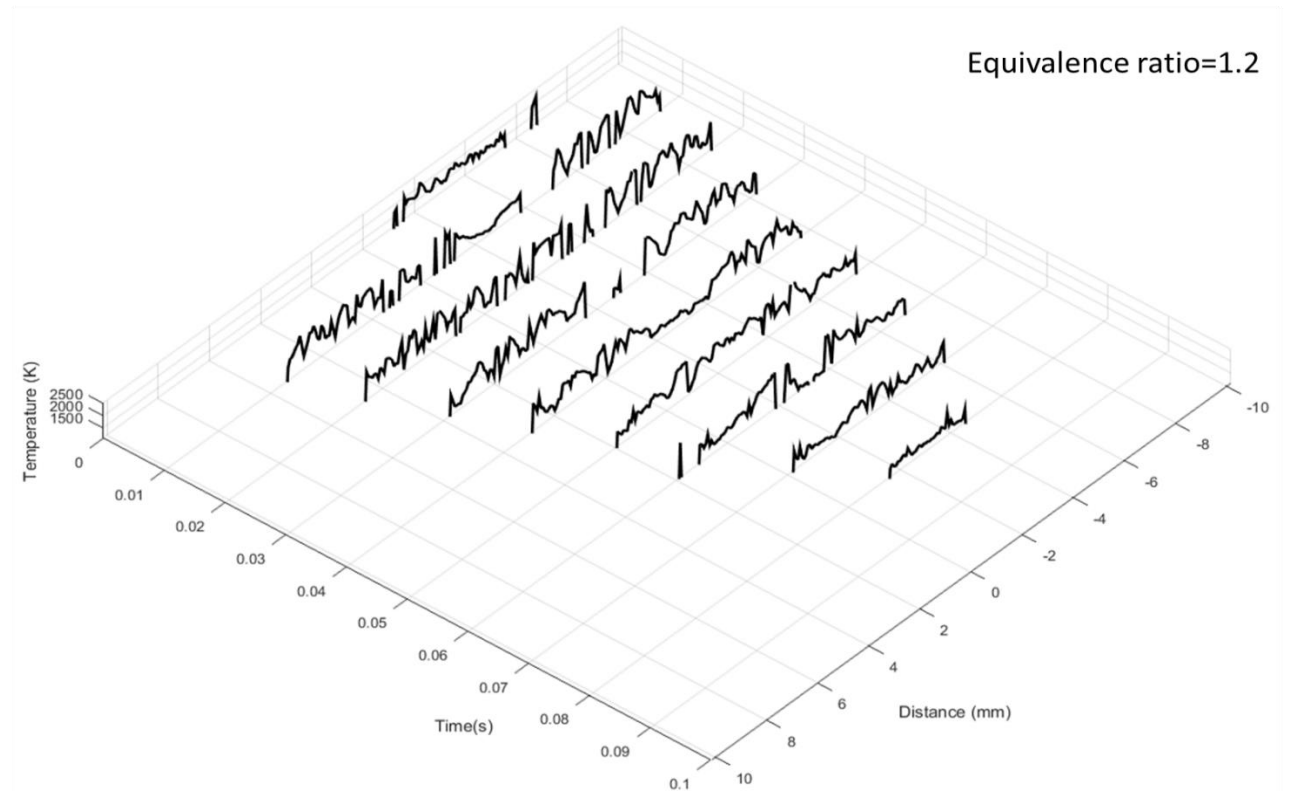
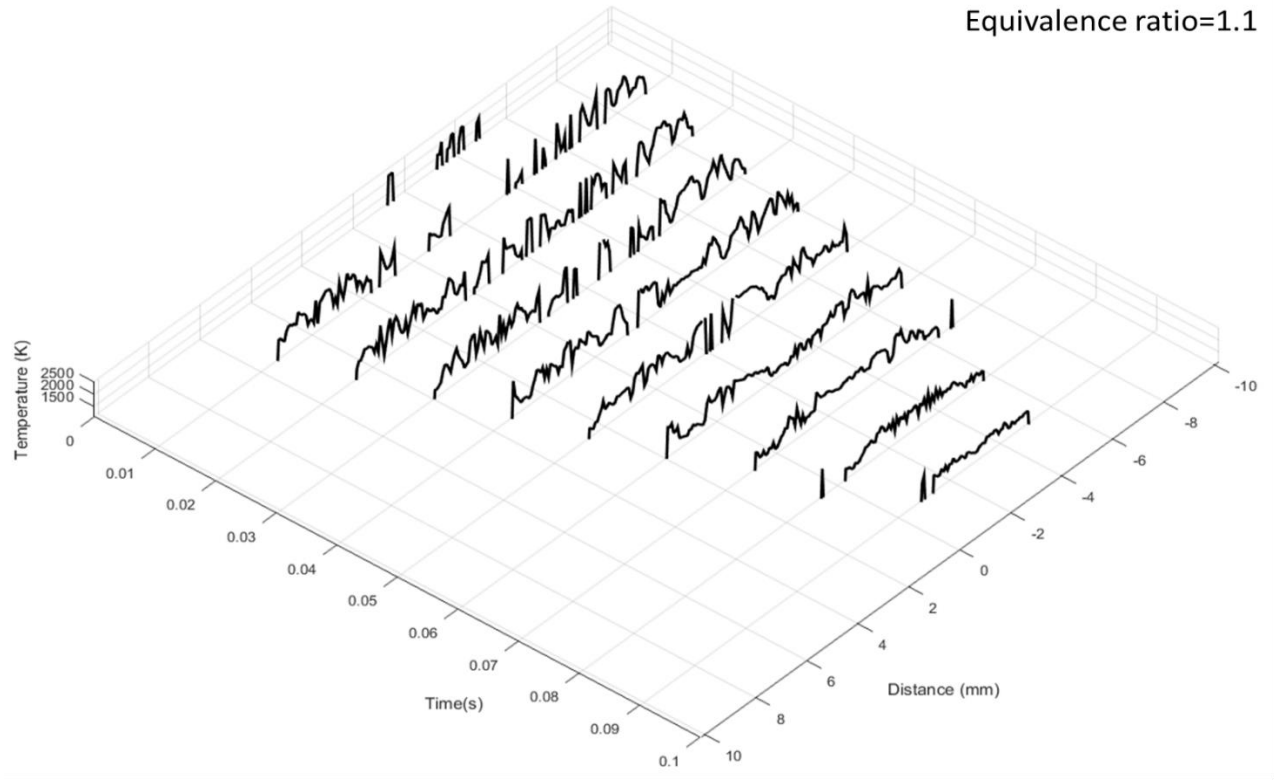


**Figure 7-13** Time-dependent flame temperature distribution, detected on fibre 3 (Tube middle)

To investigate how the flame temperature varies with the flame propagation throughout the full length of the tube, mean flame temperature was measured separately at the left-end, middle and right-end of the tube by averaging the corrected flame temperature along the length of the corresponding fibre, the results of which are shown in Figure 7-14.

The flame propagation developed initially from the left-end of the tube and firstly travelled throughout fibre 1, then crossing over fibre 2; the mean flame temperatures shown in Figure (a) derived from these two fibres exhibited a similar pattern in variation, however the trend of the mean temperature at fibre 2 tended to be more variable, signalling an increase in flame oscillation prior to approaching the middle section. In Figure (b) the temperature variation seemed to continue the pattern of the oscillation found in Figure (a), during the first 0.05s. Subsequently the mean temperature experienced a noticeable drop towards 1500K, and then peaked around 2400K in advance of the temperature becoming undetectable. This sudden change in temperature seems to mainly linked to the phenomenon of the flow perturbation shown in Figure 7-5. At the final stage of the propagation, the accumulated pressure in front of the flame tended to reduce because the flame approached the tube outlet port open to atmosphere; Both mean flame temperature variations in Figure (c) thus exhibited a relatively stable trend.

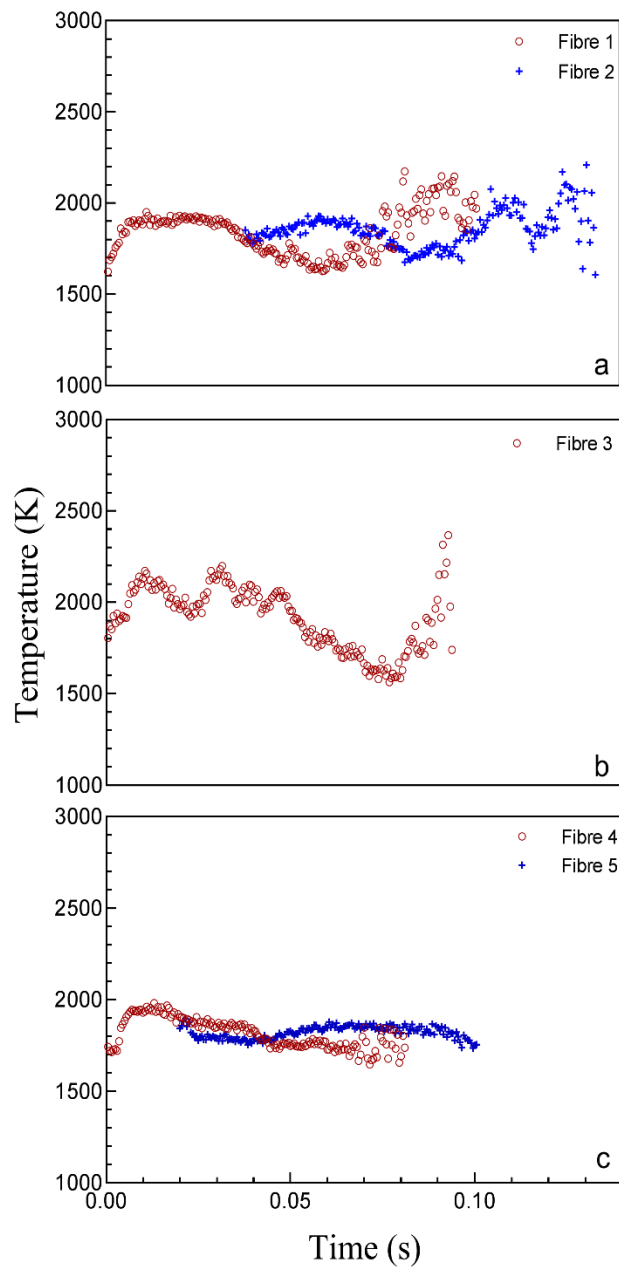


**Figure 7-14** Transient average flame temperature at different positions inside the tube; the fuel/air mixture at  $\Phi=1.1$ . (a) Tube inlet (b) In the middle of the tube (c) Tube exit

A plot of the correlation between flame temperature and equivalence ratio is shown in Figure 7-15. Blue dot lines stand for the fibre temperatures at different locations of the tube, and red solid lines are the flame temperature derived from those fibres. Each point represents the average temperature of 164 samples. As  $\Phi$  increases both the flame and the fibre temperatures tended to increase, and then peaked at  $\Phi=1.1$ , subsequently they began to decrease by  $\Phi=1.2$ . In addition, the flame temperature inside the tube was also subject to location within the tube. Irrespective of the mixture either in the lean or rich condition, the highest flame temperature always occurred in the middle section; the lowest temperature was found at the right-end next to the tube outlet port.

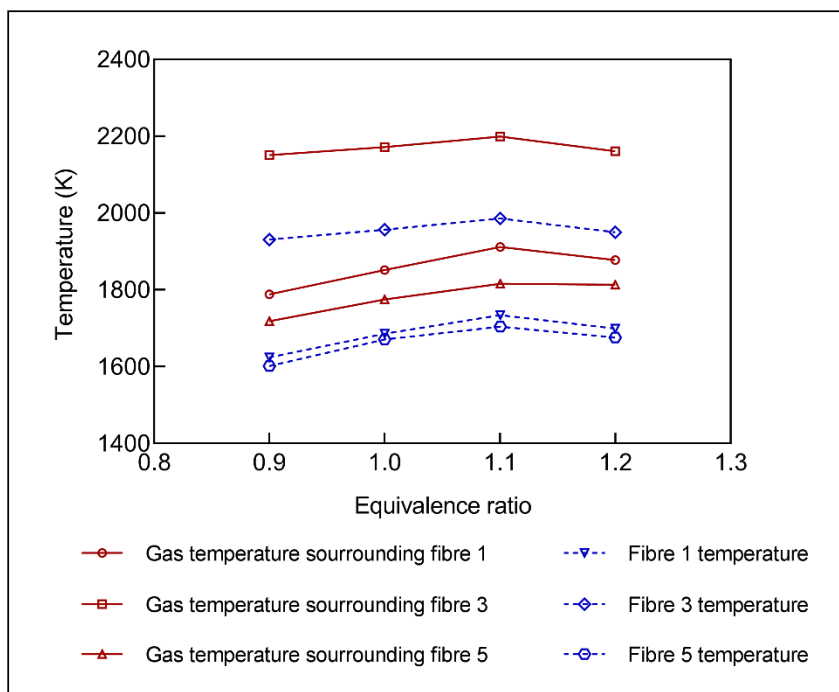


Figure 7-15 Corrected flame temperature

### 7.3.3. MEASUREMENT UNCERTAINTY

The heat loss correction between the fibre and its surrounding temperature is derived from the energy balance. This balance involves the convective heat transfer from the gas to the fibre, and heat loss via radiation from the fibre to its ambient environment. The conductive heat transfer along the fibre is discounted because it has a limited effect in the heat transfer process. Since the gas temperature is not directly measured, it is important to consider potential errors and their possible effect on the accuracy of the gas temperature measurement.

The main uncertainties with reference to gas temperature are in the calculation of the fibre temperature, the emissivity of the fibre, and the convective heat transfer coefficient. The heat coefficient comes from the  $Nu$  number correlation related to the diameter of the fibre. Furthermore, there are several sources of uncertainty remain in the determination of  $Nu$  number, Firstly, the correlation may not fully apply to the flow conditions used in the experiment. Secondly,  $Nu$  number needs the knowledge of  $Re$  number, which implies knowledge of the gas velocity perpendicular to the fibre. In this study, only the average velocity crossing the fibre was estimated by the imaging based techniques. On the other hand, the thermal properties of the gas are functions of temperature and gas composition, which are both estimated in this study. Regarding the other variables, the tolerance of the fibre diameter has been demonstrated to have less effect on temperature measurement in the previous section, but the emissivity depends on oxidation resistance and the roughness of the fibre which are probably varying in the high temperature environment.

Despite the quartz tube having a high transitivity according to the manufacturer. The question of whether or not the emission, in the two distinctive wavelength bands for temperature measurement, can be evenly filtered by the tube is still unanswered. Because of this, the resulting signal ratio of these two bands from the imaging system can be changed; this may lead to the calculated temperature deviating from its actual value.

## 7.4. SUMMARY

When flame passes along a tube that is open at both ends, a self-induced pressure oscillation is generated. Here ( $\Phi$  from 0.9 to 1.2) methane-air flames have been filmed moving along a 20mm internal diameter quartz tube. In the case of  $\Phi=1.1$ , the maximum pressure amplitude in the flame progress was observed when the flame propagated through the tube middle section. Then the amplitude decayed as the flame progressed towards the exit of the tube. As this maximum pressure amplitude occurred dramatic changes in the flame shape were observed; the original convex flame tended to flatness, and then gradually regained the semi-sphere shape after a few milliseconds, with the acceleration of the flame forward to the end section of the tube. Flame velocity and burning velocity both showed good agreement in trend as  $\Phi$  varied.

The impact of the pressure fluctuation on flame temperature was monitored by SiC based thin-filament pyrometer. SiC fibres were placed in the tube at the middle and both ends of this tube. The glowing fibre, varying with the surrounding thermal environment, was filmed by the colour imaging system when the flames passes through it. The captured grey-body emission from the fibre was used to determine flame temperature. As  $\Phi$  increased the average flame temperature tended to increase up to  $\Phi=1.1$ , then experienced a reduction by  $\Phi=1.2$ . Flame temperature fluctuation tended to be more violent near the wall of the tube. This was seen throughout the groups of one-dimensional flame temperature distribution in the tube middle. At this location the average flame temperature oscillated much more strongly than that found at either end. This can be regarded as a reaction to dramatic changes in the flame shape. The frequency of the emission intensity oscillation peaked at 109.375Hz, occurring in the middle section, meaning rapid changes in thermal environment. Finally, the major sources of uncertainty in gas temperature have been discussed. Based on results, TFP approach shows that it has the potential to track temperature variation in fast moving hot gas, and can also reflect the trend of the flame oscillation.

## 8. CONCLUSION AND RECOMMENDATIONS FOR FUTURE WORK

### 8.1. CONCLUSION

The following statements summarize the major findings from this research into the applications of the optical temperature measurement, and categorised into four sections including the temperature calibration of the optical measurement, droplet flame temperature detection, numerical study of SiC fibre, and temperature measurements on the Bunsen flame and the tube flame.

- ❖ A developed optical temperature measurement technique is proposed, which is based on the two-colour method and relies on the radiation from grey-body. Temperature calibration is compulsory to this technique prior to conducting any temperature measurement. The ratio between the R and the G channels of the high-speed imaging system was found to decrease monotonically along with temperature increase in the temperature calibration test. The obtained relationship between the RG ratio and temperature is the backbone of the proposed optical temperature measurement. By relying on this relationship, measured RG ratio from the grey body can be converted to the corresponding temperature well. The colour-banded filter was found to be an alternative technique, replacing the narrow-bandpass and beam splitting filtering method. In this way the time-consuming setup, high cost and, the problem of misalignment in the imaging processing can all be discounted. The peak spectrum response in these two channels was found to be at 580 and 630 nm in the spectrum response test of PHOTRON SA-4.
- ❖ In temperature validation, measured temperature of the tungsten filament, using the optical measurement operating at that two wavelengths, show good agreement with the reference

temperature (a pre-calibrated tungsten lamp). The parameters including the focal-length, the length of the optical path and exposure time are regarded as having less effect on the temperature measurement.

- ❖ High speed imaging system was demonstrated as an effective technique to investigate droplet fuel combustion. In the case of diesel-in-water emulsion combustion, the high imaging system imaged the secondary atomization during the combustion of fuel emulsion successfully. The distinct micro-explosion occurred only in the case of 30% water-content in diesel, and instantly followed by flame extinction with a distinctive popping sound. The lifetime of combustion of fuel emulsion droplet is mostly proportional to the water-content in the emulsion.
- ❖ Droplet flame illumination was found to intensify as the disruptive burning occurred. This burning was exacerbated by adding more water into the droplet. As the water-content approached a critical amount (30%), the most violent disruptive burning was found along with the strongest flame illumination. However once past this critical level the droplet struggled to be ignited by a pilot flame torch.
- ❖ Measurement of droplet flame temperature record exhibited a strong oscillation at the early stage of combustion. The normalized period of this oscillation was found to extend along with the water-content increasing in the fuel emulsion. The colour-map visualises how flame temperature distributes along the flame surface area during the state of the disruptive burning, and makes clear the high temperature which always surrounds the burning sub-droplets induced by secondary atomization. Thus this atomization seems to be an efficient way of generating better fuel/air mixtures, in order to a high degree of premixed combustion.
- ❖ The explicit based finite difference method has been carried out to simulate the fibre temperature variations, caused by the factors associated with the size of the fibre diameter,

the fibre ambient temperature, the heat transfer coefficient variations, and the flame instability caused temperature oscillation.

- ❖ Based on the results from the numerical solution, the increase in SiC fibre diameter can prevent the occurrence of fast heat dissipation. Meanwhile, the induced side effects such as the disturbances of the flame chemical reactions and the flow of the hot gas are not avoidable. The temperature difference between the fibre and its surrounding hot gas tends to increase along with increasing fibre diameter. Similar matching result was also found in the experimental study presented in chapter 6.
- ❖ The ambient temperature variation can significantly influence the fibre converging time. A higher heat transfer coefficient can cause fast heat dissipation that is instrumental in reducing the time taken to reach the steady-state in the stratified region, however it has the potential to reduce the fibre temperature at the flame outer boundary layer. The temperature difference between the fibre and the flame can be further enlarged. In addition, the fibre shows good ability to rapidly reflect the flame instability induced flame temperature oscillation. As a result, the two-colour method can thus detect this oscillation by monitoring the fibre temperature variation.
- ❖ The mesh density of 500 elements was found to be able to yield a converged numerical solution, with the low level of the round-off error

- ❖ At first, SiC fibre was used for the temperature measurement in a methane/air flame using a Bunsen burner. The flame frequency was found to be identical with the frequency of fibre illumination based on the image grey-level fluctuation. Gas-phase temperature tends to increase from the base of the conical flame towards the flame tip, subsequently experiencing a reduction in the field above the tip. Flame temperature fluctuation also increases along with the increasing height from the flame base. A plot of the relationship between the mean flame temperature and equivalence ratio shows a bell-shaped curve. The fibre temperatures measured by the two-colour and the infra-pyrometer show an average variance of 4.46%.
- ❖ As the fibre thickness increases, the measured fibre temperature was found to decrease. A plot of the fibre thickness against this measured temperature gives a nearly linear decreasing trend. The derived flame temperature reduced less than the fibre temperature after heat loss correction.
- ❖ As a further application of the optical pyrometer in this study, SiC fibre based two-colour pyrometer successfully detected the temperature of the flame propagating through an open-ended quartz tube with both ends open. Flame temperature was found to vary with equivalence ratio. At  $\Phi=1.1$  the maximum temperature was found at the middle section of the tube. Meanwhile, flame shape exhibited a violent oscillation, which did not occur at other equivalence ratios. The amplitude of the pressure in the middle section was also found to increase suddenly at  $\Phi=1.1$ . This may explain the instability of the flame shape. Near the ignition point flame temperature was found to be higher than that at tube outlet, and the temperature detected in the middle section was always higher than at either ends of the tube, irrespective of the change in equivalence ratio.
- ❖ Flow perturbation occurred in the middle section and decayed towards either ends. This trend was also reflected in temperature variations within the tube. It was found that the detected flame temperature varied weakly close to the tube ends, but in the middle section

## CONCLUSION AND RECOMMENDATIONS FOR FUTURE WORK

the profile of flame temperature exhibited a sinusoid variation with larger amplitude. This meant that the temperature oscillation in the middle section was much stronger than at the tube ends. The burning rate and the flame temperature both varied with equivalence ratio in a similar trend.

## 8.2. AREAS OF FUTURE WORK

The suggestions for future work are summarized as follows:

- ❖ On the temperature calibration side, a computer controlled power supply is desirable to power the pre-calibrated tungsten lamp instead of using a car battery. A more accurate and stable current will tend to produce a stable irradiance of the lamp at the corresponding temperature.
- ❖ A blackbody source cavity is recommended for use in the temperature calibration ranging from 773 to 1273K. It would be desirable to have a wider detectable temperature range in the optical pyrometer. Background noise must be assessed because of a relatively long exposure time and the utilised imaging system having a high ISO 4500 sensitivity.
- ❖ A radiator system using liquid nitrogen would be preferred for cooling the CMOS sensor of the high-speed imaging system, which would be an effective way to reduce the dark noise. This can reduce the possibility of the occurrence of noise ratio equivalent temperature during the temperature measurement. On the other hand, the generation of dark noise at different framing rate is recommended to be investigated. This will give further insight when choosing the camera imaging setting.
- ❖ A better technique is needed for pin-pointing actual velocity of the flow crossing over the fibre, instead of using average flame velocity in the heat loss correction. This would be instrumental in improving the accuracy of the proposed optical temperature measurement.
- ❖ Flame propagation in a tube with only one end closed is of interest. This configuration will lead to a quicker flame travelling velocity and a more violent combustion. Whether or not the current SiC fibre based measurement is capable of measuring flame temperature in a harsher environment will be answered by proposed tests.
- ❖ Future improvement of the proposed SiC fibre based two-colour pyrometer would be to realise two-dimensional temperature distribution. A possible route for this is shown in

Figure 8-1. As hot gas flows throughout the metal ring, the rotating fibre starts to glow at a certain angular velocity. The imaging system will give a gas temperature profile shown in Figure (A). This angular velocity is adjustable by an electric motor. As the velocity reaches a critical level, a plane temperature distribution should be formed. The time taken to give this plane distribution is subject to how fast the metal ring can rotate through a 180 degree; the faster the angular velocity of ring rotating, the shorter response time of the system. This main advantage of this design is capable of giving a plane of time-varied temperature distribution. The heat loss related problem due to the movement of the fibre must also be left for future work.

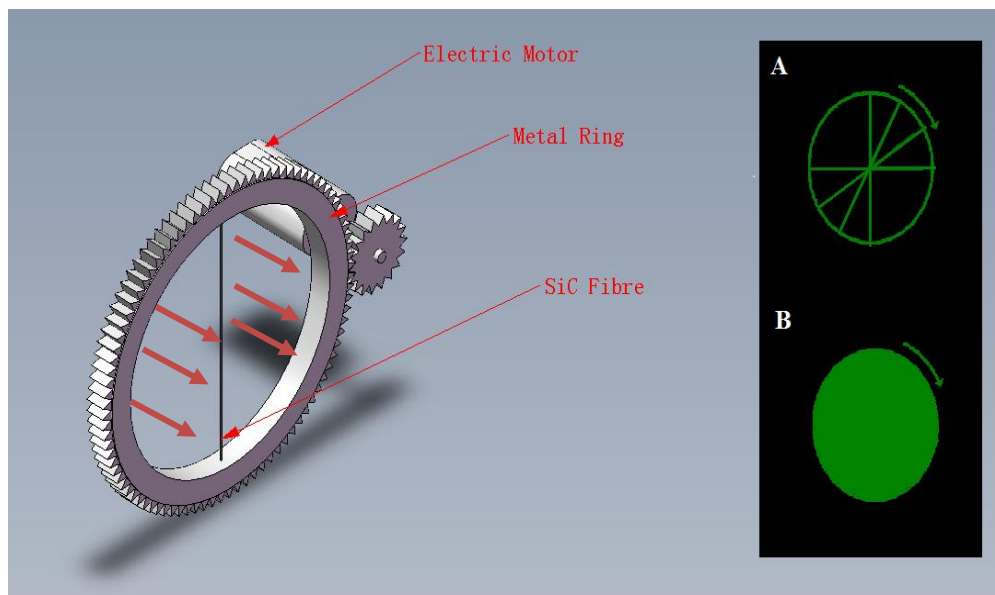


**Figure 8-1** Schematic of the prototype model for the two-dimensional temperature measurement.

- ❖ For future investigation into 3D flame temperature measurement, there are two possible routes. One is to image soot flame directly by the proposed two-colour system with the aid of a stereo adaptor, followed by the postprocess of 3D flame reconstruction and flame temperature calculation. Both based on the captured images. Another route requires the use

of SiC fibre in the form of a 3D mesh. Temperature measurement can thus be performed directly on this 3D mesh using the proposed measurement, subsequently by conducting the heat loss correction the flame temperature can be evaluated. This method is applicable to the hot gas and the flame with soot deficiency.

## REFERENCES

- [1] Y. A. Cengel, *Heat Transfer*, Second ed. New York: McGraw-Hill.
- [2] A. K. Bewoor, *Metrology & Measurement*: McGraw-Hill Education (India) Pvt Limited, 2009.
- [3] O. Uyehara, P. Myers, K. Watson, and L. Wilson, "Flame temperature measurements in internal combustion engines," *Trans. ASME*, vol. 68, pp. 17-30, 1946.
- [4] P. R. N. Childs, J. R. Greenwood, and C. A. Long, "Review of temperature measurement," *Review of Scientific Instruments*, vol. 71, p. 2959, 2000.
- [5] B. C. Connelly, S. A. Kaiser, M. D. Smooke, and M. B. Long, "Two-dimensional soot pyrometry with a color digital camera."
- [6] H. Zhao and N. Ladommatos, "Optical diagnostics for soot and temperature measurement in diesel engines," *Progress in Energy and Combustion Science*, vol. 24, pp. 221-255, // 1998.
- [7] R. Günther, "Flames – Their Structure, Radiation and Temperature. Von A. G. Gaydon und H. G. Wolfhard. Chapman and Hall Ltd., London 1979 4. Aulf., XIII, 449 S., zahlr. Abb. u. Tab., Ln., £ 18.00," *Chemie Ingenieur Technik*, vol. 51, pp. 765-765, 1979.
- [8] J. F. Griffiths and J. A. Barnard, *Flame and Combustion, 3rd Edition*: Taylor & Francis, 1995.
- [9] A. H. Lefebvre, *Gas Turbine Combustion*. London: Taylor&Francis, 1999.
- [10] S. R. Turns, *An intrduction to combustion*. New Yorker: McGraw Hill, 2000.
- [11] T. Foat, K. P. Yap, and Y. Zhang, "The visualization and mapping of turbulent premixed impinging flames," *Combustion and Flame*, vol. 125, pp. 839-851, 4// 2001.
- [12] I. K. Puri, *Environmental Implications of Combustion Processes*: Taylor & Francis, 1993.
- [13] G. A. W. Rutgers and J. C. De Vos, "Relation between brightness, temperature, true temperature and colour temperature of tungsten. Luminance of tungsten," *Physica*, vol. 20, pp. 715-720, 1954.
- [14] J. C. De Vos, "Thesis Amsterdam (V.U.)," 1953.
- [15] G. A. W. R. A. J. C. D. VOS, "RELATION BETWEEN BRIGHTNESS TEMOERATURE, TURE TEMPERATURE AN COLOUR TEMPERATURE OF TUNGSTEN. LUMINACE OF TUNGSTEN," 1954.
- [16] A. R. Bunsell and A. Piant, "A review of the development of three generations of small diameter silicon carbide fibres," *Journal of Materials Science*, vol. 41, pp. 823-839, 2006.
- [17] V. Vilimpoc and L. P. Goss, "SiC-Based thin-filament pyrometry: Theory and thermal properties," *Symposium (International) on Combustion*, vol. 22, pp. 1907-1914, 1989/01/01 1989.

## REFERENCE

- [18] E. R. Cohen and B. N. Taylor, "The 1973 Least - Squares Adjustment of the Fundamental Constants," *Journal of Physical and Chemical Reference Data*, vol. 2, pp. 663-734, 1973.
- [19] F. Pavese and P. P. M. Steur, "<sup>3</sup>He constant-volume gas thermometry: Calculations for a temperature scale between 0.8 and 25 K," *Journal of Low Temperature Physics*, vol. 69, pp. 91-117, 1987.
- [20] S. Eskin and J. Fritze, "Thermostatic bimetals," *Trans. ASME*, vol. 62, p. 433, 1940.
- [21] R. Divita, "Bimetal thermometer selection," *MEASUREMENTS & CONTROL*, pp. 93-95, 1994.
- [22] D. D. Pollock, *The Theory and Properties of Thermocouple Elements*: American Society for Testing and Materials, 1971.
- [23] K. Tobin, S. Allison, M. Cates, G. Capps, and D. Beshears, "High-temperature phosphor thermometry of rotating turbine blades," *AIAA journal*, vol. 28, pp. 1485-1490, 1990.
- [24] A. G. Gaydon and H. G. Wolfhard, "The Spectrum-Line Reversal Method of Measuring Flame Temperature," *Proceedings of the Physical Society. Section A*, vol. 65, p. 19, 1952.
- [25] D. D. Brehob and D. B. Kittelson, "A Review of CI Engine In-Cylinder Diagnostics for the Investigation of Soot Loading, Chemical Composition, and Temperature," SAE Technical Paper 0148-7191, 1988.
- [26] A. Mielke, K. Elam, and C. Sung, "Rayleigh scattering diagnostic for measurement of temperature, velocity, and density fluctuation spectra," in *44th AIAA Aerospace Sciences Meeting and Exhibit*, 2006, pp. 9-12.
- [27] Y. Sun, C. Lou, and H. Zhou, "A simple judgment method of gray property of flames based on spectral analysis and the two-color method for measurements of temperatures and emissivity," *Proceedings of the Combustion Institute*, vol. 33, pp. 735-741, 2011.
- [28] E. K. C. Helen Titus. (2001). *Imaging Sensors*. Available: <http://www.siliconimaging.com/ARTICLES/sensors.htm>
- [29] B. E. Bayer, "Color imaging array," ed: Google Patents, 1976.
- [30] F. Payri, J. V. Pastor, J. M. García, and J. M. Pastor, "Contribution to the application of two-colour imaging to diesel combustion," *Measurement Science and Technology*, vol. 18, pp. 2579-2598, 2007.
- [31] Y. Tominaga, H. Tajima, A. Strom, and K. Uno, "Flame Temperature Measurement in Diesel Engine on Two Color Method utilizing CMOS Camera (Measurement, Temperature)," in *The... international symposium on diagnostics and modeling of combustion in internal combustion engines*, 2004, pp. 7-12.
- [32] H.-C. Zhou, C. Lou, Q. Cheng, Z. Jiang, J. He, B. Huang, *et al.*, "Experimental investigations on visualization of three-dimensional temperature distributions in a large-scale pulverized-coal-fired boiler furnace," *Proceedings of the Combustion Institute*, vol. 30, pp. 1699-1706, 1// 2005.
- [33] B. Ma, G. Wang, G. Magnotti, R. S. Barlow, and M. B. Long, "Intensity-ratio and color-ratio thin-filament pyrometry: Uncertainties and accuracy," *Combustion and Flame*, vol. 161, pp. 908-916, 2014.

## REFERENCE

- [34] H. C. Hottel and F. P. Broughton, "Determination of True Temperature and Total Radiation from Luminous Gas Flames," *Industrial & Engineering Chemistry Analytical Edition*, vol. 4, pp. 166-175, 1932/04/01 1932.
- [35] Y. Huang and Y. Yan, "Transient two-dimensional temperature measurement of open flames by dual-spectral image analysis," *Transactions of the Institute of Measurement and Control*, vol. 22, pp. 371-384, 2000.
- [36] G. Lu, Y. Yan, G. Riley, and H. C. Bheemul, "Concurrent measurement of temperature and soot concentration of pulverized coal flames," *IEEE Transactions on Instrumentation and Measurement*, vol. 51, pp. 990-995, 2002.
- [37] D. Sun, G. Lu, H. Zhou, and Y. Yan, "Flame stability monitoring and characterization through digital imaging and spectral analysis," *Measurement Science and Technology*, vol. 22, p. 114007, 2011.
- [38] M. a. K. Takeuchi, "A spectroscopic detecting system of measuring the temperature distribution of solver breaking arc using a color camera," *Instrumentation and Measurement, IEEE Transactions*, pp. 678-683, 1999.
- [39] S. Simonini, Elston, S. J. and Stone, C.R., "soot temperature and concentration measurements from colour charge coupled device camera images using a three-colour method," *Journal of Mechanical Science* pp. 1041-1052, 2001.
- [40] T. k. Y.Matsui, and S.Matsuika,, "A study on the application of the two-color method to the measurement of flame temperature and soot concentration in diesel engines," *SAE*, pp. 800-970, 1980.
- [41] T. k. Y.Matsui, and S.Matsuika,, "A study on the time and space resolved measurement of flame temperature and soot concentration in a d.i. diesel engine by the two-colour method.," *SAE*, pp. 790-491, 1979.
- [42] "Certificate of calibration," 1994.
- [43] R. D. Larrabee, *The spectral emissivity and optical properties of tungsten*: Citeseer, 1957.
- [44] T. Kadota and H. Yamasaki, "Recent advances in the combustion of water fuel emulsion," *Progress in Energy and Combustion Science*, vol. 28, pp. 385-404, // 2002.
- [45] O. Armas, R. Ballesteros, F. Martos, and J. Agudelo, "Characterization of light duty Diesel engine pollutant emissions using water-emulsified fuel," *Fuel*, vol. 84, pp. 1011-1018, 2005.
- [46] Y. Suzuki, T. Harada, H. Watanabe, M. Shoji, Y. Matsushita, H. Aoki, *et al.*, "Visualization of aggregation process of dispersed water droplets and the effect of aggregation on secondary atomization of emulsified fuel droplets," *Proceedings of the Combustion Institute*, vol. 33, pp. 2063-2070, 2011.
- [47] C. T. Avedisian and R. P. Andres, "Bubble nucleation in superheated liquid-liquid emulsions," *Journal of Colloid And Interface Science*, vol. 64, pp. 438-453, 1978.
- [48] M. Abu-Zaid, "Performance of single cylinder, direct injection Diesel engine using water fuel emulsions," *Energy Conversion and Management*, vol. 45, pp. 697-705, 2004.

## REFERENCE

- [49] H. Watanabe, Y. Suzuki, T. Harada, Y. Matsushita, H. Aoki, and T. Miura, "An experimental investigation of the breakup characteristics of secondary atomization of emulsified fuel droplet," *Energy*, vol. 35, pp. 806-813, 2010.
- [50] W. B. Fu, L. Y. Hou, L. Wang, and F. H. Ma, "A unified model for the micro-explosion of emulsified droplets of oil and water," *Fuel Processing Technology*, vol. 79, pp. 107-119, 10/20/ 2002.
- [51] M. N. a. H. K. M. MIKAMI, "Clarification of the flame structure of droplet burning based on the temperature measurement in microgravity," *The combustion Institute*, pp. 439-446, 1994 1994.
- [52] G. J. W.L.saw, P.J.Ashman, Z.T.Alwahabi,M.Hupa, "Surface temperature measurement of a burning black liquor droplet using two-colour optical pyrometry," *Proceedings of the Australian Combustion Institute*, 2009.
- [53] G. Jackson and C. Avedisian, "Combustion of unsupported water-in-n-heptane emulsion droplets in a convection-free environment," *International journal of heat and mass transfer*, vol. 41, pp. 2503-2515, 1998.
- [54] V. Califano, R. Calabria, and P. Massoli, "Experimental evaluation of the effect of emulsion stability on micro-explosion phenomena for water-in-oil emulsions," *Fuel*, vol. 117, pp. 87-94, 2014.
- [55] J. C. Lasheras, A. C. Fernandez-Pello, and F. L. Dryer, "Eighteenth Symposium (International) on Combustion On the disruptive burning of free droplets of alcohol/n-paraffin solutions and emulsions," *Symposium (International) on Combustion*, vol. 18, pp. 293-305, 1981/01/01 1981.
- [56] T. Niioka and J. i. Sato, "Twenty-First Symposuim (International on Combustion) Combustion and microexplosion behavior of miscible fuel droplets under high pressure," *Symposium (International) on Combustion*, vol. 21, pp. 625-631, 1988/01/01 1988.
- [57] J. S. Basha and R. Anand, "An experimental investigation in a diesel engine using carbon nanotubes blended water–diesel emulsion fuel," *Proceedings of the Institution of Mechanical Engineers, Part A: Journal of Power and Energy*, vol. 225, pp. 279-288, 2011.
- [58] C. K. Law, "Recent advances in droplet vaporization and combustion," *Progress in Energy and Combustion Science*, vol. 8, pp. 171-201, 1982/01/01 1982.
- [59] R. Ochoterena, A. Lif, M. Nydén, S. Andersson, and I. Denbratt, "Optical studies of spray development and combustion of water-in-diesel emulsion and microemulsion fuels," *Fuel*, vol. 89, pp. 122-132, 2010.
- [60] M. V. Heitor and J. H. Whitelaw, "Velocity, temperature, and species characteristics of the flow in a gas-turbine combustor," *Combustion and Flame*, vol. 64, pp. 1-32, 1986/04/01 1986.
- [61] R. Ocampo-Barrera, R. Villasenor, and A. Diego-Marin, "An experimental study of the effect of water content on combustion of heavy fuel oil/water emulsion droplets," *Combustion and Flame*, vol. 126, pp. 1845-1855, 9// 2001.
- [62] T. Fu, Z. Wang, and X. Cheng, "Temperature Measurements of Diesel Fuel Combustion With Multicolor Pyrometry," *Journal of Heat Transfer*, vol. 132, p. 051602, 2010.

## REFERENCE

- [63] S. Pautin, A. Giovannini, and B. Bédard, "Thin filament infrared pyrometry: instantaneous temperature profile measurements in a weakly turbulent hydrocarbon premixed flame," *Experiments in Fluids*, vol. 17, pp. 397-404, 1994.
- [64] P. b. Jignesh D. Maun, and David L. Urban, "Thin-filament pyrometry with a digital still camera," *Optical Society of America*, vol. 46, pp. 483-488, 2007.
- [65] P. S. a. D. Diethrich, "Comparison of gas-phase temperature measurements in a flame using thin-filament pyrometry and thermocouple," presented at the 41st Aerospace sciences meeting and exhibit, 2003.
- [66] S. V. Patankar, *Numerical Heat Transfer and Fluid Flow*.
- [67] D. Bradley and K. Matthews, "Measurement of high gas temperatures with fine wire thermocouples," *Journal of Mechanical Engineering Science*, vol. 10, pp. 299-305, 1968.
- [68] A. Yoshida and R. Günther, "Experimental investigation of thermal structure of turbulent premixed flames," *Combustion and Flame*, vol. 38, pp. 249-258, 1980/01/01 1980.
- [69] W. M. Pitts, "Temperature Uncertainties for Bare Bead and Aspirated Thermocouple Measurements in Fire Environment," *The Foundation of Fire Standards*.
- [70] P. B. Kuhn, B. Ma, B. C. Connelly, M. D. Smooke, and M. B. Long, "Soot and thin-filament pyrometry using a color digital camera," *Proceedings of the Combustion Institute*, vol. 33, pp. 743-750, 2011.
- [71] I. Shepherd, R. Cheng, and M. Day, "The dynamics of flame flicker in conical premixed flames: an experimental and numerical study," *Lawrence Berkeley National Laboratory*, 2005.
- [72] J. P. Holman, *Heat Transfer*. New York: McGraw, 2008.
- [73] L. TECHNOLOGIES. (2016). *Pyrometer Impac IS 5*. Available: <http://www.lumasenseinc.com/EN/products/infrared-thermometers-and-switches/pyrometer-series-5/pyrometer-impac-is-5.html>
- [74] B. Lewis and G. Von Elbe, *Combustion, Flames, and Explosions of Gases*: Academic Press, 1987.
- [75] G. Ciccarelli and S. Dorofeev, "Flame acceleration and transition to detonation in ducts," *Progress in Energy and Combustion Science*, vol. 34, pp. 499-550, 2008.
- [76] J. Yang, F. M. S. Mossa, H. W. Huang, Q. Wang, R. Woolley, and Y. Zhang, "Oscillating flames in open tubes," *Proceedings of the Combustion Institute*, vol. 35, pp. 2075-2082, // 2015.
- [77] E. Mallard and H. Le Chatelier, "Combustion of explosive gas mixtures," *Ann. Mine*, 1883.
- [78] H. F. Coward and F. J. Hartwell, "277. Studies in the mechanism of flame movement. Part I. The uniform movement of flame in mixtures of methane and air, in relation to tube diameter," *Journal of the Chemical Society (Resumed)*, pp. 1996-2004, 1932.
- [79] H. Guénoche, *Non-steady Flame Propagation*. New York: Pergamon 164.
- [80] A. Gaathaug, D. Bjerketvedt, and K. Vaagsaether, "DDT in homogeneous and inhomogeneous hydrogen-air mixtures," in *Proceedings of the 7th international seminar on fire & explosion hazards*, 2013.

## REFERENCE

- [81] X. Shen, X. He, and J. Sun, "A comparative study on premixed hydrogen–air and propane–air flame propagations with tulip distortion in a closed duct," *Fuel*, vol. 161, pp. 248-253, 2015.
- [82] M. Gonzalez, "Acoustic instability of a premixed flame propagating in a tube," *Combustion and Flame*, vol. 107, pp. 245-259, 1996/11/01 1996.
- [83] V. Bychkov, V. y. Akkerman, G. Fru, A. Petchenko, and L.-E. Eriksson, "Flame acceleration in the early stages of burning in tubes," *Combustion and Flame*, vol. 150, pp. 263-276, 2007.
- [84] H. Hua-Wei and Z. Yang, "Flame colour characterization in the visible and infrared spectrum using a digital camera and image processing," *Measurement Science and Technology*, vol. 19, p. 085406, 2008.
- [85] J. Cook, "Flames in Tubes," Mechanical Engineering, University of Sheffield, Sheffield, 2008.
- [86] F.Mossa, "Flames in Tube ", Mechanical Engineering University of Sheffield, Sheffield, 2014.
- [87] M. Metghalchi and J. C. Keck, "Burning velocities of mixtures of air with methanol, isooctane, and indolene at high pressure and temperature," *Combustion and flame*, vol. 48, pp. 191-210, 1982.
- [88] M. Metghalchi and J. Keck, "Laminar burning velocity of propane-air mixtures at high temperature and pressure," *Combustion and flame*, vol. 38, pp. 143-154, 1980.
- [89] C. Ebieto, "Dynamic Characterization of Premixed Flame Oscillations in Tubes," Transfer Review Transfer Report, Department of mechanical engineering, University of Sheffield, 2015.